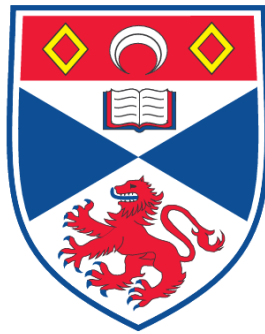


**YB-DOPED FEMTOSECOND LASERS AND THEIR  
FREQUENCY DOUBLING**

**Abdul Rahman Sarmani**

**A Thesis Submitted for the Degree of PhD  
at the  
University of St. Andrews**



**2008**

**Full metadata for this item is available in the St Andrews  
Digital Research Repository**

**at:**

**<https://research-repository.st-andrews.ac.uk/>**

**Please use this identifier to cite or link to this item:**

**<http://hdl.handle.net/10023/781>**

**This item is protected by original copyright**

# **“Yb-doped Femtosecond Lasers and Their Frequency Doubling”**



Thesis presented for the degree of  
Doctor of Philosophy  
To the University of St. Andrews  
by  
Abdul Rahman Sarmani

Supervisor: Prof. Wilson Sibbett.

The J. F. Allen Physics Research Laboratory,  
School of Physics and Astronomy,  
University of St. Andrews,  
North Haugh,  
St. Andrews,  
Scotland, KY16 9SS.

14 March 2008

## Declarations

I, Abdul Rahman Sarmani, hereby certify that this thesis, which is approximately thirty four thousand words in length, has been written by me, that it is the record of work carried out by me and that it has not been submitted in any previous application for a previous degree.

Signature of candidate

Date: 14/03/2008

I was admitted as a research student and as a candidate for the degree of Doctor of Philosophy in 2008; the higher study for which this is a record was carried out at the University of St Andrews between 2004 and 2008.

Signature of candidate

Date: 14/03/2008

I hereby certify that the candidate has fulfilled the conditions of the Resolution and Regulations appropriate for the degree of Doctor of Philosophy in the University of St Andrews and that the candidate is qualified to submit this thesis in application for that degree.

Signature of supervisor

Date: 14/03/2008

In submitting this thesis to the University of St Andrews I understand that I am giving permission for it to be made available for use in accordance with the regulations of the University Library for the time being in force, subject to any copyright vested in the work not being affected thereby. I also understand that the title and the abstract will be published, and that a copy of the work may be made and supplied to any *bona fide* library or research worker.

Signature of candidate

Date: 14/03/2008

***For those who love Science:-***

*“Proclaim! (or read!) in the name of thy Lord and Cherisher, Who created-*

*Created man, out of a (mere) clot of congealed blood:*

*Proclaim! And thy Lord is Most Bountiful,-*

*He Who taught (the use of) the pen,-*

*Taught man that which he knew not.”*

## Abstract

Ultralow threshold, compact and highly efficient femtosecond lasers based on Yb<sup>3+</sup>-doped potassium yttrium tungstate (Yb:KYW) and Yb<sup>3+</sup>-doped vanadium yttrium oxide (Yb:YVO<sub>4</sub>) have been demonstrated within this PhD-research project. For a continuous wave unmode-locked Yb:KYW laser a threshold as low as 101 mW was obtained with a slope efficiency of 74 %. By employing a single prism for dispersion control, the laser was tunable between 1012 nm to 1069 nm. When operated in the mode-locked regime, this laser produced transform-limited pulses having durations of 210 fs at a central wavelength of 1044 nm. Stable mode locking was observed for an optimised incident pulse fluence on the SESAM between 140  $\mu\text{J}/\text{cm}^2$  to 160  $\mu\text{J}/\text{cm}^2$  which was 2-3 times higher than the designed energy pulse fluence of the SESAM (70  $\mu\text{J}/\text{cm}^2$ ).

The employment of several combinations of chirped mirror designs for control of intracavity group velocity dispersion led to excellent results. The threshold for mode locking was satisfied for a pump power of 255 mW where the slope efficiency was measured to be 62 %. This is the most efficient SESAM-assisted femtosecond laser yet reported and the highest optical-to-optical efficiency of 37 % is exceptional. Transform-limited pulses with durations as short as 90 fs were produced in a spectral region centred on 1052 nm. The success of this research thus represents a good foundation on which to design and build more compact configurations that will incorporate just one chirped mirror for dispersion compensation.

A relatively high nonlinear refractive index,  $n_2$ , of  $15 \times 10^{-16} \text{ cm}^2/\text{W}$  was measured in Yb:YVO<sub>4</sub> and this affords particular potential for this candidate material in Kerr-lens mode locking. In fact, for operation in the femtosecond domain, the threshold power was 190 mW with a slope efficiency of 26 % and near-transform-limited pulses as short as 61 fs were generated at a centre wavelength of 1050 nm. The main objectives in developing this type of laser relate to a demonstration of high peak power operation in thin disc laser configurations.

The deployment of a diode-pumped Yb:KYW femtosecond laser as a pump source for frequency doubling in a periodically-poled LiTaO<sub>3</sub> crystal was realised. The maximum realized output power of 150 mW corresponded to an impressive second harmonic conversion efficiency of 43 %. 225-fs duration green pulses (centred at 525 nm) were generated under the condition of strong focusing in the nonlinear crystal.

## Contents

Declarations	ii
Abstract	iv
Contents	v
<b>1 Introduction:</b>	
1.1 Ultrashort-pulse laser phenomena in the natural world	1
1.2 Applications of ultrashort-pulse lasers	2
1.3 References	6
<b>2 Ultrashort Pulse Generation and Solid-State Laser Materials</b>	
2.1 Introduction	8
2.2 Ultrashort pulse generation	8
2.3 Mode-locking techniques	13
2.3.1 Kerr-lens mode locking	15
2.3.2 Saturable absorbers and semiconductor saturable absorber mirrors (SESAMs)	17
2.4 Pulse polarisation in the dielectric medium	21
2.5 Introduction to solid-state laser materials	25
2.5.1 Host materials	25
2.5.2 Active ions	26
2.6 Alternative solid-state laser candidates- Why Ytterbium ions ?	29
2.7 A Basic Review on Femtosecond Laser Sources	33
2.8 Conclusion	35
2.9 References	37
<b>3 Basic Parameters for Low Threshold, Compact and Highly Efficient Femtosecond Lasers.</b>	
3.1 Introduction	43
3.2 Laser performance	43
3.3 Towards Low Threshold, Compact and High-Efficiency Yb-doped Femtosecond Lasers	49

3.4	Conclusion	53
3.5	References	54
<b>4</b>	<b>Compact and Highly Efficient Yb:KYW Laser with a Single Prism for Dispersion Compensation.</b>	
4.1	Introduction	56
4.2	Ytterbium-doped crystals	57
4.3	Yb-doped KY(WO <sub>4</sub> ) <sub>2</sub> and KGd(WO <sub>4</sub> ) <sub>2</sub> crystals	58
4.4	Comparison between Yb-doped tungstate materials	60
4.5	A sequence of prisms for dispersion compensation	63
4.6	Implementation	69
4.7	Continuous wave (unmode-locked) configuration	72
4.8	Passive mode locking configuration with a SESAM	75
4.9	Optimisation of energy pulse fluence incident on the SESAM	78
4.10	Tunability of a single prism Yb:KYW femtosecond laser	80
4.11	Conclusion	82
4.12	References	83
<b>5</b>	<b>Compact and Highly Efficient Prismless Diode-Pumped Yb:KYW Femtosecond Laser.</b>	
5.1	Introduction	85
5.2	New techniques for dispersion compensation	86
5.3	Dispersive mirrors	87
5.4	Implementation	96
5.5	Prismless-cavity results (-455 fs <sup>2</sup> x 2, -370 fs <sup>2</sup> x 2)	99
5.6	Improvement of prismless-cavity results (-455 fs <sup>2</sup> x 1, -370 fs <sup>2</sup> x 1)	101
5.7	Optimisation of dispersion compensation inside the laser oscillators (-455 fs <sup>2</sup> x 1, -110 fs <sup>2</sup> x 1)	101
5.8	Optimisation of the laser configuration	103
5.9	Prismless-cavity results (-455 fs <sup>2</sup> x 1, -370 fs <sup>2</sup> x 1)	105
5.10	Conclusion	109
5.11	References	110

<b>6</b>	<b>Yb<sup>3+</sup>-doped YVO<sub>4</sub> Crystal for Efficient Kerr-lens Mode Locking in Solid-State Lasers.</b>	
6.1	Introduction	114
6.2	Optical Kerr effect in isotropic media	114
6.3	Analysis of the self-focusing effect	116
6.4	The measurement of the nonlinear refractive index $n_2$	119
6.5	A Yb <sup>3+</sup> :YVO <sub>4</sub> Laser	124
6.6	Implementations	127
	6.6.1 Measurement of $n_2$	127
	6.6.2 Kerr-lens mode locking implementation	129
6.7	Continuous wave (unmode locked) operation	130
6.8	Kerr lens mode locking results	134
6.9	Conclusion	137
6.10	References	139
<b>7</b>	<b>Efficient Ultrashort Pulse Visible Sources.</b>	
7.1	Introduction	143
7.2	Nonlinear wave phenomena in a dielectric medium	143
	7.2.1 Phase-matched second harmonic generation	146
	7.2.2 Critical and noncritical phase matching	149
	7.2.3 Phase matching bandwidth	151
7.3	Quasi-phase matched second harmonic generation	152
7.4	Periodically-poled devices for quasi-phase matching	156
7.5	Frequency doubling with a thick nonlinear crystal in an extracavity configuration	157
7.6	Implementations	159
	7.6.1 Experimental set-up	159
	7.6.2 Periodically poled Lithium Tantalate	161
7.7	Experimental results	163
7.8	Conclusion	169
7.9	References	170

<b>8</b>	<b>Final Remarks</b>	
8.1	Conclusion	173
8.2	Future Work	174
8.3	References	178
	Publication Lists	179
	Appendices	181
	Acknowledgements	192

# Chapter 1: Introduction

## 1.1 Ultrashort-pulse Laser Phenomena in the Natural World

In a couple of years after the invention of lasers by T.H. Maiman [1], many methods were developed to produce light pulses in the microsecond ( $\mu\text{s}$ ) and nanosecond (ns) regimes. De Maria and co-workers [2] produced the first ultrashort pulses using a passively mode-locked Nd:glass laser which opened up the study of lasers that operated in this picosecond regime. Extensive developments of femtosecond techniques were achieved in the 1970s and 1980s with the domination of dye lasers before the introduction of solid state Ti:sapphire lasers in the late 1980s. To date, the shortest pulse duration in the world generated directly from a Kerr lens mode locked Ti:sapphire laser is 5 fs ( $5 \times 10^{-15}$ ) [3].

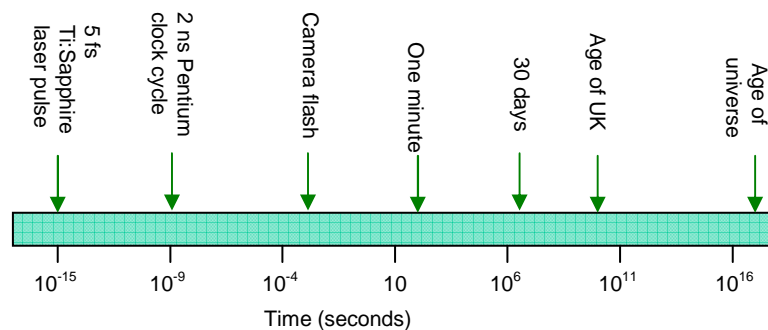


Figure 1.1. The time comparison between femtosecond scales with man-made and natural events [4].

The ratio of 5 fs to one second is about the ratio of 37 minutes to the age of the universe (14 billion years). During this shortest pulse duration, visible light travels over a distance of one thousand five hundred nanometers which is at a length scale that is not of concern in the daily lives of most individuals. However, this propagation distance corresponds to several thousands of elementary cells in a solid and this begins to illustrate the importance of the femtosecond regime in a high-resolution world. This opens up new applications of femtosecond lasers in physics, chemistry and biology due to the various basic processes in the natural world such as interactions between atoms and molecules which proceed faster than the picosecond time scale [5]. A useful example is the basic physical reaction between hydrogen atoms because it is one of the fastest in nature. The vibration of

two hydrogen atoms bound in a molecule occurs in a period of about 10 fs, which means that a metronome operating one beat per second would have to run for almost 3.2 million years to have an equivalent number of cycles to that of the hydrogen atom oscillations in a second.

## 1.2 Applications of Ultrashort-pulse Lasers

Femtosecond techniques open up new and fascinating possibilities for many applications in physics, chemistry, and biology ranging from telecommunications, high precision micromachining and spectroscopy to biomedical and biological implementations [6]. This is based on the unique properties of femtosecond light pulses such as their high repetition rate, short pulse duration, high peak power, and broad spectrum. However, in this project, the femtosecond lasers were designed to produce a relatively low average output power of a few hundred milliWatts and this limits their applications to areas such as femtochemistry, 3-dimensional imaging, biology, and biomedicine. Although the average output power of these femtosecond lasers is quite moderate, the peak power is quite high at tens of kW. The relation between peak power ( $P_{pk}$ ) with the average output power ( $P_{av}$ ) is:-

$$P_{pk} = \frac{P_{av}}{f_{rep} \times \tau_p} \quad (1.2.1)$$

where the pulse energy is:-

$$E_p = P_{pk} \times \tau_p \quad (1.2.2)$$

where  $f_{rep}$  is pulse repetition frequency and  $\tau_p$  is the pulse duration. For example, a laser that is designed at a pulse repetition rate of 212 MHz can produce an average output power of 300 mW with pulse durations of 100 fs. This corresponds to a peak power of 14 kW and a pulse energy of 1.4 nJ. An intensity as high as 2.8 MW/cm<sup>2</sup> can be exhibited if this pulse is focused to a 50  $\mu\text{m}^2$  spot.

This pulse deposits the energy at the focus too rapidly for the heat to diffuse into surrounding unirradiated areas as the atom/molecular interactions take place slower than the femtosecond regimes, thus avoiding thermal damage. This minimizes damage to the

surrounding zones in the material. This ensures precise cutting features for smooth and cleaner ablations with a reduced shock affected zone (SAZ) and heat affected zone (HAZ) in comparison to that of mechanical blades or longer laser pulses. These advantages apply, for example, to corneal laser surgeries to correct astigmatism, myopia and hyperopia [7]. During this type of surgery, laser beams can pass through the cornea without affecting the tissue to interact with the desired photo-disruption target. Since the cornea is transparent, the underneath layer can be cut to remove the overlay tissue by suction. The process is sufficiently short to avoid any damage occurring to the adjacent tissue, thus reducing any complications such as post-surgical infection, under correction, night glare, regression or backward shift. Other biomedical and biological applications of ultrashort pulses include brain surgery [8], optical tomography [9], optical tweezers [10], and multiphoton microscopy [11].

In optical tomography, ultrashort pulses can be used to detect abnormalities in the body without involving potentially harmful ionising radiation. This process is based on the principle that human tissues are partially transparent to some bands of near-infra red radiation. Data obtained from this scanning can be processed to detect changes in tissue optical properties that might for instance indicate the presence of tumors. Another technique to develop 3D images of soft tissues or skin for medical purposes is multi-photon excitation microscopy. In this technique, ultrashort pulses excite fluorescence signals in biological samples with the related exploitation of nonlinear effects. Due to the fact that different types of tissues exhibit distinctive decay rates, the measurement of the decay time of the return signal allows the mapping of some biological substances. At the same average output power, sub-100 fs pulses can image two to three times deeper inside a sample compared to that of picosecond pulses due to their higher peak power. This same mechanism applies in optical tweezers where only a few mW average power of a focused laser beam is needed for the confinement and manipulation of microscopic particles in three-spatial dimensions. Although the use of femtosecond lasers is as efficient as that of CW (continuous wave) lasers, the high pulse peak power property of the former regimes induces nonlinear processes within trapped particles such as multi-photon absorption and harmonic generation. This allows optional and controllable self-marking of tweezed nonlinear particles as the laser can be switched between the unmode-locked and femtosecond regimes. In addition, the sensitivity of fluorescence studies of biological samples can also be increased at average power levels well below their thermal damage threshold. All of these advantages are beneficial for tracking and observing biological fluorophores.

The pioneering work of Ahmad Zewail at California Institute of Technology in femtochemistry [12] is also very noteworthy in the present context. In effect, he invented the world's fastest camera which enabled researchers to see chemical reactions within the timeframe of a few hundred femtosecond regimes, earning him the Nobel Prize for Chemistry in 1999. With this technique which uses laser femtosecond pulses, the chemical reaction, bonding, and breaking within atoms or molecules can be studied in slow motion while the interdependence between the speed of reaction on temperature can be explained. In addition, the dynamics of electrons within semiconductor materials can also be effectively "freeze framed" to enable scientists to design better optoelectronic devices demanded by the telecommunications and computer industries to achieve the ever-increasing capacity needs of modern society. Other developments of this technique have provided useful insights into the function of catalysts, the vital mechanisms in life processes as well as new methods of designing electronic components. In the pharmaceutical industry, the function of certain drugs at the chemical level can also be observed, accommodating the production of new medicines.

For non-destructive techniques, terahertz radiation from ultrashort pulses can be used for thickness monitoring and quality control of semiconductor/metal layers at production lines with a high accuracy. This technique avoids any damage to the materials and can be extended to produce 3-D images for ceramic weapons detection at airports, measurement of temperature gradients across flames, and the mapping of dielectric interfaces inside a ball point or a floppy disk. Additionally, one can exploit the sensitivity of pulses to any small changes of refractive index of materials, for instance the watermark in a £ 5 note can be imaged with a high accuracy to detect forgeries. All of these industrial imaging techniques [13] are made possible, with the exploitation of the longer wavelength pulses to produce a finer resolution of images for the materials which are opaque to shorter wavelength such as plastic, semiconductor, cardboard, biological tissues, and paper.

All of the applications mentioned above can benefit from innovative research that advances the science and technology of ultrashort pulse lasers in terms of size, cost, practicability, and portability. For the achievement of these motivations, the objectives of my PhD project were to construct experimental ultralow threshold, compact and high efficiency Kerr-lens and semiconductor saturable absorber-assisted mode locked lasers based on new ytterbium-doped materials such as  $\text{Yb}^{3+}$ -doped potassium yttrium tungstate [ $\text{Yb}^{3+}:\text{KY}(\text{WO}_4)_2$ ] or  $\text{Yb}:\text{KYW}$  and  $\text{Yb}^{3+}$ -doped vanadium yttrium oxide [ $\text{Yb}^{3+}:\text{YVO}_4$ ] or  $\text{Yb}:\text{YVO}_4$ . In  $\text{Yb}:\text{KYW}$  femtosecond lasers, new cavity designs were implemented with

miniaturized dispersion compensation mechanisms by using a single prism and chirped mirrors instead of prism pairs. Later assessments were carried out for nonlinear optical frequency up-conversion by using a Yb:KYW laser as a pump source for generating femtosecond pulses in the visible regimes.

### 1.3 References.

1. T. H. Maiman, "Stimulated Optical Radiation in a Ruby," *Nature* **187**, 493-494 (1960).
2. A. J. De Maria., D. A. Stetser and H. Heynau, "Self-mode locking of Lasers with Saturable Absorbers," *Appl. Phys. Lett.* **8**, 174-176 (1966).
3. R. Ell, U. Morgner, F. X. Kartner, J. G. Fujimoto, E. P. Ippen, V. Scheuer, G. Angelow, T. Tschudi, M. J. Lederer, A. Boiko, and B. Luther-Davies, "Generation of 5-fs pulses and octave-spanning spectra directly from a Tisapphire laser," *Opt. Lett.* **26**, 373-375 (2001).
4. H. Kapteyn and M. Murnane, "Ultrashort light pulses, life in the fast lane," *Physics World*, 31-35 (Jan. 1999).
5. J. C. Diels and W. Rudolph, "Ultrashort Laser Pulse Phenomena," Academic Press, California, xv-xviii (1999).
6. S. Svanberg, "Some applications of ultrashort laser pulses in biology and medicine," *Meas. Sci. Technol.* **12**, 1777-1783 (2001).
7. J. Yuen, "Ophthalmic applications of ultrashort pulsed fiber lasers," Department of Electrical and Computer Engineering, U. of California, San Diego (2004).
8. M. H. Goetz, S. K. Fischer, A. Velten, J. F. Bille, and V. Sturm, "Computer-guided laser probe for ablation of brain tumours with ultrashort laser pulses," *Phys. Med. Biol* **44**, N119- 127 (1999).
9. J. C. Hebden, F. E. W. Schmidt, M. E. Fry, M. Schweiger, E. M. C. Hillman, D. T. Delpy, and S. R. Arridge, "Simultaneous reconstruction of absorption and scattering images by multichannel measurement of purely temporal data," *Opt. Lett.* **24**, 534-536 (1999).
10. B. Agate, C. T. A. Brown, W. Sibbett, and K. Dholakia, "Femtosecond optical tweezers for in-situ control of two-photon fluorescence," *Opt. Express* **12**, 3011-3017 (2004).
11. W. Denk, D. W. Piston, and W. Webb, "Two-photon molecular excitation in laser-scanning microscopy," *Handbook of Biological Microscopy*, Plenum Press, New York (1995).
12. A. H. Zewail, "Femtochemistry—Ultrafast Dynamics of the Chemical Bond," vols. I and II, World Scientific, New Jersey, Singapore (1994).

13. J.M. Hopkins and W. Sibbett, "Ultrashort pulse lasers: Big payoff in a flash," *Scientific American*, 55-61 (2000).

## Chapter 2

### **Ultrashort-pulse Generation and Solid-state Laser Materials.**

#### **2.1 Introduction.**

This chapter can be divided into two sections where the first relates to a description of ultrashort pulse generation while the subject of the second is solid state laser materials. The scene is set with a theoretical overview of the generation of a sequence of intense bursts of pulses in the femtosecond regime. This is followed by a consideration of polarisation effects in the laser oscillators which involve linear dispersion, self-focusing, self-phase modulation and second harmonic generation. The mode locking techniques in the laser system can be initiated by the Kerr-lensing effect and saturable absorption based on semiconductor-mirror technology which is known as semiconductor saturable absorber mirror (SESAM). The relevant optical Kerr effect and SESAM-assisted parameters needed for mode locked operations are discussed. The following section relates to solid-state laser materials which represented new laser crystals for our St. Andrews research group and the thesis material presented concerns a review of gain media that are favourable for laser action. These consist of crystalline host materials and active ions based on Ti:Sapphire and Yb-doped crystals. Significantly, the few disadvantages of Ti:Sapphire lasers which result in a high threshold and a low efficiency of operation with limited portability have opened up an opportunity and requirement for investigating new broadband gain media based on ytterbium-doped materials for the generation of femtosecond pulses. All the relevant spectroscopic and laser properties of the latter materials are explained to show their suitability to the construction of low threshold, compact and highly efficient femtosecond lasers that can address a range of scientific and industrial applications. A basic review on lasers based on Cr-doped crystals, semiconductor and fibre hosts are also reported because this gives an insight to related research on other femtosecond lasers that are under current development.

#### **2.2 Ultrashort Pulse Generation.**

Many methods were developed previously to generate short/ultrashort, intense bursts of pulses [1,2,3] such as Q-Switching [4], gain-switching [5], and cavity dumping [6]. However,

these methods produce pulses in the nanosecond regime from large-frame lasers, thus a method such as mode-locking is required to generate pulses in picosecond and femtosecond regimes.

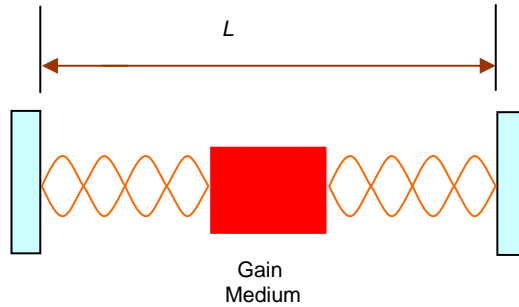


Figure 2.1. Standing wave resonator configuration [2].

A simple laser oscillator consists of a gain medium that is incorporated in a standing wave (Fabry Perot) optical cavity as shown in figure 2.1. This gain medium is pumped by a flashlamp/arclamp or a pump laser source and consists of two mirrors with one mirror that is partially transmitting. Longitudinal mode frequencies are allowed to oscillate as determined by the cavity length between the mirrors. When  $L$  is the physical separation of the mirrors, the optical length is  $nL$  and allowed mode frequencies satisfy the relationship:-

$$\frac{m\lambda}{2} = nL \quad (2.2.1)$$

where  $m$  is the order of the longitudinal mode,  $\lambda$  is the wavelength, and  $n$  is the average value of the refractive index. With the assumption that the laser is operating in the fundamental transverse mode  $TEM_{00}$ , there can be thousands of these axial modes that reach laser threshold. The allowed frequency  $\nu_m$  of the modes is given as:-

$$\nu_m = \frac{mc}{2nL} \quad (2.2.2)$$

From the derivation of the frequency mode  $\nu_m$ , the frequency separation  $\delta\nu_{rep}$  and the angular frequency  $\delta\omega_{rep}$ , between two neighbouring modes are:-

$$\partial v_{rep} = \frac{c}{2nL} \quad (2.2.3)$$

$$\delta\omega_{rep} = \frac{\pi.c}{nL} \quad (2.2.4)$$

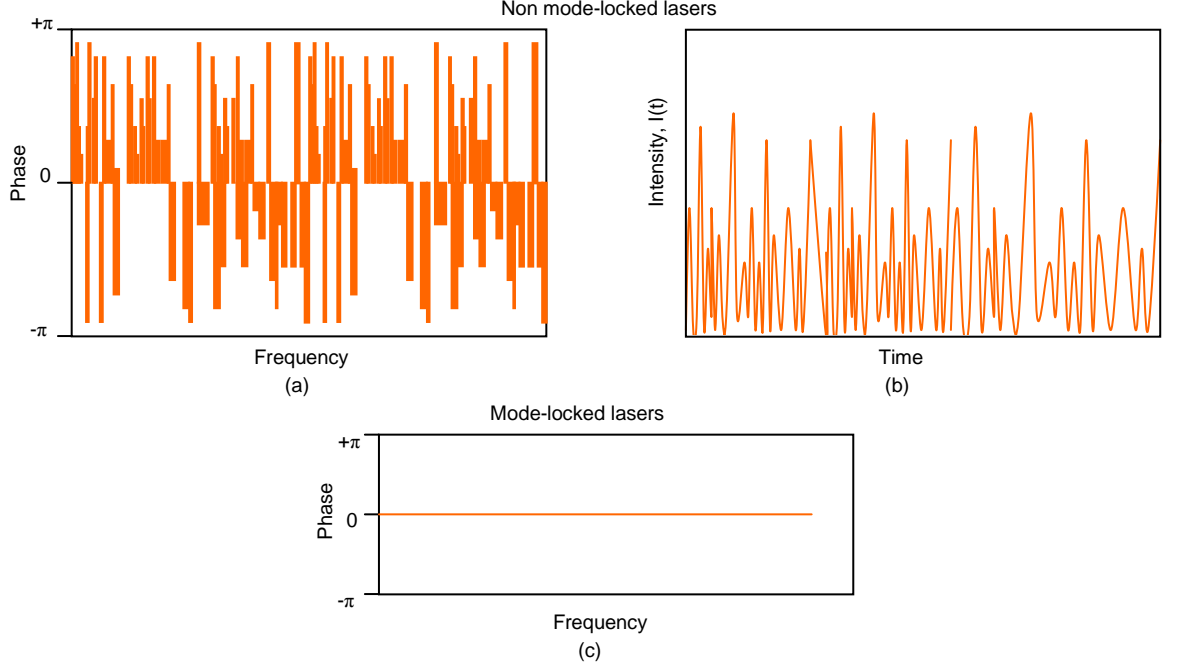


Figure 2.2. Signal emitted from non mode-locked lasers, (a) Spectral phases for random distribution in the range of  $-\pi$  to  $+\pi$  as a function of frequency domain and (b) the corresponding intensity in the time domain with the characteristics of thermal noise while (c) is spectral phases for mode-locked lasers [3].

In free running lasers, both the longitudinal and transverse modes oscillate randomly in time without fixed mode to mode amplitude and phase relationship. The spectral and temporal structure of the radiation for a non mode-locked laser are shown in figure 2.2(a) and (b). Each mode oscillates independently of the others and the phases are randomly distributed in the range of  $-\pi$  to  $+\pi$ . In the time domain, the field consists of an intensity distribution that has the characteristics of thermal noise, resulting from the random addition of each propagating mode. The corresponding electric field emitted from the output of a laser for  $N_t$  axial modes can thus be described as:-

$$E(t) = \sum_{N=-m}^m (E_0)_N \exp[i(\omega_o + N.\delta\omega_{rep})t + (\varphi_0)_N] \quad (2.2.5)$$

where  $N_t = (2N + 1)$  and  $N$  are the modes to a frequency lower than the centre frequency and they are also the modes to a frequency higher than the centre frequency. All the

parameters such as the amplitude  $(E_0)_N$  and phase  $(\varphi_0)_N$  of the  $N$ -th mode, central angular frequency of the gain bandwidth curve  $\omega_0$ , and the angular frequency separation of the adjacent modes  $\delta\omega_{rep}$ , vary independently of each other.

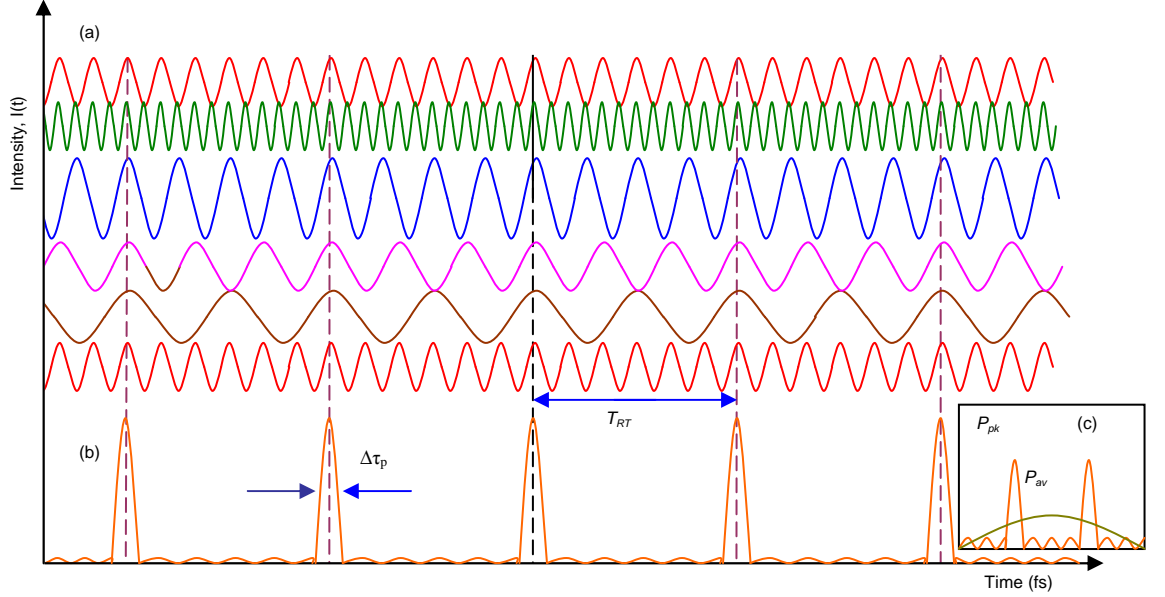


Figure 2.3. Pulse sequences from a mode locked laser, (a) random intense pulses in the laser cavity, (b) ultra short pulses in femtosecond regime which is produced when these random intense pulses add up together in phase at one instant time and (c) the corresponding peak power (orange) and average power of the pulse (green) [1].

By enforcing coherence between the phases of different modes, the output add up together in phase as a function of time, resulting in the evolution of a periodic sequence of intense ultrashort pulses from a stochastic intensity output as shown in figure 2.3. The laser is now said to be phase-locked or mode-locked and if the accessible bandwidth is sufficiently large then pulses can have durations in the femtosecond regimes. The resulting field can be expressed as:-

$$E(t) = E_0 \sum_{N=-m}^m \exp i(\omega_0 + N \cdot \delta\omega_{rep})t \quad (2.2.6)$$

where all the phases of the modes and amplitude of the electric field are equal which results in  $(\varphi_0)_N = 0$  (figure 2.2c) and  $(E_0)_N = E_0$ . The equation above describes the proportionality between  $E(t)$  with the sinusoidal carrier of frequency  $\omega_0$  where the amplitude of the pulses changing in time as shown in figure 2.3 and can be summarised as:-

$$E(t) = E_0 \left[ \frac{1 - \exp i N_t (\delta\omega_{rep}) t}{1 - \exp i (\delta\omega_{rep}) t} \right] \quad (2.2.7)$$

Therefore, the relationship between the intensity of the pulse  $I(t)$  with  $E(t)$  and the complex conjugate  $E^*(t)$  can be expressed as:-

$$I(t) = E(t)E^*(t) = E_0^2 \frac{\sin^2(N_t \pi t / T_{RT})}{\sin^2(\pi t / T_{RT})} \quad (2.2.8)$$

The equations above show that a substantial increase in peak intensity  $I(t)$  of the ultrashort pulses can be achieved with a large number of longitudinal modes being phase-locked. These intense ultrashort pulses are emitted from the output of a laser with a periodicity  $T_{RT}$  which is given by:-

$$T_{RT} = \frac{2\pi}{\partial\omega_{rep}} = \frac{1}{\partial\nu_{rep}} = \frac{2nL}{c} \quad (2.2.9)$$

From the full wave half maximum (FWHM) of the spectral intensity, the pulse duration  $\Delta\tau_p$  can be deduced from the gain bandwidth  $\Delta\nu_l$ :-

$$\Delta\nu_l \Delta\tau_p = k \quad (2.2.10a)$$

$$\Delta\tau_p = \frac{2\pi k}{N_t \delta\omega_{rep}} = \frac{k}{N_t \delta\nu_{rep}} = \frac{k}{\Delta\nu_l} \quad (2.2.10b)$$

where  $k$  is a constant which depends on the pulse shape ( $k = 0.315$  for  $\text{sech}^2$  intensity profiles and  $k = 0.441$  for Gaussian beam intensity profiles). From the equation above the number of longitudinal modes existing inside a laser can be determined. For instance, a Ti:Sapphire laser that produces 40 fs pulses with  $\text{sech}^2$  intensity profiles emitted at 875 nm would require a lasing bandwidth of 20 nm (8 THz). With a cavity round trip time of 10 ns, 80 000 phase-locked longitudinal modes can be generated. Thus the best gain media for ultrashort pulse generation will be those with the largest accessible gain bandwidths.

### 2.3 Mode-locking Techniques.

Mode locking [7,8] can be achieved actively or passively with the introduction of amplitude and frequency modulation. In passive mode locking, no external modulation is needed as the mode locking process is initiated by the interaction between the pulses themselves with the intracavity elements which is referred as “self-mode locking”. This technique has been successful to obtain pulses with durations of  $< 20$  fs. In this thesis two types of passive mode locking will be described which employ a saturable absorber or a semiconductor saturable absorber (SESAM) together with the optical Kerr effect.



Figure 2.4. Schematic of passive mode-locking configuration.

A saturable absorber is a material that has decreasing light absorption with increasing light intensity. It introduces a loss modulation in the form of a self amplitude modulation inside the laser [figure 2.4]. This mode locking mechanism can be initiated by the stochastic noise fluctuations in the cavity. As the pulse circulates for many cavity round trip times, it will be further amplified to a higher intensity. At a higher intensity, the noise saturates the absorber resulting in a lower loss and more gain in the round trip. This noise spike continues to grow stronger, producing shorter pulse duration through loss modulation because the high intensity at the peak of the pulse saturates an absorber more strongly compared to the low intensity wing. This process continues to grow until a steady state condition is achieved, forming a stable pulse sequence. There are three types of equivalent saturable absorption mechanisms which function as a *slow* saturable absorber, a *fast* saturable absorber or through *soliton* mode locking [7].

In slow saturable absorbers (SSA), mode locking occurs with the presence of dynamic gain saturation where the pulse duration (ps/fs) is shorter than the relaxation time (ns) of the saturable absorber ( $\tau_p \leq \tau_r$ ). Dynamic gain saturation means that the gain experiences a fast, pulse-induced saturation that then recovers again between two successive pulses. From figure 2.5(a), the absorber saturation recovers faster compared to the gain saturation for which an ultrashort net gain window can be formed with both the combination

of absorber and gain saturation.

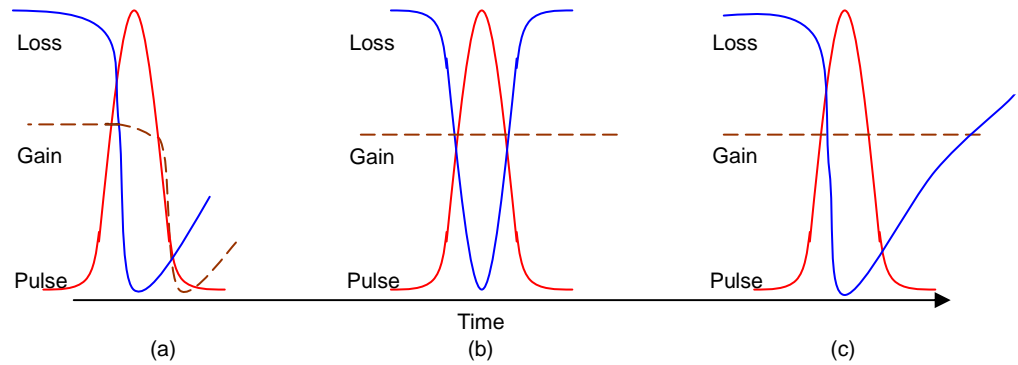


Figure 2.5. Passive mode locking mechanism in three fundamental models: (a) slow saturable absorber mode locking with dynamic gain saturation, (b) fast saturable absorber mode locking, (c) soliton mode locking [7].

In solid-state lasers, a fast saturable absorber (FSA) is required compared to SSA due to its capability of producing the short net gain window (pulse shortening mechanism) by a fast recovering saturable absorber in the absence of gain saturation [figure 2.5(b)]. In addition, for solid state lasers, there is no significant dynamic gain saturation exists because the corresponding upper state lifetimes ( $\sim\mu\text{s}$  to  $\text{ms}$ ) are typically much longer than the pulse repetition period ( $\sim\text{ns}$ ).

In soliton mode locking, soliton formation is the dominant pulse shortening mechanism with the balance of group velocity dispersion (GVD) and self-phase modulation (SPM) at steady state. This results in long net-gain windows in contrast to the short net gain in SSA and FSA [figure 2.5(c)]. In this technique, the time dependent intensity,  $I(t)$  influences the mode locking process as described by the optical Kerr effect phenomenon,  $n = n_0 + n_2 I(t)$  which in contrast to self-focusing phenomenon eliminates any critical cavity alignment due to the decoupling of mode locking mechanism with the cavity modes, thus allowing it to work over the full cavity stability regime. A saturable absorber [9] such as a Semiconductor Saturable Absorber Mirror (SESAM) and Saturable Bragg Reflector (SBR) or an acousto-optic modulator [10] is required as an additional loss mechanism to initialise the formation of solitonic pulses from background noise spikes, and to stabilise the solitonic pulses forming process. The net gain window can be open for more than 10 times of the duration of the ultrashort pulses which relaxes the constraints on the saturable absorber. Thus, ultrashort pulses in the sub-10 fs regime [11] is allowed even though the semiconductor saturable absorbers may have a recovery time that is long compared to the pulse duration.

### 2.3.1 Kerr-lens Mode Locking.

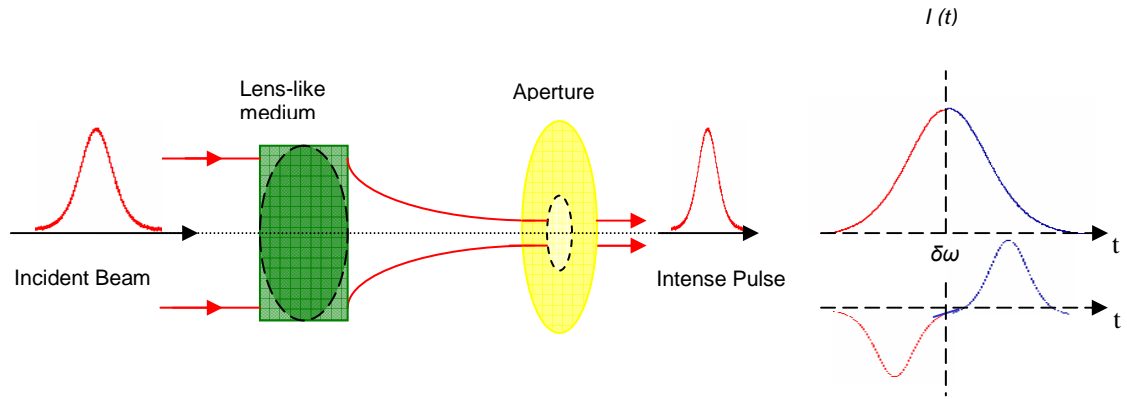


Figure 2.6. Kerr lens mode locking effect at an intracavity focus in the gain medium. The induced lens focuses the beam in the transverse propagation due to high radial dependent intensity effect  $I(r)$  while frequency chirps in the longitudinal direction are caused by temporal dependent intensity effect  $I(t)$  which results in red shifted of the leading part and blue shifted of the trailing part [13].

In 1989, Kean and co-workers reported that 60 fs pulses were produced by a Ti:sapphire laser without any physical saturable absorber [12]. This mode locking approach has been designated as Kerr-lens mode locking and takes advantage of the intensity dependent refractive index (optical Kerr effect) in the gain medium [figure 2.6]. It can also be described as self-mode locking because of the combination of self-amplitude modulation, self-phase modulation (frequency chirp) and self-focusing. With a nonlinear optical Kerr effect in the gain medium, the refractive index,  $n$  increases proportionally with the radially dependent intensity  $I(r,t)$ :-

$$n(r,t) = n_0 + n_2 I(r,t) \quad (2.3.1)$$

From the equation above,  $n_0$  is the linear refractive index and  $n_2$  is the nonlinear refractive index which is on the order of  $10^{-16} \text{ cm}^2/\text{W}$  for solid state materials. This radial form of intensity dependent refractive index  $I(r,t)$ , affects the longitudinal and transverse propagation of the beam. A self-focusing lens is produced in the transverse propagation direction due to the retardation of the most intense part of the plane wave front, while the self-phase modulation (SPM) which results in frequency chirps is produced in the longitudinal direction after retardation of the centre part of the optical pulse. SPM generates exploitable extra bandwidth in the pulse spectrum because the leading part of the pulse is red shifted while the trailing part is blue shifted as shown in figure 2.6.

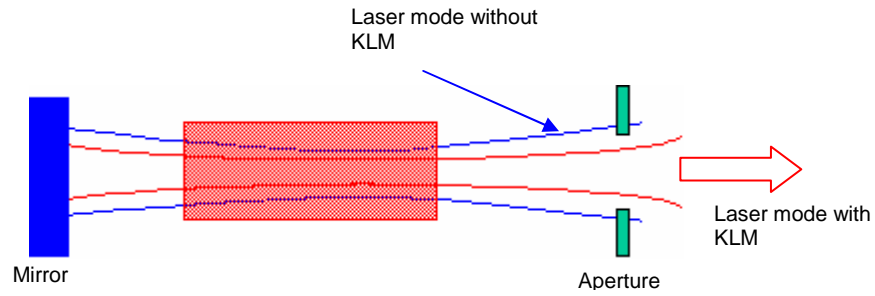


Figure 2.7. Hard aperture mode locking.

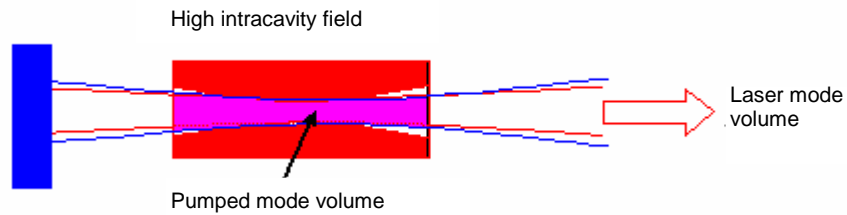


Figure 2.8. Soft aperture Kerr-lens mode locking with a high intracavity field due to overlap changes between pump and laser mode volume.

From figure 2.7, an aperture located appropriately in the cavity attenuates a low intensity beam while allowing the transmission of a more intense self-focused beam to provide an exploitable self amplitude modulation. This is described as “hard aperture” mode locking. Alternatively, the laser beam diameter can be modified as a function of intensity to give an enhanced overlap (mode-coupling) with the pump mode volume. This represents a “soft aperture” effect due to the self-focusing and gain guiding influence as shown in figure 2.8.

The advantage of KLM operation is that it produces shorter pulse durations which can reach 5 fs or just less. The Kerr lens is broadband, broader than any saturable absorber because it behaves effectively as a “non-resonant saturable absorber”. In addition, this technique enables solid state lasers (e.g. Ti:Sapphire) to have broad tunability and when all of the bandwidth is engaged the durations can be readily achieved in the sub-10 fs region [14,15]. However, a major drawback for KLM lasers is that the mode coupling between pump and laser modes for the mode locking mechanism process requires critical cavity stability. The pulse formation is not generally self-starting and additional perturbations are required to induce the stochastic noise spikes from which the ultrashort pulses evolve. One approach for producing such noise is to mechanically perturb one of the laser cavity mirrors. Partial self-starting is allowed by restrictive cavity designs [16,17] but this needs sub-

millimetre precision for cavity alignments close to the stability that limits laser cavity operation. In addition, the laser requires housing in a very clean environment to minimize intracavity losses and this secures laser operation over long periods. Therefore, the search for alternative solutions for compact ultrafast lasers is continuing to find better self-starting methods while avoiding any compromise to the pulse durations.

### **2.3.2 Saturable Absorbers and Semiconductor Saturable Absorber Mirrors (SESAMs).**

In the past, organic dyes were frequently used as saturable absorbers to produce pulse durations of less than 30 fs [18] especially for femtosecond dye lasers that had relatively shorter upper state lifetimes (ns) without the tendency for Q-switching instabilities. However, due to their disadvantages such as high toxicity and complicated handling process, new materials needed to be found for the initiation of the mode locking process. Unfortunately, some solid-state saturable absorbers that were used (eg Cr:YAG) have serious limitations in their wavelength, saturation levels and recovery times. In contrast, new alternatives such as semiconductor materials that can absorb over a broader range of wavelengths from the visible to mid-infrared region are more promising absorber media for the initiation of mode locking processes in solid-state lasers [7,13]. Their properties, as discussed later in this chapter, can also be controlled by changing the growth parameters and device designs.

A semiconductor saturable absorber is integrated into a mirror structure to produce a device that operates in reflection in which the reflectivity increases with the higher intensity of the incoming pulses [figure 2.9]. This pulse is absorbed by the semiconductor, exciting carriers to the conduction band. Under strong excitations, the absorption is saturated/bleached to achieve transparency. The carriers in each band thermalize within 60 to 300 fs of excitation which leads to a partial recovery of the absorption. These carriers will be then removed by recombination and trapping on a longer time scale (ps/ns) which results in a reduced saturation intensity for a part of the absorption, facilitating self-starting mode locking mechanisms.

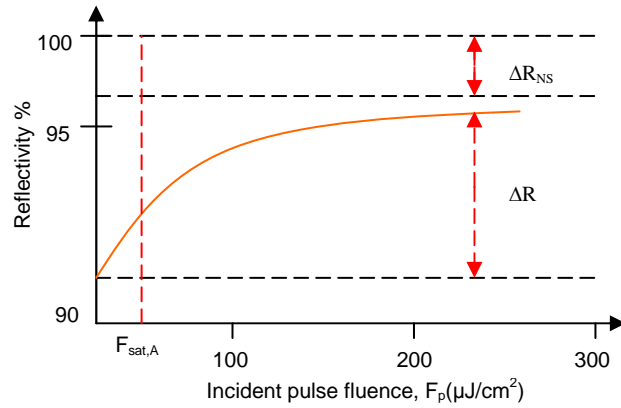


Figure 2.9. Reflectivity increases with the higher intensity of incident pulses [13].

In contrast to KLM lasers, the SESAM-assisted mode locking can be optimised with a less critical dependence on the cavity design [see soliton mode locking section 2.3] and so this allows successful mode locking to be achieved with a higher stability. The pulse itself is self-evolving (soliton-like formation) because it is less sensitive to external perturbation and the shortest pulse duration achieved to date is 13 fs without the presence of significant Kerr lensing [19]. The key parameters for a saturable absorber are its wavelength range (where it absorbs), its dynamic response (recovery time) and its saturation intensity and fluence (at what intensity or pulse energy density it saturates). The usefulness of SESAMs [20] for passively mode locked solid state lasers results from their small saturation fluence, the additional benefits of cavity mirror device integration, sophisticated band gap and defect engineering, and epitaxial wafer scale fabrication that reduces production costs.

One of the examples of SESAM structure is a low-finesse Anti-resonant Fabry Perot Saturable Absorber (A-FPSA) which consists of 25 x AlAs/AlGaAs layers of  $\lambda/4$  thickness grown on GaAs substrate and Fabry Perot cavity. The Fabry Perot cavity that exists between the two mirrors consists of a single quantum well (SQW) GaAs layer (15 nm) grown between AlAs spacer layers. The Fabry-Perot thickness is adjusted such that it operates in anti-resonance [figure 2.10].

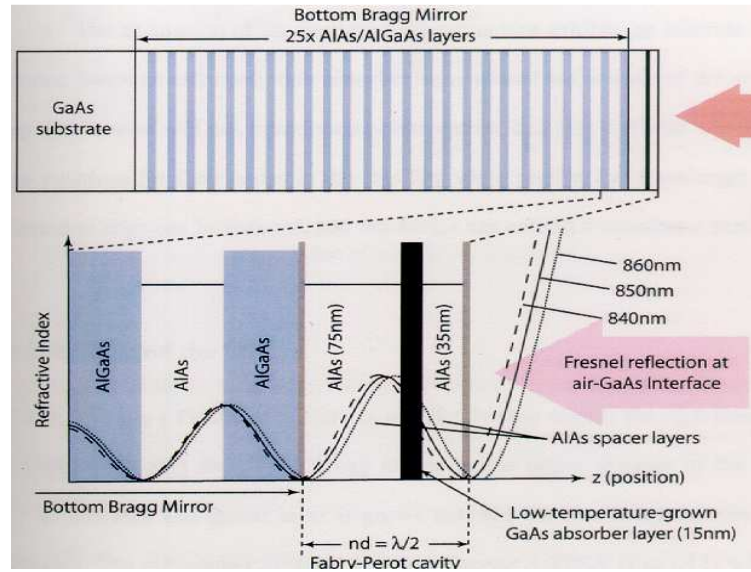


Figure 2.10. A low-finesse A-FPSA structure of SESAM [7].

In the 1970's and 1980's, CO<sub>2</sub> lasers, semiconductor diode lasers and dye lasers were passively mode locked using semiconductor saturable absorbers. However, the first reported CW passively mode-locked solid-state laser with an intracavity SESAM without the tendency for Q-switching instabilities was only produced in 1992 [21]. The challenge is due to the 1000 times smaller emission cross section and 1000 times longer upper state life time ( $\tau_u \approx \mu s$  to  $ms$ ) of the gain material compared to dye lasers. This explains the reasons why saturable absorber (SESAM) parameters such as the modulation depth  $\Delta R$ , absorber recovery time  $\tau_A$ , saturation fluence  $F_{sat}$ , the saturation intensity  $I_{sat}$ , non-saturable loss  $\Delta R_{NS}$ , and spectral bandwidth  $\Delta\lambda_A$  need to be controlled/designed [22] to meet the requirement of the solid-state lasers for the prevention of Q-switching instabilities [23].

The modulation depth  $\Delta R$  is the maximum amount of saturable loss that can be bleached. This bleaching, which provides the necessary amplitude modulation, can be achieved by an incident pulse fluence (energy density per unit area) that is a few times larger than the saturation fluence of the absorber. The modulation depth of the saturable absorber is determined by the maximum non-linear change of the reflectivity because the saturable absorber is integrated inside a mirror structure. The maximum absorber amplitude loss coefficient  $q_0$  is given by:-

$$\Delta R = 1 - e^{-2q_0} \approx 2q_0, q_0 \leq 1 \quad (2.3.2)$$

In practical laser operation, the amount of modulation depth should be controlled to provide the shortest pulse durations and optimum loss reduction at high intensity. If this quantity is too large, higher losses will be obtained with shorter pulse duration while if it is too small longer pulse duration will only be obtained with lower losses.

The non-saturable loss  $\Delta R_{NS}$  of the SESAM is the remaining losses of the device for an incident pulse energy density which is much larger than the saturation fluence.  $\Delta R_{NS}$  is obtained from less than 100 % reflectivity of the bottom Bragg mirror, remaining absorption from defect states, scattering losses due to impurities at the surface of the sample and losses introduced by two photon and free carrier absorption. In the development of low threshold laser systems, non-saturable loss should be below 1 % [14] as we couple a few percent out from the CW (continuous wave) mode-locked solid state lasers. If the  $\Delta R_{NS}$  increases the laser become less efficient, operating at fewer times over threshold thus increasing the tendency towards Q-switching instabilities.

The saturation fluence  $F_{sat}$  and saturation intensity  $I_{sat}$  can influence the mode locking build-up time and the pulse stability with respect to self-Q-switching. The saturation fluence  $F_{sat}$  is defined by the measurement of the nonlinear change in reflectivity of a pulse,  $(1 - e^{-1})\Delta R$  as a function of increased incident pulse energy [24]. In case of the pulse duration  $\tau_p$  is shorter than the recovery time of saturable absorber [20]  $\tau_A$  ( $\tau_p \leq \tau_A$ ), the saturation fluence is given by:

$$F_{sat} = \frac{h\nu}{\sigma_{abs}} \quad (2.3.3)$$

where  $h\nu$  is the photon energy and  $\sigma_{abs}$  is the absorption cross section. The saturation fluence should be kept small to allow the absorber to operate close to full saturation (near bleaching), to reduce remaining losses and maximise the use of the available absorption depth. This results in a shorter pulse duration and maximises the self starting potential. In soliton mode locking, the fluence incident on a saturable absorber (such as SESAM) should be around 3-5 times the saturation fluence of the device determined by the manufacturer which can be achieved by a careful control of beam mode size incident on the SESAM. This is because in femtosecond lasers, the increase of thermal effects and two-photon absorption at higher saturation intensity become more significant to avoid Q-switching instabilities.

The saturation intensity  $I_{sat}$  is defined as:

$$I_{sat} = \frac{h\nu}{\sigma_{abs}\tau_A} \quad (2.3.4)$$

where  $\tau_A$  is the absorber recovery time.

The absorber recovery time  $\tau_A$  is the time needed for the saturable absorber to recover from pulse-induced saturation. This is an important parameter for the selection of the dominant mode locking mechanism in solid-state lasers either based on FSA (fast saturable absorber) or soliton mode locking. SSA (slow saturable absorber) can be neglected due to the absence of dynamic gain saturation. Under the conditions where FSA mode locking such as KLM is the dominant factor,  $\tau_A$  must be shorter on the order of the pulse duration (few fs). In contrast, under the conditions where the soliton mode locking is dominant,  $\tau_A$  can be up to 10-30 times of the pulse duration [25]. However, if the  $\tau_A$  is on the order of or longer than the pulse repetition frequency (ns), Q-switching instabilities might exist. In a practical laser cavity, it should be appreciated that the recovery time is independent of the mirror structure that contains the absorber.

The spectral bandwidth is the wavelength interval in which the radiant intensity is at least 50 % of the maximum spectral range. The spectral bandwidth of the saturable absorber imposes limits on the pulse duration produced within the cavity and is usually limited by the bandwidth of the lower Bragg mirror and top mirror surrounded the absorber layer [figure 2.10]. These result in the limitation of pulses supported by SESAM within only sub-20 fs over the full cavity stability regimes. However, pulses as short as 7 fs was produced from a Ti:Sapphire laser when combining the SESAM with Kerr-lensing effect [26].

#### 2.4 Pulse Polarisation in the Dielectric Medium.

At high peak intensity, linear and nonlinear optical phenomenon play an important role for the generation of ultrashort pulses as shown in figure 2.11. The relationship between  $P$  (polarisation field) and  $E$  (electric field) deviates from the linear proportionality which can be described by the equation below:-

$$P = \epsilon_o (\chi^{(1)} E + \chi^{(2)} E^2 + \chi^{(3)} E^3 + \dots) \quad (2.4.1)$$

where the dielectric susceptibility,  $\chi$ , describes how easily the medium can be polarised by an applied  $E$ -field. The important polarisation effects [27] that become the subject of discussion in this chapter are linear dispersion described by the first-order term  $\chi^{(1)}$ , second harmonic generation described by the second-order term  $\chi^{(2)}$ , the optical Kerr-effect responsible for self-focusing and self-phase modulation described by the third-order term  $\chi^{(3)}$ . These coefficients decrease quickly for the higher-order terms where  $\chi^{(1)} \approx 1$ ,  $\chi^{(2)} \approx 10^{-8} \text{ cm}^2/\text{W}$  and  $\chi^{(3)} \approx 10^{-16} \text{ cm}^2/\text{W}$ . These nonlinear responses are readily accessible in lasers where light intensities,  $I \geq 1 \text{ MW}/\text{cm}^2$  are quite commonplace.

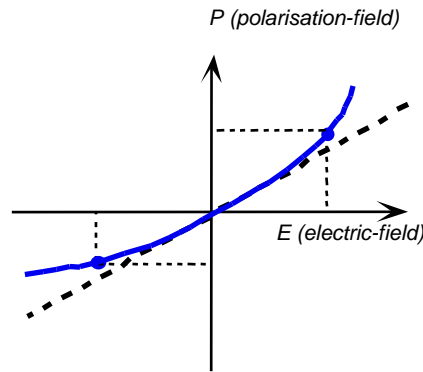


Figure 2.11. Induced polarisation as a function of electrical field in a medium with linear (black ink) and nonlinear responses (blue ink) [27].

All materials including those that are crystalline and non-crystalline possess finite  $\chi^{(3)}$  coefficients responsible for the optical Kerr-effect as described in Chapter 6. The most important consequences of the nonlinear responses are second harmonic generation (SHG) described in Chapter 7 that is based on finite  $\chi^{(2)}$  coefficients where  $\chi^{(3)}$  is negligible. However, only certain crystals with non-centrosymmetric configurations show finite values of  $\chi^{(2)}$  while for centrosymmetric crystals,  $\chi^{(2)} = 0$ .

Dispersion, which is described through the first-order term  $\chi^{(1)}$ , is a separation of a beam into its various wavelength components where the refractive index of a medium  $n$  is a function of the wavelength  $\lambda$ , so that  $n = n(\lambda)$  is responsible for material dispersion. For a pulse with a broad spectrum, dispersion causes different wavelength components to travel at different light velocities in a medium. In the dielectric medium, dispersion can be

represented mathematically by the Taylor expansion of the spectral phase function,  $\phi(\omega)$  [28]:-

$$\phi(\omega) = \phi(\omega_o) + \phi^1[\omega - \omega_o] + \frac{1}{2!}\phi^2[\omega - \omega_o]^2 + \frac{1}{3!}\phi^3[\omega - \omega_o]^3 + \dots \quad (2.4.2)$$

For a long pulse duration with small frequency bandwidth all the expansion terms above can be abandoned except the first,  $\phi(\omega_o)$  which is defined as the phase velocity,  $v_\phi = \frac{\omega}{k}$  where  $k = \frac{2\pi}{\lambda}$  is the wave number and  $\omega$  is the angular frequency of the radiation. This parameter is used to measure the propagation velocity of the central frequency,  $\omega_o$ . In contrast, for a short pulse duration with a large frequency bandwidth, the group velocity term  $\phi^1(\omega_o)$  is introduced to measure the propagation velocity of the pulse envelope,  $v_g = \frac{\delta\omega}{\delta k}$ , as the different frequency constituents travel with different phase velocities. The third term is the quadratic spectral phase  $\phi^2(\omega_o)$  with the unit  $\text{fs}^2$ , which is defined as the group velocity dispersion while the fourth term  $\phi^3(\omega_o)$  and higher are defined as the third-order and fourth-order dispersions which are less significant. These can be ignored for pulse durations exceeding 50 fs, which is typically the case for the lasers developed in this project. Analytical discussions to explain dispersive properties of a dielectric medium mentioned above can be found at many reference sources [5,29,30].

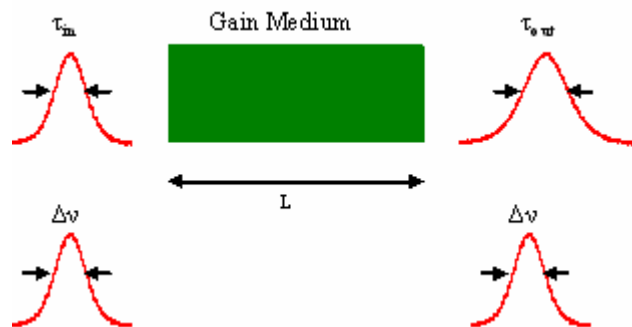


Figure 2.12. Temporal broadening due to linear frequency chirp as a pulse propagates through a gain medium [29].

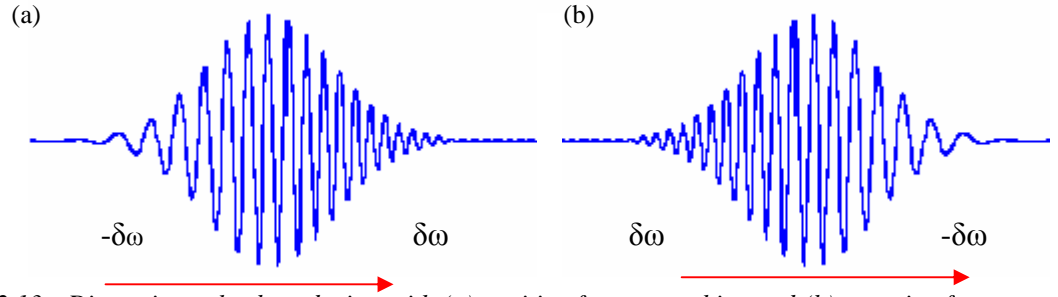


Figure 2.13. Dispersive pulse broadening with (a) positive frequency chirp and (b) negative frequency chirp [29].

The group velocity dispersion  $\phi^2(\omega_o)$  or GVD (third-order term of the spectral phase function) introduces a linear phase chirp across the pulse that leads to temporal broadening [figure 2.12] without any effect to the spectral component. It can be defined as:-

$$GVD = \frac{d}{d\omega} \left[ \frac{1}{v_g} \right] = -\frac{1}{v_g^2} \frac{dv_g}{d\omega} \quad (2.4.3)$$

where GVD is positive (up chirp) when the pulse frequency increases with time, and negative (down chirp) when the pulse frequency decreases with time [figure 2.13]. The positive chirp manifests itself as red-shifted spectral components being introduced at the leading edge of the pulse and blue shifted components at the trailing edge [figure 2.6].

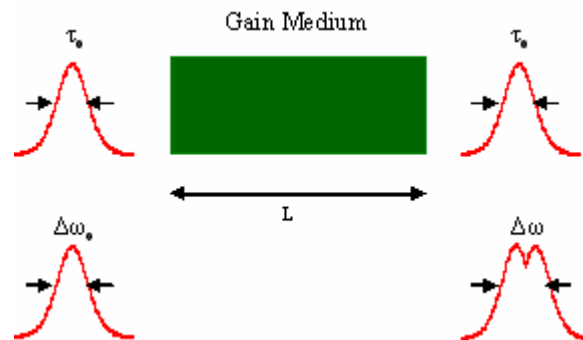


Figure 2.14. Spectral broadening in an optical pulse due to self-phase modulation [29].

Self-phase modulation (SPM) implicit in  $\chi^{(3)}$  manifests itself through the intensity dependence of the refractive index  $n_2$  as described in the optical Kerr-effect [chapter 2.3.1].  $n_2$  is positive for most materials and results in a positive frequency chirp similar to positive GVD. However, GVD produces a linear chirp where the various frequency component of a pulse is distributed in time. In contrast, SPM produces nonlinear frequency chirp by shifting

some of the frequency components to new frequencies that lead to induced spectral broadening [figure 2.14]. This is preferable for generating shorter pulse durations inside the laser cavity. For the generation of sub-100 fs pulses, GVD arises from the cavity elements such as gain medium, saturable absorber, modulators, tuning wedges, mirrors and even the air path between components. Most of these materials exhibit positive dispersion (up chirp) for wavelengths below 1300 nm which can be compensated by the insertion of materials introducing negative dispersion (down chirp) such as Brewster-angled prisms [see chapter 4], diffraction gratings, Gires-Tournois interferometers (GTI) or chirped mirrors to generate unchirped transform-limited ultrashort pulses.

## **2.5 Introduction to Solid-state Laser Materials.**

Solid-state lasers are based on materials having ion impurities introduced to transparent dielectric hosts such as crystals or glasses, pumped in the optical frequency region. In this case, semiconductor lasers [31] are not included in this group due to their electrical pumping and different physical processes. Materials needed for laser operations must exhibit strong absorption bands within the emission spectrum of readily available pump sources and high quantum efficiency for the peak emission transitions of interest. This section reviews the basic requirement of lasing action based on gain media, appropriate optical pump sources and optical elements in the cavity required for compact, low threshold and highly efficient femtosecond lasers.

### **2.5.1 Host Materials.**

Host materials in solid-state lasers can be divided into the two main groups of glasses and crystalline solids. The appropriate host chosen for laser ions must have convenient optical, mechanical, thermal, suitable microscopic lattice properties and ease of fabrication. For instance, to withstand severe conditions in high-average-power operation, the host must have appropriate thermal conductivity, hardness and fracture strength. The inhomogeneous microstructure of the host can affect the index of refraction of the propagated light that results in poor beam quality. The crystal hosts can be grown from the melt, solution or gas phase. A high purity and perfect crystal from congruent melts can be grown by the

Czochralski technique [32,33] which is the most important development of growth technology. The active lasing species for solid-state lasers are the dopant ions, thus the size and valence of the additive ions should match that of the lattice host ions that have they substituted. The host's lattice sites must also have local crystal field of symmetry and satisfactory strength required for the induction of desirable spectroscopic properties of the additive ions. Generally, ions inserted inside the hosts have long absorption and emission radiative lifetime between microsecond to millisecond regimes with cross-sections near  $10^{-20} \text{ cm}^2$ .

A crystal is a transparent, dielectric material whose atoms, ions or molecules are arranged in a definite pattern and whose surface regularity reflects its internal symmetry. The geometrical pattern of the crystal's lattices reveal well defined identical blocks or cells that are repeated in all directions. The advantages of crystal hosts compared to that of glasses are higher thermal conductivity, greater hardness in some cases, and narrower absorption line width that is very well-matched with diode pumped lasers, thus beneficial for lower laser threshold [see section 3.3]. In contrast, crystal hosts reveal poorer optical quality and doping homogeneity in comparison to that of glasses. The main group of crystal hosts can be divided into oxides and fluorides. The examples of oxides are sapphire ( $\text{Al}_2\text{O}_3$ ), garnets ( $\text{Al}_5\text{O}_{12}$ ), tungstates ( $\text{WO}_4$ )<sup>2-</sup>, molybdates ( $\text{MoO}_4$ )<sup>2-</sup>, and vanadates ( $\text{VO}_4$ )<sup>3-</sup>. Oxides are harder with better mechanical and thermo-mechanical properties that lead to higher thermal fracture limitation, while fluorides exhibit better thermo-optical properties due to the lower thermally induced lensing and birefringence.

### 2.5.2 Active Ions.

Active ions introduced into transparent dielectric media for lasing can be divided into transition metals and rare earth metals. Transition metals are ten groups in the middle of periodic table which serve as a bridge between two representative components (1A,2A...8A). These elements have similar features with metals and form positive ions during chemical and physical interactions. They are malleable, ductile and capable of conducting heat and electricity.

An element that represents transition metals is  $\text{Ti}^{22}$  with electronic configurations of  $[\text{Ar}]3d^2 4s^2$  where  $\text{Ar}^{18}$  has electronic configurations of  $1s^2 2s^2 2p^6 3s^2 3p^6$ . During chemical/physical interactions between active ions with the crystal hosts, titanium

loses two electrons from the 4s orbital and one electron from the 3d to form  $Ti^{3+}$  with electronic configurations of  $[Ar]3d^1$  as shown in table 2.1. All the effective absorption and emission spectra can be determined from the 3d-3d transitions when the remaining electrons in the 3d orbital arrange themselves in a large number of energy states. The deficiency of screening effects compared to that of rare earth ions result in stronger interactions between 3d states with lattice phonon-vibrations, thus leading to vibronic laser characteristic. These stronger interactions in transition metals are the reasons for likely allowed effective absorption and emission transitions in 3d-3d states that explain their shorter upper state lifetime to the few microsecond regimes.

Table 2.1. Electronic configurations in titanium that represent transition metals and ytterbium that represent rare earth metals. The screening effects in  $Yb^{3+}$  are shown by  $5s^2 5p^6$  electronic configurations.

Atoms	Electronic configurations	Ions	Electronic configurations
$Ti^{22}$	$[Ar] 3d^2 4s^2$	$Ti^{3+}$	$[Ar] 3d^1$
$Yb^{70}$	$[Xe] 4f^{14} 5d^0 6s^2$	$Yb^{3+}$	$[Xe] 4f^{13} \} 5s^2 5p^6$

Rare earth metals are called “inner transition elements” and can be divided into lanthanides and actinides. They are the two long rows situated at the bottom of the periodic table that show sharp fluorescent line width, representing almost every region of the visible and near infrared of the electromagnetic spectrum. They consist of 17 elements from scandium, yttrium and lanthanides. Lanthanides have atomic number between 58 to 71 and consist of 15 elements from lanthanum to lutetium. They show similar chemical properties to each other as well as to scandium, yttrium and actinides.

$Yb^{70}$  is a rare earth metal with electronic configurations of  $[Xe] 4f^{14} 5d^0 6s^2$  with  $Xe^{54}$  configurations of  $1s^2 2s^2 2p^6 3s^2 3p^6 3d^{10} 4s^2 4p^6 4d^{10} 5s^2 5p^6$ . During chemical/physical reactions between active ions with the crystal host, ionic binding can be formed when  $Yb^{70}$  loses one electron from 4f orbital and two electrons from 6s orbital. These triply ionised  $Yb^{3+}$  ions have electronic configurations of  $[Xe] 4f^{13}$  where 4f orbital is screened by  $5s^2 5p^6$  as shown in table 2.1. There are three types of interactions that split the energy states into a large number containing remaining electrons in 4f orbital. The strongest effect is caused by Coulomb interaction that splits the 4f orbital into sublevels with energy separation of  $\sim 10\,000\text{ cm}^{-1}$ . These sublevels are further split into many manifolds of  $\sim 3\,000\text{ cm}^{-1}$  due to the spin orbit coupling while the weakest alteration of lattice vibration-electronic

transition interaction splits each manifold into sublevels of  $\sim 200 \text{ cm}^{-1}$ . This latter interaction is weakened by the screening effect of  $5s^2 5p^6$  which results in limited wavelength tunability compared to that of transition metals. The upper state lifetime,  $\tau_u$ , is therefore in the hundreds of microsecond to a few millisecond regime which is longer than that of transition metals because of the weakly allowed transitions for all effective absorption and emission transitions in 4f-4f states. This higher upper state lifetime emission cross-section product  $\sigma_{se} \tau_u$ , where  $\sigma_{se}$  is the stimulated emission cross-section, leads to lower saturation intensity and laser threshold that are recommendable for laser operation as discussed in section 2.6.

The most important femtosecond laser with a wide range of applications based on transition metals is Ti:Sapphire [34]. It is a vibronic laser exhibiting a large gain bandwidth due to the good coupling between electronic transitions and electron phonon vibrations in the crystal's lattice. This produces broader wavelength tunability of laser output and shorter pulse generation to the few femtosecond regime. Ti:Sapphire lasers were introduced in 1986 to replace most of the dye lasers that had dominated the field of ultrashort pulse generation. In this crystal, a small percentage of  $\text{Ti}^{3+}$  ions ( $\sim 0.01 \%$ ) substitute  $\text{Al}^{3+}$  ions at the centre of octahedral site surrounding by six  $\text{O}^{2-}$  ions in the sapphire crystal.

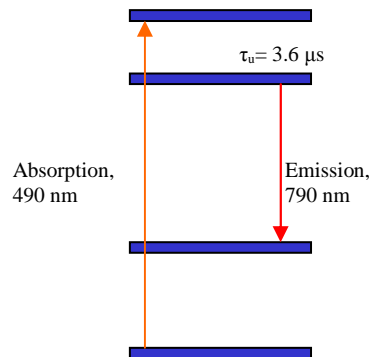


Figure 2.15. Energy levels in Ti:Sapphire [36].

The energy levels in Ti:Sapphire are shown in figure 2.15. The peak absorption spectrum from the ground state to the excited state occurs at 490 nm where pump sources can be provided by the output of argon-ion lasers at 488 and 514.5 nm or by frequency doubled Nd:YAG or Nd:YLF lasers at  $\sim 532 \text{ nm}$ . The upper state lifetime is  $3.6 \mu\text{s}$  while the peak emission spectrum is at 790 nm for  $\pi$ -polarization. It has the largest gain bandwidth of any laser ( $\Delta\nu_0 \geq 100 \text{ THz}$ ), and is widely tunable between 600 and 1200 nm with the shortest pulse duration of 5 fs [14] for Kerr-lens mode locking obtained directly from the laser output. In a compact configuration of 30 X 45 cm, 23 fs pulse duration was obtained in a prismless

cavity Ti:Sapphire laser at a repetition rate of 31.25 MHz based on a novel multipass cavity design pumped by a frequency doubled Nd:YVO<sub>4</sub> laser [35].

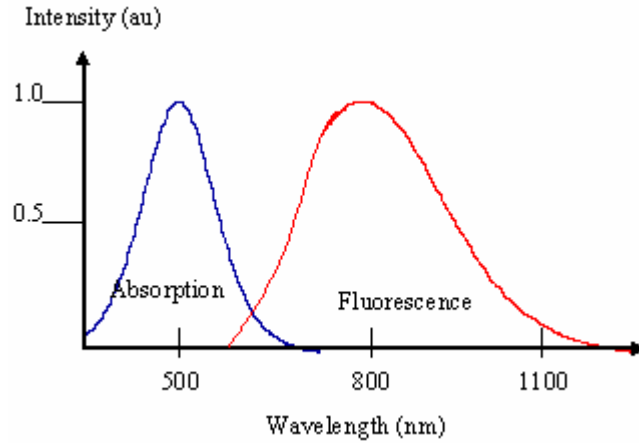


Figure 2.16. Absorption and emission spectra of Ti:Sapphire [34].

An example of the spectroscopic properties of Ti:Sapphire can be seen in figure 2.16. From these spectra, the broad and widely separated absorption and fluorescence bands are associated with the strong coupling between ions and the host lattice which is the main criterion to this widely tunable laser operation. This laser can produce very high pump intensity due to its good beam quality and capability to work at high average power operation of several Watts. These advantages are due to sapphire crystal properties of high thermal conductivity, mechanical hardness and exceptional chemical inactivity. This laser has many applications as a pump source for optical parametric oscillators, generating and amplifying femtosecond lasers, spectroscopy and scientific research.

## 2.6 Alternative Solid-state Laser Candidates - Why Ytterbium Ions?

To date, Ti:Sapphire laser is the most widely used solid-state tunable laser which has many favourable properties of its material as shown in table 2.2. It requires zero minimum pump intensity  $I_{\min}$  [37] to achieve transparency due to the absence of thermal population at the terminal level in four laser level systems. The high stimulated emission cross-section  $\sigma_{se}$  of this laser produces a high gain coefficient,  $g \propto [N_2\sigma_{se}^{\lambda_{se}} - N_1\sigma_{abs}^{\lambda_{se}}]$  [38] where  $N_1$  and  $N_2$  are the population densities in the lower and upper laser level while  $\sigma_{se}^{\lambda_{se}}$  and  $\sigma_{abs}^{\lambda_{se}}$  are the stimulated emission and absorption cross-sections at the emission wavelength. In addition, the broad emission linewidth of this gain material of up to  $\sim 230$  nm explains the generation

of ultrashort pulses as short as 5 fs [14]. However, the disadvantages of this material are due to the high quantum defect of up to 0.37, and a shorter upper state lifetime  $\tau_u$  of up to 3.6  $\mu$ s. This short upper state lifetime product is responsible for a higher pump saturation intensity  $\left( I_{sat} \propto \frac{1}{\sigma_{abs}^{\lambda_p} \tau_u} \right)$  and higher power threshold requirement  $\left( P_{th} \propto \frac{1}{\sigma_{se}^{\lambda_{se}} \tau_u} \right)$  [37] in the order of one to two magnitudes compared to that of Yb-doped materials. These features reinforce the requirement to search for alternative active ions that have several times longer  $\tau_u$  than that of Ti:Sapphire for lower threshold operation. In addition, it is a bulky and lab bound system due to the complicated requirement of pump sources with the absence of any diode laser manufactured to date in the green spectral region. These have opened up the exploration of new materials for higher efficiency, more compact and portable femtosecond lasers. As a result, the rare-earth doped-lasers that will be discussed specifically in this Chapter are based on Yb-doped materials [39] which are seen as especially suitable active ions to address the requirements mentioned above.

Table 2.2: Comparison of spectroscopic laser parameters between Ti:sapphire [3,36] and Yb-doped materials [39].

Parameters	Ti:Sapphire	Yb-doped materials
Stimulated emission wavelength, $\lambda_{se}$ (nm)	790	1030-1060
Emission linewidth, $\Delta\lambda_{se}$ (nm)	~ 230	25- 30
Pump absorption wavelength, $\lambda_p$ (nm)	490	900-980
Absorption linewidth, $\Delta\lambda_p$ (nm)	~ 100	2-18
Emission cross-section, $\sigma_{se}$ ( $10^{-20}$ cm <sup>2</sup> )	28	0.8-6
Pumping cross-section, $\sigma_p$ ( $10^{-20}$ cm <sup>2</sup> )	41	0.7-13
Fluorescence lifetime, $\tau_u$ ( $\mu$ s)	3.6	600-2600
Pulse duration, $\Delta\tau_p$ (fs)	5 [14]	~ 50 [40]
Quantum defect fraction, $QD_f$	~ 0.37	$\leq$ 0.14
Min. pump intensity, $I_{min}$ (kW/cm <sup>2</sup> )	0	0.1-4

The two Stark-split energy levels in Yb-doped materials, for instance Yb:YAG [41,42] are shown in figure 2.17. An electron short in  $4f^{13}$  shell acts as containing one electron hole that explains the existence of only one excited state of  ${}^2F_{5/2}$  in this material. The peak absorption transitions from the ground level  ${}^2F_{7/2}$  occur at 942 nm while the peak laser transitions occur at 1030 nm where the terminal laser level is  $\sim 600 \text{ cm}^{-1}$  above the ground state. This system exhibits an absence of parasitic losses such as excited-state absorption (ESA), up-conversion, concentration quenching, and cross relaxation.

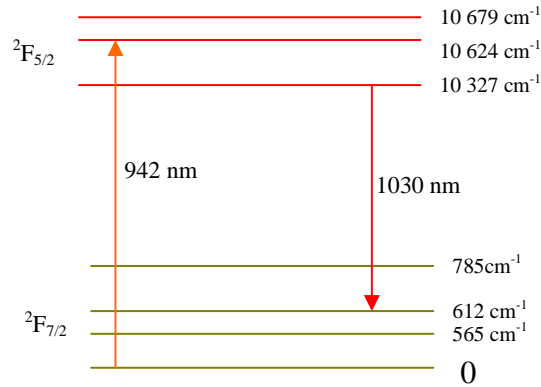


Figure 2.17. Energy levels of Yb:YAG [30].

However, the disadvantage of this laser is due to the quasi-three level nature [43,44] at room temperature where the final laser level is thermally populated, thus resulting in the partial reabsorption of the photons emitted during lasing as shown in figure 2.18. This can lead to a higher laser threshold due to the higher minimum pump intensity ( $I_{\min} > 0$ ) compared to that of Ti:Sapphire [table 2.2]. In the past this high pump intensity requirement couldn't be satisfied by incoherent optical pumping, thus limiting their applications for generating femtosecond pulses. However, the emergence of high brightness diode lasers emitting in the near infra-red spectral region with pump intensity at least 5-6 times above threshold has increased the output powers of Yb lasers from several hundred milliwatts to more than 1kW. The pumping requirement of Yb-doped lasers between 900 and 980 nm can be provided by InGaAs quantum well diode lasers which were very well developed in 1990's to pump erbium-doped fibre amplifiers for applications in telecommunications. This increases the economic appeal of this system especially with the longer upper state lifetime in between 0.6 to 2.6 ms which enhances energy storage, that is recommended for low threshold operation. Furthermore, other advantages of using diode lasers instead of flashlamps as pump sources are due to the generation of lower thermal loading in the gain medium, improvement in output beam quality  $M^2$  from several hundreds to several tens, increased

laser efficiency, compactness, and wider operating availability. In addition, the good properties of the crystal hosts such as high conductivity and tensile strength, for instance in Yb:YAG can also contribute to the potential of this laser for high power applications.

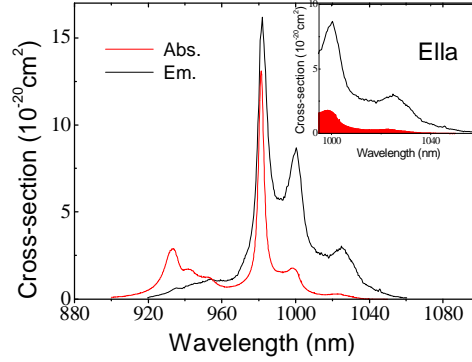


Figure 2.18. Spectroscopic properties of Yb:KYW as a representative for Yb-doped materials. The red fill area under curve shows partial reabsorption of the emitted photon (insert picture).

The quantum defect fraction,  $QD_f$  is defined as the small energy difference between the absorbed photon to the emitted laser radiation where the difference in photon energy goes into heating. This can be described as:-

$$QD_f = \left[ \frac{h\nu_{abs} - h\nu_{se}}{h\nu_{abs}} \right] = \left[ \frac{\lambda_{se} - \lambda_{abs}}{\lambda_{se}} \right] \quad (2.6.1)$$

where  $\nu_{abs}$  and  $\nu_{se}$  are the frequency of the absorbed and emitted photons, while  $\lambda_{abs}$  and  $\lambda_{se}$  are the wavelength of the absorbed and emitted photons. In Yb materials, the quantum defect fraction is lower ( $\leq 0.14$ ) compared to that of Ti:Sapphire (0.37) where the amount of heat dissipation inside the former material is reduced for each photon emitted during lasing [39]. In addition, the thermal heat load in Yb-doped material [45] is four to five times lower than that in Ti:Sapphire due to the significant self-quenching effect in the latter material. This fractional thermal loading which is also known as “chi” or specific heating factor is defined as the ratio of heat generated to the absorbed energy. This lower thermal heat load in Yb-based materials contributes to the promotion of these materials for high power operation due to their better beam quality compared to that of Ti:Sapphire. Furthermore, Yb-doped lasers can produce wide wavelength tunability due to the broad emission bandwidths in their crystals (25-30 nm in Yb:YCOB, Yb:GdCoB, and Yb:BOYS) that facilitate the generation of

sub-50 femtosecond pulses [40] which have many scientific and industrial-orientated applications.

## 2.7 A Basic Review on Femtosecond Laser Sources.

Solid-state gain media with broad accessible bandwidth exploited for generating ultrashort pulses vary from Ti:Sapphire, and Chromium-doped crystals to Ytterbium-doped crystals. The most-widely used femtosecond laser to date is Ti:Sapphire with a wide tunability range from 600-1200 nm and pulse durations as short as 5 fs [14]. The applications of Ti:Sapphire involve scientific research, spectroscopy, generating and amplifying femtosecond lasers and as a pump source for optical parametric oscillators/amplifiers. Other femtosecond sources are based on chromium-doped lasers that are pumped in green and red spectral region and these are chromium forsterite ( $\text{Cr:Mg}_2\text{SiO}_4$ ), Cr:LiSAF, Cr:LiCAF, Cr:YAG and Cr:LiSGAF. The advantages of these lasers derive from their chemical stability, broad pump bands, large energy level splitting, low excited state absorption (ESA), and wide tuning range (700-900 nm for Cr:LiSAF and Cr:LiCAF, 1200-1600 nm for Cr:forsterite). The shortest pulse duration obtained to date from chromium-doped lasers are 10 fs for Kerr-lens mode locking [46] and 45 fs [47] for soliton mode locking. However, the disadvantages of chromium-doped lasers are lower thermal conductivity and stronger preference to upper-state lifetime quenching [48] that explains the limitation of their average output power. Together with the disadvantages existing in Ti:Sapphire laser such as low upper state lifetime ( $\sigma_p \tau_u, \sigma_{se} \tau_u$ ) [table 2.2] and large cavity dimensions [section 2.6], the needs to explore alternative femtosecond sources have been increased.

Recent competing research science and technology developments have shown tremendous progress in the areas of semiconductor and fibre lasers. To achieve the objective of generating femtosecond optical pulses from these laser types, semiconductors are promising gain media. Semiconductor lasers exhibit many advantages such as compactness, highly efficient operation due to the high wall-plug efficiency, reliability and convenience. These lasers can be electrically pumped as shown by the conventional diode lasers and vertical cavity semiconductor lasers (VCSELs) [49-51]. A few hundred femtosecond pulse durations within the range of 600 fs can also be produced from passively mode-locked distributed-Bragg-reflector laser diodes [52]. Other reports that implemented these

established techniques based on quantum-well heterostructures have demonstrated the generation of pulses in picosecond regimes [53,54]. Current research performed by Rafailov, Sibbett and co-workers at the University of St. Andrews has demonstrated that pulses as short as 390 fs can be produced by an electrically pumped mode-locked quantum-dot laser [55]. This is to date the shortest pulse obtained from a semiconductor laser. The advantages of these devices derive from the design of multi-gigahertz repetition rate cavity dimensions that can be applied in high capacity optical fibre communication links, ultrafast optical data processing systems, photonics switching devices and optical interconnects. Despite these advantages, the main drawbacks associated with these lasers are their lower average output powers (typically up to a few 10's mW) and longer pulse durations of several 100's femtoseconds for mode locking operation in comparison to those of solid-state lasers. However, the problem associated with the average power limitation can be addressed by the design of novel optically pumped passively mode-locked vertical external cavity semiconductor lasers (VECSELs) [56,57] that allow the scaling of output power up to a few hundred mW with sub-picosecond pulses up to 500 fs [58]. Further research in this work is continuing towards the achievement of shorter pulse durations, higher output power and excellent beam quality for femtosecond operation.

Mode-locked fibre lasers exhibit excellent stability and have many advantages such as robustness and reliability. Due to the nature of the fibre hosts that imply the total internal reflection of the propagating beams, reduction in unnecessary optical elements can be realized. This allows the design of compact cavity dimension that is beneficial for cost-reduction and high-efficiency operation. The broad fluorescence spectrum of the fibre gain media increases the tunability of these devices for ultrashort pulse generation. Several rare-earth materials have been doped to the fibre silica hosts based on erbium, neodymium and ytterbium that can provide a wide wavelength range of operation between 0.9 and 1.6  $\mu\text{m}$ . Initial development in fibre lasers was based on Er-doped materials [59,60] with output wavelengths at around 1.5  $\mu\text{m}$  to satisfy the high increasing demand for telecommunication industry. Pulse durations as short as 63 fs [61] were obtained in Er-doped fibre and 42 fs [62] in Nd-doped fibre lasers. In nonlinear optical frequency up-conversion assessment with the fundamental wavelength at 1.6  $\mu\text{m}$  [63], sub-100 fs second harmonic pulses were obtained. The nonlinear crystal used was a periodically-poled lithium niobate (PPLN) and second harmonic conversion efficiency up to 50 % was achieved. In mode-locked Yb-fibre lasers [62,64,65], pulse durations that are comparable to those produced in the glass hosts can be achieved. Wide wavelength tunability between 980 and 1070 nm [66] had been

demonstrated in a SESAM-assisted femtosecond operation. Pulses as short as 36 fs [67] had been produced and it was assumed that shorter durations can be generated from this laser once the limitation due to the intracavity third-order dispersion can be sorted out.

In parallel to the rapid development of femtosecond laser sources based on semiconductor and fibre hosts, further simplifications in solid-state lasers are very successful. Yb-doped materials are seen as alternative sources for femtosecond lasers and these represented the main objective within my PhD. project. The advantages of developing these materials for femtosecond lasers are due to the simple pumping requirement provided by high brightness InGaAs quantum well diode lasers between 900-980 nm which permit the construction of cost-effective, low threshold, compact and highly efficient femtosecond lasers. In addition the simple two level energy structure, broad spectral bandwidth  $\sim 30$  nm, and low quantum defect  $\leq 0.14$  are beneficial to facilitate the generation of ultrashort pulses with efficient thermal management. To date, sub-50 fs pulse durations [40] can be produced from Yb-doped lasers which have a wide range of applications [section 1.2].

## **2.8 Conclusion.**

New emerging applications in femtosecond laser science has led to rapid developments in semiconductor, fibre and solid-state lasers. This allows the exploration of new previously inaccessible parameters that opens up many applications in biology, medicine, femtochemistry, optical telecommunications and industry. The shortest pulses of a few femtoseconds duration can be generated in SESAM-assisted and Kerr-lens based mode locking laser arrangements. Each type of laser system is not in direct competition with others and the application sectors tend to dictate which type of laser is to be preferred. For both the optimisation of output power and multi-gigahertz repetition rate, semiconductor lasers show particular potential. Although fibre lasers are notable for their low threshold characteristics as well as their compact and highly efficient operation configuration, the requirement for the long gain media restricts their repetition rate. (A part of my project aim was to produce a compact and efficient femtosecond solid-state laser).

Instead of the current achievement in sub-50 fs pulse regimes [40], from the author's opinion, the continuing exploration of new Yb-doped materials as gain media [section 2.6] for portable and highly efficient solid-state femtosecond lasers would in the future allow the generation of ultrashort pulses within sub-10 fs with the approximate spectral bandwidths of

100 nm. These features could increase many new applications that are previously inaccessible to the lab-bound device footprints of their predecessors.

## 2.9 References:

1. J. M. Hopkins and W. Sibbett, "Ultrashort pulse lasers: Big payoff in a flash," *Scientific American*, 55-61 (2000).
2. W. Sibbett, "Ultrashort pulse sources," *Laser Sources and Applications, Proceedings of the Forty Seventh Scottish Universities Summer School in Physics, St. Andrews*, 255-289 (1995).
3. W. Koechner, "Solid state laser engineering," 5th. Edition, Springer-Verlag Berlin and Heidelberg , 29- 87 (1999).
4. R. Paschotta, R. Hring, E. Gini, H. Melchior, U. Keller, H. L. Ferhaus, and D. J. Richardson, "Passively Q-switched 0.1-mJ fiber laser system at 1.53  $\mu\text{m}$ ," *Opt. Lett.* **24**, 388-390 (1999).
5. A. E. Siegmann "Lasers," University Science Book, Mill Valley, California (1986).
6. M.H. Dunn, "Lasers 2," MSc. in Photonics and Optoelectronic Devices, School of Physics and Astronomy, University of St. Andrews (2001).
7. U. Keller, "Ultrashort pulse generation," *Advances in Lasers and Applications, Proceedings of the Fifty Second Scottish Universities Summer School in Physics, St. Andrews*, 83-115 (1998).
8. C. T. A. Brown and W. Sibbett, "Femtosecond sources based on vibronic crystals," *Ultrafast Photonics, Proceedings of the Fifty Sixth Scottish Universities Summer School in Physics, St. Andrews*, 21-42 (2004).
9. F. X. Kartner and U. Keller, "Stabilization of soliton like pulses with a slow saturable absorber," *Opt. Lett.* **20**, 16-18 (1995).
10. F. X. Kartner, D. Kopf, and U. Keller, "Solitary pulse stabilization and shortening in actively mode-locked lasers," *J. Opt. Soc. Am. B* **12**, 426-438 (1995).
11. I. D. Jung, F. X. Kartner, N. Matuschek, D. H. Sutter, F. Morier-Genoud, Z. Shi, V. Scheuer, M. Tilsch, T. Tschudi, and U. Keller, "Semiconductor saturable absorber mirrors supporting sub-10 fs pulses," *Appl. Phys. B* **65**, 137-150 (1997).
12. D. E. Spence, P. N. Kean, and W. Sibbett, "60 fs pulse generation from a self mode-locked Ti:sapphire laser," *Opt. Lett.* **16**, 42-44, (1991).
13. U. Keller, "Recent developments in compact ultrafast lasers," *Nature* **424**, 831-838 (2003).
14. R. Ell, U. Morgner, F. X. Krtner, J. G. Fujimoto, E. P. Ippen, V. Scheuer, G. Angelow, T. Tschudi, M. J. Lederer, A. Boiko, and B. Luther-Davies, "Generation of 5-fs

- pulses and octave-spanning spectra directly from a Ti:sapphire laser,” *Opt. Lett.* **26**, 373-375 (2001).
15. D.H. Sutter, “Semiconductor saturable-absorber mirror-assisted Kerr-lens mode-locked Ti:Sapphire laser producing pulses in the two cycle regime,” *Opt. Lett.* **24**, 631-633 (1999).
  16. G. Cerullo, S. De. Silvestri, V. Magni, and L. Pallaro, “Resonators for Kerr-lens mode-locked femtosecond Ti:Sapphire lasers,” *Opt. Lett.* **19**, 807-809 (1994).
  17. G. Cerullo, S. De. Silvestri, and V. Magni, “Self-starting Kerr-lens mode locking of a Ti:Sapphire laser,” *Opt. Lett.* **19**, 1040-1042 (1994).
  18. J. A. Valdmanis and R. L. Fork, “Design considerations for a femtosecond pulse laser balancing self phase modulation, group velocity dispersion, saturable absorption, and saturable gain,” *IEEE J. Quantum Electron.* **22**, 112-118 (1986).
  19. F. X. Kartner, I. D. Jung, and U. Keller, “Soliton modelocking with saturable absorbers,” *IEEE J. Select. Topics Quantum Electron.* **2**, 540-556 (1996).
  20. U. Keller, F. X. Kartner, D. Kopf, B. Braun, I. D. Jung, R. Fluck, C. Honninger, N. Matuschek, and J. A. der Au, “Semiconductor saturable absorber mirrors (SESAM’s) for femtosecond to nanosecond pulse generation in solid state lasers,” *IEEE. J. Select Topics Quantum Electron.* **2**, 435-453 (1996).
  21. U. Keller, D. A. B. Miller, G. D. Boyd, T. H. Chiu, J. F. Ferguson, and M. T. Asom, “Solid-state low-loss intracavity saturable absorber,” *Opt. Lett.* **17**, 505-507 (1992).
  22. L. R. Brovelli, U. Keller, and T.H. Chiu, “Design and operation of antiresonant Fabry-Perot semiconductor saturable absorber for mode-locked solid-state lasers,” *J. Opt. Soc. Am. B* **12**, 311-322 (1995).
  23. C. Honninger, R. Paschotta, F. Morier-Genoud, M. Moser, and U. Keller, “Q-switching stability limits of continuous-wave passive mode locking,” *J. Opt. Soc. Am. B* **16**, 46-56 (1999).
  24. U. Keller, “Semiconductor nonlinearities for solid state laser mode locking and Q-switching,” E. Garmire, A. Kost Eds. (Academic Press Inc. Boston), *Nonlinear optics in Semiconductor* **59**, 211 (1999).
  25. R. Paschotta and U. Keller, “Passive mode locking with slow saturable absorbers,” *Appl. Phys. B* **73**, 653-662 (2001).
  26. D. H. Sutter, I. D. Jung, F. X. Kartner, N. Matuschek, F. Morier-Genoud, V. Scheuer, M. Tilsch, T. Tschudi, and U. Keller, “Self-starting 6.5 fs pulses from a Ti:Sapphire

- laser using a semiconductor saturable absorber and double-chirped mirrors,” *IEEE J. Select. Topics Quantum Electron.* **4**, 1691-178 (1998).
27. S. O. Kasap, “Optoelectronics and photonics: principles and practices,” Prentice Hall, New Jersey, 311-321 (2001).
  28. I. Walmsley, L. Waxer, and C. Dorrer, “The role of dispersion in ultrafast optics,” *Rev. of Scientific Instruments* **72**, 1-29 (2001).
  29. P. M. W. French, “The generation of ultrashort laser pulses,” *Rep. Prog. Phys.* **58**, 169-252 (1995).
  30. O. Svelto, “Principles of lasers,” 4<sup>th</sup> edition, Plenum Press New York and London, 342-374 (1998).
  31. R. Penty, “Short pulse generation using semiconductor lasers,” *Ultrafast Photonics, Proceedings of the Fifty Sixth Scottish Universities Summer School in Physics*, St. Andrews, 43-71 (2004).
  32. G. Huber, “Solid-state laser materials,” *Laser Sources and Applications, Proceedings of the Forty Seventh Scottish Universities Summer School in Physics*, St. Andrews, 141-162 (1996).
  33. W. F. Krupke, “Materials for lasers and nonlinear optics,” *Advances in Lasers and Applications, Proceedings of the Fifty Second Scottish Universities Summer School in Physics*, St. Andrews, 124-125 (1998).
  34. P. F. Moulton, “Spectroscopic and laser characteristics of Ti:Al<sub>2</sub>O<sub>3</sub>,” *J. Opt. Soc. Am B* **3**, 125-133 (1986).
  35. A. Sennaroglu, A. M. Kowalewicz, F. X. Kartner, and J. G. Fujimoto, “High performance, compact, prismless, low threshold 30 MHz. Ti:Al<sub>2</sub>O<sub>3</sub>,” *Opt. Lett.* **28**, 1674-1676 (2003).
  36. E.D. Nelson, J. Y. Wong, and A. L. Shawlow, “Far infrared spectra of Al<sub>2</sub>O<sub>3</sub>:Cr<sup>3+</sup> and Al<sub>2</sub>O<sub>3</sub>:Ti<sup>3+</sup>,” *Phys. Review* **156**, 298-308 (1967).
  37. S. A. Payne; L. K Smith; L. D. De Loach, W. L. Kway, J. B. Tassano, and W. F. Krupke, “Laser, optical and thermomechanical properties of Yb-doped fluorapatite,” *IEEE J. Quantum Electron.* **30**, 170-179 (1994).
  38. C. Honninger, R. Paschotta, M. Graf, F. Morier-Genoud, G. Zhang, M. Moser, S. Biswal, J. Nees, A. Braun, G. A. Mourou, I. Johannsen, A. Giesen, W. Seeber, and U. Keller, “Ultrafast Ytterbium-doped bulk lasers and laser amplifiers,” *Appl. Phys. B* **69**,3-17 (1999).

39. W. F. Krupke, "Ytterbium solid state lasers- The first decade," *IEEE J. Select. Topics Quantum Electron.* **6**, 1287-1296 (2000).
40. Y. Zaouter, J. Didierjean, F. Balembois, G. L. Leclin, F. Druon, P. Georges, J. Petit, P. Goldner, and B. Viana, "47-fs diode-pumped  $\text{Yb}^{3+}:\text{CaGdAlO}_4$  laser," *Opt. Lett.* **31**, 119-121 (2006).
41. E. Innerhofer, T. Sudmeyer, F. Brunner, R. Hring, A. A. Aschwanden, R. Paschotta, C. Honninger, M. Kumkar, and U. Keller, "60W average power in 810-fs pulses from a thin-disk Yb:YAG laser," *Opt. Lett.* **28**, 367-369 (2003).
42. C. Honninger, G. Zhang, U. Keller, and A. Giesen, "Femtosecond Yb:YAG laser using semiconductor saturable absorbers," *Opt. Lett.* **20**, 2402-2404 (2003).
43. T. Y. Fan and R. L. Byer, "Modelling and CW operation of a quasi-three-level 946 nm Nd:YAG laser," *IEEE J. Quantum Electron.* **23**, 605-612 (1987).
44. W. P. Risk "Modelling of longitudinally pumped solid-state lasers exhibiting re-absorption losses," *J. Opt. Soc. Am. B* **5**, 1412-1423 (1988).
45. T. Y. Fan, "Heat generation in Nd:YAG and Yb:YAG," *IEEE J. Quantum Electron.* **29**, 1457-1459 (1993).
46. S. Uemera and K. Torizuka, "Development of a diode-pumped Kerr-lens mode-locked Cr:LiSAF laser," *IEEE J. Quantum Electron.* **39**, 68-73 (2003).
47. D. Kopf, A. Prasad, G. Zhang, M. Moser, and U. Keller, "Broadly tunable femtosecond Cr:LiSAF laser," *Opt. Lett.* **22**, 621-623 (1997).
48. M. Stalder, M. Bass, B. H. T. Chai, "Thermal quenching of fluorescence in chromium-doped fluoride laser crystals," *J. Opt. Soc. Am. B* **9**, 2271-2273 (1992).
49. K. Iga, "Surface emitting laser-its birth and generation of new optoelectronics field," *IEEE J. Select. Topics Quantum Electron.* **6**, 1201-1215 (2000).
50. S. Hoogland, S. Dhanjal, A. C. Tropper., J. S. Roberts., R. Haring, R. Paschotta, F. Morier-Denoud, and U. Keller, "Passively mode-locked diode-pumped surface-emitting semiconductor laser," *IEEE Photonic Tech. Lett.* **12**, 1135-1137 (2000).
51. R. Paschotta, R. Häring, A. Garnache, S. Hoogland, A. C. Tropper, and U. Keller, "Soliton-like pulse shaping mechanism in passively mode-locked surface-emitting semiconductor lasers," *Appl. Phys. B* **75**, 445 (2002).
52. S. Arahira, Y. Matsui, and Y. Ogawa, "Mode-locking at very high repetition rates more than Terahertz in passively mode-locked distributed-bragg-reflector laser diodes," *IEEE. J. Quantum Electron.* **32**, 1211-1223 (1996).

53. P. Vasil'ev, "Ultrafast diode lasers: fundamental and applications," Ch. 4, Artech House, Boston, 95-150 (1995).
54. E. A. Avrutin, J. H. Marsh, and E. L. Portnoi, "Monolithic and multi-gigahertz mode-locked semiconductor lasers: construction, experiments, models and applications," *IEEE. Proc. Optoelectron.* **147**, 251-278 (2000).
55. E. U. Rafailov and M. A. Cataluna, "Mode-locked quantum-dot lasers," *Nature Photonics* **1**, 395-401 (2007).
56. A. C. Tropper, H. D. Foreman, A. Garnache, K. G. Wilcox, and S. H. Hoogland, "Vertical-external-cavity semiconductor lasers," *J. Phys. D: Appl. Phys.* **37**, R75-R85 (2004).
57. S. Calvez, J. M. Hopkins, S. A. Smith, A. H. Clark, R. Macaluso, H. D. Sun, M. D. Dawson, T. Jouhti, M. Pessa, K. Gundogdu, K. C. Hall, and T. F. Boggess, "GaInNAs/GaAs Bragg-mirror-based structures for novel 1.3  $\mu\text{m}$  device applications," *J. Crystal Growth* **268**, 457-465 (2004).
58. A. Garnache, S. Hoogland, A. C. Tropper, I. Sagnes, G. Saint-Girons, and J. S. Roberts, "Sub-500 fs soliton-like pulse in a passively mode-locked broadband surface-emitting laser with 100 mW average power," *Appl. Phys. Lett.* **80**, 3892-3894 (2002).
59. R. J. Mears, L. Reekie, I. M. Jauncey, and D. N. Payne, "Low-noise Erbium-doped fiber amplifier at 1.54  $\mu\text{m}$ ," *Electron. Lett.* **23**, 1026-1028 (1987).
60. E. Desurvive, J. Simpson, and P. C. Becker, "High-gain Erbium-doped travelling-wave fiber amplifier," *Opt. Lett.* **12**, 888-890 (1987).
61. K. Tamura, E. P. Ippen, and H. A. Haus, "Pulse dynamics in stretched-pulse fiber lasers," *Appl. Phys. Lett.* **67**, 158-160 (1995).
62. M. H. Ober, M. Hofer, and M. E. Fermann, "42 fs pulse generation from a mode-locked fiber laser started with a moving mirror," *Opt. Lett.* **18**, 367-369 (1993).
63. O. Okhotnikov, A. Grudinin, and M. Pessa, "Ultrafast fiber laser systems based on SESAM technology: new horizons and applications," *New J. Phys.* **6**, 177-206 (2004).
64. H. Lim, F. O. Ilday, and F. W. Wise, "Generation of 2 nJ pulses from a femtosecond ytterbium fiber laser," *Opt. Lett.* **28**, 660-662 (2003).
65. F. O. Ilday, J. R. Buckley, H. Lim, F. W. Wise, and W. G. Clark, "Generation of 50 fs, 5 nJ pulses at 1.03  $\mu\text{m}$  from a wave-breaking-free fiber laser," *Opt. Lett.* **28**, 1365-1367 (2003).

66. O. G. Okhotnikov, L. Gomes, N. Xiang, and T. Jouhti, "Mode-locked ytterbium fiber laser tunable in the 980-1070 nm spectral range," *Opt. Lett.* **28**, 1522-1524 (2003).
67. F. O. Ilday, J. Buckley, L. Kuznetsova, and F. W. Wise, "Generation of 36 femtosecond pulses from a ytterbium fiber laser," *Opt. Express* **11**, 3550-3554 (2003).

## **Chapter 3**

### **Basic Parameters for Low Threshold, Compact and Highly Efficient Femtosecond Lasers.**

#### **3.1 Introduction.**

This chapter discusses several characteristics that influence the lasing performance. These include spectroscopic properties such as the fraction of Yb-ions required for optical transparency/population inversion, saturation intensity, threshold power, and slope-efficiency. Other important laser parameters are the use of high intensity diffraction-limited pump source, laser cavity design, optical components and appropriate pump/laser mode overlap. The optimisation of these factors favours the achievement of low threshold continuous wave operation that becomes the main prerequisite for the establishment of low mode locking threshold. This is one of the main objective of performing assessments in this PhD. project. A few elements such as quantum defect, doping concentration, and optical component properties are also mentioned to increase the efficiency of the laser operation. Reduction in optical elements can be realised to achieve compactness and portability in the device footprint. This increases many unprecedented applications in photobiology, medicine, surgery, microscopy, imaging and diagnostic measurements which are previously less accessible to the larger-scale predecessors. The basic structure of this thesis is explained in section 3.3 to give an insight to the works carried out in this project.

#### **3.2 Laser Performance.**

Given the quasi three level energy manifold in Yb-doped materials, a minimum fraction of Yb-ions ( $\beta_{\min}^{\lambda_{se}}$ ) need to be pumped to the upper state to achieve transparency. By assuming that the bulk parasitic losses are negligible, at the specified emission wavelength ( $\lambda_{se}$ ) this implies as [1,2]:-

$$\beta_{\min}^{\lambda_{se}} = \frac{\sigma_{abs}^{\lambda_{se}}}{\sigma_{abs}^{\lambda_{se}} + \sigma_{se}^{\lambda_{se}}} = \frac{1}{1 + \frac{\sigma_{se}^{\lambda_{se}}}{\sigma_{abs}^{\lambda_{se}}}} \quad (3.2.1)$$

where  $\sigma_{abs}^{\lambda_{se}}$  and  $\sigma_{se}^{\lambda_{se}}$  are the absorption and stimulated emission cross-sections at  $\lambda_{se}$ . From figure 3.1,  $\beta_{\min}^{\lambda_{se}}$  in Yb-doped materials can be measured from the upper and lower state energies  $E_{U,S}$  and  $E_{L,S}$  where the subscript 's' denotes the Stark energy levels. By substituting the fraction of Boltzman occupation factor,  $f_U$  and  $f_L$  in the upper and lower state energy level into equation (3.2.1), it can be deduced that [3]:-

$$\beta_{\min}^{\lambda_{se}} = \frac{1}{1 + f_u/f_l} \quad (3.2.2a)$$

where  $f_u = 1/Z_u e^{\frac{E_{U,1} - E_{U,S}}{kT}}$  and  $f_l = 1/Z_L e^{\frac{E_{L,1} - E_{L,S}}{kT}}$ . The ratio between these two parameters can be expressed as:-

$$f_u/f_l = Z_L/Z_U e^{\frac{\Delta E_{ZL} - (hc/\lambda)}{kT}} \quad (3.2.2b)$$

where the energy difference  $E_{L,S} - E_{U,S} = -hc/\lambda$ , the zero line energy  $\Delta E_{ZL} = E_{U,1} - E_{L,1}$  is the difference between the lowest Stark level in the upper and lower state,  $h = 6.634 \times 10^{-34}$  Js is the Planck's constant and  $\lambda$  is the corresponding wavelength.  $k = 1.381 \times 10^{-23}$  J/K or  $0.695 \text{ cm}^{-1}/\text{K}$  is the Boltzmann constant,  $T$  is the absolute temperature while  $Z_U$  and  $Z_L$  are partition functions for both of the states [3,4] that can be obtained from:-

$$Z_m = \sum_s e^{\frac{E_{m,1} - E_{m,s}}{kT}} \quad (3.2.3)$$

From this equation,  $E_{m,1}$  represents the energy value of the  $m$ -state in the lowest Stark level where  $m = 1$  for  ${}^2F_{7/2}$  and  $m = 2$  for  ${}^2F_{5/2}$ . All of these equations allow  $\beta_{\min}^{\lambda_{se}}$  to be obtained

from the Stark level energies in  $cm^{-1}$  as indicated in figure 3.1 without accounting for the cross-section values [5]. From the values presented in table 3.1, 5.8 % of the Yb-ions need to be pumped from the lower state  $E_{L,3}$  to the upper state  $E_{U,1}$  to achieve optical transparency at the emission wavelength of 1030 nm as illustrated in figure 3.1.

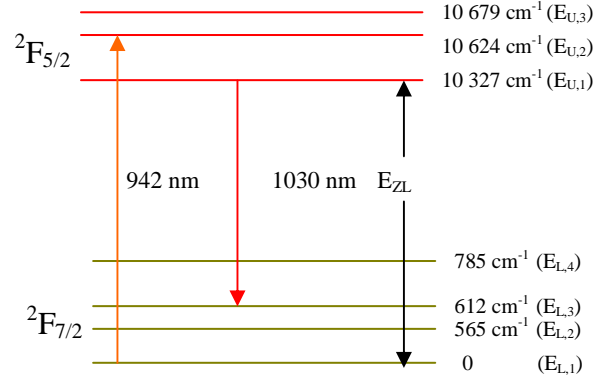


Figure 3.1. Energy levels of Yb:YAG for the upper manifold  ${}^2F_{5/2}$  and lower manifold  ${}^2F_{7/2}$  where all the energy for each Stark level are given in  $cm^{-1}$  and  $E_{ZL} = 10\,327\,cm^{-1}$  [6]

Table 3.1. The fractions of Boltzmann occupation factor for each Stark level in Yb:YAG where  $Z_L/Z_U = 0.803527$  at the room temperature of  $20^{\circ}C$ . These fractions were calculated from the energy values in  $cm^{-1}$  given from figure 3.1.

Manifold (m)	Stark Level (s)	$f_U$ (%)	Manifold (m)	Stark Level (s)	$f_L$ (%)
${}^2F_{5/2}$	3	12.6	${}^2F_{7/2}$	4	1.9
	2	16.5		3	4.4
	1	70.9		2	5.5
		1		88.3	

Once  $\beta_{\min}^{\lambda_{se}}$  has been reached, the gain medium is said to be transparent/bleached at the emission wavelength because the upper state and the terminal laser level will have equal populations. As the consequence, the minimum pump intensity  $I_{\min}$  required to pump  $\beta_{\min}^{\lambda_{se}}$  to the upper state can be shown as:-

$$I_{\min} = \beta_{\min}^{\lambda_{se}} I_{sat} \quad (3.2.4)$$

where  $I_{\min}$  is also described as the absorbed pump intensity required to reach threshold in a zero-loss laser cavity and  $I_{sat}$  is the pump saturation. The definition of  $I_{sat}$  with respect to the absorption cross-section  $\sigma_{abs}^{\lambda_p}$  and upper state lifetime  $\tau_u$  is given as [7]:-

$$I_{sat} = \frac{h\nu_p}{(\sigma_{abs}^{\lambda_p} + \sigma_{se}^{\lambda_p})\tau_u} \quad (3.2.5)$$

where  $h\nu_p$  is the pump photon energy at  $\lambda_p$ . For Yb:YAG where  $\lambda_p = 942$  nm  $\sigma_{se}^{\lambda_p}$  is quite small and can be ignored whereas for Yb-doped tungstates, where  $\lambda_p = 981$  nm,  $\sigma_{se}^{\lambda_p}$  is higher and must be included. For instance, from the energy level structures of Yb:YAG in figure 3.1,  $I_{sat}$  is calculated to be 30.2 kW/cm<sup>2</sup> for  $\tau_u = 1$  ms and  $\sigma_{abs}^{\lambda_p} = 0.7 \times 10^{-20}$  cm<sup>2</sup> [8]. This corresponds to the minimum pump intensity of 1.75 kW/cm<sup>2</sup> required to pump 5.8 % of  $\beta_{\min}^{\lambda_{se}}$  to the upper state level.  $I_{sat}$  also indicates the useful merit of the Yb-crystal to achieve transparency where the lower the value of  $I_{sat}$  can lead to lower threshold power,  $P_{th}$ . This can give a useful indication in the selection of Yb-doped gain media. The cw (continuous wave) threshold power [3,9] in a laser cavity can then be shown to be:-

$$P_{th} = \frac{(\pi \cdot w_p^2 + \pi \cdot w_l^2) h\nu_p (T_{OC} + L_d + 2L_{Yb})}{4\eta_{abs} \tau_u \sigma_{se}^{\lambda_{se}}} \quad (3.2.6a)$$

and,

$$L_{Yb} = \sigma_{abs}^{\lambda_{se}} \cdot N_{Yb} \cdot l \quad (3.2.6b)$$

where  $w_p$  and  $w_l$  are the diverging pump and laser spot sizes through the crystal,  $T_{OC}$  is the output coupling transmission,  $\eta_{abs} = 1 - e^{-\alpha_p l}$  is the pump absorption efficiency at  $\lambda_p$  where  $\alpha_p$  is the pump absorption coefficient and  $L_d$  is the double pass passive-loss in the cavity that is influenced by the scattering or Fresnel reflection from the crystal. From equation (3.2.6b),  $L_{Yb}$  is the single pass absorption loss at the emission wavelength due to the Yb-doping concentration  $N_{Yb}$ , inside the crystal, and  $l$  is the length of the gain medium. In the

absence of excited-state-absorption and a sub-unity quantum efficiency, the Yb. absorption loss ( $L_{Yb}$ ) does not affect the slope efficiency  $\eta$  at many times above threshold but results in an increase of pump power required to reach threshold [10]. Thus, as expected, for two laser media having similar slope efficiency, the output power is higher for a crystal that has a lower laser threshold. When the system is operating above threshold, a greater proportion of Yb-ions are pumped to the upper state to provide the necessary population inversion. The gain is higher than the re-absorption loss in the gain medium at  $\lambda_{se}$  which therefore favours the laser operation. This small signal gain coefficient [11] is given as:-

$$g = 2l.[N_U\sigma_{se}^{\lambda_{se}} - N_L\sigma_{abs}^{\lambda_{se}}] \quad (3.2.7)$$

where  $N_U$  and  $N_L$  are the population density at the upper and lower states respectively. The factor 2 is the number of passes through the gain medium per cavity round trip in a standing wave resonator. The fraction of excited Yb-ions ( $\beta$ ) during lasing that is derived from equation (3.2.4) and (3.2.5) can then be expressed as:-

$$\beta = I_{abs} / I_{sat} \quad (3.2.8)$$

where  $I_{abs}$  is the absorbed pump intensity.

To produce the maximum output power ( $P_{out}$ ), effective alignment of the cavity lengths and reduction in the cavity round trip loss ( $T + L_d + 2L_{Yb}$ ) are required. The optical-to-optical conversion efficiency of a laser system can be obtained from the ratio between the output power ( $P_{out}$ ) and the absorbed pump power ( $P_{abs}$ ). By plotting a graph of  $P_{abs}$  versus  $P_{out}$ , a slope efficiency  $\eta$  can be measured. This value depends on the relevant lasing parameters that is described as [12]:-

$$\eta = \eta_0 \frac{T_{OC}}{[T_{OC} + L_d]} \eta_{ol} \quad (3.2.9)$$

where  $\eta_{ol}$  contains the geometrical factors associated with the conversion of pump photons

to laser photons and  $\eta_0 = \lambda_p / \lambda_{se}$  is the quantum efficiency of the gain medium that indicates the effectiveness of laser performance in the absence of excited state absorption. Assuming the geometrical factors are arranged such that  $\eta_{ol} \approx 1$ , the equation (3.2.9) above can be transposed into:-

$$\frac{1}{\eta} = \frac{1}{\eta_0} + \frac{L_d}{\eta_0} \left( \frac{1}{T_{OC}} \right) \quad (3.2.10)$$

By plotting a graph of  $1/\eta$  versus  $1/T_{OC}$ , the slope is  $L_d/\eta_0$  and the intercept is  $1/\eta_0$ . This equation describes the linear relationship between the inverse slope efficiency and the output coupling where  $\eta$  is a maximum when  $T_{OC}$  is optimised [4].

Table 3.2. An example of slope-efficiency and threshold power for Ti:sapphire crystal I and II [this imaginary data is presented to demonstrate the relationship between  $1/T_{OC}$  and  $1/\eta$ ].

Crystal Type	$T_{OC}$ (%)	$\eta$ (%)	$P_{th}$ (mW)
I	3	42.7	98
II	3	27.5	70
I	5	51.8	87
II	5	36.2	64
I	10	55.9	80
II	10	47.6	60
I	20	59.5	102
II	20	52.63	90

By studying the results obtained in [9], an imaginary example is given in table 3.2 above to determine the values of  $L_d$  in Ti:Sapphire laser. Two types of crystals are used that are labelled as crystal I and II. The laser is pumped at 532 nm and the peak emission wavelength is 805 nm that relates to a quantum efficiency of 66.1 %. The graph obtained was plotted in figure 3.2 below. From this figure, the linear fit for crystal I implies an intercept of 1.54 that corresponds to a quantum efficiency of 64.9 % and the linear fit for crystal II implies an intercept of 1.53 that corresponds to a quantum efficiency of 65.4 %. These values are almost close to the quantum efficiency of the laser medium. From the

slope of the graph, the double passive loss of crystal I is calculated to be 1.5 % and for crystal II is 4.12 %.

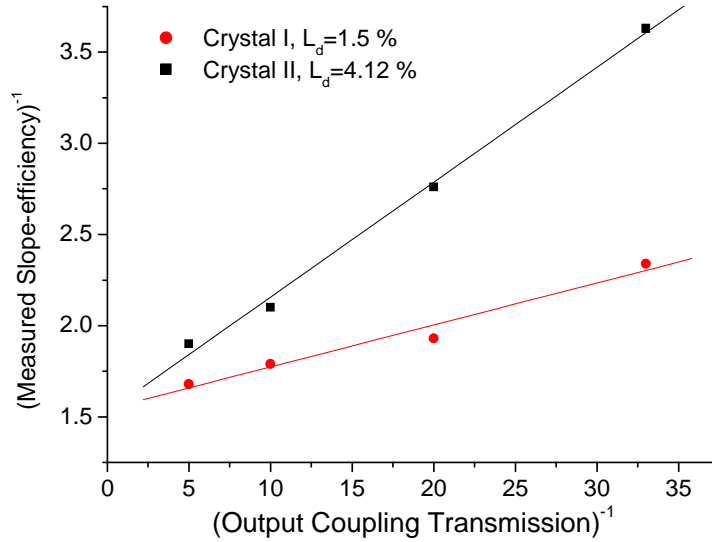


Figure 3.2. The inverse slope-efficiency of the crystals as a function of the inverse output coupling transmission based on the fictional data presented in table 3.2.

### 3.3 Towards Low-threshold, Compact, and High-efficiency Yb-doped Femtosecond Lasers.

The use of diode lasers as pump sources for solid-state lasers [13] in the near-infrared region, has facilitated the development of more compact, highly efficient, robust, stable and portable femtosecond lasers. This characteristic of compactness and portability opens up many applications in photobiology, medicine, surgery, microscopy, imaging and diagnostic measurements that are less accessible to the larger size of their predecessors. All the conditions mentioned above can be satisfied by Yb-doped lasers because their pumping wavelength requirement matches closely with InGaAs quantum well diode lasers that operate in the 900-980 nm band. Another technique to achieve compactness in the laser configuration is by using fewer optical components to favour the achievement of high-efficiency operation that will be mentioned in the conclusion part of this chapter.

To address the problem of quasi-three level systems where the laser threshold is increased due to the partial reabsorption of the emitted radiation, a high pump intensity source that offers a diffraction limited pump beam is required. The improvements in the beam quality parameter ( $M^2 \approx 1$ ) that became available from the commercial diode lasers that produce output powers up to 0.5 W during the course of my PhD. project satisfied the

requirement to provide a strong overlap between the pump and laser modes in the gain medium as shown in figure 3.3(a). In addition, with smaller beam spot sizes, the pump intensity is higher and this reduces the threshold pump power required for continuous wave (CW) laser operation.

This mechanism can be illustrated in figure 3.3 below where, for a diffraction limited pump beam, a larger volume of the crystal is exposed to the tight-focusing geometry in comparison to that with poorer beam quality ( $M^2 > 1$ ). A greater percentage of the pumped Yb-ions are thus excited to the upper state to produce a greater population inversion [see (a)] which subsequently increases the rate of the stimulated emission [compared to that in (b)]. As the consequence, a lower threshold is achieved for condition (a).

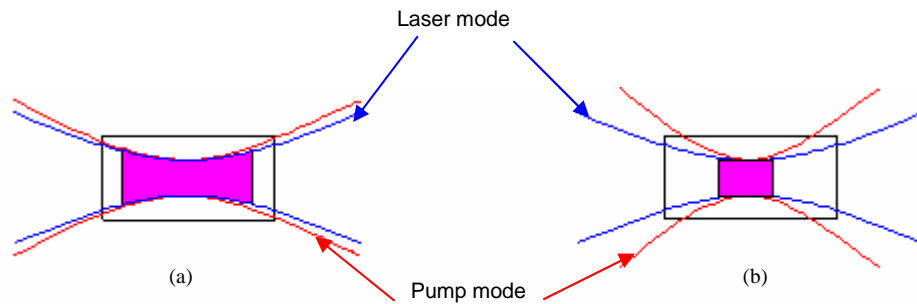


Figure 3.3(a). Strong overlap between the pump/laser mode ( $w_p:w_l$ ) for a diffraction limited pump beam source and (b) poor overlap between the pump/laser mode for the multimode source where  $M^2 > 1$ . The pink colour shows region under strong mode-coupling for both conditions where for a comparable waist size the Rayleigh range is longer in (a) compared to that in (b).

Alfrey [14] and Piche [15] have described the conditions required to achieve a low pump threshold and optical nonlinearity. In cw operation, the important criteria that are required to ensure low threshold [equation 3.2.6a] are the spectroscopic properties of the gain media that include upper state lifetime product  $\sigma_{se}\tau_u$ , laser parameters such as the pump photon energy ( $h\nu_p$ ) and the optical component properties. Favourable properties of  $\sigma_{se}\tau_u$ , optimum pump wavelength ( $\lambda_p$ ) and reduction in cavity round trip loss ( $T + L_d + 2L_{yb}$ ) all contribute to the achievement of a low pump threshold [9,16]. Specifically, Yb-doped gain materials have advantages over other solid-state materials due to their longer pump wavelength bands,  $\lambda_p$ , around 980 nm compared to that in Cr:LiSAF with  $\lambda_p = 670$  nm and Ti:Sapphire with  $\lambda_p = 530$  nm.

A low threshold for cw laser operation is the main prerequisite for low mode locking thresholds at low pump power levels to be established. Femtosecond laser operation can be initiated by optimisation of the laser cavity that includes the exploitation of Kerr-lens effect and/or saturating the absorption of an intracavity semiconductor saturable absorber mirror (SESAM) element. By comparing the energy emitted from the laser with respect to the emission cross-section  $\sigma_{se}$  of the gain medium, the saturation fluence  $F_{sat,L}^{\lambda_{se}}$  can be obtained at  $\lambda_{se}$  [17] to be:-

$$F_{sat,L}^{\lambda_{se}} = hc / m\sigma_{se}\lambda_{se} \quad (3.3.1)$$

where  $m=2$  for a standing wave cavity. The optimisation of saturation fluence incident on the SESAM,  $F_{SE}^{\lambda_{se}}$  can be important in solid-state-lasers for the initiation of stable mode locking as will be discussed later in the next chapter [Chapter 4]. In addition, by an appropriate cavity alignment between the mirrors and the gain medium, the tight focusing geometry between pump and laser mode on the front end-face of Kerr gain medium can be obtained to induce a self-focusing effect and gain-guiding influence [KLM, see 2.3.1]. This increases the self-amplitude modulation effect in the transverse propagation of the beam where the reduction in the beam spot size serves to increase the nonlinear intensity dependent refractive index,  $I(r,t)$  of the propagating waves. The higher intensity existing in the pulsed operation over the lower intensity in the cw regime thus leads to a reduction in the mode locking threshold. (More explanations on laser threshold can also be obtained from the work done by B. Agate and J. M. Hopkins [18,19]). It should also be pointed out here, however, that another disadvantage arising from quasi-three-level media is the limited wavelength tunability from the laser output due to the overlap between the absorption and emission bands [see figure 2.18]. The spectral characteristics of the saturable absorption features of the SESAM must therefore be designed to match precisely the principal lasing band of the gain crystal.

Several parameters such as the quantum defect, the doping concentration and the optical component properties are important if a high laser efficiency is to be achieved. The low quantum defect in Yb-doped materials, for instance  $\sim 0.04$  in Yb-doped tungstate materials is especially attractive to reduce the heat dissipation requirements. The laser crystals studied in this project (notably Yb:KYW) can also provide the possibility of high

doping levels which in turn reduces the crystal length. Optical component properties such as high transmissivity at the pump wavelength and high reflectivity at the laser wavelength contribute to a low cw threshold while an optimum output coupling transmission is responsible for a high efficiency operation. From figure 3.3, it can be seen that for a comparable waist size, the Rayleigh range of the propagating waves in the material pumped by a diffraction limited pump beam is significantly more extended than that when the pump source is multimode. The former thus increases the interaction length of the crystal where this optimisation is beneficial for high-efficiency operation.

Compactness and high efficiency in femtosecond laser configurations can also be achieved by reduction in optical cavity components. It will be seen in the following work that the major limitation to reducing this cavity length is due to the minimum separation between the prism pair [20] responsible for dispersion compensation. Therefore, for the achievement of this objective [see Chapter 4] a single prism was used in laser oscillators based on Yb:KYW as a gain material where a SESAM was implemented for the modelocking operation. This asymmetric four mirror cavity provides a simpler alignment which is beneficial for wider wavelength tunability. To further reduce power output losses caused by the single prism, negatively dispersive mirrors were used that allow the compact dispersion compensation mechanism by reflecting multiple bounces of the laser beam inside the oscillators [Chapter 5].

In Chapter 6, further simplification of the laser cavity was achieved in a three-mirror cavity by implementing the Kerr-lens effect for the initiation of the mode-locked operation in Yb:YVO<sub>4</sub> femtosecond lasers. Sub-60 fs pulse durations were produced where this laser has the potential for high peak power operation due to the satisfactory thermal conductivity property of its gain material. Analysis of spectroscopic properties and lasing performance will be carried out based on the results obtained in this assessment. In nonlinear optics applications, the current widely used method to produce femtosecond visible pulses involves second harmonic generation in nonlinear materials by using Ti:Sapphire lasers as a pump source. However, due to the complicated pumping requirements of this device as described in section 2.5.2, the simpler femtosecond visible source alternative involving a periodically-poled lithium tantalate (PPLT) crystal with a Yb:KYW femtosecond laser as a pump source was investigated [Chapter 7]. The experimental results presented in this thesis have shown that it is possible to demonstrate ultralow-threshold, compact and high efficiency femtosecond lasers based on Yb-doped crystals that produce average output powers in a few hundreds mW with relatively high peak powers of up to tens of kW.

### 3.4 Conclusion.

In this chapter, several factors that influence the design of low threshold, compact, and highly efficient femtosecond lasers were described. The physical processes that occur during lasing depend on the material and optical properties of the gain medium. The small pump/laser beam overlap ( $w_p : w_l$ ), the reduction in the cavity round trip loss ( $T_{OC} + L_d + 2L_{Yb}$ ), the long fluorescence lifetime  $\tau_u$ , the appropriate pump photon energy  $h\nu_p$ , and the high emission cross-section  $\sigma_{se}$  lead to the realisation of a low cw threshold operation. This results in the attainment of a low mode-locking threshold where the ultrashort lasers can be constructed by involving the efficient exploitation of Kerr-lensing effect and saturable absorber characteristics. In addition, the utilisation of a diffraction-limited pump beam source facilitated the low threshold [see figure 3.3a] where the extended Rayleigh range for the mode overlap supports a high-efficiency performance. Optimised optical component properties and a suitable gain medium that implies low quantum defect and appropriate doping concentration can also favour a high efficiency operation. It is thus believed from this research work that the prescription for developing compact Yb-doped fs lasers with considerable reductions in pump power requirements will also be applicable to other lasers. These offer the possibility of portable low cost fs lasers that can bring the scientifically-designed devices to the industrially-orientated applications.

### 3.5 References:

1. W. F. Krupke and L. L. Chase, "Ground-state depleted solid state lasers: principles, characteristics and scaling," *Opt. Quantum Electron.* **22**, S1-22 (1990).
2. T. Y. Fan and R. L. Byer, "Modeling and CW operation of a quasi-three-level 946 nm Nd:YAG laser," *IEEE J. of Quantum Electron.* **23**, 605-612 (1987).
3. C. Bollig, "Single-frequency diode-pumped solid-state lasers," PhD. Thesis, Optoelectronic Research Centre, U. of Southampton, 101-124 (1997).
4. L. D. DeLoach, S. A. Payne; L. L. Chase.; L. K. Smith; W. L. Kway; W. F. Krupke, "Evaluation of absorption and emission properties of Yb<sup>3+</sup> doped crystals for laser applications," *IEEE J. Quantum Electron.* **29**, 1179-1191 (1993).
5. S. A. Payne, L. L. Chase, L. K. Smith, W. L. Kway, and W. F. Krupke, "Infrared cross-section measurements for crystals doped with Er<sup>3+</sup>, Tm<sup>3+</sup>, and Ho<sup>3+</sup>," *IEEE J. of Quantum Electron.* **28**, 2619-2630 (1992).
6. O. Svelto, "Principles of lasers," 4<sup>th</sup> edition, Plenum Press New York and London, 342-374 (1998).
7. S. Chenais, F. Balembois, F. Druon, G. Lucas-Leclin, and P. Georges, "Thermal lensing in diode-pumped ytterbium lasers-part 1: theoretical analysis and wavefront measurements," *IEEE J. of Quantum Electron.* **40**, 1217-1233 (2004).
8. W. F. Krupke, "Ytterbium solid-state lasers-The first decade," *IEEE J. Select. Top. Quantum Electron.* **6**, 1287-1296 (2000).
9. S. A. Payne, L. K. Smith, L. D. DeLoach, W. L. Kway, J. B. Tassano, and W. F. Krupke, "Laser, optical and thermomechanical properties of Yb-doped fluorapatite," *IEEE J. of Quantum Electron.* **30**, 170-179 (1994).
10. S. A. Payne, L. L. Chase, H. W. Newkirk, L. K. Smith; and W. F. Krupke, "LiCaAlF<sub>6</sub>:Cr<sup>3+</sup>:A promising new solid-state laser material," *IEEE J. of Quantum Electron.* **24**, 2243-2252 (1988).
11. C. Honninger, R. Paschotta, M. Graf, F. Morier-Genoud, G. Zhang, M. Moser, S. Biswal, J. Nees, A. Braun, G. A. Mourou, I. Johannsen, A. Giesen, W. Seeber, and U. Keller, "Ultrafast Ytterbium-doped bulk lasers and laser amplifiers," *Appl. Phys. B* **69**, 3-17 (1999).
12. W. P. Risk, "Modeling of longitudinally pumped solid-state lasers exhibiting reabsorption losses," *J. Opt. Soc. Am. B* **5**, 1412-1423 (1988).

13. T. Y. Fan, "Diode-pumped solid-state lasers," *Laser Sources and Applications, Proceedings of the Forty Seventh Scottish Universities Summer School in Physics*, St. Andrews, 163-208 (1996).
14. A. J. Alfrey, "Modeling of longitudinally pumped CW Ti:sapphire laser oscillators," *IEEE J. Quantum Electron.* **25**, 760-766 (1989).
15. M. Piché "Beam reshaping and self-mode-locking in nonlinear laser resonators," *Opt. Commun.* **86**, 156-160 (1991).
16. G. J. Valentine and W. Sibbett, "Compact, low-threshold, femtosecond lasers," *Recent Res. Devel. Quantum Electron.* **1**, 43-58 (1999).
17. W. Koechner, "Solid-state laser engineering," New York:Springer, pp 17 (1986).
18. M. B. Agate, "Portable and efficient femtosecond Cr:LiSAF lasers," PhD. Thesis, School of Physics and Astronomy, U. of St. Andrews, 2:1-2:19 (2003).
19. J. M. Hopkins, "Compact, low-threshold, femtosecond lasers," PhD. Thesis, School of Physics and Astronomy, U. of St. Andrews, 5:1-5:30 (1998).
20. R. L. Fork, O. E. Martinez, and J. P. Gordon, "Negative dispersion using pair of prisms," *Opt. Lett.* **9**, 150-152 (1984).

## **Chapter 4**

### **Compact and Highly Efficient Yb:KYW Laser with a Single Prism for Dispersion Compensation.**

#### **4.1 Introduction.**

In this chapter a selection of Yb-doped gain materials is described that offers a particular compatibility for incorporation into femtosecond lasers. These are tungstate crystals with Yb<sup>3+</sup>-doping and they include potassium yttrium tungstate Yb<sup>3+</sup>:KY(WO<sub>4</sub>)<sub>2</sub> (Yb:KYW) and potassium gadolinium tungstate Yb<sup>3+</sup>:KGd(WO<sub>4</sub>)<sub>2</sub> (Yb:KGW). The spectroscopic properties of these materials are discussed to show the favourability of such materials for low threshold, and highly efficient laser operation. For the realisation of a solitonic pulse shaping mechanism, theoretical discussion on a sequence of prisms is presented. These arrangements include waveguide structures in two slabs as a representation of four prisms, a pair of prisms and a single prism. In order to achieve the optimisation of pulse minimisation, a prism pair can introduce a necessary amount of net group delay dispersion (GDD) in the laser cavity. Theoretical derivations based on this fundamental principle are demonstrated to facilitate the choices of suitable prism materials and their effective separation length responsible for the dispersion control scheme. Simplification of this dispersive arrangement is manifested with the use of a single prism approach that exhibits similar geometrical effect to the prism pair set up which is beneficial for reduced device footprints. In the experimental section, the operation of continuous wave (CW) and passively mode-locked Yb:KYW lasers pumped by an InGaAs diode laser in an asymmetric 4-mirror cavity are explained. During passive mode locking, a single prism and a SESAM were used instead of a high reflector to initiate and support operation in an ultrashort-pulse regime. Improvement to this system through the optimisation of the saturation fluence of the SESAM is described as a means to produce shorter pulse durations. Finally, all the relevant results obtained are discussed in the context of design criteria for efficient Yb:KYW femtosecond lasers in compact cavity configurations.

## 4.2 Ytterbium-doped Crystals.

$\text{Yb}^{3+}$  ions have been doped into many crystals such as  $\text{Ca}_5(\text{PO}_4)_3\text{F}$  (C-FAP),  $\text{KY}(\text{WO}_4)_2$  (KYW),  $\text{KGd}(\text{WO}_4)_2$  (KGdW),  $\text{Sr}_5(\text{PO}_4)_3\text{F}$  (S-FAP), and  $\text{Sc}_2\text{O}_3$  (sesquioxides). In previously reported work by De Loach [1], useful properties of Yb-doped materials were identified for laser operation based on the two spectroscopic parameters of stimulated emission cross-section at laser transitions,  $\sigma_{se}^{\lambda_{se}}$  and the minimum pump intensity,  $I_{\min}$  required to achieve transparency. The results showed that S-FAP and C-FAP are the most recommendable gain media while YAG ( $\text{Y}_3\text{Al}_5\text{O}_{12}$ ), YAB ( $\text{YAl}_3(\text{BO}_3)_4$ ) and GdCOB ( $\text{Ca}_4\text{GdO}(\text{BO}_3)_3$ ) were less suitable for laser operation. These results are in contradiction to other experimental results [1] that showed high slope efficiencies could have been obtained in YAB and GdCOB host gain media. These inaccuracies led to a new evaluation of gain media [2,3] based on quasi 3-level systems which links better to the experimental data as shown in figure 4.1. In this figure, oscillator output yield is the ratio between output power with respect to the input ( $P_0/P_{in}$ ) while small signal gain is proportional to the difference between emission cross sections ( $\sigma_{se}^{\lambda_{se}}$ ) and absorption cross-sections ( $\sigma_{abs}^{\lambda_{se}}$ ) at the emission wavelength.

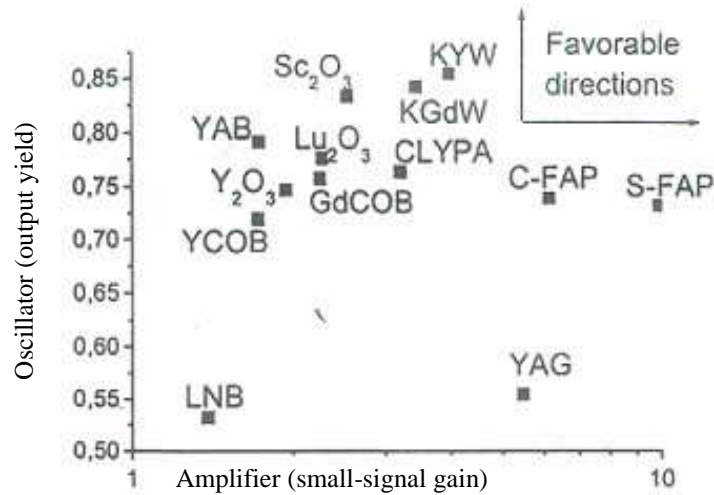


Figure 4.1. Plot of merit for Yb-doped crystal hosts based on quasi three level systems [3].

It can be seen from this figure that the preferred host crystals in CW laser regimes are KYW, KGdW, and  $\text{Sc}_2\text{O}_3$  while YAG is the lowest. Other doped-sesquioxides such as  $\text{Lu}_2\text{O}_3$  and  $\text{Y}_2\text{O}_3$  show excellent laser efficiency in this evaluation while C-FAP and S-FAP are less efficient compared to that of GdCOB and YAB. However, for small-signal gain, Yb-doped S-FAP, C-FAP and YAG are better crystals than those of the tungstate and sesquioxide alternatives. This arises because of the different interactions between the crystal

fields and the  $\text{Yb}^{3+}$ -ion electronic structure which leads to differences in the absorption and emission cross-section characteristics. Hosts such as the sesquioxide crystals have higher thermal conductivities compared to other hosts that can be preferable for high power operation, thus opening up some possibilities for specific scientific and industrial applications.

Some previous work has been reported on Yb-doped femtosecond lasers based on SESAM-assisted mode locking. The shortest pulse duration obtained to date from a Yb:YAG laser was 340 fs at a central wavelength of 1033 nm [4]. Other broadband Yb-doped materials that have been investigated such as  $\text{Yb}^{3+}:\text{Ca}_4\text{GdO}(\text{BO}_3)_3$  (Yb:GdCOB),  $\text{Yb}^{3+}:\text{Sr}_3\text{Y}(\text{BO}_3)_3$  (Yb:BOYS), and  $\text{Yb}^{3+}:\text{CaGdAlO}_4$  have generated shorter femtosecond pulses. For example, a pulse duration of 90 fs at 1054 nm was demonstrated from a Yb:GdCOB laser [5] with 40 mW average output power at a repetition rate of 100 MHz. For a laser incorporating a Yb:BOYS gain crystal [6], 69 fs pulses were produced at a central wavelength of 1062 nm with 80 mW average power at a repetition rate of 113 MHz. This laser could also be tuned from 1051 nm to 1070 nm and produced an impressive output power of 300 mW with pulse duration of 86 fs around 1068 nm. Further research was done by using  $\text{Yb}^{3+}:\text{CaGdAlO}_4$  [7] which produced 47 fs pulse duration at 1050 nm with a pulse repetition frequency of 109 MHz. To date, this is the shortest pulse duration obtained from any Yb-doped femtosecond laser. However, these materials demonstrated low efficiency during laser operation and the exploration for alternative gain materials based on tungstate hosts that characterised high efficiency during femtosecond operation is important as will be discussed in the next section.

### **4.3 Yb-doped $\text{KY}(\text{WO}_4)_2$ and $\text{KGd}(\text{WO}_4)_2$ Crystals**

With reference to the evaluation of gain materials for femtosecond lasers based on quasi 3-level systems, two different types of  $\text{Yb}^{3+}$ -doped tungstates are the subject of research described in this chapter. These are  $\text{Yb}^{3+}$ -doped potassium yttrium tungstate [ $\text{Yb}^{3+}:\text{KY}(\text{WO}_4)_2$ ] or Yb:KYW and  $\text{Yb}^{3+}$ -doped potassium gadolinium tungstate [ $\text{Yb}^{3+}:\text{KGd}(\text{WO}_4)_2$ ] or Yb:KGW [8]. These crystals can be grown from flux by a modified Czochralski method with a doping concentration between 1 and 10 at.% of  $\text{Yb}^{3+}$  ion.

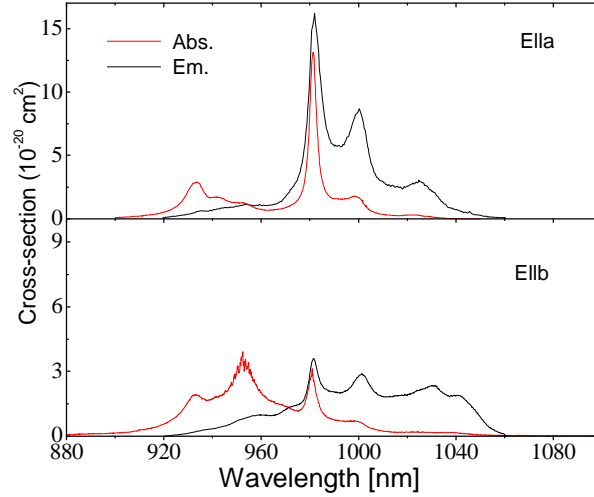


Figure 4.2. Polarised absorption and emission cross-sections of 10-at. % Yb:KYW at room temperature [8].

The polarised absorption and emission cross-sections of 10 at.% Yb:KYW at room temperature is shown in figure 4.2. Yb:KYW has a peak absorption coefficient of  $79 \text{ cm}^{-1}$  at  $981.2 \text{ nm}$  for E || 'a' polarisation and the absorption linewidth [FWHM] is  $3.5 \text{ nm}$ . The absorption coefficient  $\alpha$  of this material is given by:-

$$\alpha = \sigma_{abs}^{\lambda_p} N_{Yb} \quad (4.3.1)$$

where  $N_{Yb} (\text{cm}^{-3})$  is the density of  $\text{Yb}^{3+}$  ion dopant in the host material. The value of  $\alpha$  mentioned above is obtained by accounting  $N_{Yb} = 6 \times 10^{20} \text{ ions/cm}^3$  [8] and  $\sigma_{abs}^{\lambda_p}$  measured from figure 4.2 to be  $13 \times 10^{-20} \text{ cm}^2$ . The peak stimulated emission cross-sections  $\sigma_{se}^{\lambda_{se}}$  calculated in Yb:KYW for E || 'a' polarisation is  $3 \times 10^{-20} \text{ cm}^2$  at  $1025 \text{ nm}$  while in Yb:KGW it is  $2.8 \times 10^{-20} \text{ cm}^2$  at  $1023 \text{ nm}$ . The spectral width of the emission wavelength is  $16 \text{ nm}$  in Yb:KYW and  $20 \text{ nm}$  in Yb:KGW respectively. Although the absorption and emission cross-sections are greater for the E || 'a' polarisation compared to that of E || 'b' polarisation, the lasing transition with E || 'b' polarisation is sometimes preferable due to its broader emission spectrum.

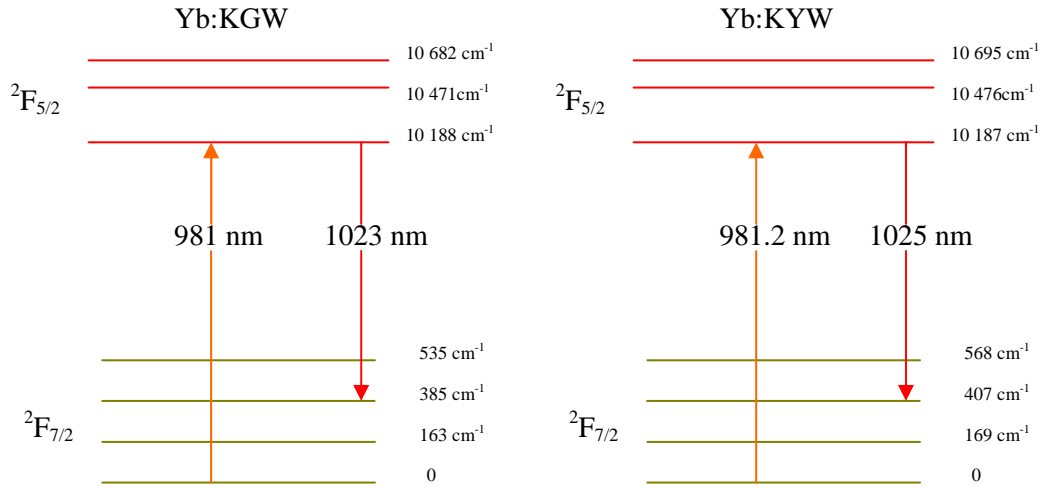


Figure 4.3. Two Stark energy levels of Yb:KGW and Yb:KYW at 77 K. The orange arrow shows the peak absorption transition at 981 nm while the red arrow shows the peak laser transition at 1023/1025 nm [8].

In the simple two Stark electronic levels of Yb:KYW and Yb:KGW [figure 4.3], the peak absorption band occurs at 981 nm from the ground state  $^2F_{7/2}$  to the excited state  $^2F_{5/2}$ . The upper state lifetimes for both of these crystals are around 0.6ms and the peak laser transitions occur at 1025 nm (Yb:KYW) and 1023 nm (Yb:KGW) from the excited-state  $^2F_{5/2}$  to the ground state  $^2F_{7/2}$  where the terminal laser level is  $\sim 400 \text{ cm}^{-1}$  above the ground state. The potential of Yb-doped tungstates lasers is quite promising due to the lower Stokes shift in the range  $\sim 100\text{-}600 \text{ cm}^{-1}$  under the zero-phonon line pumping which reduces thermal loading during laser operation. In addition, the broad absorption bandwidth in tungstate materials is very well suited to optical pumping by InGaAs quantum well diode lasers in the 900-980 nm range.

#### 4.4 Comparison between Yb-doped Tungstate Materials.

The benefits of choosing tungstate materials (Yb:KYW and Yb:KGW) for laser operation can be seen by comparing their spectroscopic properties with another Yb-doped medium, for instance Yb:YAG as shown in table 4.1. The favourable properties of Yb-doped tungstates (KYW and KGW) compared to that of Yb:YAG include the smaller quantum defect  $\sim 0.04$  which reduces heat dissipation in the gain media and their larger amplification bandwidth ( $\Delta\lambda_{se} \approx 16\text{-}20 \text{ nm}$ ) which facilitates the generation of ultrashort pulses in sub-100 fs regimes with wider tunability. For high power operation, the broad peak absorption bandwidth of

Yb:YAG (18 nm) is needed as the pump source is usually provided by a multi-mode laser. However, the narrow peak absorption bandwidth of tungstates ( $\Delta\lambda_{pump} \sim 3.5$  nm) is very well-matched to the single-mode InGaAs diode laser which was used as a pump source in this work.

Table 4.1. Comparison between spectroscopic properties of Yb:KYW, Yb:KGW [8] and Yb:YAG [9].

Parameters	Yb:KYW	Yb:KGW	Yb:YAG
$\lambda_{pump}$ (nm)	981.2	981	942
$\Delta\lambda_{pump}$ (nm)	3.5	3.7	18
$\lambda_{se}$ (nm)	1025	1023	1030
$\Delta\lambda_{se}$ (nm)	16	20	~ 6
$\sigma_{abs}^{\lambda_p}$ ( $10^{-20}$ cm <sup>2</sup> )	13.3	12	0.7
$\sigma_{se}^{\lambda_{se}}$ ( $10^{-20}$ cm <sup>2</sup> )	3	2.8	2.1
$\tau_u$ (ms)	0.6	0.6	~ 1
$QD_f$	0.04	0.04	0.08

By taking  $\sigma_{se}^{\lambda_p}$  for tungstate materials as  $14 \times 10^{-20}$  cm<sup>2</sup>, the larger value of  $(\sigma_{abs}^{\lambda_p} + \sigma_{se}^{\lambda_{se}})\tau_u$  in tungstates allows more than 20 times reduction in the pump saturation intensity,  $I_{sat}$  [equation 3.2.5] needed to drive a significant amount of Yb<sup>3+</sup> ions into the excited-state in comparison to that of Yb:YAG. However, the laser thresholds [equation 3.2.6a] between these materials are similar due to the close value of their upper state lifetime product  $\sigma_{se}^{\lambda_{se}}\tau_u$ . Based on the values demonstrated in table 4.2 for Yb:KYW, a minimum fraction of Yb-ions ( $\beta_{min}^{\lambda_{se}}$ ) of 9.9 % need to be pumped from the lower state of  $E_{L,3}$  to the upper state of  $E_{U,1}$  to achieve equal populations at the emission wavelength of 1025 nm as illustrated in figure 4.3. This corresponds to the minimum pump intensity of 122.56 W/cm<sup>2</sup> with respect to the saturation intensity of 1.238 kW/cm<sup>2</sup> which is 14 times lower than that of Yb:YAG ( $I_{min} = 1.75$  kW/cm<sup>2</sup>) [see section 3.2]. The stimulated emission cross-sections  $\sigma_{se}^{\lambda_{se}}$  of these crystals (KYW and KGW) are slightly larger than that of Yb:YAG. This reduces the gain saturation fluence  $F_{sat,L}^{\lambda_{se}}$  needed for the suppression of Q-switching

instabilities [10] during modelocking, thus resulting in more stable femtosecond operation. For the typical Yb-doped gain materials that have low laser cross-sections, the Q-switching tendency is stronger especially for those with larger amplification bandwidths. This tendency is one of the critical challenges in the optimisation of the passive mode locking of solid-state lasers.

Table 4.2. The fractions of Boltzmann occupation factor for each Stark level in Yb:KYW where  $Z_L/Z_U = 1.233031$  at the room temperature of  $20^{\circ}\text{C}$ . These fractions were calculated from the energy values in  $\text{cm}^{-1}$  given in figure 4.3.

Manifold (m)	Stark Level (s)	$f_U$ (%)	Manifold (m)	Stark Level (s)	$f_L$ (%)
${}^2F_{5/2}$	3	6.2	${}^2F_{7/2}$	4	3.8
	2	18.3		3	8.3
	1	75.5		2	26.7
		1		61.2	

Another contribution to the larger value of  $\sigma_{abs}^{\lambda_p}$  can be seen to be the reduction in crystal length as a gain medium [see equation 4.3.1]. The reduction in length requirement of the crystal hosts can also be achieved due to the facility of high  $\text{Yb}^{3+}$  doping concentrations that can be up to 100 % [11]. This facilitates a good overlap between laser and pump beam mode for highly efficient operation. However, the disadvantage of this system is due to the extremely short absorption length of KYbW crystal ( $13.3\ \mu\text{m}$  near  $981\ \text{nm}$ ) which causes a thermal lensing effect. This effect is due to the generation of high temperature within the short absorption length of the crystals as the consequence of the lower thermal conductivity property of these media. This is  $3.3\ \text{Wm}^{-1}\text{K}^{-1}$  which is two times smaller than that of a Yb:YAG crystal, thus restricting their utilization for high power operation. In addition, this effect can also produce instability in the laser cavity and reduces upper state lifetimes of Yb-doped materials thus leading to a reduction in the energy storage lifetime for economic efficiency. Despite these few drawbacks, in my low power laser operation, Yb:KYW was chosen as a gain medium for a test femtosecond laser due to its potential for low threshold and high efficiency.

Previous reports were done on passively mode-locked Yb-doped tungstate lasers based on semiconductor saturable absorber mirror (SESAM) for passive mode locking operation.

The first reported passively mode-locked Yb:KGd(WO<sub>4</sub>)<sub>2</sub> [12] pumped by two high brightness diode lasers produced 176 fs pulse duration with 1.1 W average power and the shortest pulse duration achieved was 112 fs with 200 mW output power. During cw operation, an optical-to-optical efficiency of 33 % was obtained with a slope efficiency of 57 % with respect to the absorbed pump power. In contrast, a slope efficiency as high as 78 % was obtained in Yb:KYW and 72 % in Yb:KGW by using Ti:sapphire lasers as pump sources [13]. From the work done by Keller and co-workers [14], a pulse duration of 240 fs with 22 W average power was produced when a thin disk Yb:KY(WO<sub>4</sub>)<sub>2</sub> was pumped by a 100 W incident power from fibre coupled bars. Further work done by Lagatsky and co-workers achieved an optical-to-optical efficiency of 35 % during femtosecond operation where the corresponding electrical-to-optical efficiency exceeded 14 %. A pulse duration of 123 fs was produced at 1047 nm when the Yb:KYW crystal was pumped by a single narrow-stripe diode laser [15]. However, in the Kerr-lens mode locking operation, the shortest pulse duration obtained to date in Yb:KYW laser was 71 fs with 120 mW average output power at a centre wavelength of 1057 nm [16].

The most important effects which influence the duration of pulses produced in laser oscillators are self-phase modulation mentioned in section 2.4, absorption saturation fluence of the SESAM and total intracavity dispersion. Dispersion broadens the pulse duration, thus becoming one of the limiting factors for the generation of ultrashort pulses. Previously reported work has used a prism pair for dispersion compensation in the laser cavity. By contrast, the main objective of this experiment was to design and assess a Yb:KYW femtosecond laser that had a more compact configuration. The aim was to eliminate some optical elements in this cavity and the first option was to determine whether the use of a single prism for dispersion compensation would be acceptable.

#### **4.5 A Sequence of Prisms For Dispersion Compensation.**

As a pulse propagates through the dielectric media, group velocity dispersion (GVD) is initiated in the resonator as the group velocity of light decreases with the increasing frequency. The consequence effect of this physical phenomena is that the lower frequency components (red) travel faster over those of the higher frequency components (blue). This leads to an increase in the temporal broadening of the pulse envelope as the outcome of the positive dispersion. As part of optical elements in the cavity, prisms also contribute to

positive dispersion through their wavelength dependent refractive index  $n(\lambda)$  described by the Sellmeier equation which can be expressed as:-

$$n(\lambda) = \sqrt{1 + \frac{a\lambda^2}{\lambda^2 - d} + \frac{b\lambda^2}{\lambda^2 - e} + \frac{c\lambda^2}{\lambda^2 - f}} \quad (4.5.1)$$

where  $\lambda$  is the wavelength,  $a, b, c, d, e$  and  $f$  are constants and their values depend on the material properties of the prisms. From the second derivation of this equation  $\frac{d^2n}{d\lambda^2}$ , the amount of group velocity dispersion (GVD) contributed by the material implicit in the third term of the Taylor expansion [see equation 2.4.2] can be measured. GVD that has a unit of  $\text{fs}^2/\text{mm}$  is the wavelength dependent of the group velocity of light in a medium and it is presented as [17]:-

$$GVD = \frac{\lambda^3}{2\pi c^2} \left( \frac{d^2n}{d\lambda^2} \right) \quad (4.5.2)$$

where  $c$  is the speed of light and by accounting for the intraprism length  $L_{mat}$  that is defined as the propagation distance of the beam in the prism material, the group delay dispersion (GDD) that has a unit of  $\text{fs}^2$  can be derived from the GVD.

To compensate the effect of positive dispersion in order to achieve the optimisation of pulse compression, Martinez et. al. [18] had demonstrated that negative GDD can be introduced by the material that does not exhibit negative material dispersion. This can be done by the exploitation of angular dispersion irrespective of the sign of  $\frac{d\theta}{d\lambda}$ . One example of this scheme is the introduction of a sequence of four-prisms that was demonstrated by Fork and co-workers (see figure 1[19]). The selection of prisms over diffraction gratings or Gires-Tournois interferometers is due to their lower insertion losses. These are explained by the design of prisms apices that are cut and polished at the Brewster angle to minimise losses for the incident and reflected beams and generally they are used at minimum deviation (eg. incident angle is equal to exiting angle). The arrangement of these four prisms can be summarised to be equivalent to the waveguide structures introduced by two slabs in the laser resonator that is illustrated in figure 4.4 below.

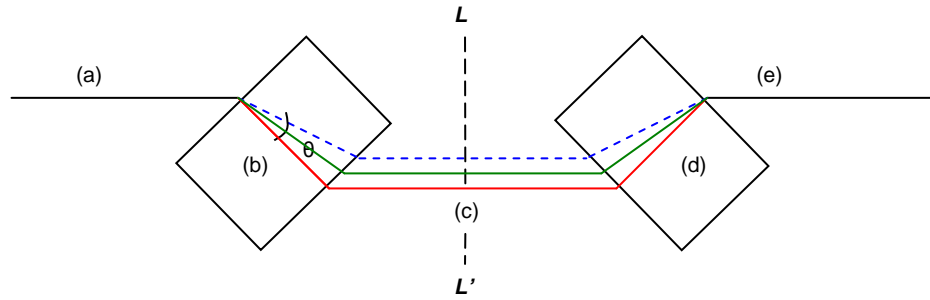


Figure 4.4. Waveguide structures in the laser resonator introduced by two slabs that represent a sequence of four prism arrangements.  $L$  to  $L'$  represents an axis of symmetry [18].

From this figure, the collinear incident beam path propagates through the entrance part of the first slab is demonstrated in region (a). The adjustment of appropriate angular dispersion in region (b) introduces longer phase delay for longer wavelengths over those of shorter wavelengths to reverse the previous effect of positive dispersion. The transmitted beam that consists of parallel spatial components propagates along region (c) with transverse displacement properties. In this region, each wavelength that propagates at different position is called as spatial chirp. The same physical mechanism that occur in region (b) applies in region (d) but with opposite direction. The consequence effect is that the output waves are transmitted on the same straight line from the exit part of the second slab as illustrated in region (e).

By symmetry, the optical arrangement shown in figure 4.4 can be simplified into the implementation of two prisms. This reduces optical elements required in a laser resonator that favour the achievement of compact device footprints. Figure 4.5 illustrates a spatial dispersion in two prisms that is comparable to the waveguide structures in the first part of the slab [figure 4.4].

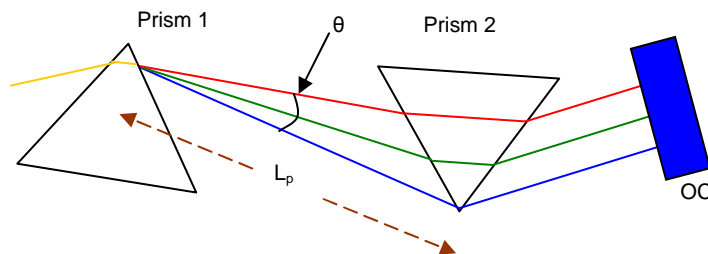


Figure 4.5. A schematic of a prism pair configuration for dispersion compensation.  $L_p$  is effective separation length and OC is output coupler [20].

From the figure above, the optical path length that manifests the distance of the propagating waves bouncing back and forth inside the resonator is given as [19]:-

$$P = 2L_p \cos \theta \quad (4.5.3)$$

where the angular dispersion  $\theta$  can be determined from the first derivation of Sellmeier equation  $\frac{dn}{d\lambda}$ , and it is presented as:-

$$\theta \approx -2 \frac{dn}{d\lambda} \Delta\lambda \quad (4.5.4)$$

where  $\Delta\lambda$  is the spectral width in nm. The amount of net negative dispersion introduced by the prisms can be controlled by variations in the separation length  $L_p$  and intraprism length  $L_{mat}$ . This net GDD that is the summation between the GDD of the material [equation 4.5.2] and the GDD induced by the angular dispersion is presented as [17]:-

$$GDD_{p.net} = \frac{\lambda^3}{2\pi.c^2} \left( \frac{d^2P}{d\lambda^2} + L_m \frac{d^2n}{d\lambda^2} \right) (\text{fs}^2) \quad (4.5.5)$$

where  $\frac{d^2P}{d\lambda^2}$  is the second derivation of the optical path length explicit in equation 4.5.3 as a function of the propagating waves that can be expressed as:-

$$\left( \frac{d^2P}{d\lambda^2} \right) = 4L_p \sin \theta \left[ \frac{d^2n}{d\lambda^2} + \left( 2n - \frac{1}{n^3} \right) \left( \frac{dn}{d\lambda} \right)^2 \right] - 8 \left( \frac{dn}{d\lambda} \right)^2 L_p \cos \theta \quad (4.5.6)$$

The selection of prism materials required for pulse compression is important depending on the parameters involved in the laser resonator. In the UV region where the wavelengths are shorter than 380 nm, fused silica is recommendable due to its highly transmitting property in this spectral line. It can also compensate for higher-order dispersion that favour the generation of pulses shorter than 25 fs. In contrast, for wavelengths longer than 400 nm, Lak L21 and SF 10 prisms can be implemented. These two materials can compensate for second order dispersion that is influential for pulses exceeding 50 fs which is particularly the case for lasers developed in this project. SF10 is used to compensate a large amount of net negative dispersion in the cavity and LAK L21 is preferred to compensate relatively less.

The values of material group velocity dispersion for each type of prism as a function of wavelengths from 800 to 1300 nm is provided in figure 4.6. From this figure, for most prism materials these values decrease with the increasing wavelengths and they are positive for wavelengths below 1300 nm. For fused silica, BK 7 and Lak L21 the maximum amount of material dispersions range from 36 to 60 fs<sup>2</sup>/mm at 800 nm before reducing to negative values at wavelengths between 1300 to 1350 nm. However for the same range of wavelengths, GVD in SF 10 prisms varies from 160 fs<sup>2</sup>/mm at 800 nm to 60 fs<sup>2</sup>/mm at 1350 nm.

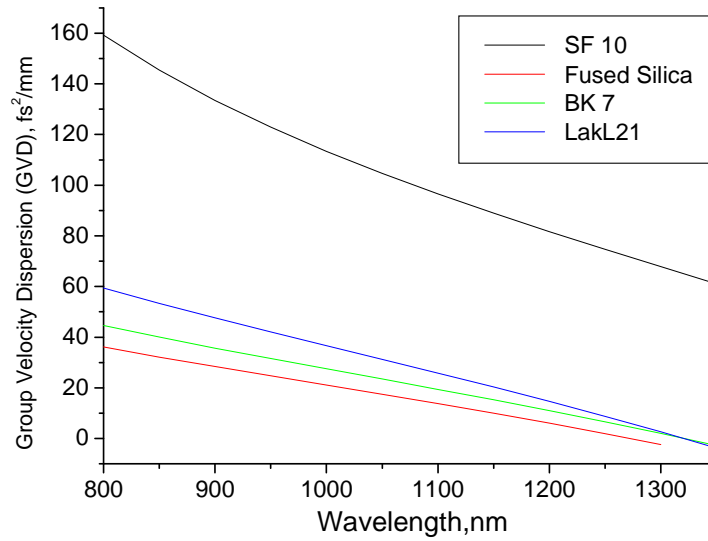


Figure 4.6. Prism material dispersion (fs<sup>2</sup>/mm) as a function of wavelength (nm).

To measure the effective separation length  $L_p$  between two prisms required for optimum pulse compression, equation (4.5.5) can be used. For instance in a Ti:sapphire laser, the total  $GDD$  of the optical elements and air path length in the cavity is estimated as 2400 fs<sup>2</sup>. This gives the amount of  $-GDD$  that need to be introduced. Before operating any laser system, the prisms are arranged at an appropriate distance in the setup illustrated in figure 4.5. Once nice Gaussian-limited pulses are produced at around 850 nm ( $\tau_p = 90$  fs), the separation length is correct and the dispersion is compensated. By taking  $dn/d\lambda$  as  $-0.01771 \mu\text{m}^{-1}$  (BK7),  $-0.02338 \mu\text{m}^{-1}$  (LAKL21), and  $-0.04201 \mu\text{m}^{-1}$  (SF10),  $\theta$  is evaluated from equation (4.5.4) to be between  $0.02^\circ$  to  $0.06^\circ$  depends on the type of prism materials. These small angular dispersions are due to the limited bandwidth in femtosecond assessment ( $\Delta\lambda \approx 12$  nm) and bigger value is expected in attosecond regime. For  $L_m = 10$  mm, if using

a sequence of BK 7 prisms,  $L_p$  is measured to be 1029 mm. If Lak L21 prisms or SF 10 prisms are implemented, this length is measured to be 618 mm or 252 mm correspondingly.

Another alternative to achieve pulse compression that reduces cavity dimensions was suggested by Keller and co-workers [20] by using a single prism instead of a pair of prism which is demonstrated in figure 4.7. By an appropriate design of cavity optics, an intersection point  $X$  might exist at the focal length distance  $f$  of the cavity optics. It is not a beam waist of the Gaussian cavity mode but it is defined as a point where the axes of the resonator modes with different frequency intersect. The insertion of a single prism at any distance from  $X$  can introduce a net negative dispersion between  $X$  and the output coupler and this is comparable to the two-prism configuration where the apex of prism one is at the intersection  $X$  [figure 4.5,4.7].

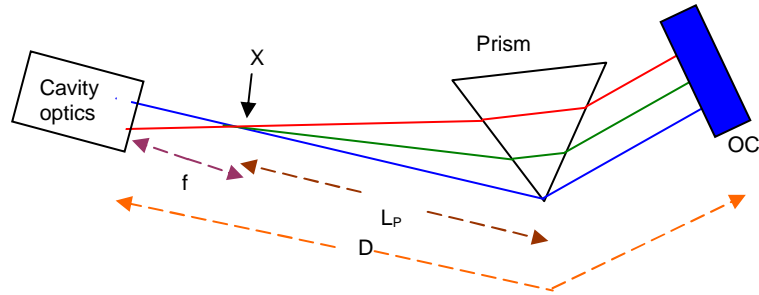


Figure 4.7. A single prism approach that has an equivalent net GDD to the prism pair set up illustrated in figure 4.5 [20].

The amount of negative dispersion introduced by the single prism is proportional to the effective prism separation,  $L_p$  that exist in a prism pair configuration. Due to the fact that the position of  $X$  is determined by the arrangement of cavity optics, the possibility exists for a negative focal length (ie.  $L_p > D$ ) to occur and this can lead to a greater compactness in the cavity design. Therefore, the requirement needed to achieve a desired length  $L_p$  for negative GVD can be shown as:-

$$D \geq L_p + f \quad (4.5.7)$$

where  $D$  is the total length of the cavity arm containing the prism. The advantages of using a single prism instead of a prism pair are easier alignment and low-loss tuning. This can be done by tilting the output coupler or shifting the pump beam sideways with the absence of an aperture that introduces additional loss. Moreover, fewer intracavity elements that

increase efficiencies can be achieved which therefore favour the design of a more compact configuration.

#### 4.6 Implementation.

A Yb:KYW femtosecond laser was designed in a compact configuration based on a single prism for dispersion compensation as depicted in figure 4.8. A single mode pump laser diode was used for this quasi-three-level system to achieve a good overlap between pump/laser modes to enable a reduction in the laser threshold and an improvement in laser efficiency.

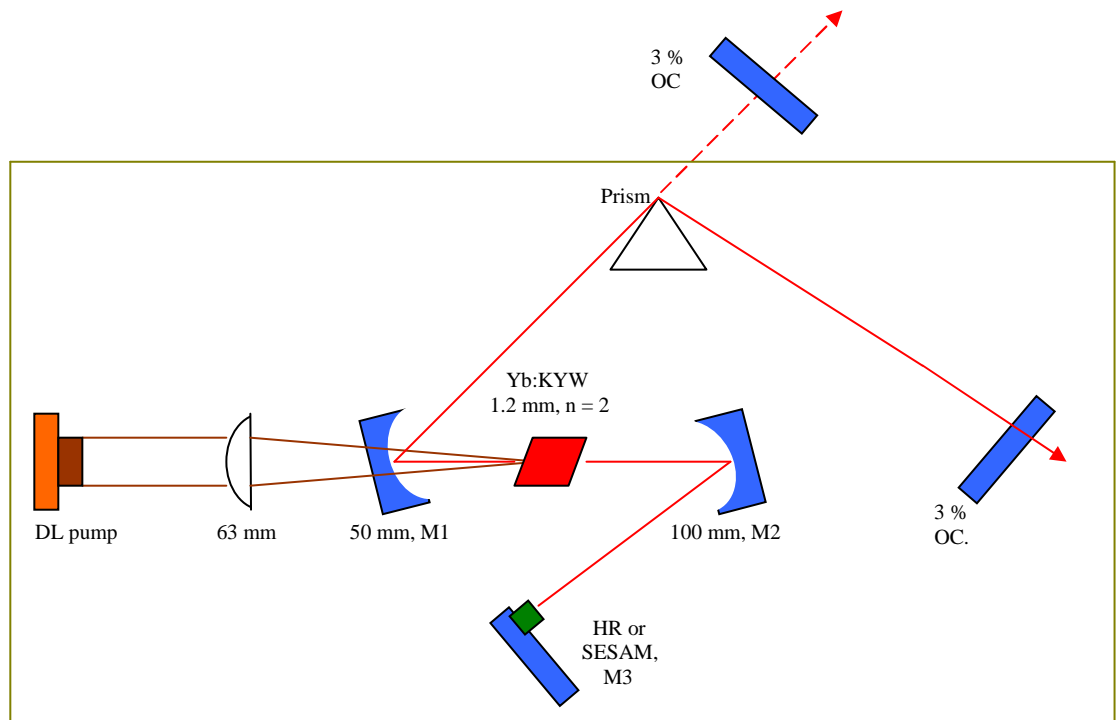


Figure 4.8. An overall schematic diagram of a femtosecond Yb:KYW laser where DL is single-mode InGaAs diode laser, HR is high reflector used as mirror 3 (M3), M1 and M2 are spherically curved mirrors with radii of curvature of 50 mm (M1) and 100 mm (M2), SESAM is semiconductor saturable absorber, and OC is 3 % output coupler.

The resonator consisting of four mirrors was designed by using an ABCD matrix formalism. This provided all the values for the various beam mode sizes such as the beam waist focussed at the crystal  $w_{l,o}$ , and at the end of the short arm cavity,  $w_{SESAM}$ . It was important to ensure that the laser mode  $w_{l,o}$  focussed inside the crystal has an equivalent

diameter with the pump mode  $w_{p,0}$  for a good overlap as mentioned previously. In addition, this design package (ABCD matrix formalism) was also used to determine the correct positions and folding angles of the cavity mirrors and the Yb-doped crystal. The 10 at.% Yb<sup>3+</sup> doped KY(WO<sub>4</sub>)<sub>2</sub> Brewster-angled crystal with 1.2 mm long was oriented in the cavity for propagation along the b axis (N<sub>p</sub>) with the polarisation parallel to the crystallo-optic N<sub>m</sub> axis. The crystal was pumped by a single narrow-stripe InGaAs diode laser (p-polarised) that produced an average output power of 350 mW at 981 nm with a spectral width of ~ 0.5 nm.

This Brewster-angled crystal was the source of astigmatism [21] inside the resonator due to the displacement of geometrical positions in the sagittal (*xz* -plane) and tangential (*yz* -plane) directions. The mirrors (M1 and M2) were used to compensate this scheme where in this case, two focal points for M1 at an off-axis angle are given as:-

$$f_x = \frac{\left(\frac{R}{2}\right)}{\cos \theta} \quad (4.6.1a)$$

and:-

$$f_y = \left(\frac{R}{2}\right)\cos \theta \quad (4.6.1b)$$

where  $\theta$  is the angle of incidence and  $R$  is the radius of curvature. In addition, the effective lengths  $l_x$  and  $l_y$  through which the beam in the Brewster-angled crystal has to propagate is:-

$$l_x = \frac{t\sqrt{n^2 + 1}}{n^2} \quad (4.6.2a)$$

and:-

$$l_y = \frac{t\sqrt{n^2 + 1}}{n^4} \quad (4.6.2b)$$

where  $t$  and  $n$  represent the length and the refractive index of the laser medium respectively. The main objectives of designing an astigmatically-compensated resonator are to achieve similar beam-waist diameters and focal points in the  $x$  and  $y$  directions. These can be realised by tilting the cavity mirrors with the incidence angle,  $\theta$  that is presented as [22]:-

$$\sin \theta \tan \theta = \frac{2t(n^2 - 1)\sqrt{n^2 + 1}}{R.n^4} \quad (4.6.3)$$

with  $t = 1.2$  mm and  $n = 2$ , the effective lengths  $l_x$  and  $l_y$  of the crystal were estimated to be 0.67 mm and 0.17 mm correspondingly. From figure 4.8 in order to minimise astigmatism,  $\theta$  was determined to be  $8.1^\circ$  for M1 that had  $R = 50$  mm and it is  $5.7^\circ$  for M2 that had  $R = 100$  mm. By substituting  $\theta$  for M1 to equation (4.6.1a) and (4.6.1b), the focal positions of this mirror were calculated to be 25.3 mm for  $f_x$  and 24.8 mm for  $f_y$ .

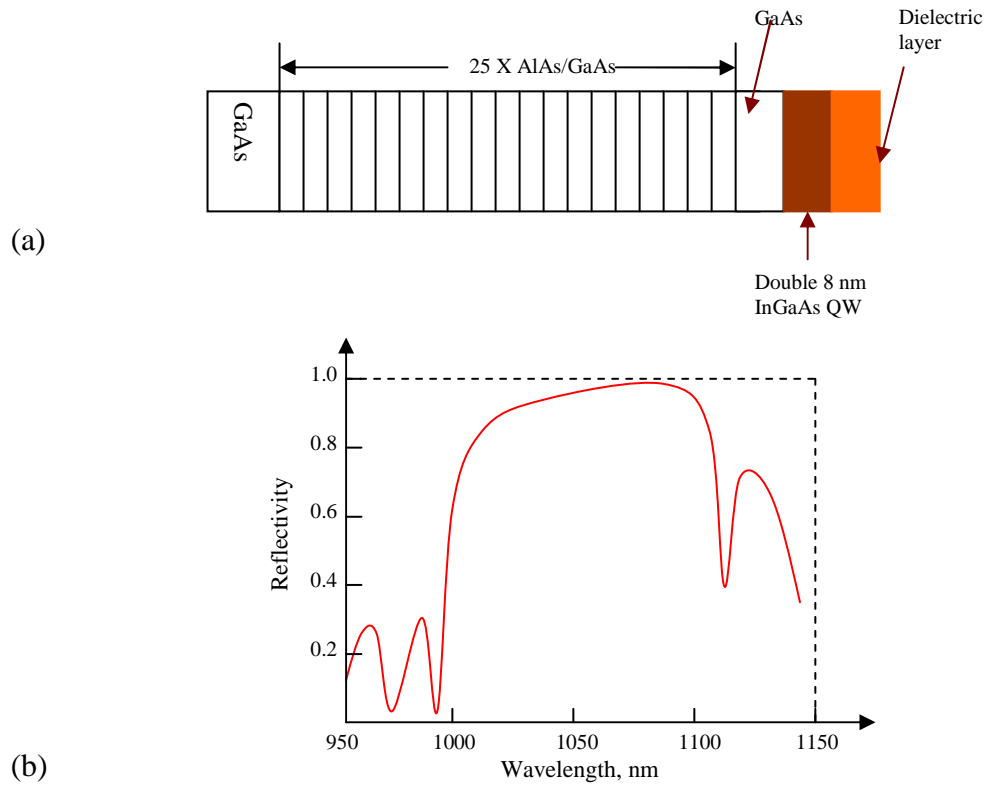


Figure 4.9. (a) Diagram of SESAM with (b) spectral reflectivity of the absorber layer (brown region) as a function of wavelength.

A spherical lens ( $f = 63$  mm) was used to collect and focus the pump beam at the gain material. Both mirrors (M1 and M2) had a high transmission at the pump wavelength of 981 nm and a high reflectivity at the laser wavelengths between 1020 and 1100 nm where the transmission property for M1 was optimised to be 95 %. Mirror 3 was a high reflector (HR) used in continuous wave (cw unmode-locked) configuration while a SESAM was used for passive mode locking. The HR mirror had a high reflectivity properties ( $> 99.95$  %) at 1052 nm while the SESAM used to passively mode locked the laser was a low-finesse anti-

resonance Fabry-Perot saturable absorber (A-FPSA). During cw operation, the beam bounces back and forth between mirror 1, mirror 2, and high reflector to the output coupler directly without any prism. However during passive mode locking operation, a SESAM (semiconductor saturable absorber mirror) was used instead of a high reflector where the dispersion control mechanism was introduced with the insertion of a single prism in the cavity configuration as indicated by the green rectangle in figure 4.8. The output coupler was a plane-wedged mirror which has 3 % transmission at 1064 nm and was used for the entire evaluation of performance during the unmode-locked and mode-locked regimes of operation.

A semiconductor saturable absorber (SESAM) [figure 4.9] was used for the initiation and stabilisation of the mode locking process. This SESAM sample was grown by all- solid-source molecular beam epitaxy and consisted of the Bragg mirror, comprising 25 pairs of AlAs/GaAs with thickness  $\lambda/4$  grown between two substrate layers of GaAs [figure 4.9a]. This Bragg mirror forms a distributed Bragg reflector (DBR) at a centre wavelength of 1055 nm. An 8 nm double quantum well (DQW) InGaAs saturable absorber layer was then grown within the Fabry Perot cavity on top of the GaAs layer. A dielectric layer with thickness approximately 20 to 30 nm was implanted on top of the Fabry perot mirror to protect the InGaAs QW structure from any dust or chemical reaction. These layers were also implanted with doses of  $10^{12} \text{ cm}^{-2}$  of 10 MeV N-ions and this device had a modulation depth,  $\Delta R$  of  $\approx 1.4 \%$  at 1045 nm. An appropriate value of  $\Delta R$  should be selected carefully in this experiment, since a higher value of  $\Delta R$  results in a shorter pulse duration  $\tau_p$  at a lower average output power. The Fabry-Perot cavity was formed by the lower semiconductor Bragg mirror and a dielectric top mirror with a saturable absorber and the transparent layers in between. The relaxation time of this saturable absorber was 20 ps and the pump saturation fluence to achieve transparency was  $\approx 70 \mu\text{J}/\text{cm}^2$ . The spectral reflectivity of this device at the laser operating wavelengths between 1040 to 1050 nm was approximately 97 % [see figure 4.9b].

#### **4.7 Continuous Wave (Unmode-locked) Configuration.**

Before any performance assessments were conducted on the system, a pump beam profile measurement was done by using a Beam Master Profiler when the lens focal length was 50

mm [figure 4.10]. However, it was found later that this lens could not be used for laser construction because of the very short distance from M1, thus the result obtained can be used to calculate the pump beam waist  $w_{p,0}$  for 63 mm lens. A filter was used to reduce the incident beam power on the detector head, thus preventing any damage. The detector head was placed at the focussed pump beam position to determine  $w_{p,0}$ . The beam measurement was later carried out at 50 % full width half maximum and the results obtained are shown in figure 4.11.

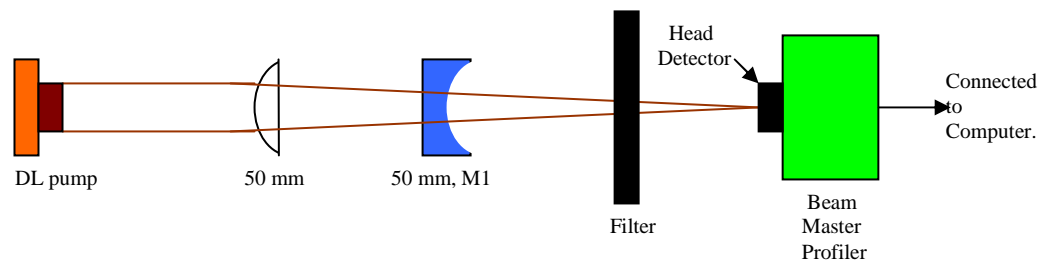


Figure 4.10. A schematic diagram for measurement of pump beam profile from the diode laser.

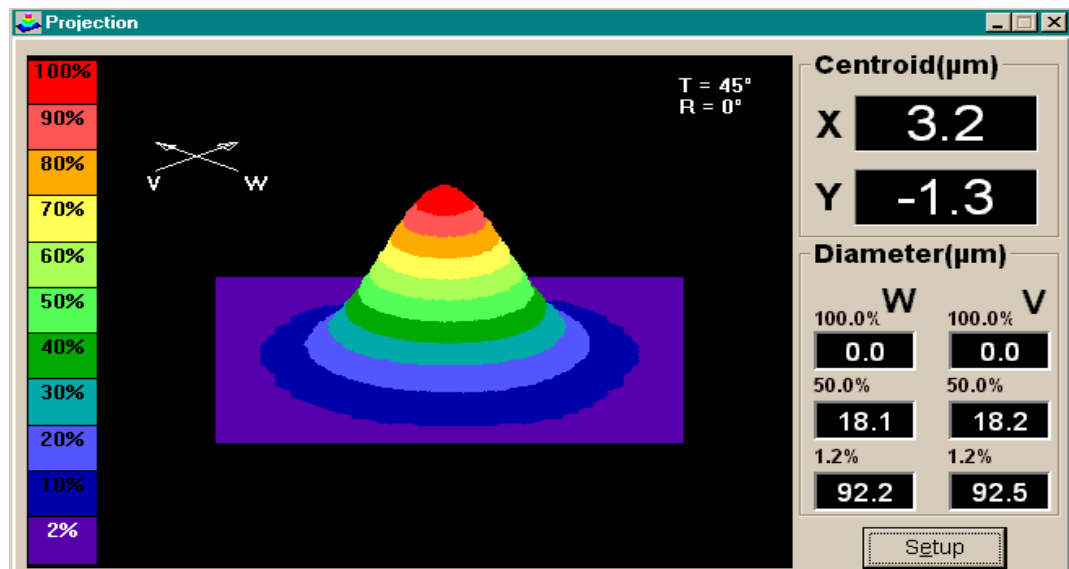


Figure 4.11. The pump beam mode for profile V X W of the diode laser focussed at the crystal in three dimensions.

The Gaussian correlation of ~ 91 % was obtained for both V and W profiles which are equivalent to X-Y axes where it shows how close the actual beam profile in comparison to the ideal Gaussian beam. From figure 4.11, it is shown that the full width half maximum

pump beam mode radius  $w_{50\%}$  focussed at the crystal was approximately  $9 \mu\text{m}$ . However, for the later evaluation which used a 63 mm lens, the  $w_{p,0}$  can be estimated as :-

$$w_{focus,50\%} = \frac{f.M^2\lambda_{pump}}{\pi.w_{incident}} \quad (4.7.1a)$$

and:-

$$w_{focus,50\%} = 0.59.w_{pump} \quad (4.7.1b)$$

where  $M^2$  is the beam quality which was approximately 1.2,  $f$  is the lens focal length,  $w_{focus}$  and  $w_{incident}$  is the focussed and incident beam at full width half maximum respectively. Thus, from equation 4.7.1a and 4.7.1b,  $w_{p,0}$  for 63 mm lens was approximately  $19 \mu\text{m}$ .

For the cw lasing experiment [figure 4.8], the laser beam waist  $w_{l,o}$  calculated at the crystal was  $17 \times 33 \mu\text{m}$  while the laser beam waist at the high reflector (M3) mirror,  $w_{HR}$  was  $35 \mu\text{m}$ . The maximum incident pump power focussed at the crystal was 323 mW compared to 351 mW average output power emitted from the diode laser pump. The crystal absorption was then measured and found to be  $\sim 93 \%$  for polarisation  $E \parallel N_m$  axis (this crystal is birefringence and supports the propagation of light in two polarisation eigenstates,  $N_p$  and  $N_m$  axis)

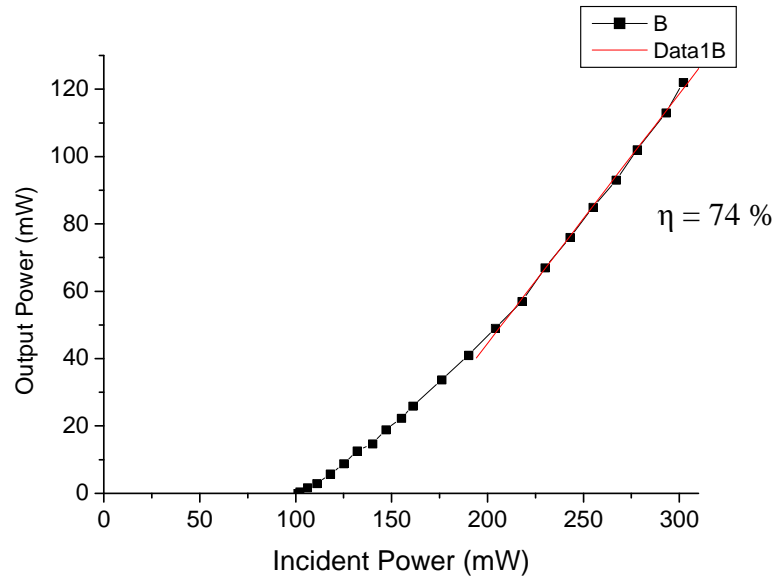


Figure 4.12. The slope efficiency of the cw (unmode-locked) laser.

First, the laser threshold and slope efficiency were measured for this cw operation. During this measurement, the maximum average output power was 122 mW with respect to 302 mW incident pump power on the crystal which results in a slope efficiency of  $\sim 74\%$  as shown in figure 4.12. This slope efficiency was almost equivalent to the results obtained when the Yb-doped tungstate lasers were pumped by a Ti:sapphire laser [13]. In this figure, it can be seen that after achieving a laser threshold power of  $\sim 101$  mW, the laser output power increases as a function of the incident power as expected. Double-pass loss,  $L_d$  was determined from equation (3.2.10) to be  $\sim 0.9\%$ . From equation (3.2.6a), theoretical threshold was found to be 32 mW approximately around 1044 nm which was two to three times lower than the measured result. This big difference can be improved by checking the cavity lengths in the resonator to determine the exact spot sizes.

After a careful alignment of the laser set up, the maximum output power produced from the laser was 136 mW at 1045 nm which corresponds to the optical-to-optical efficiency of 42 % with respect to the incident pump power of 323 mW. The next assessment was carried out on a passively mode-locked version of this laser with the introduction of a SESAM and a mechanism of dispersion compensation by using a single prism as outlined before.

#### 4.8 Passive Mode Locking Configuration with a SESAM.

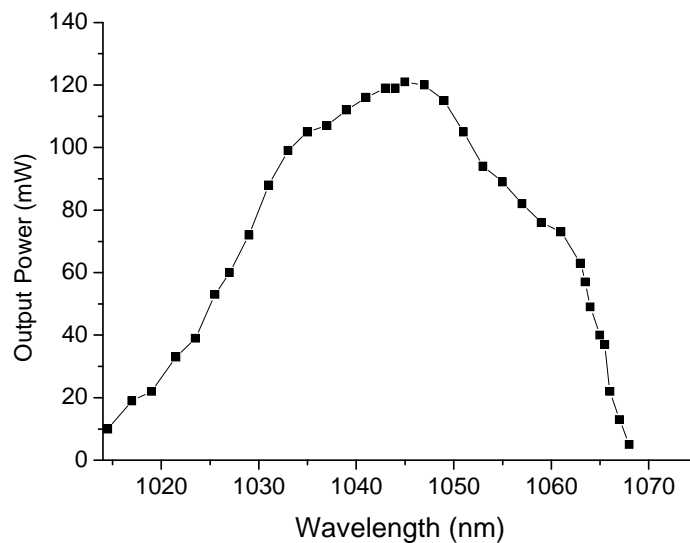


Figure 4.13. The wavelength tunability after inserting a prism inside the cavity.

Before passive mode locking assessments were carried out, the second-order dispersion of the crystal had to be determined by using the formula presented in equation 4.5.2. The refractive index of the crystal as a function of wavelength,  $n(\lambda)$  can also be calculated from equation 4.5.1 where constants  $a = 2.184443$ ,  $b = 0.811851$ ,  $c = 0.805159$ ,  $d = 0.019644$ ,  $e = 0.019289$  and  $f = 82.203164$ . Therefore, the positive group velocity dispersion of this crystal for the wavelength range between 1012-1069 nm could be estimated to be 141-153 fs<sup>2</sup>/mm while its refractive index was deduced to be  $\sim 2$ . By accounting the length of the crystal as mentioned in section 4.6, the GDD of the crystal at 1040 nm was determined to be around 180 fs<sup>2</sup>. At this wavelength regime, M1 and M2 were designed by the manufacturer to imply positive dispersion of about 50 fs<sup>2</sup>. Both OC and SESAM [figure 4.8] had broadband reflection curves that explain their dispersionless properties. As the consequence, positive GDD in the laser cavity implemented in this evaluation was estimated to be around 300 fs<sup>2</sup> at 1040 nm where the dispersion in the air was negligible (this value will be determined in the next chapter). This passive mode locking experimentation was carried out to satisfy two objectives. The first was for the optimisation of energy pulse fluence incident on the SESAM to support stable mode locking operation and the second was to achieve optimised pulse compression. To satisfy both of these objectives coincidentally, the prism was placed at a similar position for the whole evaluation, but  $w_{SESAM}$  and intraprism length  $L_m$  were varied.

To determine the tunability of the laser, a single prism was inserted inside the cavity with a distance of 310 mm from M1 [figure 4.8] when a high reflector (M3) was maintained at the short arm cavity. This distance was decided based on the previous assessment on Yb:KYW laser [15] where the separation length between two prisms,  $L_p$  was 390 mm. With an output coupler of 3 %, a maximum of 121 mW output power was produced around 1045 nm. This shows that the prism had induced losses  $\sim 5$  % inside the cavity and as a consequence the optical-to-optical efficiency was reduced to 37 %. The laser was then tuned from 1012 nm to 1069 nm which was comparable to the previously report done by Lagatsky [15] where the laser tunability was found to be between 1012 nm to 1079 nm.

In the configuration for passive mode locking, the high reflector mirror (M3) was substituted with a low-finesse SESAM in the short arm of the cavity. The introduction of a SESAM allowed mode locking to be initiated within an appropriate cavity length without any additional perturbation being required. Pulses that demonstrated multipulse operation

were produced when the average output power was 84 mW. This occurred because the beam mode at the SESAM,  $w_{SESAM}$  of 35  $\mu\text{m}$  implied a very high intracavity fluence incident on the SESAM compared to the saturation fluence of the SESAM ( $70 \mu\text{J}/\text{cm}^2$ ). By reducing the pump power on the laser medium, the pulses showed a stable mode-locked shape when the average output power was 50 mW that was 1.7 times lower than the earlier result. This provided an indication to which extent the  $w_{SESAM}$  need to be increased for the reduction of this fluence. As this stable mode locked process was produced at the unoptimised output power, it was predicted that  $w_{SESAM}$  needed to be increased approximately between 1.3 to 1.6 times from the original beam mode size. As the consequence, an initial attempt was performed by adjusting the cavity length between M2 and SESAM to increase  $w_{SESAM}$  to 47  $\mu\text{m}$  while  $w_{l,o}$  was not changed ( $w_{l,o}=17 \times 33 \mu\text{m}$ ). To produce ultrashort pulses, the prism was then inserted vertically at an appropriate distance to control the group velocity dispersion compensation inside the cavity. The pulse duration was then characterised by using a Femtochrome autocorrelator.

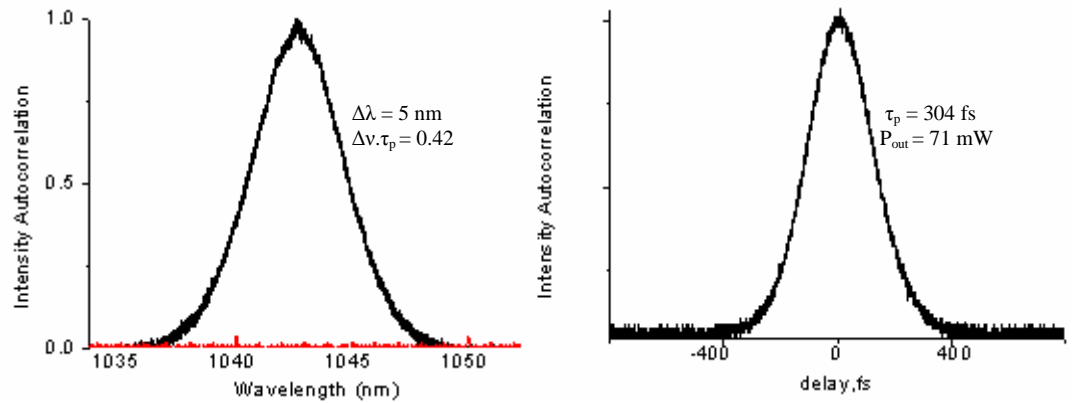


Figure 4.14. (a). The corresponding optical spectrum and (b) measured intensity autocorrelation for pulse duration of  $\sim 304 \text{ fs}$ .

From this measurement, a pulse duration of 304 fs was obtained at 1043 nm with pulse repetition frequency of 220 MHz. The spectral width was 5 nm while the average output power was 71 mW. From the output power of the laser  $P_{out}$ , intracavity power  $P_{int r}$  can be calculated with respect to the output coupler transmission  $T$  which is given as:-

$$P_{int r} = \frac{P_{out}}{T} \quad (4.8.1)$$

From the equation above, the intracavity power obtained inside the cavity was 2.37 W. The gain bandwidth of the laser,  $\Delta\nu$  was 1.38 THz. while the time-bandwidth product was 0.42. This was not a good  $\text{sech}^2$  transform-limited product as required ( $\Delta\nu\tau_p \approx 0.32$ ) while the pulse duration of 304 fs was longer than what was expected. As the consequence, the current beam waist ( $w_{\text{SESAM}} = 47 \mu\text{m}$ ) had to be increased to optimize the pulse fluence on the SESAM for the generation of shorter pulse durations.

#### 4.9 Optimisation of Energy Pulse Fluence Incident on the SESAM.

In this final evaluation, the pulse repetition frequency of the device was reduced to 212 MHz (optical path length  $\sim 1414$  mm) as a consequence of the increase in the beam waist at the SESAM to  $55 \mu\text{m}$  while the beam waist at the crystal was similar to before,  $w_{l,o} = 17 \times 33 \mu\text{m}$ . A careful vertical adjustment of the prism was done until an appropriate group velocity dispersion compensation was achieved inside the cavity. Meanwhile, precise control of the cavity length between mirrors especially the alignment of M2 and SESAM [figure 4.8] was also undertaken until a mode-locked beam was produced reliably.

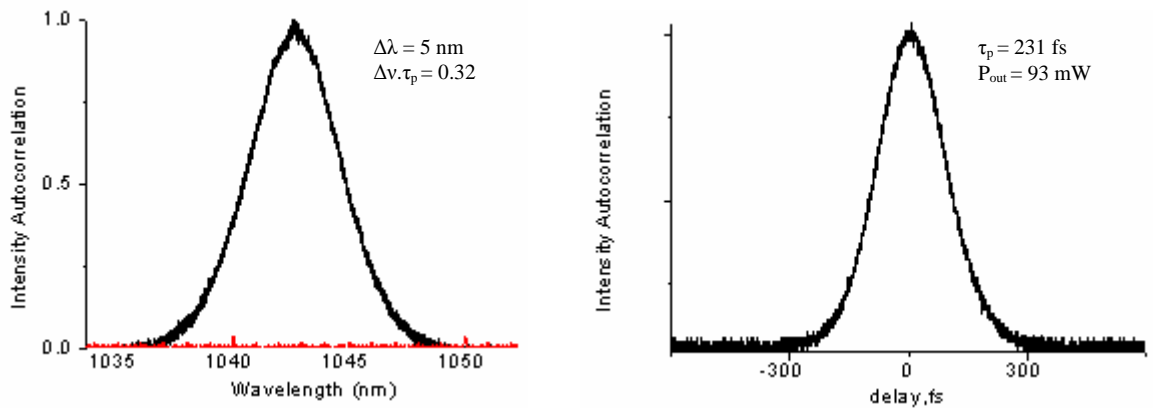


Figure 4.15. (a) The corresponding optical spectrum of mode locked Yb:KYW laser and (b) measured intensity autocorrelation for pulse duration of 231 fs.

The results of this performance assessment are shown in figure 4.15 where the pulse duration was 231 fs at 1043 nm. The laser gain bandwidth,  $\Delta\nu$  was 1.38 THz with a transform limited bandwidth product of 0.32. In addition, the spectral width was 5 nm while the peak power was 1.9 kW from the average output power of 93 mW. This corresponds to the optical-to-optical efficiency of 29 % while the electrical-to-optical efficiency was 12.6 %

which was three times higher than that obtained with a Cr:LiSAF laser [23]. The reduced efficiency for passive mode locking compared to the efficiency in the unmode-locked performance ( $\sim 42\%$ ) was attributable to the losses caused by the insertion of the prism and the SESAM. The pulse fluence incident on the SESAM,  $F_{SE}^{\lambda_{se}}$  can be shown to be:-

$$F_{SE}^{\lambda_{se}} = \frac{P_{int r}}{f_{rep} \times \pi \cdot (w_{SESAM})^2} \quad (4.9.1)$$

where  $f_{rep}$  is the pulse repetition rate. From this equation, the intracavity power inside the laser oscillators was 3.1 W while the pulse fluence calculated on the SESAM was  $154 \mu\text{J}/\text{cm}^2$  in comparison to the saturation fluence of the SESAM,  $F_{sat}^{\lambda_{se}}$  of  $70 \mu\text{J}/\text{cm}^2$ . This shows that the intracavity fluence on the SESAM should be optimised to be two or three times higher than the saturation fluence of the SESAM to achieve appropriate mode locking stability.

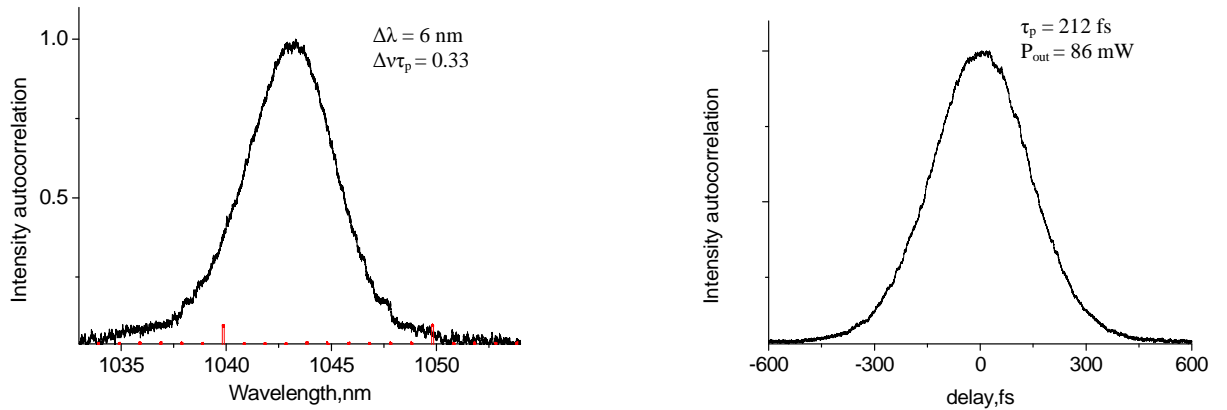


Figure 4.16. (a) The corresponding optical spectrum of mode-locked Yb:KYW laser and (b) measured intensity autocorrelation for pulse duration of 212 fs.

The laser was then adjusted further to obtain a pulse duration as short as 212 fs with an output average power of 86 mW [figure 4.16]. This is to date the shortest pulse duration produced from this cavity arrangement with a high peak power of 1.9 kW emitted at 1044 nm and a spectral width of 6 nm. The pulse was nearly transform limited, as implied by the duration-bandwidth product of 0.33, with the laser gain bandwidth  $\Delta\nu$  of 1.65 THz. The intracavity power inside the laser oscillator was calculated to be 2.9 W while the pulse fluence on the SESAM was  $143 \mu\text{J}/\text{cm}^2$  in comparison to the saturation fluence of the SESAM of  $70 \mu\text{J}/\text{cm}^2$ . The shorter pulse duration with a more broadened spectrum obtained

in this new setup was due to the optimization of the pulse fluence on the SESAM compared to the saturation fluence of the SESAM. There was also better control of group velocity dispersion for compensation by a careful re-insertion of the prism inside the laser cavity. From both of these results, it is seen that a shorter pulse duration can be obtained at a lower average output power which corresponds to a lower intracavity power and optimised pulse fluence incident on the SESAM in comparison to that of longer pulse duration. However, the peak power for both of these pulses were similar at 1.9 kW as calculated from equation 1.2.1 and thus feasible for biological, medical and imaging applications within this spectral region.

By considering positive GDD inside the laser oscillator as  $300 \text{ fs}^2$  at around 1040 nm,  $L_p$  was calculated from equation 4.5.5 to be 157 mm for intraprism length,  $L_m$  of approximately 12.5 mm. However, this result was obtained by ignoring the dispersion value of air path length between the optical elements. If this value contributes to two times of the positive GDD implied in the optical elements [see section 5.7],  $L_p$  was estimated to be around 186 mm. In both of these cases,  $X$  – intersection point was assumed to be between 120 to 150 mm from M1 as depicted in figure 4.8. Further improvement to these results were suggested by moving the prism back or forward inside the laser oscillator to produce shorter pulses. This chapter just concentrates to discuss the optimisation of pulse fluence incident on the SESAM and the achievement of optimised optical pulse compression by the variation in  $L_m$  when  $L_p$  was fixed at a similar distance. Precise value of the net GDD need to be introduced in the laser set-up by accounting the exact amount of dispersion in the air will be carried out in the next chapter [Chapter 5] by implementing a combination of chirped mirrors.

#### **4.10 Tunability of a Single-prism Yb:KYW Femtosecond Laser.**

The most interesting advantage of inserting a single prism in this laser cavity instead of a pair of prisms was the simpler alignment which also allowed wider tunability [figure 4.13]. All the results presented in this section were obtained when the laser beam passed through the prism with a similar intraprism length,  $L_m$  thus exhibiting similar group velocity dispersion for compensation. When these pulse durations were plotted as a function of wavelength as demonstrated in figure 4.17, the pulses are seen to be shorter at longer

wavelength ranges. This can be explained because at longer wavelengths, the reflectivity of the SESAM [figure 4.9b] increases to  $\sim 97\%$ , which gives rise to an increase in the intensity of the pulses. With the combinations between self-amplitude and loss modulation, the stronger saturation properties of the higher intensity at the peak of the pulses compared to the lower intensity wing leads to improved pulse shortening mechanisms. In contrast, the longer pulses obtained at wavelength less than 1040 nm were caused by the increase in the non-saturable loss  $\Delta R_{NS}$  inside the SESAM as well as the higher transmission properties of the folding mirrors M1 and M2.

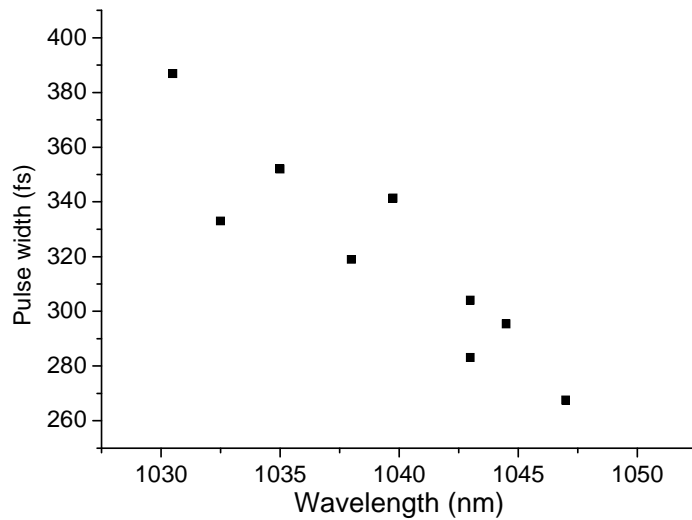


Figure 4.17. Pulse width as a function of wavelength.

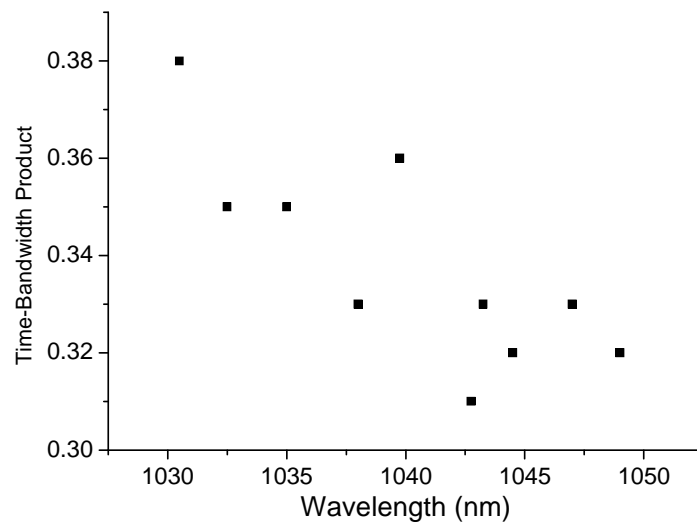


Figure 4.18. Time-bandwidth product as a function of wavelength

Meanwhile, it is also shown that the pulses exhibit a near-transform limited product of

~ 0.32 at the longer wavelength ranges between 1042 nm and 1047 nm [figure 4.18] in a full analogy with the results shown previously [figure 4.17].

#### **4.11 Conclusion.**

Some work carried out for the construction of an asymmetric 4-mirror cavity for a Yb:KYW femtosecond laser pumped by a single-mode narrow stripe InGaAs diode laser has been presented here. The use of a single prism instead of a prism pair, as used by other investigators, has been proven to be effective as a means of achieving a more compact and efficient laser. This provided both a simpler alignment and a wider tunability due to the reduction of optical elements in the cavity. The maximum optical-to-optical efficiency of 29 % was obtained during femtosecond operation while the electrical-to-optical efficiency was 12.6 % which was three times higher compared to that obtained in a Cr:LiSAF laser [23]. By a proper control of group velocity dispersion inside the resonator and the optimisation of incident fluence on the SESAM compared to the saturation fluence of the SESAM, the shortest pulse duration of 212 fs at 1044 nm was obtained with a peak power of 1.9 kW. Further improvements can be made to this resonator by using mirrors with shorter radii of curvature to increase the beam intensity focussed on the crystal perunit area and the use of chirped mirrors instead of a prism for dispersion compensation. This should lead to designs for more compact, lower threshold and higher efficiency femtosecond lasers.

#### 4.12 References:

1. L. D. DeLoach, S. A. Payne, L. L. Chase, L. K. Smith, W. L. Kway, and W. F. Krupke, "Evaluation of absorption and emission properties of  $\text{Yb}^{3+}$ -doped crystals for laser applications", *IEEE J. Quantum Electron.* **29**, 1179-1191 (1993).
2. A. Brenier and G. Boulon, "Overview of the best  $\text{Yb}^{3+}$ -doped laser crystals", *J. Alloys and Compounds* **323-324**, 210-213 (2001).
3. G. Boulon, A. Brenier, L. Laetitia, Y. Gunot, C. Goutaudier, M. T. Cohen-Adad, G. Metrat, and N. Muhlstein, "Search of optimised trivalent Ytterbium doped inorganic crystals for laser applications", *Journal of Alloys and Compounds* **341**, 2-7 (2002).
4. C. Honninger, R. Paschotta, M. Graf, F. Morier-Genoud, G. Zhang, M. Moser, S. Biswal, J. Nees, A. Braun, G. A. Mourou, I. Johannsen, A. Giesen, W. Seeber, and U. Keller, "Ultrafast Ytterbium-doped bulk lasers and laser amplifiers", *Appl. Phys. B* **69**, 3-17 (1999).
5. F. Druon, F. Balembois, P. Georges, A. Brun, A. Courjaud, C. Honninger, F. Salin, A. Aron, F. Mougel, G. Aka, and D. Vivien, "Generation of 90 fs pulses from a mode-locked diode-pumped  $\text{Yb}^{3+}:\text{Ca}_4\text{GdO}(\text{BO}_3)_3$  laser", *Opt. Lett.* **25**, 423-425 (2000)
6. F. Druon, S. Chenais, P. Raybaut, F. Balembois, P. Georges, R. Gaume, G. Aka, B. Viana, S. Mohr, and D. Kopf, "Diode-pumped  $\text{Yb}:\text{Sr}_3\text{Y}(\text{BO}_3)_3$  femtosecond laser", *Opt. Lett.* **27**, 197-199 (2002).
7. Y. Zaouter, J. Didierjean, F. Balembois, G. Lucas Leclin, F. Druon, P. Georges, J. Petit, P. Goldner, and B. Viana, "47-fs diode-pumped  $\text{Yb}^{3+}:\text{CaGdAlO}_4$  laser," *Opt. Lett.* **31**, 119-121 (2006).
8. N. V. Kuleshov, A. A. Lagatsky, A. V. Podlipensky, V. P. Mikhailov, and G. Huber, "Pulsed laser operation of Yb-doped  $\text{KY}(\text{WO}_4)_2$  and  $\text{KGd}(\text{WO}_4)_2$ ", *Opt. Lett.* **22**, 1317-1319 (1997).
9. W. F. Krupke, "Ytterbium solid-state lasers-The first decade", *IEEE J. Select. Topics Quantum Electron.* **6**, 1287-1296 (2000).
10. C. Honninger, R. Paschotta, F. Morier Genoud, M. Moser, and U. Keller, "Q-switching stability limits of continuous wave passive mode locking", *J. Opt. Soc. Am. B* **16**, 46-56 (1999).
11. P. Klopp, V. Petrov, U. Griebner, V. Nesterenko, V. Nikolov, M. Marinov, M. A. Bursukova, and M. Galan, "Continuous-wave lasing of a stoichiometric Yb laser material:  $\text{KYb}(\text{WO}_4)_2$ ", *Opt. Lett.* **28**, 322-324 (2003).

12. F. Brunner, G. J. Spuhler, J. Aus der Au, L. Krainer, F. Morier-Genoud, R. Paschotta, N. Lichtenstein, S. Weiss, C. Harder, A. A. Lagatsky, A. Abdolvand, N. V. Kuleshov, and U. Keller, "Diode-pumped femtosecond Yb:KGd(WO<sub>4</sub>)<sub>2</sub> laser with 1.1-W average power", *Opt. Lett.* **25**, 1119-1121 (2000).
13. N. V. Kuleshov, A. A. Lagatsky, V. G. Scherbitsky, V. P. Mikhailov, E. Heumann, T. Jensen, A. Diening, and G. Huber, "CW laser performance of Yb and Er, Yb doped tungstates", *Appl. Phys. B* **64**, 409-413 (1997).
14. F. Brunner, T. Sudmeyer, E. Innerhofer, F. Morier-Genoud, R. Paschotta, V. E. Kisel, V. G. Shcherbitsky, N.V. Kuleshov, J. Gao, K. Contag, A. Giesen, and U. Keller, "240 fs pulses with 22-W average power from a mode-locked thin-disk Yb:KY(WO<sub>4</sub>)<sub>2</sub> laser", *Opt. Lett.* **27**, 1162-1164 (2002).
15. A.A. Lagatsky, E.U. Rafailov, C.G. Leburn, C.T.A. Brown, N. Xiang, O.G. Okhotnikov, and W. Sibbett, "Highly efficient femtosecond Yb:KYW laser pumped by a single narrow stripe laser diode", *Electron. Lett.* **39**, 1108-1110 (2003).
16. H. Liu, J. Nees, and G. Mourou, "Diode-pumped Kerr-lens mode-locked Yb:KY(WO<sub>4</sub>)<sub>2</sub> laser", *Opt. Lett.* **26**, 1723-1725 (2001).
17. R. L. Fork, C. H. Brito Cruz, P. C. Becker, and C. V. Shank, "Compression of optical pulses to six femtoseconds by using cubic phase compensation," *Opt. Lett.* **12**, 483-485 (1987).
18. O. E. Martinez, J. P. Gordon, and R. L. Fork, "Negative group-velocity dispersion using refraction," *J. Opt. Soc. Am. A* **1**, 1003-1006 (1984).
19. R. L. Fork, O. E. Martinez, and J. P. Gordon, "Negative dispersion using pair of prism," *Opt. Lett.* **9**, 150-152 (1984).
20. D. Kopf, G. J. Spuhler, K. J. Weingarten, and U. Keller, "Mode-locked laser cavities with a single prism for dispersion compensation," *Appl. Opt.* **35**, 912-915 (1996).
21. H. W. Kogelnik, E. P. Ippen, A. Dienes, and C. V. Shank, "Astigmatically compensated cavities for CW dye lasers", *IEEE J. Quantum Electron.* **QE-8**, 373-379 (1972).
22. W. Koechner, "Solid-state laser engineering", New York:Springer, 232-233 (1986).
23. B. Agate, B. Stormont, A. J. Kemp, C. T. A. Brown, U. Keller, and W. Sibbett, "Simplified cavity designs for efficient and compact femtosecond Cr:LiSAF lasers", *Opt. Comm.* **205**, 207-213 (2002).

## **Chapter 5**

### **Compact and Highly Efficient Prismless Diode-Pumped Yb:KYW Femtosecond Laser**

#### **5.1 Introduction.**

In this chapter I introduce the advantages of dispersive mirrors that are based on a chirped dielectric structure that can be used to control dispersion in a laser cavity. This contrasts with a standard Bragg mirror where the dielectric layers have a constant structure throughout the device. Along with the desired dispersion profile, the differences in dielectric structure result in broader bandwidth characteristics for chirped mirrors compared to those associated with Bragg mirrors. The dispersive mirrors discussed in this project ranged from a simple dielectric mirror, to a double-chirped mirror and then to an integrated double-chirped-semiconductor mirror technology. The main objective in this work was to construct Yb:KYW femtosecond lasers based on a dielectric chirped mirror that represented a simpler and cheaper fabrication requirement compared to that of a double-chirped mirror. The optimisation of compact dispersion compensation mechanisms were carried out in the laser oscillator to increase optical-to-optical efficiency, reduce device footprint and produce shorter pulse durations than might have been the case using prisms for dispersion compensation.

The initial assessment was carried out by using a single-mode narrow-stripe InGaAs diode laser having an output power of 350 mW as a pump source while the second was carried out by using more powerful pump sources based on single-mode fibre-coupled polarisation maintaining InGaAs diode lasers producing output powers up to 930 mW. The main objective of using the more powerful pump sources was to further improve the results obtained in the initial evaluation. Any extra heating generated could be neglected due to the low quantum defect of  $\sim 0.04$  in tungstates and the relatively low power ( $<10$  W) of the pump source. Some suggestions for the improvement of these results towards an optimised design for a more compact and highly efficient femtosecond laser are included as concluding remarks.

## 5.2 New Techniques for Dispersion Compensation.

In femtosecond lasers emitting at wavelengths shorter than 1300 nm, the positive dispersive properties exhibited by the optical elements and gain media in the laser cavity can be compensated by a range of techniques that provide the desired amount of negative group delay dispersion (GDD) in relatively simple configurations [1,2]. Techniques reported by other investigators involved the deployment of prism-based dispersion control such as prism pairs [3], a single prism [4] or a prismatic end mirror [5]. In these implementations, the material dependent factor and effective prism separation  $L$  between the Brewster interface and the axes of different frequencies intersection of the resonator modes play important roles in determining the amount of negative GDD introduced within laser oscillators [4]. These contribute to the relatively complicated cavity designs that take account of the interdependence between pulse durations to cavity and prism alignment. Any slight cavity-mirror alignment changes the position of the resonator axis and glass path through the prisms. In order to maintain the original pulse duration and corresponding spectrum, some readjustments of prism position and orientation with other optical elements are required. As a consequence, this increases the complexity in the integration of these devices to pump other optical systems especially for optical parametric oscillators/amplifiers and second harmonic generation. Furthermore, the insertion of additional prism elements leads to a loss in laser efficiency and it also sets limits to cavity dimensions because large values of negative GDD require relatively large effective prism separations.

An earlier investigation used an integrated prismatic output coupler and gain medium [5] as a compact dispersion-compensation scheme in a Kerr-lens mode-locked Ti:Sapphire laser. In this configuration, the end mirror was a single prism coated to perform as a 1 % transmitting output coupler thereby eliminating any need for a prism pair. This has the advantage that the laser cavity could be reduced in size and the tolerance on cavity alignment was relaxed. A pulse duration of 111 fs was obtained at a pulse-repetition rate of 1 GHz and 54 fs at a pulse repetition rate of 385 MHz, but this geometry was found to be incompatible for GHz repetition-rates and sub-100 fs regimes.

In the case of broadband solid-state femtosecond lasers capable of generating pulse duration less than 50 fs, a prism-pair is a primary source of higher-order dispersion. This can be described by the Taylor expansion [equation 2.4.2] that includes the third-order and fourth-order terms [6,7,8]. Third-order dispersion is found as a major limitation to

dispersion-control mechanisms. Although prism-pair-controlled Ti:sapphire lasers can generate nearly transform-limited pulses with pulse durations of 10-15 fs [9,10,11], the generation of pulses below 10 fs is more problematical as shown by the time-bandwidth product  $\Delta\nu\tau_p$  of 0.6. Alternative intracavity elements based on negatively dispersive mirrors have therefore been designed for the control of group velocity dispersion in laser oscillators. In such mirror-dispersion-controlled Ti:sapphire lasers, pulse durations as short as 8 fs with a near sech<sup>2</sup> duration-bandwidth product  $\Delta\nu\tau_p$  of 0.38 was obtained at around 800 nm [12].

### 5.3 Dispersive Mirrors.

Three types of dispersive mirrors are outlined in this section. These are the Bragg mirror, the chirped mirror and the double-chirped mirror that are based on thin film designs. A Bragg mirror is a standard dielectric structure that is designed to have high-reflectivity characteristics at a certain wavelength range and it is a principal optical component in a laser cavity. It consists of multiple layers of alternating high and low index transparent films, typically fabricated from TiO<sub>2</sub>/SiO<sub>2</sub> where all of the optical layer thicknesses are one-quarter ( $\lambda/4$ ) of the centre operating wavelength [figure 5.1].

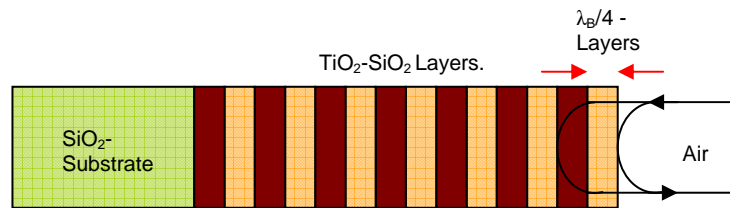


Figure 5.1. The basic structure of a Bragg mirror [13].

The geometrical thickness  $d_{h,m}$  and  $d_{l,m}$  of these layers with m-th index step [figure 5.2] can be described as:-

$$d_{h,m} = \lambda/4n_h \text{ and } d_{l,m} = \lambda/4n_l \quad (5.3.1a)$$

$$d_{h,m}n_h = d_{l,m}n_l = \lambda/4 \quad (5.3.1b)$$

where  $n_h$  and  $n_l$  are the indices of refraction of high and low index films [ $n(\text{TiO}_2) = 2.4$ ,

$n(\text{SiO}_2)=1.45]$  and  $\lambda$  is the centre wavelength of the Bragg mirror.

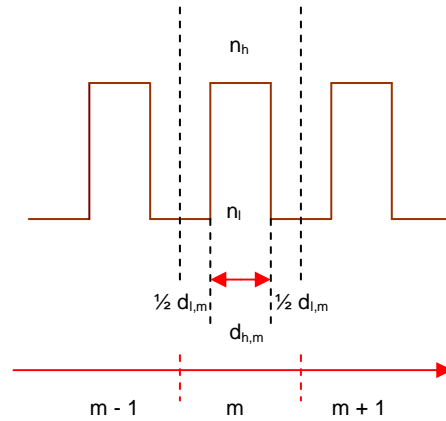


Figure 5.2. A general Bragg structure with  $m$ -th index layer [14].

For the design wavelength transmitted on each mirror/air and mirror/mirror interface, a part of the incident light will be reflected back due to Fresnel reflection. The reflection coefficients for the interfaces have a phase shift of  $180^\circ$  due to the difference in refractive index while the optical path length difference between subsequent interfaces is  $\lambda/2$  (one-half of the wavelength). The relative phase difference of all reflected beam components should be zero which implies constructive interference amongst all the reflective components. For the optimization of laser performance, the quality of optical coatings in the mirrors such as high reflectors should approach 100 % reflectance at the operating wavelength range to minimize intracavity losses as shown in figure 5.3.

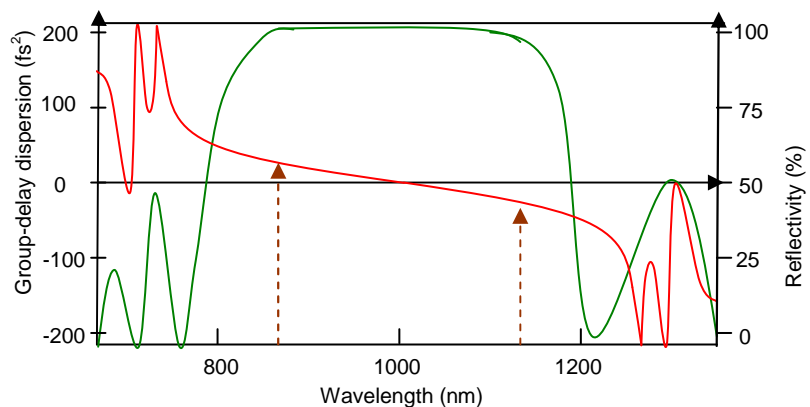


Figure 5.3. An example of the reflection (green curve) and dispersion (red curve) profiles of a standard Bragg mirror where the brown arrow shows the dispersion profile over the reflection bandwidth of this device [15].

The disadvantages of this mirror are the restricted bandwidth characteristics that place constraints on the pulse durations that are possible in ultrashort pulse lasers. These

arise through the restricted difference in refractive index between transparent layers of SiO<sub>2</sub> and TiO<sub>2</sub> which results in a limitation of the high-reflectivity bandwidth of a standard quarter-wave Bragg mirror. For instance, at the wavelength of 1000 nm the bandwidth of this mirror is just 300 nm. This means that the mirror is dispersionless at the designed wavelength but exhibits a relatively small group delay dispersion over the reflection bandwidth. A different phenomenon is shown at the edge of this wavelength range where a significant amount of dispersion occurs (figure 5.3). In addition, this mirror produces higher-order dispersion as shown by the investigation involving CPM dye lasers [16]. However, these problems can be solved with chirped dielectric mirrors that can be designed for dispersion compensation in laser oscillators.

In 1994, Szipocs and Krausz designed the first chirped mirror [13,17,18] that offered a wide reflectivity range and a controlled negative dispersion profile [2,19] that could provide dispersion compensation through the whole reflectivity bandwidth. This was achieved through the provision of a linear chirp in the Bragg wavelength associated with the individual layer pairs where longer wavelengths penetrate deeper into the mirror structure compared to shorter wavelengths as shown in figure 5.4 [13]. In the case of high reflectivity chirped mirrors, preference is shown towards a combination of materials having the highest refractive index ratio ( $n_h/n_l$ ) that produce a broader bandwidth. For commercial applications, the TiO<sub>2</sub>/SiO<sub>2</sub> pair has the highest ratio in the near-infrared spectral region.

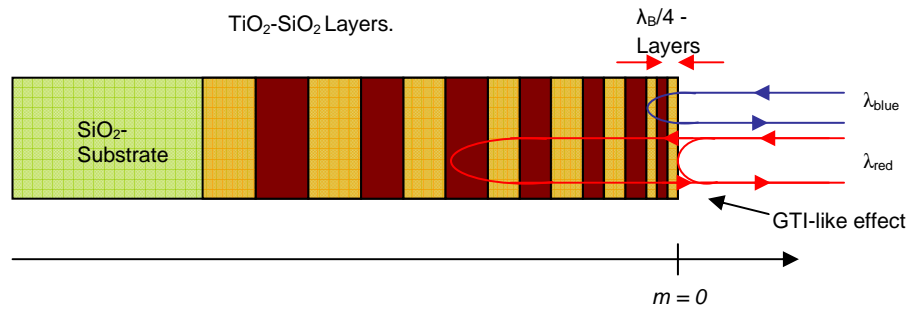


Figure 5.4 The structure of a chirped mirror [13].

From the theoretical derivations explained by Keller and co-workers [13], the group delay dispersion in chirped mirrors can be described as:-

$$D_2^0 = -\frac{2\pi}{c^2 \Delta k k_{\max,0}} \left( \frac{k_{\max,0}}{k_\lambda} \right) \quad (5.3.2)$$

and, the formula for third-order dispersion is given by:-

$$D_3^0(k) = \frac{2\pi}{c^3 \Delta k k_{\max,0}^2} \left( \frac{k_{\max,0}}{k_\lambda} \right)^2 > 0 \quad (5.3.3)$$

where  $k_\lambda$  is the wave number of the incoming wavelength,  $k_{\max,0}$  is the maximum wave number for the first index step ( $m = 0$ ) and  $k_{\min,m}$  is the minimum wave number for the final index step.  $\Delta k$  is the linear decrease in the chirped wavenumber for each individual layer that is given as:-

$$\Delta k = \frac{k_{\max,0} - k_{\min,m}}{|m|} \quad (5.3.4)$$

From figure 5.4,  $m$  is negative for the designed chirped mirror due to its position at the left side of this index step and  $m$  is positive for the incoming/reflected propagating waves due to its position at the right side of this index step. For the first layer of the chirped mirror  $m = 0$  while for the subsequent layers  $|m| = l - 1$  where  $l$  is the individual layer pair sequence ( $l = 1, 2, 3 \dots$  and  $m = 0, -1, -2, -3 \dots$ ).

From equation (5.3.3), it is shown that a linearly chirped mirror implies a low value of positive third-order dispersion in a laser oscillator even though it was previously thought that a linear chirp in the Bragg wave number would lead to a linear group delay, and zero third-order dispersion. However, the fabrication and design technology [18] of this device can be implemented to cancel or reduce any contributions to higher-order dispersion (equation 2.4.2) as exhibited for instance in the gain medium or prism-based dispersive elements. A chirped mirror overcomes the bandwidth limitation of a standard Bragg mirror and can provide compensation for higher-order dispersion. Multiple bounces on a chirped mirror can achieve an adequate amount of negative dispersion to compensate for material dispersion inside the laser cavity without the existence of prism pairs, thus reducing the insertion of any additional material in the beam path. This approach leads to cavity design simplification that enables the construction of more compact, portable and highly efficient femtosecond lasers with shorter pulse durations. To date, pulse durations with sub-10 fs pulses from Ti:sapphire lasers [20,21] at around 800 nm and sub-20 fs

pulses from Cr:LiSAF and Cr:LiSGaF lasers [22,23] at around 840 nm have been reported with the use of chirped dielectric mirrors.

Chirped mirrors have a wide range of applications for dispersion control in optical parametric oscillators [24], continuous wave and mode-locked solid-state lasers [17], pulse compression in chirped pulse amplification (CPA) systems [25,26], or in white light continuum compression experiments [27] that support the generation of sub-5 fs pulses [28,29]. However, these devices exhibit strong oscillations in the mirror structure due to the chirping of Bragg wavelength in a full analogy with Gires-Tournois interferometer effect [30]. For longer wavelengths with deeper mirror penetration, Fresnel reflection at the mirror/air interface interferes constructively with the strong reflection from the back, contributing to additional material dispersion with an amplitude of several tens of femtoseconds which is not useful for ultrashort pulse generation. Another source of oscillation is the generation of “impedance mismatch” due to immediate switching of the counter propagating waves from “0” in the air to a “finite value” in the mirror structure.

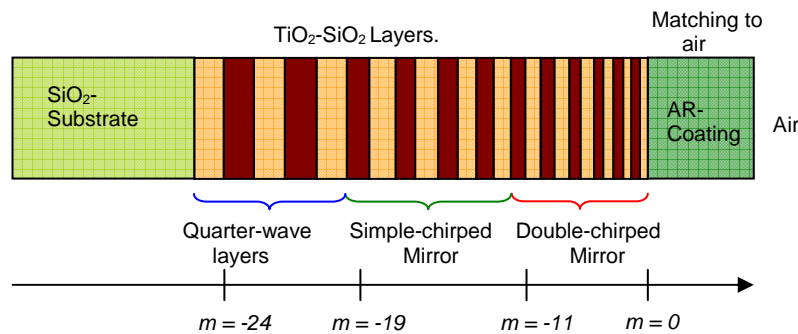


Figure 5.5. The structure of a double chirped mirror [31].

Both problems described above can be solved with the double-chirped mirror (DCM) pattern [14,32] as shown in figure 5.5 above. An anti-reflection coating that is the initial part of this mirror is implanted on top of the mirror structure. The design of this coating can affect the relative phase and amplitude of the reflected waves to be perfectly matched to the surrounding medium. This can eliminate any GTI-effect into the mirror by avoiding a refractive-index jump between the top mirror layer and the air. In addition to the linear chirp in the Bragg wavelength, an “impedance matching” mechanism is also included as the second part of this mirror that therefore consists of double-chirped layers. This is achieved by chirping in the coupling strength along the grating period to produce a smoother group delay dispersion inside the mirror structure. This can be done by controlling the thickness ratio between high and low index layers of the transparent films

where the optical thickness of the high-index layers are lower than those of the low-index layers,  $n_h d_{h,m} \leq n_l d_{l,m}$ . The Bragg wave number for the m-th index step  $k_{B,m}$  is given as:-

$$k_{B,m} = \frac{2\pi}{\lambda_{B,m}} = \frac{\pi}{n_h d_{h,m} + n_l d_{l,m}} \quad (5.3.5)$$

and the Fresnel reflectivity,  $r$  of the mirror structure is shown as:-

$$r = \frac{n_h - n_l}{n_h + n_l} \quad (5.3.6)$$

where coupling coefficient between the incident to the reflected waves is given as,  $\kappa_0 = -2r$ .

The third part of this mirror [figure 5.5] consists of simple chirped-layers and the last part on top of the  $SiO_2$  substrate is the quarter-wave layers. These two layers are optional in the designed DCM but are sometimes required to obtain high reflectivities over broadband wavelength ranges.

Based on the work reported by Keller et al. [13], the chirp in the Bragg wavelength of the DCM is chosen to be:-

$$k_{B,m} = k_{\max,0} - \left[ (l-1) \left( \frac{k_{\max,0} - k_{\min,m}}{|m|} \right) \right] \quad (5.3.7)$$

and the physical thickness of the high-index layer  $d_{h,m}$  is given as:-

$$d_{h,m} = \frac{\left( \frac{l}{12} \right)^\alpha \lambda_{B,m}}{4n_h} \quad (5.3.8)$$

where  $\alpha = 1$  is for a linearly-chirped and  $\alpha = 2$  is for a quadratically-chirped high-index layers. From equation 5.3.5, the low-index layer  $d_{l,m}$  can be obtained by substituting the values of  $d_{h,m}$  obtained in equation 5.3.8 into equation:-

$$d_{l,m} = \frac{\left(\frac{\lambda_{B,m}}{2}\right) - n_h d_{h,m}}{n_l} \quad (5.3.9)$$

For instance, by choosing randomly a wavelength range of operation for the DCM between 750 nm and 1200 nm, the value of  $k_{\max,0}$  is  $8.3 \mu\text{m}^{-1}$  and  $k_{\min,m}$  is  $5.23 \mu\text{m}^{-1}$ . Linear variation in the Bragg wave number over the first 20 index layers ( $m = 19$ ) [figure 5.5] can be implemented by using equation 5.3.7. The corresponding results as a function of m-th index step are presented in Figure 5.6 below where the last 5 index layers of the Bragg structure are kept constant at  $k_{\min,m}$ . It is demonstrated from this figure that the first layer of the double-chirped structure is normalised to the maximum wave number  $k_{\max,0}$  and the final structure of the chirped-mirror is normalised to the minimum Bragg wave number  $k_{\min,m}$ . This is as the consequence of the deeper penetration of longer wavelengths inside the mirror over that of shorter wavelengths [figure 5.6].

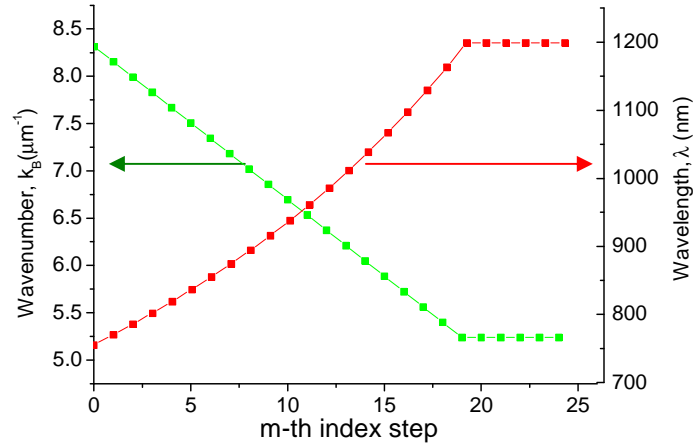


Figure 5.6. Properties of double-chirped and simple-chirped structures for the designed DCM illustrated in figure 5.5 for the first 20-index layers. Green colour represents chirped Bragg wave number and red colour represents the corresponding wavelength for each layer.

Impedance matching for the first 12 index layers of the double-chirped structure is implemented by varying the physical thicknesses of high- and low-index layers through linear and quadratic functions. The results are plotted in figure 5.7 where  $d_{h,m}$  increases slowly along the m-th index steps in contrast to the decreasing thicknesses of  $d_{l,m}$ . However, in AR-coating  $d_{h,m}$  and  $d_{l,m}$  alternate randomly and in the simple chirped-structure these thicknesses increases simultaneously along the Bragg grating as presented

in (figure 8 [31]). The effects for reflection and dispersion profiles in a chirped mirror [figure 5.4] and in double-chirped mirrors are demonstrated in figure 5.8 above. The reflection profile in a quadratically impedance-matched double chirped mirror is smoother over that of a linearly impedance-matched and mismatch structures. In addition, the introduction of double-chirped structures generate a controlled group delay over a wide reflectivity range for the suppression of oscillations in a mismatch chirped mirror where the quadratically-matched structure is more favourable for smoother dispersion compensation scheme in ultrashort pulse generation over that of a linearly-matched structure. The higher the order of the matched-structure leads to the restriction in the reflectivity bandwidth as a reduced tolerance is imposed.

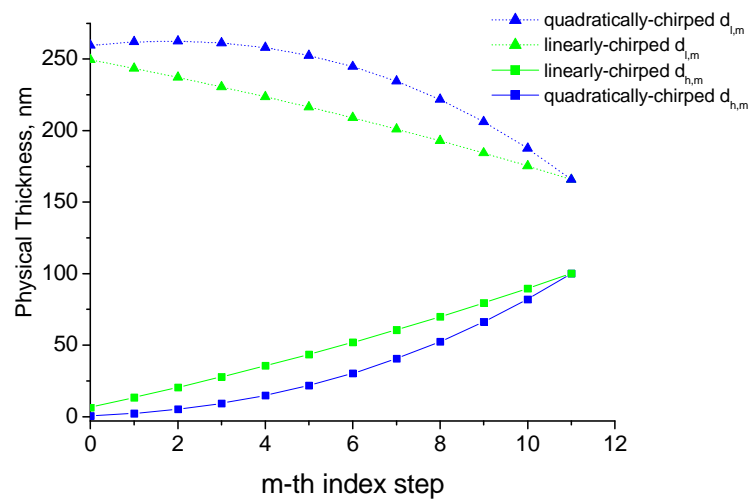


Figure 5.7. Physical thicknesses in the first 12 index steps of the double-chirping structure for the DCM shown in figure 5.5 where the solid lines are for high-index layers  $d_{h,m}$  and the dotted lines are for low-index layers  $d_{l,m}$ .

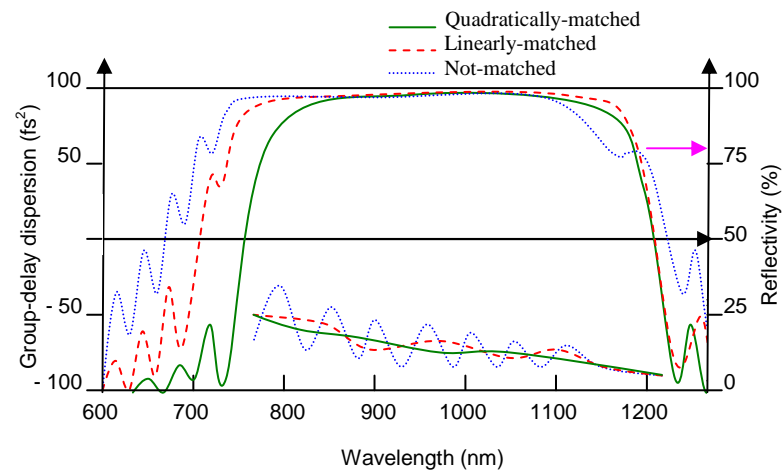


Figure 5.8. Example of reflection (upper plot) and dispersion profiles (lower plot) in a chirped mirror (blue curve) and double chirped mirror structures. The coupling coefficient in the double-chirped structure is matched linearly (red curve) and quadratically (green curve) to the surrounding medium [13].

From equation 5.3.2 and 5.3.3, dispersive properties in the DCM with the optical property of  $k_{\max,0} = 8.3 \mu\text{m}^{-1}$  discussed in figure 5.5 can be evaluated. For  $\text{TiO}_2/\text{SiO}_2$  pairs with refractive indexes of 2.4 for  $n_h$  and 1.45 for  $n_l$ , the coupling coefficient  $\kappa_0$  is given as -0.49. With  $\Delta k = 0.162 \mu\text{m}^{-1}$  obtained from equation 5.3.4, group delay dispersions in the mirror structure are calculated to be  $D_2^0 = -51.92 \left( \frac{k_{\max,0}}{k_\lambda} \right) \text{fs}^2$  for second-order dispersion and  $D_3^0(k) = 20.8 \left( \frac{k_{\max,0}}{k_\lambda} \right)^2 \text{fs}^3$  for third-order dispersion. For the incoming wavelength at 1045 nm ( $k_\lambda = 6.012 \mu\text{m}^{-1}$ ), the second-order dispersion  $D_2^0$  is calculated to be  $-71.61 \text{fs}^2$  and the third-order dispersion  $D_3^0$  is calculated to be  $28.7 \text{fs}^3$ . Due to its wavelength range of operation between 750 nm and 1200 nm, this type of broadband DCM mirror is the most compatible as a dispersion compensation scheme in Cr-doped/Yb-doped femtosecond lasers.

Although the DCM allows the generation of sub-10 fs directly from a Ti:sapphire laser [33,34], there are some limitations concerning the quantity of higher-order dispersion that can be compensated by this device, so a combination with prisms is sometimes required in the lasers. Multiple bounces between two double-chirped mirrors are needed to produce a sufficient amount of negative dispersion in a laser cavity and this tends to limit reductions in cavity dimensions.

To further reduce the device footprint, a DCM can be integrated into semiconductor technology [35]. In comparison to the typical  $\text{TiO}_2/\text{SiO}_2$  chirped mirrors, the chirp of the Bragg wavelength has to be weaker to achieve a sufficiently wide reflectivity wavelength range owing to the smaller refractive index ratio between GaAs/AlAs semiconductor layers. This requires a higher number of layer pairs to achieve an appropriate amount of reflection bandwidth and this contributes to a rather complicated fabrication requirement. However, a large amount of negative dispersion can be obtained as the consequence of weak coupling coefficient along the grating period and the weak chirp in the Bragg wavelength. This leads to an increase of the penetration depth for a pre-designed wavelength. Consequently, only a single bounce on the mirror is required for dispersion control which reduces losses inside the laser oscillators. This device can also be integrated into a SESAM structure, combining negative dispersion with soliton-like pulses and a soliton mode locking process [36] in a compact femtosecond configuration. A nearly transform-

limited product of 0.31 was obtained with 200 fs pulse durations in a compact Nd-glass laser using a chirped semiconductor mirror for dispersion compensation [35]. The insertion loss of the dispersive mirror was only 0.4 % and a separate SESAM was employed for mode locking mechanism.

Before designing any double-chirped semiconductor mirror, negative dispersion within a specified wavelength range required for compensation in a laser oscillator had to be investigated first. Different types of oscillators might have different amounts of material dispersion depending on the mirrors/gain elements inside the cavity. Therefore, a specific dispersive element in a semiconductor chirped mirror is designed for the requirement inside a particular laser. This specialised fabrication requirement becomes more complicated and expensive if the device is integrated into a SESAM structure. As a consequence, a simple chirped-mirror based on  $\text{TiO}_2/\text{SiO}_2$  technology is preferred as a cheaper alternative source for the net dispersive element for laser oscillators having MHz repetition rate as will be discussed in the next section.

#### **5.4 Implementation.**

The experimental set-up as shown in figure 5.9 was designed to enable the use of chirped mirrors for dispersion compensation in a more compact laser configuration. The cavity length used provided a pulse repetition rate of 212 MHz during mode-locking operation. In common with the previous experimental set-up of figure 4.8, the gain medium was a 1.2 mm long, 10 at. %  $\text{Yb}^{3+}$  doped  $\text{KY}(\text{WO}_4)_2$  Brewster-angled crystal pumped by a single-mode narrow-stripe InGaAs diode laser (p-polarised). Mirror 1 had a radius of curvature of 50 mm with 95 % transmission while mirror 2 had a radius of curvature of 100 mm. Both of these mirrors exhibit a high transmission at the pump wavelength of 981 nm and high reflectivity in the lasing band of 1020-1100 nm. The SESAM [figure 4.9] used for passive mode locking operation was a low-finesse anti-resonant Fabry-Perot saturable absorber (A-FPSA) with a modulation depth of 1.4 % at 1045 nm while the output coupler was a plane-wedged mirror with 3 % transmission at 1064 nm.

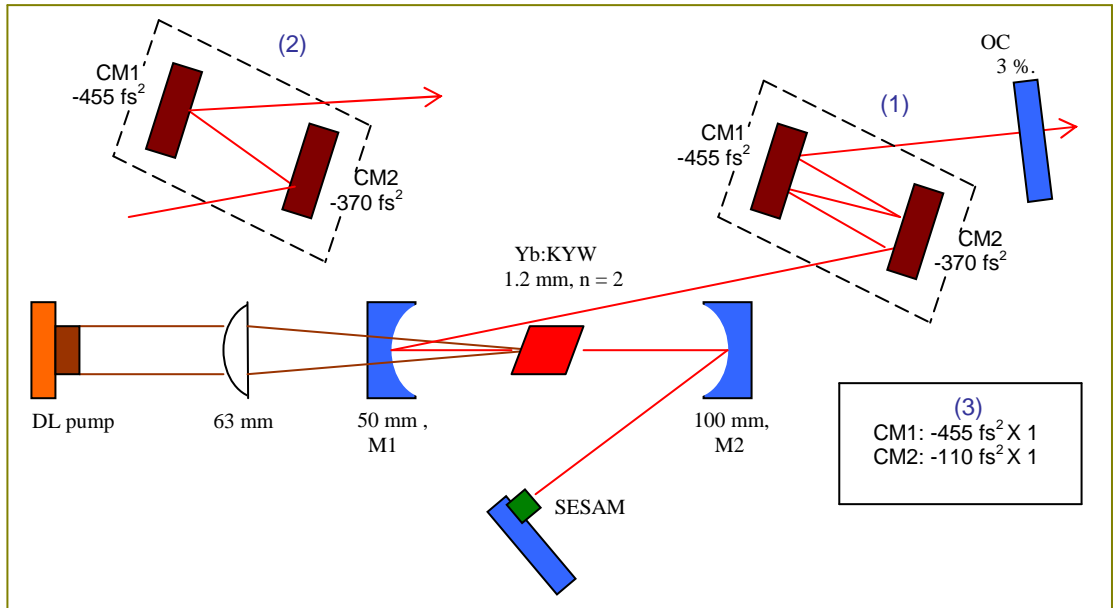


Figure 5.9. An overall schematic diagram of femtosecond Yb:KYW laser that incorporates 3-combinations of chirped mirrors CM1 and CM2, DL is single-mode InGaAs diode laser, M1 and M2 are spherically curved mirrors with radii of curvature of 50 mm and 100 mm respectively, SESAM is semiconductor saturable absorber mirror, while OC is 3 % output coupler.

A 63 mm lens was used to focus the pump beam to a waist,  $w_{p,0}$  of 12  $\mu\text{m}$  and a typical incident pump power on the crystal was 320 mW. From the ABCD matrix formalism, the laser beam waist,  $w_{l,o}$  at the crystal was 17 X 33  $\mu\text{m}$  while the laser beam focussed on the SESAM,  $w_{SESAM}$  was 55  $\mu\text{m}$ . This  $w_{SESAM}$  was found to be the optimum beam waist incident on the SESAM that produced the shortest pulse duration,  $\tau_p$  as mentioned already in section 4.9.

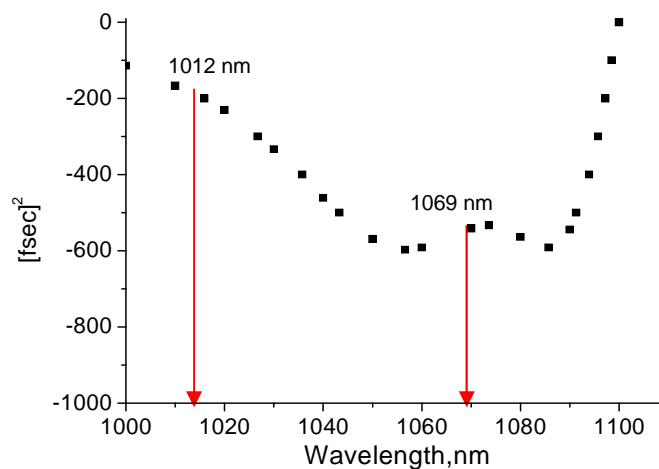


Figure 5.10. Measured negative group delay dispersion of  $-455 \pm 200 \text{ fs}^2$  in the first chirped mirror for the wavelength range of 1012-1069 nm [see Appendix A].

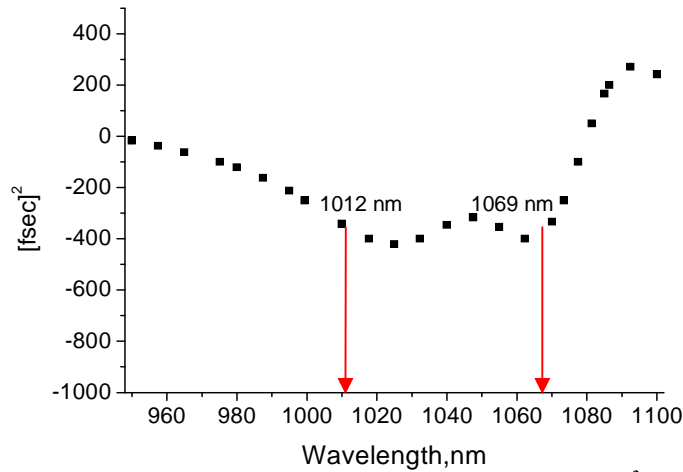


Figure 5.11. Measured negative group delay dispersion of  $-370 \pm 50 \text{ fs}^2$  in the second chirped mirror for the wavelength range of 1012-1069 nm [see Appendix B]

From previous assessment carried out in Chapter 4 [see section 4.8], positive GDD introduced by the optical elements was estimated to be  $\sim 300 \text{ fs}^2$  by neglecting the dispersion implied between the air path. This gives a general idea about the combination of chirped mirrors that need to be incorporated into the passive mode locking set up. Three types of chirped mirrors were used instead of a single prism for dispersion control scheme. The mirror structures of these devices were similar to the simple dielectric chirped mirror as shown in figure 5.4 where their negative dispersion profiles are shown in figures 5.10, 5.11 and 5.12.

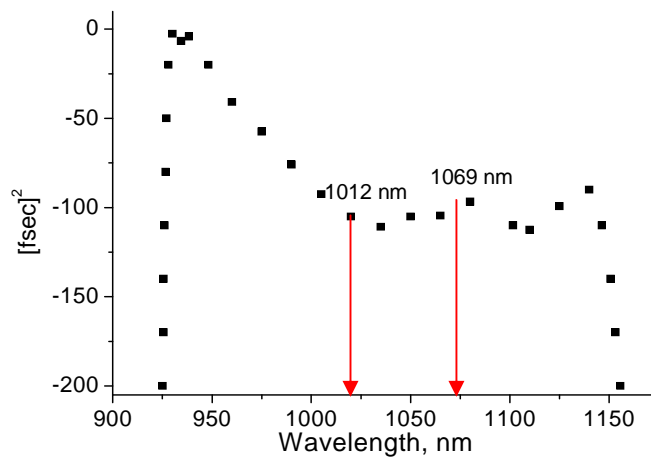


Figure 5.12. Measured negative group delay dispersion of  $-110 \pm 20 \text{ fs}^2$  in the third chirped mirror for the wavelength range of 1012-1069 nm [see Appendix C].

These chirped mirrors can only compensate for the group delay dispersion while the higher-order dispersions such as third-order and fourth-order dispersion can be neglected in the pulse width regime of operation. All of these chirped mirrors exhibited

high reflectivity of  $> 99.9\%$  at laser wavelengths between 960 to 1200 nm and offered negative dispersion values of  $-455 \pm 200 \text{ fs}^2$ ,  $-370 \pm 50 \text{ fs}^2$  and  $-110 \pm 20 \text{ fs}^2$  for the laser centre wavelengths between 1012 nm to 1069 nm. The original graphs that demonstrate transmission, reflection and dispersion profiles of these chirped mirrors manufactured by Layertec GmbH are shown in appendices A, B and C.

The main objective in this part of my project was to implement an optimised dispersion compensation scheme based on chirped mirrors that would be compatible with a compact cavity design. Three combinations of chirped mirrors [figure 5.9] were assessed. For combination one, a double reflection of the laser beam took place between chirped mirrors 1 and 2 that had negative dispersions of  $-455 \text{ fs}^2$  and  $-370 \text{ fs}^2$ . For combination two, only a single bounce was reflected between these two mirrors while for combination three a single bounce was reflected between chirped mirrors having negative dispersions of  $-455 \text{ fs}^2$  and  $-110 \text{ fs}^2$ .

### 5.5 Prismless-cavity Results ( $-455 \text{ fs}^2 \times 2$ , $-370 \text{ fs}^2 \times 2$ ).

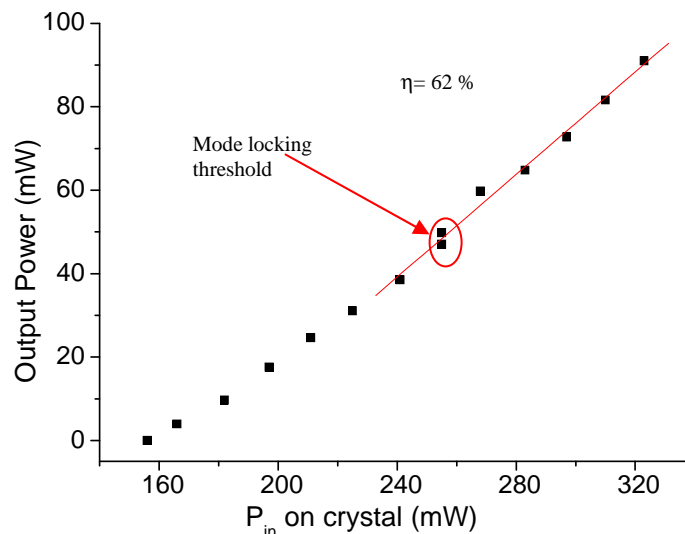


Figure 5.13. Slope-efficiency of the laser during the passive mode locking operation.

The first assessment was carried out with the double bounces between two chirped mirrors having negative dispersions of  $-455 \text{ fs}^2$  and  $-370 \text{ fs}^2$  [figure 5.9]. After a self-starting mode-locked operation was produced, the slope efficiency and laser threshold were measured during femtosecond operation. The slope efficiency obtained during this operation was 62 % as shown in figure 5.13 while the mode locking threshold was satisfied for a pump power of 255 mW at which the average output power from the mode-locked

laser was 50 mW. This corresponds to an intracavity average power  $P_{int,r}$  of 1.7 W and a threshold pulse energy of 7.9 nJ. In addition, the pulse fluence on the SESAM to reach the mode locking threshold was calculated to be  $83 \mu\text{J}/\text{cm}^2$  which was slightly above the saturation fluence of the SESAM of  $70 \mu\text{J}/\text{cm}^2$ . Once threshold had been established the laser output power increased linearly as a function of pump power incident on the crystal.

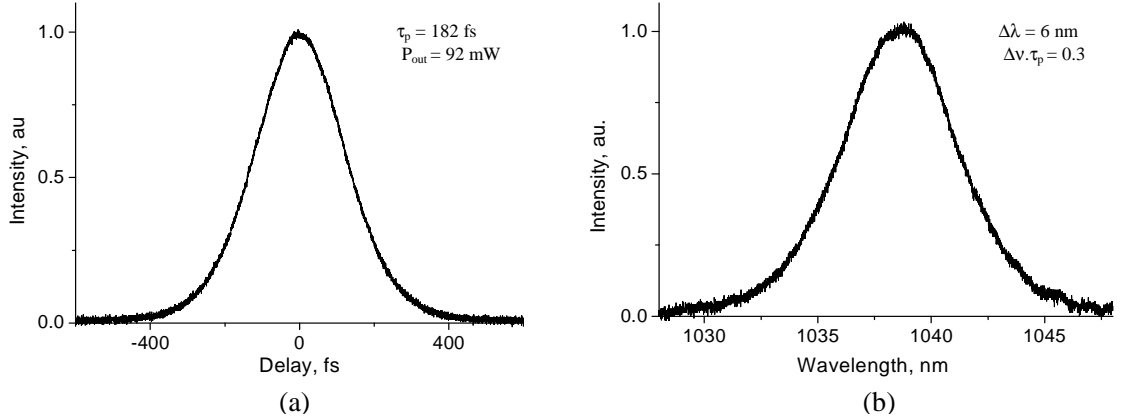


Figure 5.14. (a) A pulse duration of 182 fs and (b) the corresponding optical spectrum of pulses at 1038 nm from a mode-locked Yb:KYW laser.

The next step was to measure the pulse duration by using an autocorrelator based on second harmonic generation using an instrument purchased from Femtochrome Research, Inc. With negative group delay dispersion of approximately  $1600 \text{ fs}^2$ , a pulse duration of 182 fs with a nearly transform limited product of 0.3 was obtained at 1038 nm [figure 5.14]. The spectral width was 6 nm and the gain bandwidth,  $\Delta\nu$  of the laser was 1.7 THz. The maximum output power was 92 mW and this corresponds to an optical-to-optical efficiency of 28 %. In addition, the intracavity average power was deduced to be 3.1 W while the peak power exiting this laser was 2.4 kW. On the basis of these results and with expectations to produce shorter pulse durations  $\tau_p$ , higher optical-to-optical efficiency ( $\eta > 28 \%$ ), and higher peak power operation, further experiments were carried out by reducing the amount of negative dispersion needed for intracavity compensation.

## 5.6 Improvement of Prismless-cavity Results (-455 fs<sup>2</sup> X 1, -370 fs<sup>2</sup> X 1).

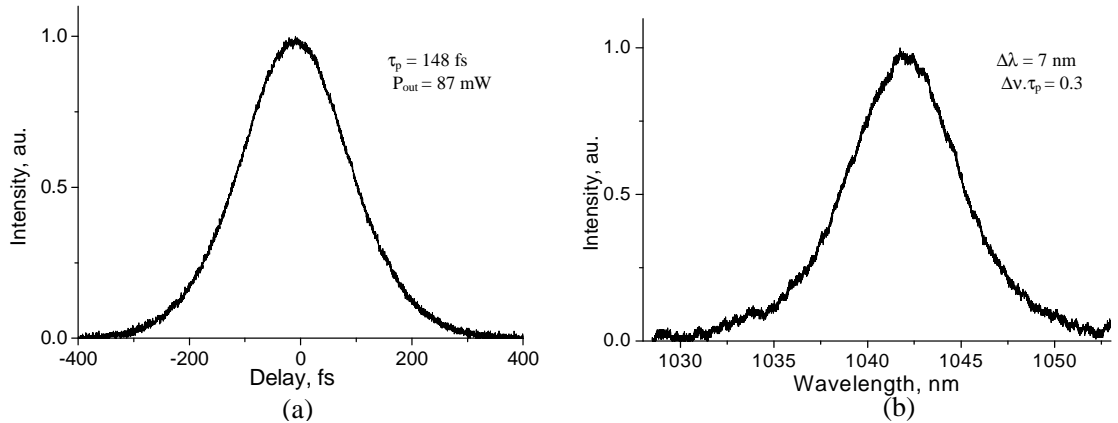


Figure 5.15. (a) A pulse duration of 148 fs and (b) the corresponding optical spectrum of pulses at 1042 nm from a mode-locked Yb:KYW laser.

In this assessment, the laser reflection was reduced to a single bounce between the two chirped mirrors of -455 fs<sup>2</sup> and -370 fs<sup>2</sup> mentioned previously. The precise control of the cavity configuration, especially the length between mirror 2 and the SESAM was adjusted to produce a self-starting mode-locked beam. With negative group delay dispersion of approximately 823 fs<sup>2</sup>, a pulse duration of 148 fs with a nearly transform limited product of 0.3 was obtained at 1042 nm. The maximum output power was 87 mW while the spectral width of 7 nm implies a lasing bandwidth,  $\Delta\nu$  of 1.9 THz. With the objective to further reduce the pulse duration obtained from this laser set up, the subsequent studies were carried out to optimize the net negative dispersion needed for compensation inside the laser cavity.

## 5.7 Optimisation of Dispersion Compensation inside the Laser Oscillators (-455 fs<sup>2</sup> X 1, -110 fs<sup>2</sup> X 1).

While retaining a single bounce on both mirrors, chirped mirror 2 was substituted with one having a negative dispersion of 110 fs<sup>2</sup> as shown in figure 5.9. With the negative dispersion of this mirror combination of approximately 590 fs<sup>2</sup>, a nearly transform-limited pulse of 0.33 was obtained with a pulse duration of 187 fs at 1042 nm as shown in figure 5.16. The spectral width of 6.5 nm implies a lasing bandwidth,  $\Delta\nu$  of 1.8 THz. The maximum output power was 110 mW and this corresponds to an optical-to-optical

efficiency of 34 % that is comparable to the efficiency obtained in previous work reported by Lagatsky and co-workers [37].

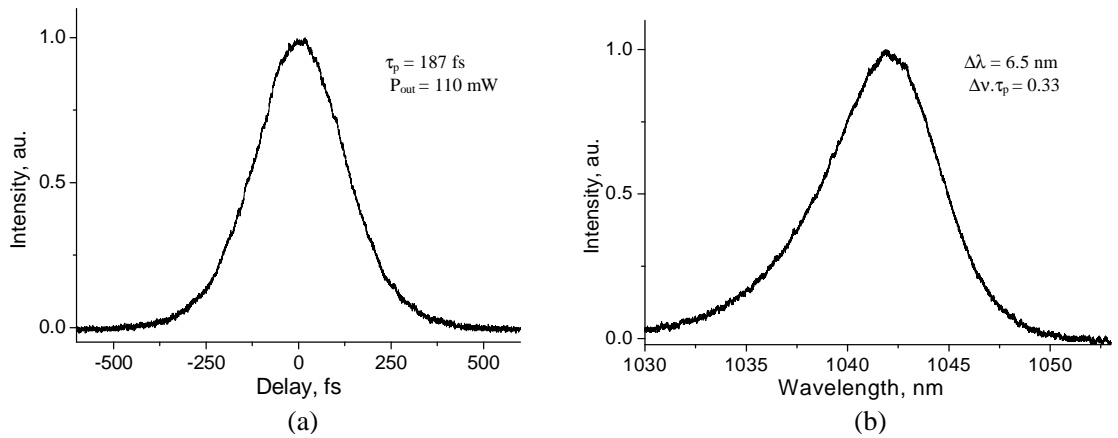


Figure 5.16. (a) A pulse duration of 187 fs and (b) the corresponding optical spectrum of pulses at 1042 nm from a mode-locked Yb:KYW laser.

In addition, the average power inside the laser oscillator was 3.7 W which implies a pulse fluence incident on the SESAM of  $183 \mu\text{J}/\text{cm}^2$  compared to the saturation fluence of the SESAM of  $70 \mu\text{J}/\text{cm}^2$ . The increase in efficiency for this observed passive mode locking compared to that of 29 % when a single prism was used (see section 4.9) can be attributed to the reduced intracavity losses in the dispersive mirrors. The electrical-to-optical efficiency was up to 15 % which was almost 3-4 times higher than that reported in a diode-pumped femtosecond Cr:LiSAF laser [38]. This can be explained in terms of the smaller quantum defect fraction of  $\sim 0.04$  in Yb:KYW crystal which reduces the energy difference released as heat dissipation between the absorbed pumped power to the emitted output power from the laser. A nearly diffraction-limited pumping technique and a low-loss SESAM for mode locking can also contribute to the excellent performance of this laser.

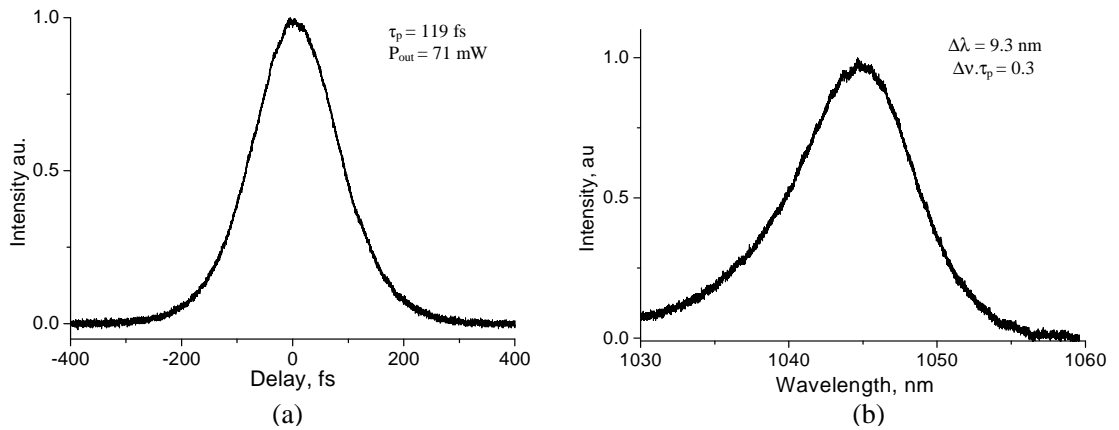


Figure 5.17. (a) A pulse duration of 119 fs and (b) the corresponding optical spectrum of pulses at 1045 nm from a mode-locked Yb:KYW laser.

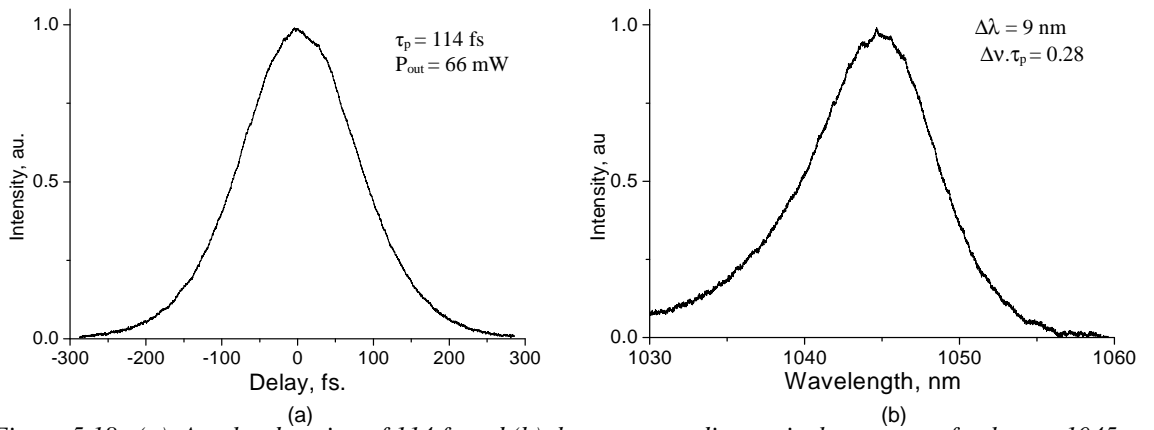


Figure 5.18. (a) A pulse duration of 114 fs and (b) the corresponding optical spectrum of pulses at 1045 nm from a mode-locked Yb:KYW laser.

In further measurements, a pulse duration as short as 119 fs was obtained at 1045 nm with a nearly transform-limited product around 0.3 as presented in figure 5.17. However, a more careful alignment between the cavity lengths led to the production of a slightly shorter pulse duration of 114 fs at 1045 nm [figure 5.18]. This is the shortest pulse duration produced to date from this cavity configuration with an average output power of 66 mW that corresponds to a high peak power of 2.7 kW. In addition, the spectral width was 9 nm that implies a lasing bandwidth,  $\Delta\nu$  of 2.5 THz. An interesting issue arose due to the implied duration-bandwidth product of 0.28 as distinct from 0.32 that applies to an ideal  $\text{sech}^2$  profile. This will be discussed briefly in section 5.9. Shorter pulse durations with more broadened spectral widths obtained in this assessment were due to the increase in the negative dispersion up to  $\sim 626$  fs<sup>2</sup> which I believe to be closer to the optimum for this laser cavity. In fact, from all of these measurements it was observed that the optimum negative group delay dispersion needed for intracavity dispersion compensation was between 590 and 630 fs<sup>2</sup>. This ascertains that positive GDD induced by the air path was between 300 to 330 fs<sup>2</sup> which was comparable to the value introduced by the optical elements in the laser oscillator [see section 4.9].

## 5.8 Optimisation of the Laser Configuration.

In this experimental set up [figure 5.19], more powerful pump sources with a combined output power of 926 mW were used as a scaling up of the pump power of 351 mW used for the arrangement illustrated in figure 5.9. The pump sources (LD1 and LD2) used to

pump the gain material were a single mode fibre-coupled polarization-maintaining InGaAs diode laser (supplied by JDS Uniphase) emitting at 981 nm with the laser reflection from the crystal of  $\sim 5.6\%$ . The cavity length was designed to provide a pulse repetition rate of 149 MHz, using almost similar optical elements to that shown in figure 5.9.

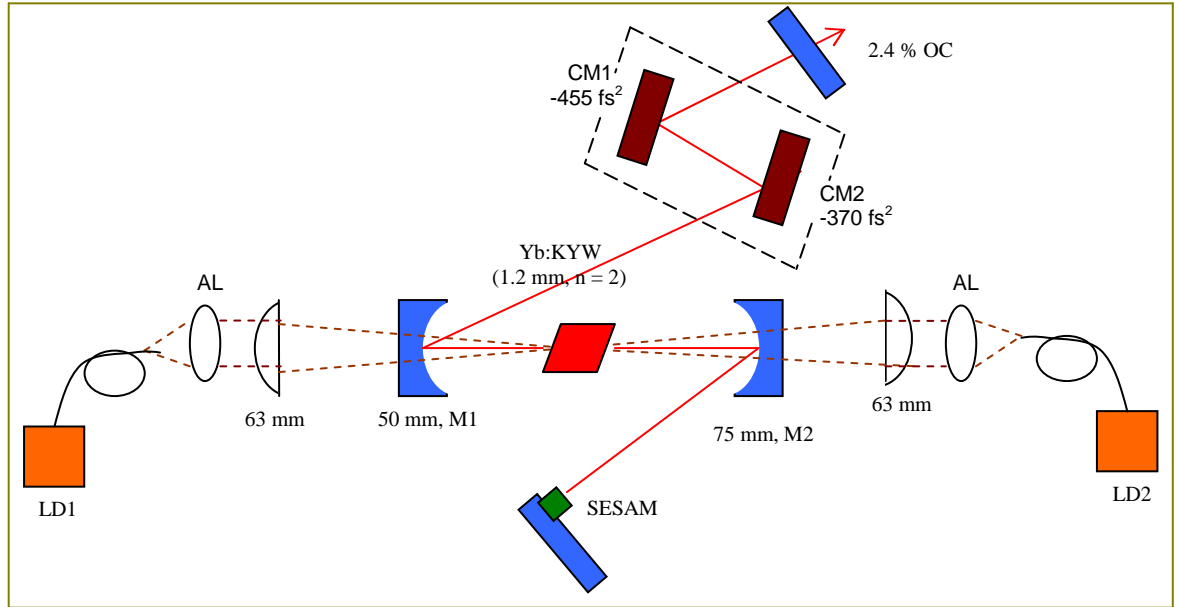


Figure 5.19. An overall schematic diagram of a femtosecond Yb:KYW laser that incorporates chirped mirrors CM1 and CM2 for dispersion compensation.

Mirror 2 (M2) had a 75 mm radius of curvature, the output coupler (OC) had a transmission of 2.4 % at 1064 nm while mirror 1 (M1), the SESAM and the gain material were as before. From the ABCD matrix formalism, the laser beam waist  $w_{l,o}$  focussed on the crystal was  $18 \times 36 \mu\text{m}$  while the laser beam focussed on the SESAM  $w_{SESAM}$  had a spot of  $125 \mu\text{m}$  which was the optimum beam waist for the mode locking operation.

From the previous assessments, the net negative dispersion required to compensate for the material dispersion inside the laser oscillator had been determined approximately. Thus, from this experiment a single bounce of laser was reflected between the two chirped-mirrors CM1 and CM2 having negative dispersion values of  $-455 \text{ fs}^2$  and  $-370 \text{ fs}^2$ . The objective of this follow-up work was to produce shorter pulse durations from the Yb:KYW laser and to compare the results with the previous observations.

## 5.9 Prismless-cavity Results (-455 fs<sup>2</sup> X 1, -370 fs<sup>2</sup> X 1).

Following an optimisation of the overall setup and especially the precise separation between mirror 2 and SESAM, a pulse duration of 157 fs with a nearly transform-limited product of 0.29 was obtained at 1042 nm as shown in figure 5.20. The negative group delay dispersion needed for compensation at this centre wavelength was  $\sim 823$  fs<sup>2</sup> while the spectral width was 6.8 nm which implies a lasing bandwidth,  $\Delta\nu$  of 1.9 THz. In addition, the maximum output power produced from this system was 323 mW, which corresponds to a high peak power of 13.8 kW and an optical-to-optical efficiency of 37 %. This slight increase in laser efficiency compared to that of the previous assessment ( $\sim 34$  %) in section 5.7 during femtosecond operation could be attributed to the higher pump power sources that increase the nonlinear effects as shown in figure 2.11. The intracavity power was calculated to be 13.5 W while the energy pulse fluence incident on the SESAM was 184  $\mu\text{J}/\text{cm}^2$  which was similar to that obtained in the earlier work [section 5.7] for the maximum average output power. In contrast to this pulse that had a lower bandwidth-product than 0.32, a more ideal  $\text{sech}^2$  pulse shape of 0.31 was produced with a longer pulse duration of 179 fs at 1042 nm as presented in figure 5.21.

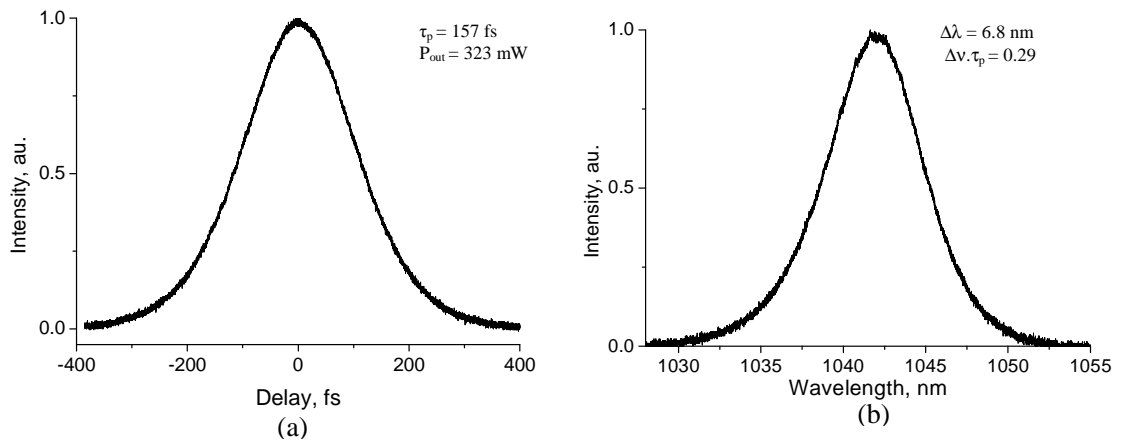


Figure 5.20. (a) A pulse duration of 157 fs and (b) the corresponding optical spectrum of pulses at 1042 nm from a mode-locked Yb:KYW laser.

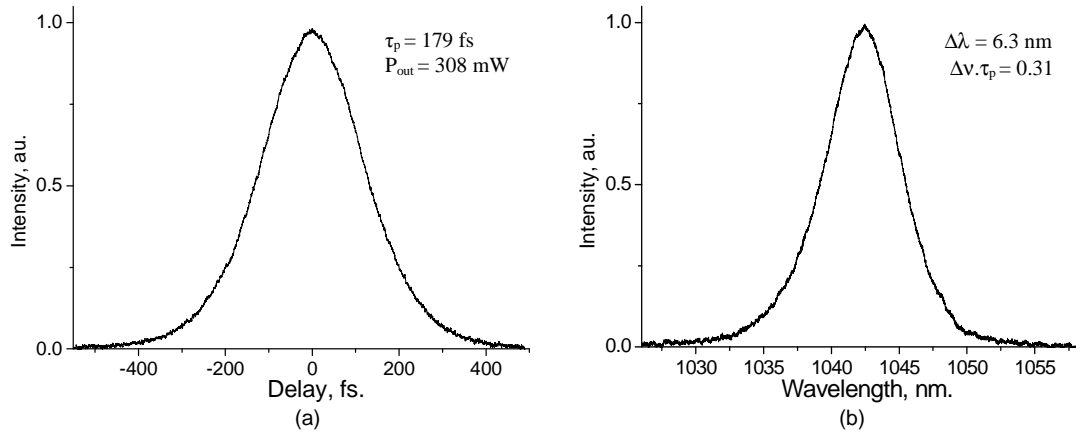


Figure 5.21. (a) A pulse duration of 179 fs and (b) the corresponding optical spectrum of pulses at 1042 nm from a mode-locked Yb:KYW laser.

In this final assessment, a pulse duration as short as 100 fs with a nearly transform-limited product of 0.31 was obtained at 1054 nm as shown in figure 5.22 below. This is comparable to the earlier report that had a measured duration of 101 fs centred at 1046 nm [39]. The average output power was 231 mW that corresponds to a peak power of 15.5 kW while the spectral width of 11.5 nm implies a lasing bandwidth,  $\Delta\nu$  of 3.1 THz. Interestingly, a pulse duration as short as 97 fs was produced around 1053 nm with a nearly transform-limited product of 0.3 as demonstrated in figure 5.23. At a centre wavelength of 1052 nm, the pulse duration from the laser beam was further compressed to 90 fs with a duration-bandwidth product of 0.27 as demonstrated in figure 5.24. This is the shortest pulse duration reported to date from a SESAM-assisted Yb:KYW laser. The average output power was 215 mW that corresponds to a peak power of 16 kW. The spectral width was then measured to be 11.3 nm that implies a lasing bandwidth,  $\Delta\nu$  of 3 THz. For these three measurements, the output wavelengths emitting from this laser should be similar, however, the reduction in these recorded parameters was due to some difficulties in the characterization of these shorter pulses. In addition, shorter pulse durations in the sub-100 fs regimes with more broadened spectral widths obtained in this assessment were due to the optimization of the negative dispersion up to  $\sim 903$  fs<sup>2</sup> provided by the dispersive mirrors. It is perhaps worth mentioning here that these pulse peak powers between 15 and 16 kW at lower average output powers of less than 250 mW could probably be useful for biological, and medical applications in this spectral region.

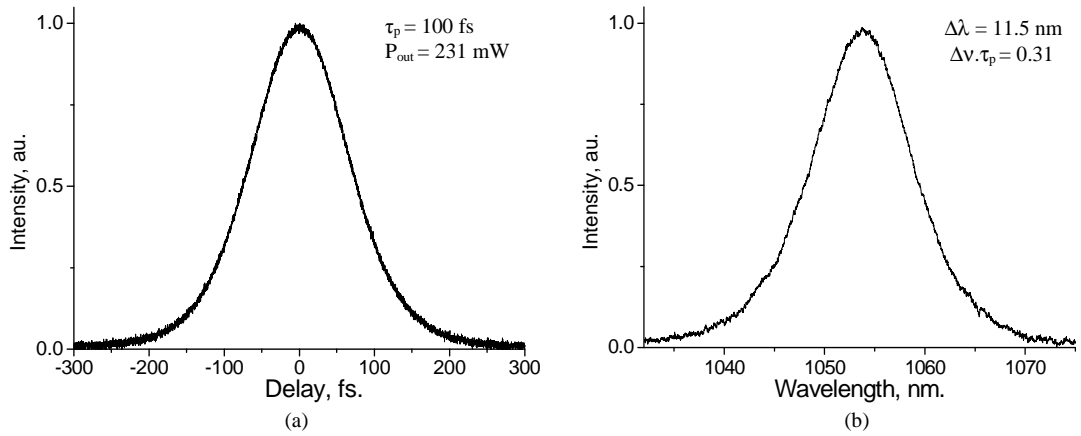


Figure 5.22. (a) A pulse duration of 100 fs and (b) the corresponding optical spectrum of pulses at 1054 nm from a mode-locked Yb:KYW laser.

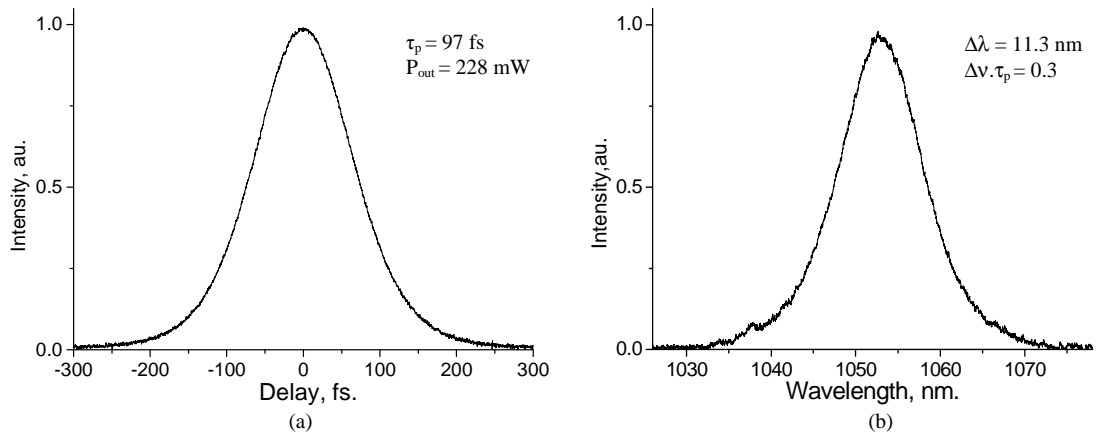


Figure 5.23. (a) A pulse duration of 97 fs and (b) the corresponding optical spectrum of pulses at 1053 nm from a mode-locked Yb:KYW laser.

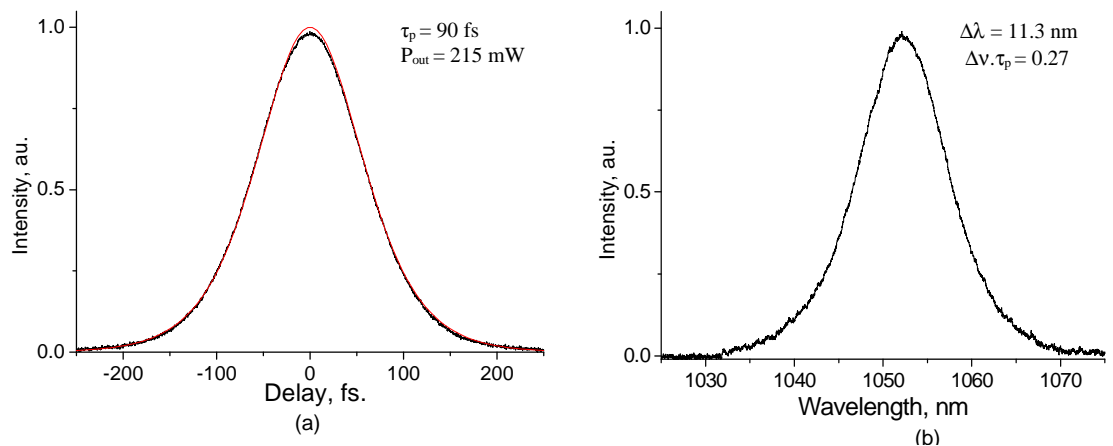


Figure 5.24. (a) A nonlinear  $\text{sech}^2$  curve fit for a pulse duration of 90 fs and (b) the corresponding optical spectrum of pulses centred at 1052 nm from a mode-locked Yb:KYW laser.

A brief analysis of the pulse shapes measured from this laser was carried out. For the pulse with a bandwidth product higher than 0.32, a longer duration that exhibits a chirp

in its frequency as shown in figure 2.13 was expected. In contrast, an ideal  $\text{sech}^2$  pulse shape with a transform-limited product of  $\approx 0.32$  exhibits an absence in the frequency chirp that leads to optimised reduction in the pulse duration for the available spectral bandwidth. This achievement ascertains the success of introducing a net negative dispersion for compensation in the laser oscillator. However, at specific spectral widths [figure 5.17, 5.18, 5.20-5.24] the mode-locked pulses were successfully obtained where the slightly longer durations were produced with a time-bandwidth product of  $\geq 0.3$  and the shortest possible durations were produced with a lower time-bandwidth product than that expected ( $\Delta\nu\tau_p < 0.3$ ). This eliminates any claim that suggests these latter pulses might imply the presence of some residual frequency chirp.

To determine the actual shape of these latter pulses, one of the temporal profile depicted in figure 5.24 was compared to the nonlinear curve of  $\text{sech}^2$ . It was found that this pulse fits the curve, thus, from the author's opinion a slight deviation from an ideal  $\text{sech}^2$  pulse shape might probably occur that explains the property of its lower duration-bandwidth product. This result indicates that further optimisation of efficient Kerr-lensing effect in the laser configuration lead to a slight evolution in the pulse shape formation. Owing to the lack of phase informations presented in the intensity autocorrelation technique, no evidence can be shown to make any firm conclusions. However, several techniques are recommended to eliminate suspicions existing within the autocorrelation data. These techniques are such as frequency-resolved optical gating (FROG) [40-42], dispersive propagation time-resolved optical gating (DP-TROG) [43] and spectral phase interferometry for direct electric-field reconstruction (SPIDER) [44-45] that can provide comprehensive intensity and phase informations without guessing the correct shape of the characterised ultrashort pulses.

Observation on the pulse durations as a function of wavelengths obtained in this assessment was also performed. At longer wavelengths, shorter pulse durations can be obtained as the laser beam penetrates deeper inside the chirped-mirror structure. This produces higher negative group delay dispersion compared to that of shorter wavelength for intracavity compensation of the material dispersion in the laser. It was observed from this last piece of work that the negative group delay dispersion needed for dispersion compensation inside the oscillators was between 800 to 900  $\text{fs}^2$ . Further research could therefore be carried out by designing a single chirped mirror that could satisfy the optimum specifications for dispersion compensation. If this could be integrated with the output

coupler and mirror 1 [figure 5.19] in a two element cavity, then this could form the basis for a compact laser design that would have reduced losses due to the minimum number of optical elements in the laser cavity.

## **5.10 Conclusion.**

The construction of Yb:KYW femtosecond lasers by using chirped dielectric mirrors for dispersion compensation instead of prisms has been successfully accomplished for the achievement of ultralow threshold and high efficiency in a relatively more compact configuration. It was observed that by optimising the dispersion compensation mechanism in the laser cavity, improvements in terms of optical-to-optical efficiency and pulse durations could be achieved. A slope efficiency of 62 % and an optical-to-optical efficiency of 37 % were obtained during optimised femtosecond operation of one of the Yb:KYW lasers. Pulse durations as short as 90 fs at 1052 nm were obtained which are the shortest duration reported to date for any SESAM-assisted mode-locked Yb:tungstate lasers. In addition to the optimised dispersion compensation mechanism, proper cleaning of the optical elements and the low intracavity loss of the chirped mirrors were also important to increase the intensity dependent refractive index of the optical Kerr effect that is responsible for the pulse shortening mechanism. Future work on this system could lead to even more impressive performance because options remain to increase the pulse repetition rate in a configuration having a reduced footprint and therefore compactness, scaling to higher power with more powerful pump laser diodes, and nonlinear frequency conversion to gain access to other spectral ranges.

## 5.11 References:

1. J. Aus Der Au, R. Paschotta, and U. Keller, "New technique for dispersion-compensation in compact femtosecond lasers," *Lasers and Electro-Optics, CLEO'99*, 459-460 (1999).
2. A. Stingl, Ch. Spielmann, and F. Krausz, "Chirped dielectric mirrors for dispersion control in femtosecond laser systems", *Proc. SPIE* **2377**, 11-21 (1995).
3. R. L. Fork, O. E. Martinez, and J. P. Gordon, "Negative dispersion using pairs of prisms," *Opt. Lett.* **9**, 150-152 (1984).
4. D. Kopf, G. J. Spuhler, K. J. Weingarten, and U. Keller, "Mode-locked laser cavities with a single prism for dispersion compensation," *Appl. Opt.* **35**, 912-915 (1996).
5. M. Ramaswamy-Paye and J. G. Fujimoto, "Compact dispersion-compensating geometry for Kerr-lens mode-locked femtosecond lasers," *Opt. Lett.* **19**, 1756-1758 (1994).
6. C. Spielmann, P. F. Curley, T. Brabec, and F. Krausz, "Ultrabroadband femtosecond lasers," *IEEE J. Quantum Electron.* **30**, 1100-1114 (1994).
7. CP. Huang, H. C. Kapteyn, J. W. McIntosh, and M. M. Murnane, "Generation of transform-limited 32-fs pulses from a self-mode-locked Ti:sapphire laser," *Opt. Lett.* **17**, 139-141 (1992).
8. F. Krausz, Ch. Spielmann, T. Brabec, E. Wintner, and A. J. Schmidt, "Generation of 33-fs optical pulses from a solid-state laser," *Opt. Lett.* **17**, 204-206 (1992).
9. P. F. Curley, Ch. Spielmann, T. Brabec, F. Krausz, E. Wintner, and A. J. Schmidt, "Operation of a femtosecond Ti:Sapphire solitary laser in the vicinity of zero group-delay dispersion," *Opt. Lett.* **18**, 54-56 (1993).
10. M. T. Asaki, CP. Huang, D. Garvey, J. Zhou, H. C. Kapteyn, and M. M. Murnane, "Generation of 11-fs pulses from a self-mode-locked Ti:sapphire laser," *Opt. Lett.* **18**, 977-979 (1993).
11. B. Proctor and F. Wise, "Generation of 13-fs pulses from a mode-locked Ti:Sapphire laser with reduced 3<sup>rd</sup>-order dispersion," *Appl. Phys. Lett.* **62**, 470-472 (1993).
12. A. Stingl, M. Lenzner, Ch. Spielmann, F. Krausz, and R. Szipocs, "Sub-10-fs mirror-dispersion-controlled Ti:Sapphire laser," *Opt. Lett.* **20**, 602-604 (1995).

13. N. Matuschek, F. X. Kartner, and U. Keller, "Theory of Double Chirped Mirrors," *IEEE J. Sel. Top. Quantum Electron.* **4**, 197-208 (1998).
14. F. X. Kartner, N. Matuschek, T. Schibli, U. Keller, H. Haus, C. Heine, R. Morf, V. Scheuer, M. Tilsch, and T. Tschudi, "Design and fabrication of double-chirped mirrors," *Opt. Lett.* **22**, 831-833 (1997).
15. R. Paschotta, "Encyclopedia of laser physics and technology," [http://www.rp-photonics.com/bragg\\_mirrors.html](http://www.rp-photonics.com/bragg_mirrors.html).
16. S. De Silvestri, P. Laporta, and O. Svelto, "Analysis of quarter-wave dielectric-mirror dispersion in femtosecond dye-laser cavities," *Opt. Lett.* **9**, 335-337 (1984).
17. E. Mayer, J. Mbius, A. Euteneuer, W. Rhle, and R. Szipocs, "Ultrabroadband chirped mirrors for femtosecond lasers," *Opt. Lett.* **22**, 528-530 (1997).
18. R. Szipocs, and A. Kohazi-Kis, "Theory and design of chirped dielectric laser mirrors," *Appl. Phys. B* **65**, 115-135 (1997).
19. R. Szipocs, K. Ferencz, C. Spielmann, and F. Krausz, "Chirped multilayer coatings for broadband dispersion control in femtosecond lasers," *Opt. Lett.* **19**, 201-203 (1994).
20. A. Kasper and K. J. Witte, "10-fs pulse generation from a unidirectional Kerr-lens mode-locked Ti:Sapphire ring laser," *Opt. Lett.* **21**, 360-362 (1996).
21. L. Xu, C. Spielmann, F. Krausz, and R. Szipocs, "Ultrabroadband ring oscillator for sub-10-fs pulse generation," *Opt. Lett.* **21**, 1259-1261 (1996).
22. I. Sorokina, E. Sorokin, E. Wintner, A. Cassanho, H. Jenssen, and R. Szipocs, "Prismless passively mode-locked femtosecond Cr:LiSGaF laser," *Opt. Lett.* **21**, 1165-1167 (1996).
23. I. Sorokina, E. Sorokin, E. Wintner, A. Cassanho, H. Jenssen, and R. Szipocs, "Sub-20 fs pulse generation from the mirror dispersion controlled Cr:LiSGaF and Cr:LiSAF lasers," *Appl. Phys. B* **65**, 245-253 (1997).
24. J. Hebling, E. J. Mayer, J. Kuhl, and R. Szipocs, "Chirped-mirror dispersion-compensated femtosecond optical parametric oscillator," *Opt. Lett.* **20**, 919-921 (1995).
25. Ch. Spielmann, M. Lenzner, F. Krausz, and R. Szipocs, "Compact, high-throughput expansion-compression scheme for chirped pulse amplification in the 10 fs range," *Opt. Commun.* **120**, 321-324 (1999).
26. D. Strickland and G. Mourou, "Compression of amplified chirped optical pulses," *Opt. Commun.* **56**, 219-221 (1985).

27. R. L. Fork, C. Brito Cruz, P. Becker, and C. Shank, "Compression of optical pulses to six femtoseconds by using cubic phase compensation," *Opt. Lett.* **12**, 483-485 (1987).
28. M. Nisoli, S. Stagira, S. De Silvestri, O. Svelto, S. Sartania, Z. Cheng, M. Lenzner, Ch. Spielmann, and F. Krausz, "A Novel high energy pulse compression system generation of multigigawatt sub-5 fs pulses," *Appl. Phys. B* **65**, 189-196 (1997).
29. A. Baltuska, Z. Wei, M. S. Pshenichnikov, D. A. Wiersma, and R. Szipocs, "All-solid-state cavity dumped sub-5 fs laser," *Appl. Phys. B* **65**, 175-188 (1997).
30. F. Gires and P. Tournois, "Interferometre utilisable pour la compression D'impulsions lumineuses modulees en frequence," *C. R. Acad. Sci. Paris* **258**, 6112-6115 (1964).
31. N. Matuschek.; F. X. Kartner; and U. Keller, "Analytical design of double-chirped mirrors with custom-tailored dispersion characteristics," *IEEE J. Quantum Electron.* **35**, 129-137 (1999).
32. N. Matuschek.; F. X. Kartner; and U. Keller, "Exact coupled-mode theories for multilayer interference coatings with arbitrary strong index modulations," *IEEE J. Quantum Electron.* **33**, 295-302 (1997).
33. R. Ell, U. Morgner, F. X. Kartner, J. G. Fujimoto, E. P. Ippen, V. Scheuer, G. Angelow, T. Tschudi, M. J. Lederer, A. Boiko, and B. Luther-Davies, "Generation of 5-fs pulses and octave-spanning spectra directly from a Ti:sapphire laser," *Opt. Lett.* **26**, 373-375 (2001).
34. D. H Sutter, I. D. Jung, F. X. Kartner, N. Matuschek, F. Morier-Genoud, V. Scheuer, M. Tilsch, T. Tschudi, and U Keller, "Self-Starting 6.5-fs pulses from a Ti:Sapphire laser using a semiconductor saturable absorber and double chirped-mirrors," *IEEE J. Quantum Electron.* **4**, 169-178 (1998).
35. R. Paschotta, G. J. Spühler, D. H. Sutter, N. Matuschek, U. Keller, M. Moser, R. Hövel, V. Scheuer, G. Angelow, and T. Tschudi, "Double-chirped semiconductor mirror for dispersion compensation in femtosecond lasers," *Appl. Phys. Lett.* **75**, 2166-2168 (1999).
36. F. X Kartner; I. D Jung; and U Keller, "Soliton mode-locking with saturable absorbers," *IEEE J. Quantum Electron.* **2**, 540-556 (1996).
37. A. A. Lagatsky, E. U. Rafailov, C. G. Leburn, C. T. A. Brown, N. Xiang, O. G. Okhotnikov, and W. Sibbett, "Highly efficient femtosecond Yb:KYW laser pumped by a single narrow-stripe laser diode," *Electron. Lett.* **39**, 1108-1110 (2003).

38. B. Agate, B. Stormont, A. J. Kemp, C. T. A. Brown, U. Keller, and W. Sibbett, "Simplified cavity designs for efficient and compact femtosecond Cr:LiSAF lasers," *Opt. Commun.* **205**, 207-213 (2002).
39. P. Klopp, V. Petrov, U. Griebner, and G. Erbert, "Passively mode-locked Yb:KYW laser pumped by a tapered diode laser," *Opt. Express* **10**, 108-113(2002).
40. D. J. Kane and R. Trebino, "Characterization of arbitrary femtosecond pulses using frequency-resolved optical gating," *IEEE J. Quantum Electron.* **29**, 571-579 (1993).
41. D. J. Kane and R. Trebino, "Single-shot measurement of the intensity and phase of an arbitrary ultrashort pulse by using frequency-resolved optical gating," *Opt. Lett.* **18**, 823-825, (1993).
42. D. J. Kane and R. Trebino, "Using phase retrieval to measure the intensity and phase of ultrashort pulses- frequency-resolved optical gating," *J. Opt. Soc. Am. A-Opt. Image Science and Vision* **10**, 1101-1111 (1993).
43. I. G. Cormack, W. Sibbett, and D. T. Reid, "Practical measurement of femtosecond optical pulses using time-resolved optical gating," *Opt. Commun.* **194**, 415-424 (2001).
44. C. Iaconis and I. A. Walmsley, "Spectral phase interferometry for direct electric-field reconstruction of ultrashort optical pulses," *Opt. Lett.* **23**, 792-794 (1998).
45. C. Iaconis, and I. A. Walmsley, "Self-referencing spectral interferometry for measuring ultrashort optical pulses," *IEEE J. of Quantum Electron.* **35**, 501-509 (1999).

## Chapter 6

### **Yb<sup>3+</sup>-doped YVO<sub>4</sub> Crystal for Efficient Kerr-lens Mode Locking in Solid-State Lasers.**

#### **6.1 Introduction.**

In this chapter Kerr-lens mode locking of a Yb:YVO<sub>4</sub> laser in a compact 3-mirror cavity is introduced through the exploitation of intensity dependent nonlinear refractive index of the gain medium,  $n_2$ . This value can be assessed through the z-scan technique where a high value of  $n_2$  in Yb:YVO<sub>4</sub> compared to that obtained in Ti:sapphire and other Yb-doped crystals contributes to stronger Kerr-lensing and self-phase modulation effects. These features reinforce the potential of this material for producing shorter femtosecond pulses in low threshold, compact and highly efficient configurations. The main objective in investigating this material for femtosecond lasers is to find an alternative source to Yb:YAG for high peak power operation. This can be met because Yb:YVO<sub>4</sub> has broad gain bandwidth and good thermal conductivity properties. A few analysis based on several qualities that influence the lasing performance are discussed. These include spectroscopic parameters such as saturation intensity, threshold power and slope efficiency. Other beneficial laser parameters for the efficient Kerr-lens mode-locking operation are the use of high intensity diffraction-limited pump source, laser cavity design and appropriate pump/laser mode overlap. The optimisation of laser cavity design leads to the formation of high beam quality output pulses with  $M^2 \approx 1$ . This research provides a basis for exploration of this femtosecond laser for many industrially and scientifically orientated applications. These include the pumping of optical parametric oscillators/amplifiers, high power thin disk lasers and the generation of visible femtosecond optical pulses.

#### **6.2 Optical Kerr Effect in Isotropic Media.**

The refractive index  $n$  of optical materials [see section 2.3.1] for propagating radiation with an intensity having temporal and radial dependence of  $I(r,t)$  can be written as:-

$$n(r,t) = n_0 + n_2 I(r,t) \quad (6.2.1a)$$

and

$$n(r,t) = \sqrt{1 + \chi} \quad (6.2.1b)$$

where  $n_0$  and  $n_2$  are the linear and nonlinear refractive indices while  $\chi = \chi^{(1)} + \chi^{(3)}E(r,t)^2$  represents the dielectric susceptibility of a material. In an isotropic and centrosymmetric crystal  $\chi^{(2)} = 0$  and can therefore be neglected. By substituting the value of  $\chi$  into equation (6.2.1b), it can be shown that the refractive index of a material is given by:-

$$n(r,t) = \sqrt{1 + (\chi^{(1)} + \chi^{(3)}E(r,t)^2)} = \sqrt{n_0^2 + \chi^{(3)}E(r,t)^2} \quad (6.2.2a)$$

$$= \sqrt{n_0^2 \left( 1 + \frac{\chi^{(3)}E(r,t)^2}{n_0^2} \right)} \quad (6.2.2b)$$

For a small value of  $\chi$ , the equation  $\sqrt{1 + \chi} = 1 + \frac{\chi}{2}$ , and so equation (6.2.2b) can be rewritten as:-

$$n(r,t) = n_0 \left( 1 + \frac{\chi^{(3)}E(r,t)^2}{2n_0^2} \right) = n_0 + \frac{\chi^{(3)}E(r,t)^2}{2n_0} \quad (6.2.3)$$

In comparison with equation (6.2.1a), it can be shown that the value of the nonlinear refractive index  $n_2$  is:-

$$n_2 = \frac{\chi^{(3)}}{n_0^2 c \epsilon_0} \quad (6.2.4)$$

where the temporally and radially dependent intensity of the optical field  $I(r,t) = \frac{n_0 c \epsilon_0 E(r,t)^2}{2}$ . The unit for intensity  $I(r,t)$  is given as  $\text{W}/\text{cm}^2$  and it follows that the unit for  $n_2$  will be given as  $\text{cm}^2/\text{W}$ . By substituting the value of absolute permittivity  $\epsilon_0 = 8.8542 \times 10^{-8} \text{ Fcm}^{-1}$ , it is found that:-

$$n_2 \left( \frac{cm^2}{W} \right) = 0.0376 \times \frac{\chi^{(3)}(esu)}{n_0^2} \quad (6.2.5)$$

These equations explain how a weak positive lens can be generated within an optical material if the  $I(r,t)$  is sufficiently high. This is brought about through a physical process known as self-focusing effect.

### 6.3 Analysis of the Self-focusing Effect.

An intense beam propagating in a dielectric medium can exhibit some similarity with the physical process that applies in an optical waveguide. Self-trapping [1] of the beam can occur when the tendency to diverge due to diffraction is balanced by convergence due to a self-focusing effect. Consequently, when the tendency to converge due to nonlinear refraction is greater than that to diverge due to diffraction, self-focusing can be a dominating mechanism. This phenomenon occurs in the transverse propagation direction inside a solid-state medium and can be described as the optical Kerr-effect [see section 2.3.1] due to the intensity dependence of the refractive index. By assuming that the nonlinear refractive index  $n_2$  is positive, the higher refractive index at the centre of the beam in comparison to its surrounding region [figure 6.1] delays the wavefronts more in the centre and consequently creates a self-focusing effect. This can be compared directly to the refractive effects of a positive lens.

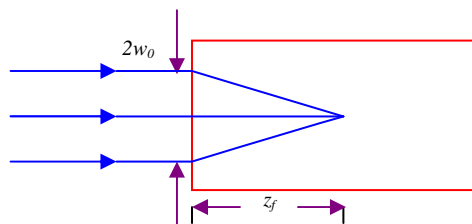


Figure 6.1. Self-focusing effect in a gain medium [2].

With the intensity of light:  $I = \frac{4P}{\pi.d^2}$  where  $P$  is the power and  $d$  is the diameter,

the critical power of the laser beam can be described as [2]:-

$$P_{cr} = \frac{\pi(1.22\lambda)^2}{8n_0n_2} \quad (6.3.1)$$

It is observed that  $P_{cr}$  is independent of laser beam diameter,  $d$  and the power of a laser beam rather than the intensity is the crucial parameter that determines the limitation to self-focusing. A more relevant definition of  $P_{cr}$  with the work discussed in this chapter can be explained as the upper limit of power that sets a limitation before a Gaussian beam eventually experiences catastrophic beam collapse. As a consequence, the peak power of the beam in KLM lasers has to be large enough to induce a suitable amount of nonlinearity but it should be below  $P_{cr}$  in a range of kW to MW to produce an exploitable self-focusing effect. In a thin slab, beam convergence leads to a focus outside the gain medium [see figure 2.6] while for a thicker slab, focusing can occur inside the gain medium [see figure 2.7 and 2.8] and this could result in optical damage during high power operation. For instance, in a tight-focusing geometry in a Ti:sapphire crystal,  $n_0$  is equal to 2.0,  $n_2$  is equal to  $3.1 \times 10^{-16}$  cm<sup>2</sup>/W and  $P_{cr}$  at a laser wavelength of 800 nm is 6 MW. An amplified mode locked laser with 10 nJ pulses and durations around 60 fs can produce a peak power of 166 kW which is below  $P_{cr}$ , thus leading to a useful self-focusing effect.

With the assumption that the laser beam has a Gaussian transverse intensity distribution, another important parameter to describe self-focusing effect is the distance  $z_f$ . This is defined as the distance from the input face to the focus created by the self-focused beam as shown in figure 6.1. The optical path length for the central ray is described as  $(n_0 + n_2 I)z_f$  while the optical path length for the outer ray is  $\left(n_0 + \frac{n_2 I}{2}\right)\sqrt{z_f^2 + w_0^2}$ . In the first part in the bracket of the latter formula,  $n_0 + \frac{n_2 I}{2}$  is the mean refractive index and its factor of  $\frac{1}{2}$  accounts to the fact that the nonlinear refractive index of the outer ray is smaller compared to the central one. According to the recommendation given by Fermat's principle, the optical path length for both the outer and central rays focused in a medium are equal, thus, by comparing both of these equations it is found that [2]:-

$$z_f \left( n_0 + \frac{n_2 I}{2} \right) \sqrt{1 + \frac{w_0^2}{z_f^2}} = z_f (n_0 + n_2 I) \quad (6.3.2)$$

From a Taylor expansion that implies  $\sqrt{1 + \mathcal{X}} = \left( 1 + \frac{\mathcal{X}}{2} + \dots \right)$ , so the equation above can be written as:-

$$\left( n_0 + \frac{n_2 I}{2} \right) \left( 1 + \frac{w_0^2}{2z_f^2} \right) = (n_0 + n_2 I) \quad (6.3.3a)$$

$$n_0 + \frac{n_0}{2} \left( \frac{w_0}{z_f} \right)^2 + \frac{n_2 I}{2} + \dots = n_0 + n_2 I \quad (6.3.3b)$$

The fourth term of the left hand side in equation (6.3.3b) above is very small and can be neglected. Thus, the simplification of this equation can be presented as:-

$$z_f = w_0 \sqrt{\frac{n_0}{n_2 I}} \quad (6.3.4)$$

By substituting  $I = \frac{P_{pk}}{\pi w_0^2}$ , gives:-

$$z_f = w_0^2 \sqrt{\frac{\pi n_0}{n_2 P_{pk}}} \quad (6.3.5)$$

This equation shows the relationship between  $z_f$  and  $P_{pk}$  (peak power) of the laser beam where  $z_f$  decreases as the  $P_{pk}$  increases. By comparing  $P_{cr}$  from equation (6.3.1) with equation (6.3.5), it can be shown that:-

$$z_f = w_0^2 \sqrt{\frac{\pi n_0}{n_2 P_{pk}}} \times \frac{\sqrt{P_{cr} \times P_{cr}}}{P_{cr}} \quad (6.3.6a)$$

$$= \frac{2n_0\sqrt{2}.w_0^2}{1.22\lambda} \times \sqrt{\frac{P_{cr}}{P_{pk}}} \quad (6.3.6b)$$

For the Ti:sapphire crystal as mentioned previously,  $n_0$  is equal to 2.0, and  $P_{cr}$  at laser wavelength of 800 nm is 6 MW. By taking  $w_0$  to be 50  $\mu\text{m}$ , the calculated value of  $z_f$  is 87 mm for an amplified mode locked laser at a peak power of 166 kW.

#### 6.4 The Measurement of the Nonlinear Refractive Index $n_2$ .

Mode locking based on the Kerr-lens effect [3] exploits the intensity dependent change in nonlinear refractive index of a gain medium to facilitate the generation of femtosecond pulses. Due to the absence of any physical saturable absorber (eg. SESAM), which can contribute to the additional intracavity losses, the Kerr-lens mode locking approach leads to an increase in optical-to-optical efficiency of a laser system during modelocking. The non-resonant nature of Kerr-lens produces a broader laser tunability that can support the direct generation of pulses having durations around a few femtoseconds and lends itself to a wide range of gain media in comparison to that of other mode locking techniques. The magnitude of  $n_2$  in a gain medium is a critical parameter that dictates the crystal's potential for efficient KLM laser operation.  $n_2$  also determines the overall KLM stability and the limitation for multipulse operation [4]. A higher value of  $n_2$  results in a larger change of refractive index in a gain medium that subsequently produces stronger Kerr-lensing and self-phase modulation effects. These features have been proven to be beneficial for the generation of shorter femtosecond pulses [5] with durations closer to the laser's spectral bandwidth limit. However, practical disadvantages associated with Kerr-lens mode locking (KLM) lasers include the requirement of critical cavity stability alignment and sensitivity to external perturbations.

Several techniques exist for the measurement of  $n_2$  in the gain materials such as nonlinear interferometry [6], degenerate four-wave mixing [7], nearly degenerate three-wave mixing [8], ellipse rotation [9], and beam-distortion measurements. Although the interferometric and wave-mixing techniques exhibit high sensitivity, they are less practical because of their need for complex instrumentation. On the other hand, the beam distortion

measurements need rigid beam scans followed by a complicated analysis of wave-propagation. The disadvantages of these techniques open up an alternative measurement approach that can provide a simple configuration but with high sensitivity. In this chapter, the z-scan technique [10], which can satisfy these requirements, is discussed briefly as the preferred technique to measure nonlinearity of several materials in the near-infrared and visible spectral regions.

Figure 6.2 shows a schematic diagram for conducting z-scan transmission measurements based on the transformation of phase to amplitude distortion during beam propagation in a laser material. The pump source [11,12] usually consists of a pulsed (nanosecond or picosecond) laser such as Nd:YAlO<sub>3</sub> or Ti:sapphire-pumped optical parametric amplifier. A 50-50 beam splitter is used to split the input beam into photodetectors D1 and D2. Photodetectors D1 and D2 are used to detect the incoming beam where the transmittance ratio D1/D2 is recorded as a function of the sample position  $z$ . The gain medium sample must have a thickness much thinner than the beam depth of focus. An aperture placed in front of D2 measures the far-field on axis transmission from the sample. Measurements are taken while the sample is translated from  $-z$  to  $+z$  positions and the subsequent transmission ratio is recorded to determine the magnitude of the nonlinear refractive index  $n_2$ .

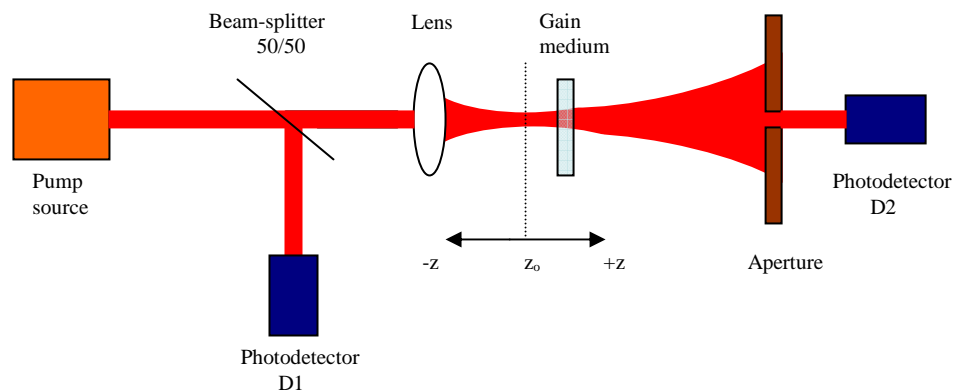


Figure 6.2. Simple z-scan experimental implementation where the transmittance ratio  $D_2/D_1$  is recorded as a function of the sample position  $z$  [10.]

The results obtained are plotted in a graph where the vertical axis is the normalized transmission while the horizontal axis is the sample position  $z$  as shown in figure 6.3. At  $z_0$ , the transmittance is normalized to unity while at  $z \neq z_0$ , the beam tends to converge due to self-focusing or to diverge due to diffraction depending on the magnitude of Kerr-lensing effect. As a consequence of the positive lensing mechanism in a medium, a valley

to peak feature is produced as the sample is moved from  $-z$  to  $+z$ . At  $z_0 - \delta z$ , a minimum transmission [figure 6.3 (a),(c)] is obtained as the gain medium behaves as a diverging lens which diverges the transmitted beam before passing through the aperture while at  $z_0 + \delta z$ , maximum transmission [figure 6.3 (b),(c)] is obtained as the gain medium behaves as a converging lens which focuses the beam before passing through the aperture. However, the opposite effects occur for negative lensing mechanism where a higher transmittance occurs at  $-z$  and a lower transmittance occurs at  $+z$ , thus generating a peak-to-valley feature.

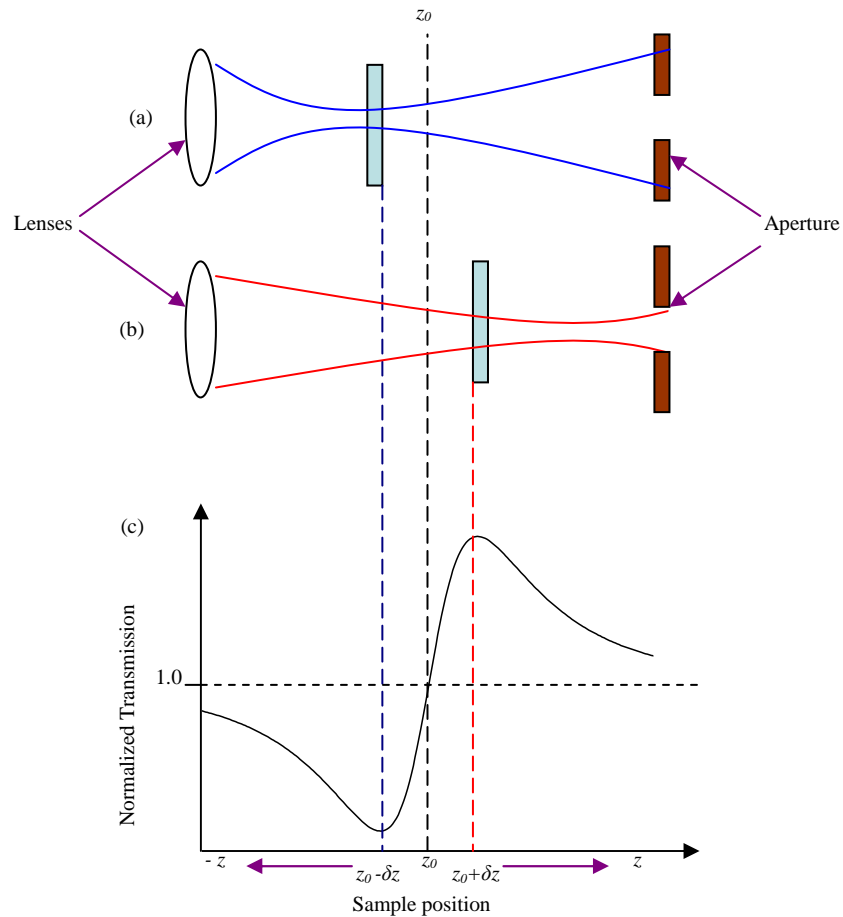


Figure 6.3. (a) Laser beam is diverged as the gain medium is placed at position  $z_0 - \delta z$ , while (b) the beam is converged when the gain medium is placed at position  $z_0 + \delta z$  and (c) is the corresponding valley to peak profile for positive lensing effects produced in the gain medium.

The magnitude of  $n_2$  can be determined from equation (6.2.1a) where the change in the time-averaged refractive index  $\Delta n_0(t)$  at a focus position is given as:-

$$\Delta n_0(t) = n_2 I_0(0, t) \quad (6.4.1)$$

where  $I_0(0,t)$  is the on-axis intensity at  $z = 0$ . The time-averaged phase shift of the laser field  $[\Delta\phi_0(t)]$  at the focus is then described as [10]:-

$$[\Delta\phi_0(t)] = \frac{2\pi}{\lambda} \Delta n_0(t) \frac{1 - e^{-\alpha l}}{\alpha} \quad (6.4.2)$$

where  $L_{eff} = \frac{1 - e^{-\alpha l}}{\alpha}$  is the effective length of the sample,  $l$  is the length of the sample,  $\lambda$  is the wavelength of the pump source and  $\alpha$  is the absorption coefficients of the gain medium. The relation between  $\Delta n_0(t)$  with  $\Delta\phi_0(t)$  can then be simplified as:-

$$\Delta n_0(t) = \frac{\lambda}{2\pi L_{eff}} [\Delta\phi_0(t)] \quad (6.4.3)$$

For a Gaussian pulse shape a factor of  $1/\sqrt{2}$  is introduced, so equation (6.4.1) can also be written as [11]:-

$$\Delta n_0(t) = \frac{\Delta n_0}{\sqrt{2}} \quad (6.4.4)$$

where  $\Delta n_0$  is the peak on-axis index change at the focus. When the z-scan technique was conducted on a Yb:KYW sample [11] at a pump source wavelength  $\lambda = 1.08 \mu\text{m}$ ,  $l = 1.5$  mm and  $\alpha = 3 \times 10^{-4} \text{ cm}^{-1}$ , the phase shift of the laser field  $[\Delta\phi_0(t)]$  was calculated to be 1.5.

The pump source emission wavelength was selected at a centre wavelength that was far from the peak absorption spectrum of the gain medium. This was done to ensure that the change in the laser beam propagation inside the medium was influenced primarily by the self-focusing mechanism rather through absorptive effects. Owing to the small value of  $\alpha$  ( $\sim 10^{-4} \text{ cm}^{-1}$ ),  $L_{eff}$  can be assumed to be similar to  $l$ , thus the value of  $\Delta n_0(t)$  obtained from this material was  $1.7 \times 10^{-4}$  while for  $\Delta n_0$  was  $2.4 \times 10^{-4}$ . With the peak

intensity  $I_0 = 280 \text{ GW/cm}^2$ , the  $n_2$  calculated for this crystal was  $8.7 \times 10^{-16} \text{ cm}^2/\text{W}$  [11]. A comparison of  $n_2$  for other laser materials is shown in table 6.1 below.

Table 6.1.  $n_2$  values for several laser materials [13].

Host	$n_2 (\times 10^{-16} \text{ cm}^2 / \text{W})$
Yb:GdCOB [Yb <sup>3+</sup> :Ca <sub>4</sub> GdO(BO <sub>3</sub> ) <sub>3</sub> ]	11.4
Yb:YCOB [Yb <sup>3+</sup> :Ca <sub>4</sub> YO(BO <sub>3</sub> ) <sub>3</sub> ]	9.0
Yb:BOYS [Yb <sup>3+</sup> :Sr <sub>3</sub> Y(BO <sub>3</sub> ) <sub>3</sub> ]	8.8
Yb:KYW [Yb <sup>3+</sup> :KY(WO <sub>4</sub> ) <sub>2</sub> ] [14]	8.7
Yb:KGW [Yb <sup>3+</sup> :KGd(WO <sub>4</sub> ) <sub>2</sub> ] [12]	20
Yb:YAG [Yb <sup>3+</sup> :Y <sub>3</sub> Al <sub>5</sub> O <sub>12</sub> ] [15]	6.2
Yb:Y <sub>2</sub> O <sub>3</sub> [15]	11.6
Ti:Sapphire [Ti <sup>3+</sup> :Al <sub>2</sub> O <sub>3</sub> ] [16]	3.1
Cr:F [Cr <sup>4+</sup> :MgSiO <sub>4</sub> ] [17]	6

From the table above it can be seen that most crystalline materials have a positive  $n_2$ . These values for the Yb-doped gain crystals are higher than that of Ti:sapphire ( $3.1 \times 10^{-16} \text{ cm}^2/\text{W}$ ) and Cr:Forsterite ( $6 \times 10^{-16} \text{ cm}^2/\text{W}$ ) which show their potential for efficient Kerr-lensing effects. Thus shorter pulse durations are possible for GdCOB/BOYS/YCOB materials due to their broader amplification bandwidth and high value of  $n_2$ . In addition,  $n_2$  is useful for diode pumped KLM lasers because the poor beam quality of laser diodes limits the minimum pump spot size inside the crystal.

The KLM technique has been applied successfully in lasers with Yb-doped gain media such as Yb:fluoride glass and Yb:KYW. The first attempt to self-mode lock Yb-doped fluoride phosphate glass [18] produced pulse durations of 160 fs at a centre wavelength of 1040 nm. The optical-to-optical efficiency with respect to the absorbed pump power was 21 % at a pulse repetition rate of 170 MHz. In a KLM Yb:KYW [19] laser end-pumped by two 1.6 W laser diodes, pulse durations of 71 fs were obtained at 1057 nm. The average output power was 120 mW while the pulse repetition frequency was 110 MHz. This is the shortest pulse duration obtained to date from any Yb-tungstate lasers. Further minimization on the device footprint of KLM Yb:KYW lasers [20] has produced near-transform-limited pulses of 107 fs at 1056 nm. The pulse repetition

frequency during this operation was 294 MHz. while the mode-locking threshold was satisfied for a pump power of 250 mW and the laser tunability was between 1042 to 1075 nm. This is the most efficient femtosecond laser in the world reported to date where the optical-to-optical efficiency is 53 %.

In high power lasers, the most critical issues are the control of heat dissipation and thermal conductivity in the crystal. The low quantum defect of Yb-doped materials ( $\leq 0.14$ ) [Table 2.2] results in the suitability of these materials for high power operation due to the reduction of heat dissipation while high thermal conductivity is important for the efficient removal of this heat from the gain media. Although shorter pulses ( $\leq 100$  fs) can be obtained from Yb-doped KYW, KGW, BOYS, and GdCOB [21-27] due to their broader amplification bandwidth ( $\geq 16$  nm), the lower thermal conductivity of these materials between 2-3 W/mK has severely restricted their capability in respect of high power outputs. The highest output power [28] obtained to date is from Yb:YAG femtosecond lasers that have a higher thermal conductivity of 6.8 W/mK. However, the narrow emission spectra of  $\sim 6$  nm from this crystal [29] places constraints on the pulse duration to  $\sim 700$ -800 fs for high power laser operation or to 340 fs for low power lasers [30]. Although, Yb:CaF<sub>2</sub> has similar thermal conductivity to Yb:YAG, the shortest pulse duration obtained to date is 150 fs [31]. These limitations have reinforced continuing research to find a new Yb-doped material that can satisfy a requirement for sub-100 fs pulse durations at high average output power levels.

## 6.5 A Yb<sup>3+</sup>:YVO<sub>4</sub> Laser.

Yttrium vanadate (YVO<sub>4</sub>) [32] is a uniaxial crystal that has broad transparency region from 0.4 to 5  $\mu\text{m}$ . This crystal is non-hygroscopic with a Mohs hardness factor of 5, and a thermal expansion coefficient  $\beta_c$  of  $11.37 \times 10^{-6} \text{ K}^{-1}$ . As a consequence of its strong birefringence property ( $\Delta n = 0.225 @ 633 \text{ nm}$ ), it has a wide range of applications in isolators, circulators, polarisers and beam displacers. YVO<sub>4</sub> has been doped with rare earth ions (Nd, Er, Tm, Ho, Yb) [32,33] and these crystals when used as gain media have supported efficient laser operation with large absorption and emission cross-sections in the near-infrared spectral region. These lasers, for instance, Nd:YVO<sub>4</sub> have a wide range of applications especially in microchip and thin-disc laser operation [34]. In Yb:YVO<sub>4</sub>, the

$\text{Yb}^{3+}$  ion substitutes for the  $\text{Y}^{3+}$  which is bonded to triply charged vanadate ions  $(\text{VO}_4)^{3-}$ . This crystal can be grown by use of the Czochralski technique which accommodates the doping concentration of up to 18 % of  $\text{Yb}^{3+}$  ions [35].

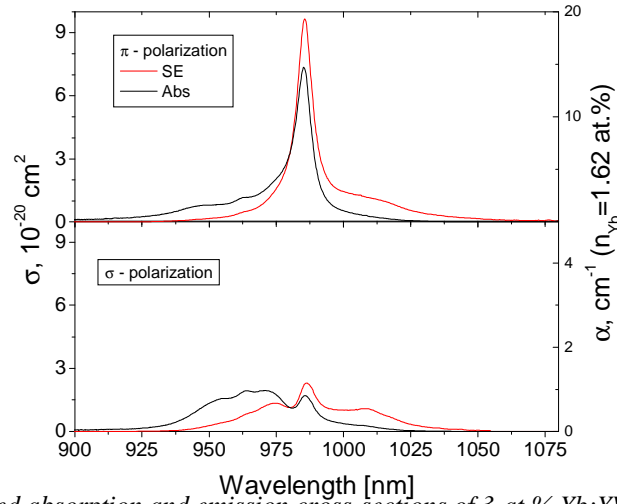


Figure 6.4. Polarized absorption and emission cross-sections of 3-at %  $\text{Yb:YVO}_4$  at room temperature [36].

The polarized absorption and emission spectra of 3-at %  $\text{Yb:YVO}_4$  at room temperature are shown in figure 6.4. This crystal has a peak absorption coefficient  $\sigma_a$  of  $7.4 \times 10^{-20} \text{ cm}^2$  for  $\pi$ -polarization ( $E \parallel c$ ) at 985 nm with an absorption linewidth of  $\sim 8$  nm which is very well suited for optical pumping by the well-developed InGaAs diode lasers. The peak stimulated emission cross-section  $\sigma_{se}$  calculated in  $\text{Yb:YVO}_4$  for  $\pi$ -polarization is  $1.25 \times 10^{-20} \text{ cm}^2$  at 1008 nm while the upper state lifetime is 0.25 ms. The comparison of spectroscopic properties between a  $\text{Yb:YVO}_4$  crystal and one of  $\text{Yb:KYW}$  is shown in table 6.2 below:-

Table 6.2. Spectroscopic properties of  $\text{Yb:KYW}$  [37] and  $\text{Yb:YVO}_4$ . [38].

Spectroscopic parameters	$\text{Yb:KYW}$	$\text{Yb: YVO}_4$
Upper state lifetime, $\tau_u$ (ms)	0.6	0.25
Absorption cross-section, $\sigma_{abs}^{\lambda_p}$ ( $\times 10^{-20} \text{ cm}^2$ )	13.3	7.4
Stimulated emission cross-section, $\sigma_{se}^{\lambda_{se}}$ ( $\times 10^{-20} \text{ cm}^2$ )	3	1.25
Axis	Biaxial	Uniaxial
Stimulated emission wavelength, $\lambda_{se}$ (nm)	1025	1008
Pump wavelength, $\lambda_p$ (nm)	981.2	985

Spectroscopic parameters	Yb:KYW	Yb: YVO <sub>4</sub>
Emission linewidth, $\Delta\lambda_{se}$ (nm)	16	28
Absorption linewidth, $\Delta\lambda_{abs}$ (nm)	3.5	8
Thermal conductivity (W/mK)	3.3	5.23
Pump saturation intensity, $I_{sat}$ (kW/cm <sup>2</sup> )	1.24	4.72
Gain saturation fluence, $F_{sat}^{\lambda_{se}}$ (mJ/cm <sup>2</sup> )	64.6	158
Quantum defect fraction	0.043	0.035

Based on the spectroscopic values given in table 6.2, the pump saturation intensity  $I_{sat}$  [equation 3.2.5] of Yb:YVO<sub>4</sub> is four times higher while the laser threshold  $\left( P_{th} \alpha \frac{1}{\sigma_{se}^{\lambda_{se}} \tau_u} \right)$  needed for lasing is six times higher compared to that of Yb:KYW. These are obtained due to the lower upper state lifetime products,  $\sigma \tau_u$  in vanadates.  $I_{sat}$  mentioned above is calculated by accounting  $\sigma_{se}^{\lambda_p} = 9.7 \times 10^{-20} \text{ cm}^2$  and  $14 \times 10^{-20} \text{ cm}^2$  for Yb:YVO<sub>4</sub> [figure 6.4] and Yb:KYW [figure 4.2] respectively. In addition, the smaller value of stimulated emission cross-section  $\sigma_{se}^{\lambda_{se}}$  in vanadate over that of tungstate increases the gain saturation fluence  $F_{sat,L}^{\lambda_{se}}$  needed for the suppression of Q-switching instabilities [equation 3.3.1]. As a result, the Q-switching tendency in this former crystal is stronger than that of the tungstate counterpart.

However, the properties that favour the use of this material (Yb:YVO<sub>4</sub>) for lasing are its slightly smaller quantum defect fraction of  $\sim 0.03$  [equation 2.6.1] that reduces heat dissipation and its larger amplification bandwidth ( $\sim 28 \text{ nm}$ ) which facilitates the generation of shorter (femtosecond) pulses with wider tunability. This vanadate crystal also exhibits thermal conductivity [39] of up to 5.3 W/mK which is 40 % higher than that of the tungstates, thus providing efficient heat removal from the gain medium during laser operation. All of these advantages together with a broad and smooth (glasslike) gain spectrum [35] show the potential of Yb:YVO<sub>4</sub> crystals as promising gain media for compact, efficient and high power diode-pumped solid-state femtosecond lasers in the 1  $\mu\text{m}$  region. Previously, efficient continuous wave laser operation has been demonstrated in Yb:YVO<sub>4</sub> when pumped with either a Ti:sapphire laser [40] or a diode laser [38]. By passively mode-locking the laser using a semiconductor saturable absorber mirror, 120 fs

pulses were generated at a centre wavelength of 1021 nm with an average output power of 300 mW [41].

As a consequence of the excellent opto-mechanical and spectroscopic properties of this material for lasing, Yb:YVO<sub>4</sub> was chosen as a gain medium around which a compact and efficient femtosecond laser was designed. The mode locking was based on the optical Kerr effect with the expectations of shorter pulse durations and low threshold operation. This work is expected to become a basis for future implementation of this material for high power thin disc operation and as a pump source for optical parametric oscillator/amplifier and for harmonic generation.

## 6.6 Implementations.

Two types of evaluations were carried out on this gain medium. The first that was performed by my collaborator in Belarus (N. V. Kuleshov) was to determine the nonlinear refractive index  $n_2$  of Yb:YVO<sub>4</sub> crystal by using the standard z-scan technique [10] and the second was to build a three-mirror laser cavity based on Kerr lens mode-locking.

### 6.6.1 Measurement of $n_2$

This experimental set-up was similar to that in figure 6.2 where the pump source was a passively mode-locked Nd<sup>3+</sup>:YAlO<sub>3</sub> laser generating 100 ps pulses at 1.08  $\mu\text{m}$  at a pulse repetition frequency of 1 Hz. The beam quality factor  $M^2$  of the output beam was determined to be  $< 1.1$  while the peak power was 4.7 MW. The lens used had a focal length of 10 cm that collected and focused the laser radiation into a beam waist,  $w_{p,0}$  of 32

$\mu\text{m}$  which corresponds to a confocal parameter of 6 mm  $\left( b = \frac{2\pi w_p^2}{\lambda_p} \right)$ . The sample used

was a 0.96 mm length 2-at % Yb:YVO<sub>4</sub> that allows the analysis of a “thin” medium during the horizontal z-scanning. An aperture with a diameter of 0.5 mm was placed 40 cm from the focal position  $z_0$ , to allow the measurement of far-field on-axis Z-scan transmittance.

The overall  $n_2$  experimental error was in the range of  $\pm 20\%$  due to external noise. This

noise that was generated mainly by the scattering from the gain medium can be reduced by subtracting a low-intensity z-scan from the high-intensity counterpart.

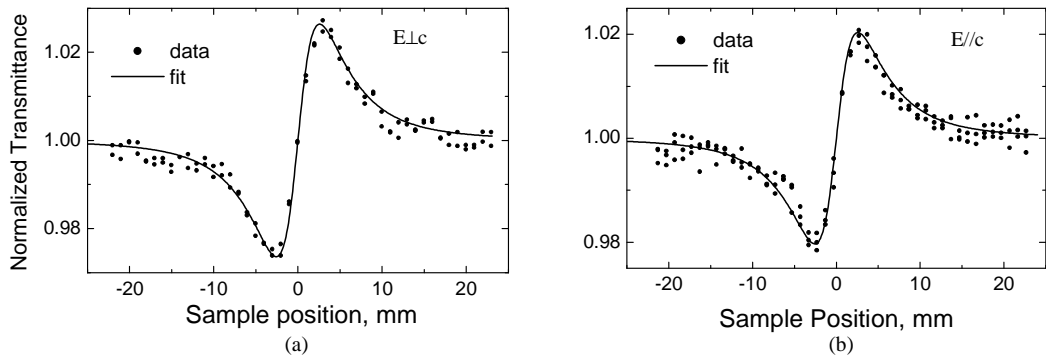


Figure 6.5 . Normalized Z-scan data of Yb:YVO<sub>4</sub> crystal for (a) E<sub>⊥</sub>c and (b) E//c polarizations at 1080 nm. Solid curves are the theoretical fits.

During scanning, a peak power as high as 317 kW was used which corresponds to focal on-axis intensities of 19.6 GW/cm<sup>2</sup>. The measurements were carried out on the gain medium for  $\pi$  – (E//c) and  $\sigma$  – (E<sub>⊥</sub>c) polarisation. The results obtained are shown in figure 6.5 where the valley-to-peak features imply positive lensing effects in the gain medium. From the best fits to the experimental data, the values of  $n_2$  for  $\pi$  – polarisation was  $15 \times 10^{-16}$  cm<sup>2</sup>/W while for  $\sigma$  – polarisation was  $19 \times 10^{-16}$  cm<sup>2</sup>/W respectively. Another  $n_2$  measurement was also carried out by using a 5-at % of Yb<sup>3+</sup>-doped KYW for E//N<sub>m</sub> polarisation that is an outstanding active medium for KLM operation [19,20]. The value of  $n_2$  obtained was  $10 \times 10^{-16}$  cm<sup>2</sup>/W which is comparable with  $n_2$  value of  $8.7 \times 10^{-16}$  cm<sup>2</sup>/W reported previously in Yb:KYW for E//a polarisation at 1.08  $\mu$ m [11]. As a result the highest value of  $n_2$  in Yb:YVO<sub>4</sub> is observed for  $\sigma$  – polarisation while for the preferred  $\pi$  – polarisation the value of  $n_2$  is higher by a factor of  $\sim 1.5$  compared to that of Yb:KYW for E//N<sub>m</sub> at 1080 nm.

## 6.6.2 Kerr-lens Mode Locking Implementation.

The experimental set-up for a three-mirror cavity Kerr-lens mode locked Yb:YVO<sub>4</sub> laser that was designed by using ABCD matrix formalism is illustrated in figure 6.6 above. The pump source was a single mode fibre-coupled (mode-field diameter of 6.6 μm) polarisation-maintaining InGaAs diode laser (JDS Uniphase) emitting at a centre wavelength of 981 nm with an average output power of ~ 0.5 W. The absorption coefficient of Yb:YVO<sub>4</sub>,  $\alpha$  was ~ 8 cm<sup>-1</sup> at the pump wavelength of 981 nm as measured from figure 6.4. The appropriate length of the crystal,  $l$  selected to satisfy the optimum requirement of this assessment can be obtained from the equation below:-

$$T = e^{-\alpha l} \quad (6.6.1)$$

where  $T$  is the transmission properties of the crystal. With  $T = 0.19$  (absorption = 81 %) as will be mentioned in the next section, the appropriate length of the crystal was calculated to be ~ 2.1 mm. As a consequence, the gain medium used for these assessments was a 2-mm long 3 at. % Yb<sup>3+</sup>-doped YVO<sub>4</sub> Brewster-angled crystal oriented in the cavity for polarisation parallel to the crystallographic axis  $c$  ( $\pi$  – polarisation).

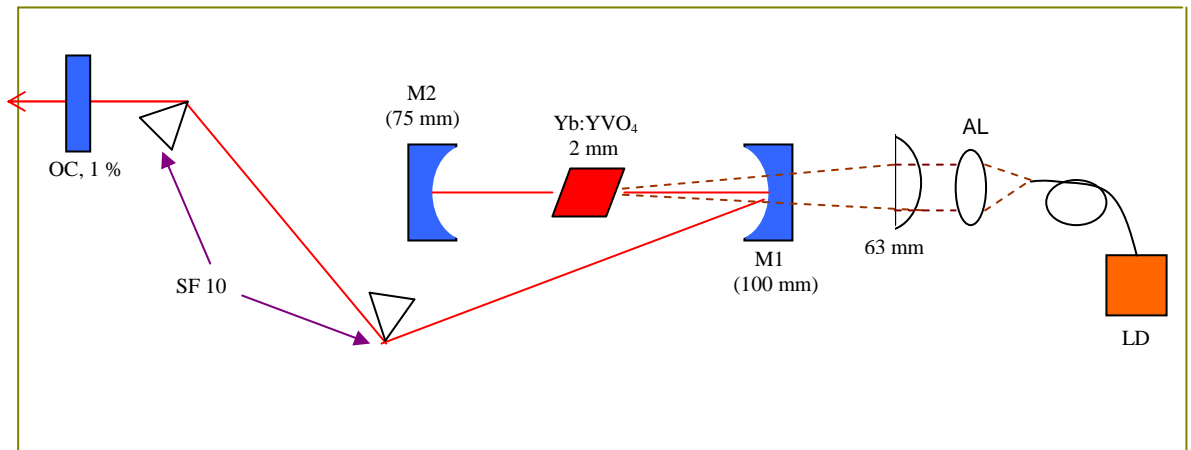


Figure 6.6. Schematic of Kerr-lens mode locking experiment.

Aspherical ( $f = 15$  mm) and spherical ( $f = 63$  mm) lenses were used to collect and focus the pump beam into the gain medium and the pump beam waist,  $w_{p,0}$  was measured to be 17 μm ( $1/e^2$  intensity). The laser beam waist,  $w_{l,0}$  inside this medium designed from ABCD matrix formalism was 18 x 36 μm and this correlates to a confocal parameter,  $b$  of 4 mm. The mirrors M1 and M2 had radii of curvature of 100 mm and 75 mm respectively,

exhibiting  $\approx 98\%$  transmission at around 980 nm and high reflection at wavelength ranges between 1025-1100 nm. Two types of plane-wedged output couplers (OC) with 1% and 3% transmissions at around 1050 nm were used as the end mirrors to compare the results obtained in these assessments. The total length of the cavity corresponded to the pulse repetition rate of around 105 MHz when passively mode locked. As the peak power is proportional to the inverse repetition rate  $\frac{1}{f_{rep}}$ , this longer cavity with lower repetition rate over those built in Chapter 4 and 5 ( $\sim 212$  MHz) induced higher intracavity peak power incident on the gain medium. This implied higher intensity-dependent refractive index,  $I(r,t)$  that was responsible for Kerr-lensing effect [equation 6.2.1a].

### 6.7 Continuous Wave (Unmode-locked) Operation.

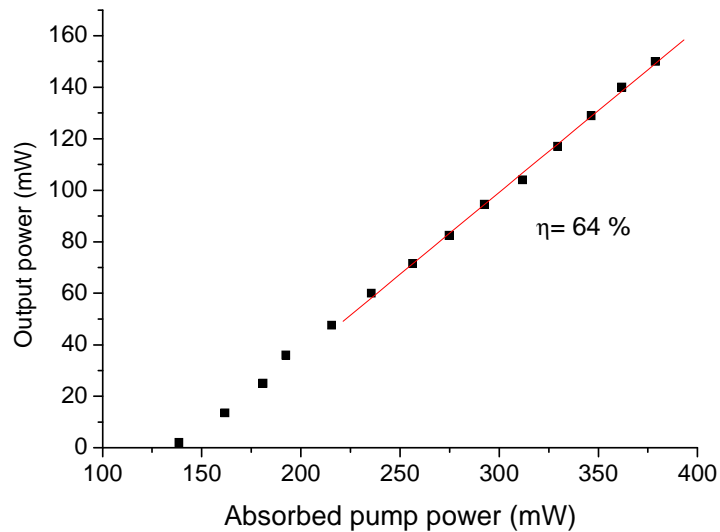


Figure 6.7. Slope efficiency of continuous wave four-mirror cavity operation with a 3% output coupler.

Before any performance assessments were carried out, the cavity was designed in a four-mirror cavity at a pulse repetition rate of 81.4 Mhz. A high reflector was placed at the short arm cavity in a full analogy with the set up in figure 4.8 to measure laser threshold and slope efficiency during cw operation. This was done to give a general idea on CW performance in four-mirror cavity that could potentially be useful for any future SESAM-assisted mode locking attempt on this laser material. Absorption evaluations of the crystal were then carried out by implementing 3% and 1% output couplers at the end mirror. These were done during lasing by placing the power meter behind M2 [figure 6.6] and

taking into account that M2 provided around 95 % transmission at the pump wavelength. The absorption percentage of the crystal can be calculated from the difference between the incident and the transmitted pump powers. It was found that the absorption of the medium was 77 % and 81 % for output coupler transmission of 3 % and 1 % correspondingly. These reasonable results that were achieved with the existence of gain saturation during lasing can be explained microscopically. At the high intensity of pumped source, gain saturation that occur inside the gain medium equalizes both populations at the lower state  $N_1$  and upper state levels  $N_2$ . The medium is said to be “bleached” or transparent that might lead to the reduction in its absorption properties. However during lasing, populations at lower state  $N_1$  were increased back due to the existence of stimulated emission rate  $-B_{21}$ , as well as spontaneous emission rate  $-A_{21}$ , that recover back the rate of stimulated absorption,  $B_{12}$ .

When a 3 % output coupler was employed, a maximum output power of 150 mW was obtained with respect to the incident pump power on the crystal of 492 mW. This corresponds to an optical-to-optical efficiency of 39 % and a slope efficiency of 64 % with respect to the absorbed pump power as depicted in figure 6.7. With a small signal gain coefficient,  $g\alpha(\sigma_{se}^{\lambda_{se}} - \sigma_{abs}^{\lambda_{se}})$  [30], it was expected earlier to obtain a lower optical-to-optical efficiency in Yb:YVO<sub>4</sub> crystal due to its lower gain properties [figure 6.4] in comparison to that of Yb:KYW [figure 4.2]. The threshold power of this laser was reached at 139 mW which was slightly higher compared to that obtained in Yb:KYW in Chapter 4 ( $P_{th} = 101$  mW). After achieving this threshold, the laser output increased linearly as a function of absorbed pump power on the crystal.

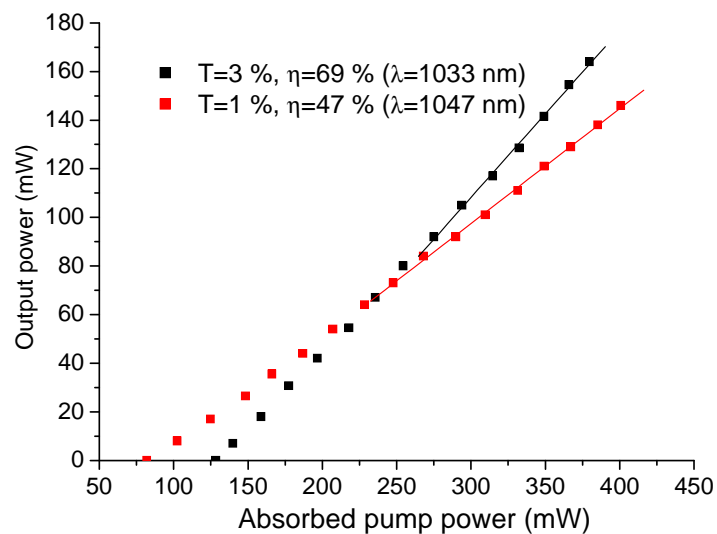


Figure 6.8. Slope efficiency of continuous wave three-mirror cavity operation by using 1 % and 3 % output coupler.

The next step was to reconfigure and to re-align the laser to carry out the entire evaluation of cw assessments in a three-mirror cavity from the previous 4-mirror set-up. This was done by removing the high reflector from the short arm cavity. By using a 3 % output coupler the laser threshold was satisfied at an absorbed pump power of 129 mW. A maximum output power of 164 mW was then obtained at a centre wavelength of 1033 nm with respect to the absorbed pump power of 380 mW. This produces an optical-to-optical efficiency of 43 % while the slope efficiency was 69 % as shown in figure 6.8 above. This performance was superior to that obtained from the previous reports in Ti:sapphire pumped and cw diode-pumped Yb:YVO<sub>4</sub> laser configurations where the slope efficiencies were up to 41.4 % and 11 % respectively [38,40]. This improvement was due to better pump beam quality,  $M^2 \sim 1$  which results in better pump beam and laser mode overlap in the laser crystal [see section 3.3].

By substituting the previous output coupler of 3 % with that of 1 %, the laser threshold was reduced to 82 mW which was almost similar to 76 mW threshold power achieved in Ti:Sapphire-pumped Yb:YVO<sub>4</sub> laser [40]. A maximum output power of 146 mW was obtained at 1047 nm with respect to the absorbed pump power of 401 mW. This corresponds to an optical-to-optical efficiency of 36 % while the subsequent slope efficiency was 47 %. From these assessments it was found that by using a lower transmission of output coupler, lower optical-to-optical and slope efficiencies were obtained at a lower laser threshold power as reported previously [42]. The reduction in cavity round trip loss ( $T_{OC} + L_d + 2L_{yb}$ ) explained the attainment of this lower threshold.

From the results presented in figure 6.8, a graph of  $\frac{1}{\eta}$  versus  $\frac{1}{T_{OC}}$  was plotted to determine the double-pass losses in the cavity  $L_d$  [see equation 3.2.10]. This is illustrated in figure 6.9 where the linear fit from this graph implies an intercept of 1.15 that leads to the quantum efficiency,  $\eta_0$  of  $\sim 90$  %. However, from the peak emission wavelengths for this laser that were obtained at 1033 nm and 1047 nm [figure 6.8], the experimental value of  $\eta_0$  was around 95 %. This was slightly higher than the measured value due to the fact that  $\eta_{ol}$  in eq. (3.2.9) might be less than 1. Further improvement is suggested by assessing this laser performance when implementing more output couplers to reduce this discrepancy. From the slope of this graph,  $L_d$  in Yb:YVO<sub>4</sub> crystal was determined to be 0.9 %.

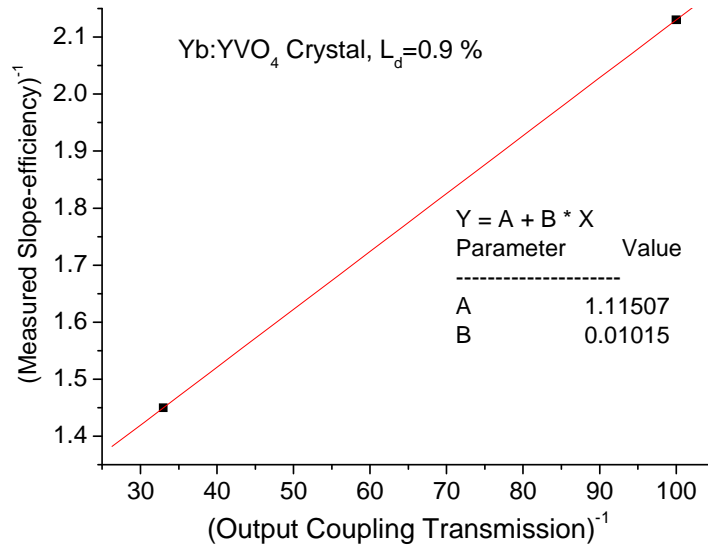


Figure 6.9 Inverse slope-efficiency of the crystal as a function of inverse output coupling transmission based on the results depicted in figure 6.8.

By considering that 1 at. % Nd-ions in the crystal's host of YVO<sub>4</sub> consist of  $1.26 \times 10^{20}$  ions-cm<sup>-3</sup> [43], Yb-doping concentrations  $N_{Yb}$  for 3 at. % Yb-ions in this crystal's lattice were calculated to be  $3.8 \times 10^{20}$  ions-cm<sup>-3</sup>. At the emission wavelength,  $\lambda_{se}$  of 1047 nm (OC= 1 %) single pass absorption loss in the crystal,  $L_{Yb}$  was deduced from equation (3.2.6b) to be around 0.006 ( $\sigma_{abs}^{\lambda_{se}} = 7.47 \times 10^{-23}$  cm<sup>2</sup>) and at  $\lambda_{se}$  of 1033 nm (OC= 3 %)  $L_{Yb}$  was deduced to be 0.021 ( $\sigma_{abs}^{\lambda_{se}} = 2.76 \times 10^{-22}$  cm<sup>2</sup>). Once  $L_d$  and  $L_{Yb}$  of this crystal were estimated, theoretical and experimental comparisons for threshold powers can be performed based on the results demonstrated in figure 6.8. From equation (3.2.6a) by excluding  $\eta_{ab}$  for the absorbed pump power evaluations, these thresholds were 148 mW and 113 mW for the implementation of 3 % and 1 % output couplers correspondingly which were slightly higher than those obtained experimentally (for simplification, all the data taken are presented in [appendix F]).

These results can be explained using figure 3.3a where as a consequence of the implementation of a diffraction limited pump beam source  $M^2 \approx 1$ , a strong mode overlap between the spot sizes imply a larger volume of the crystal that was exposed to the tight-focusing geometry. A greater population inversion is induced in the gain medium due to the high percentage of the pumped Yb-ions that were excited to the upper state. An increase in the stimulated emission rate was subsequently achieved that was responsible for lower thresholds measured during the experiment. In addition, experimental uncertainties

especially the change in the beam waists during the alignment of the laser might also contribute to this small discrepancy.

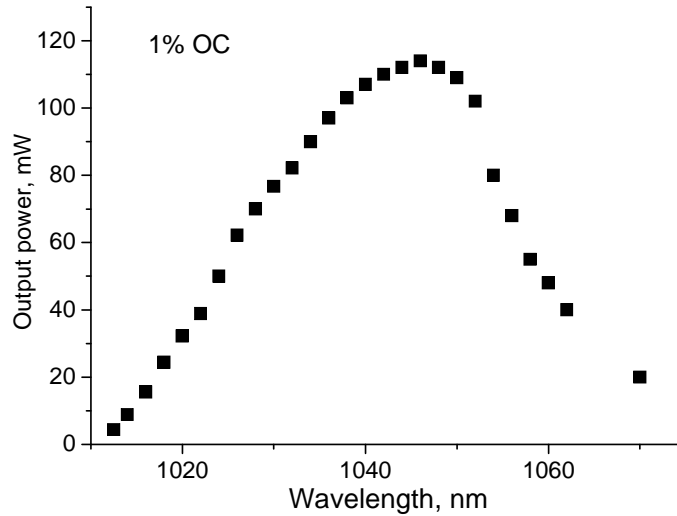


Figure 6.10. Wavelength tunability after inserting prism pairs inside the laser cavity with a 1 % output coupler.

A pair of prisms for dispersion control were then inserted into the laser oscillator with an effective separation of 44 cm. By maintaining a 1 % output coupler as the end mirror for the entire evaluation of performance (section 6.8), a maximum output power of 134 mW was obtained at a centre wavelength of 1046 nm. This corresponds to 8 % losses inside the oscillator which reduced the optical-to-optical efficiency of the system to 28 % with respect to the absorbed pump power. The laser was then tuned from 1012 nm to 1070 nm as illustrated in figure 6.10 above.

## 6.8 Kerr-lens Mode Locking Results.

Before carrying out any KLM assessments on the laser cavity, a map of stability that shows the variation of cw output power as a function of distance separation between the crystal with folding mirror 2 for the Yb:KYW laser was taken as an example to prove the critical cavity stability requirement needed during KLM operation [figure 6.11(a)]. The unstable cw output power region was observed in this figure which was preferable for KLM mechanism as shown by the arrow. The output beam profile in figure 6.11(b) upper part exhibits strong aberrations due to a gap in the output power where the CW operation was unstable. However, further adjustment of the cavity led to a soft-aperture Kerr-lensing

effect where the output beam profile was transformed into a near-diffraction limited feature as shown in figure 6.11(b) bottom part.

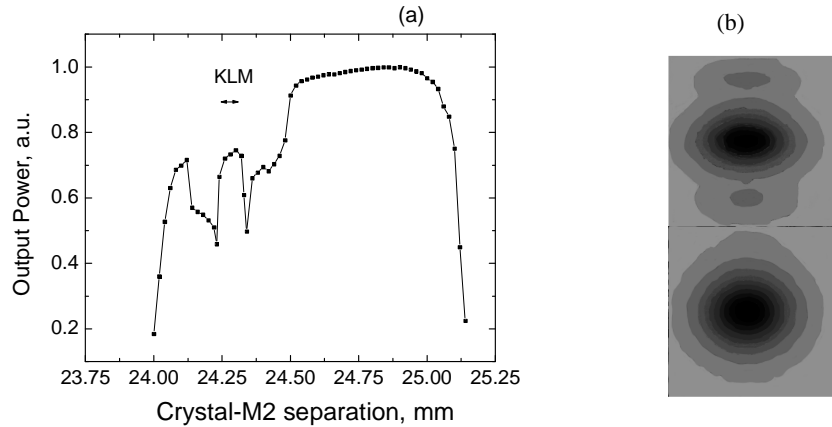


Figure 6.11(a) Example of measured stability map for the three-element cavity Yb:KYW laser with the soft-aperture region is shown by the arrow and (b) the output beam profile during the un-mode locked (top) and the KLM (bottom) operations [20].

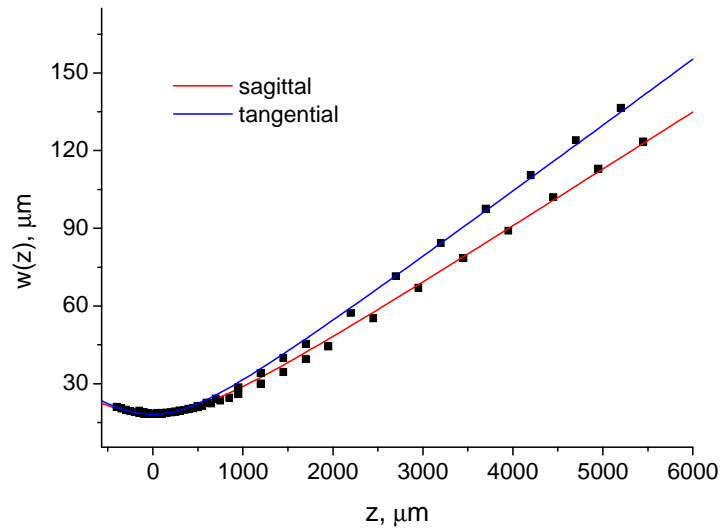


Figure 6.12. Linear fits for  $M^2$  beam quality evaluation in a KLM Yb:YVO<sub>4</sub> laser in the sagittal and tangential directions correspondingly.

The beam quality factor  $M^2$  of this output beam was then measured by A. A. Lagatsky by using a Beam Master Profiler. The results obtained were plotted in a graph of  $w(z)$  that signifies the beam spot size as a function of  $z$  that signifies the distance from the minimum beam waist,  $w_{l,o}$  [figure 6.12]. Initially, several values of spot sizes were taken very close to each other to determine the exact location of the beam waist,  $w_{l,o}$  before introducing a distance of 500  $\mu\text{m}$  for the each following data.  $M^2$  can then be deducted from the measured spot size values as given from the formula below:-

$$w(z) = w_{l,o} \sqrt{1 + \left( \frac{\lambda \cdot z \cdot M^2}{n\pi \cdot w_{l,o}^2} \right)^2} \quad (6.8.1)$$

where  $\lambda$  is the wavelength of the laser. From figure 6.12 above, black squares indicate the measured experimental data while the red and blue lines are linear fits to the corresponding data by implementing equation 6.8.1. In the sagittal direction, the best fit was obtained when  $M^2$  was taken to be 1.2 for the beam waist of 18.5  $\mu\text{m}$ . Coincidentally in the tangential direction,  $M^2$  was taken to be 1.4 for the beam waist of 18.2  $\mu\text{m}$ . The deviation from the diffraction limited value was due to the non-ideal overlap between the pump and laser beam modes in the laser crystal during KLM operation.

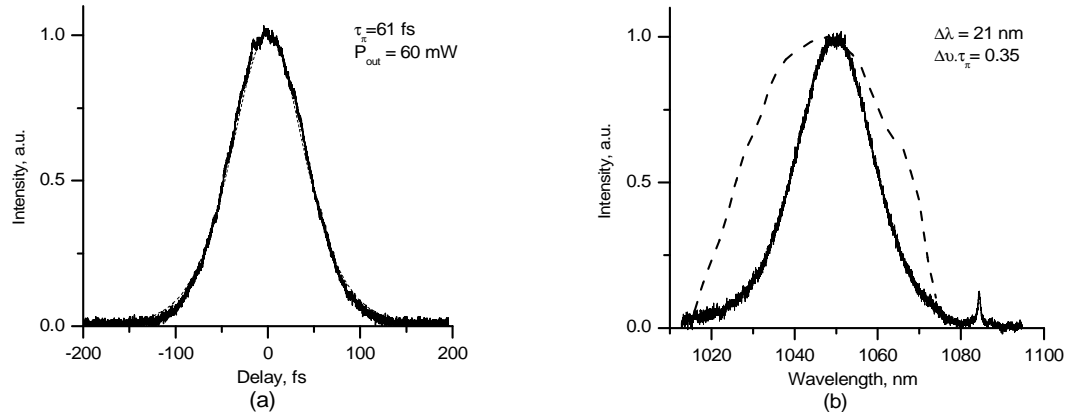


Figure 6.13. (a) Measured intensity autocorrelation for a pulse duration of 61 fs, (b) the corresponding optical spectrum of the pulses at 1050 nm and the range of the laser tunability between 1015 nm to 1075 nm as shown by the dotted curve.

Precise alignments of mirror 1, mirror 2 and the crystal's position were required to initiate modelocking. Once KLM was initiated with the 1 % output coupler in place, the prism pair inside the laser oscillators was adjusted carefully to introduce intracavity dispersion needed for group velocity compensation for the optimised compression of the pulse duration. A nearly-transform-limited product of 0.35 was obtained with a pulse duration of 61 fs emitting at 1050 nm [figure 6.13]. The spectral width of the pulses was 21 nm which implies a lasing bandwidth of  $\sim 6$  THz. In addition, the maximum output power achieved during this operation was 60 mW that corresponds to an optical-to-optical efficiency of 15 %. The peak power obtained from this laser was 9.41 kW while the critical power  $P_{cr}$  was 2.15 MW ( $n_2 = 15 \times 10^{-16} \text{ cm}^2/\text{W}$ ). These features implied a

positive lens behaviour of the crystal with a beam focus at  $z_f = 21.6$  mm. During this operation the laser was tunable from 1015 nm to 1075 nm as shown in figure 6.13(b).

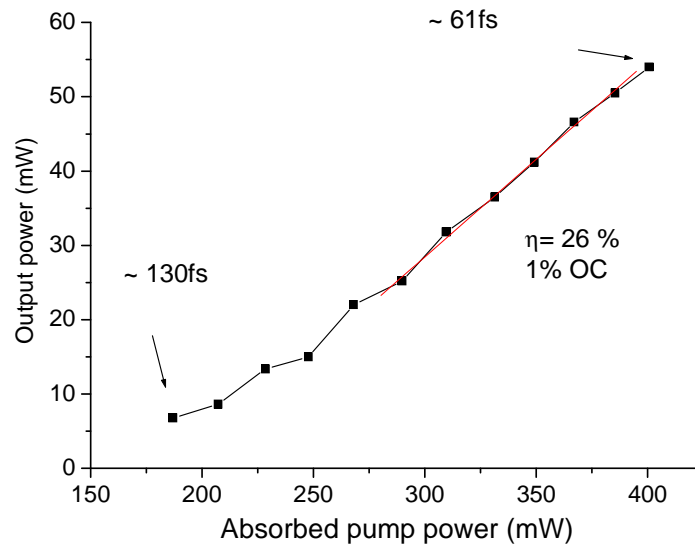


Figure 6.14. Slope efficiency during KLM operation by using a 1 % output coupler.

The slope efficiency of the laser was determined by reducing the absorbed pump power on the crystal until a KLM threshold was achieved. A self-induced KLM operation was sometimes observed even though external perturbation or fine translation of the mirror 2 was needed for the initiation of mode-locking process. The pulses were stable over an experimental period of more than 1 hour. These features were obtained due to the optimisation of laser cavity design that assists the establishment of high beam quality mode-locked output pulses. This was because the excitation to a higher order transverse modes would deteriorate the pulse evolution process. A slope efficiency of up to 26 % was obtained while the threshold power for Kerr-lens mode locking was satisfied for an absorbed pump power of 190 mW [figure 6.14]. The pulse duration generated during this time was 130 fs with an average output power of 8 mW.

## 6.9 Conclusion.

A stable, ultralow threshold and efficient Yb:YVO<sub>4</sub> femtosecond laser was successfully constructed in this part of my project based on a Kerr-lens mode locking scheme. The potential of Kerr-lens effects in this medium was shown by the relatively large value of  $n_2$  measured using a z-scan technique.  $n_2$  for this crystal was  $15 \times 10^{-16}$  cm<sup>2</sup>/W for

$\pi$ -polarization and  $19 \times 10^{-16} \text{ cm}^2/\text{W}$  for  $\sigma$ -polarisation respectively which are higher than that of Ti:sapphire ( $3.1 \times 10^{-16} \text{ cm}^2/\text{W}$ ) and Cr:forsterite ( $6 \times 10^{-16} \text{ cm}^2/\text{W}$ ). A time-bandwidth product of 0.35 was achieved with a pulse duration as short as 61 fs. The maximum output power was 60 mW which corresponds to an optical-to-optical efficiency of 15 % with respect to the absorbed pump power. This ultrashort pulse duration which was shorter than a previous assessment in Yb:Sr<sub>3</sub>Y(BO<sub>3</sub>)<sub>3</sub> ( $\tau_p = 69$  fs) [25] with a reasonable 15 % optical-to-optical efficiency opens up future investigations for high peak power operation. This choice of gain crystal is further supported by a suitably high thermal conductivity of up to 5.3 W/mK which enhances the figure of merit of this material as an alternative source instead of Yb:YAG. The use of this femtosecond laser in high power thin disc and as a pump source for optical parametric oscillators/amplifiers and harmonic generation merits particular consideration in my view.

## 6.10 References:

- 1 J. E. Bjorkholm and A. Ashkin, "CW self-focusing and self-trapping of light in sodium vapor," *Phys. Rev. Lett.* **32**, 129-132 (1974).
- 2 R. W. Boyd, "Nonlinear Optics", Academic Press Inc., New York, pp 11-262, 1992.
- 3 D. E. Spence, P. N. Kean, and W. Sibbett, "60-fsec pulse generation from a self-mode-locked Ti:sapphire laser," *Opt. Lett.* **16**, 42-44 (1991).
- 4 V. L. Kalashnikov, E. Sorokin; and I. T. Sorokina, "Multipulse operation and limits of the Kerr-lens mode-locking stability," *IEEE J. of Quantum Electron.* **39**, 323-336 (2003).
- 5 U. Morgner, F. X. Kartner, S. H. Cho, Y. Chen, H. A. Haus, J. G. Fujimoto, E. P. Ippen, V. Scheuer, G. Angelow, and T. Tschudi, "Sub-two-cycle pulses from a Kerr-lens mode-locked Ti:sapphire laser," *Opt. Lett.* **24**, 411-413 (1999).
- 6 M. J. Moran, C. Y. She; and R. L. Carman, "Interferometric measurements of the nonlinear refractive-index coefficient relative to CS<sub>2</sub> in laser-system-related materials," *IEEE J. Quantum Electrons* **11**, 259- 263 (1975).
- 7 S. R. Friberg and P. W. Smith "Nonlinear optical glasses for ultrafast optical switches," *IEEE J. Quantum Electrons* **23**, 2089- 2094 (1987).
- 8 R. Adair, L. L. Chase, and S. A. Payne, "Nonlinear refractive-index measurements of glasses using three-wave frequency mixing," *J. Opt. Soc. Am. B* **4**, 875-881 (1987).
- 9 A. Owyong, "Ellipse rotation studies in laser host materials," *IEEE J. Quantum Electrons* **9**, 1064- 1069 (1973).
- 10 M. Sheik-Bahae, A. A. Said, and E. W. Van Stryland, "High-sensitivity, single-beam  $n_2$  measurements," *Opt. Lett.* **14**, 955-957 (1989).
- 11 K. V. Yumashev, N. N. Posnov, P. V. Prokoshin, V. L. Kalashnikov, F. Mejid, I. G. Poloyko, V. P. Mikhailov, and V. P. Kozich, "Z-scan measurements of nonlinear refraction and Kerr-lens mode-locking with Yb<sup>3+</sup>:KY(WO<sub>4</sub>)<sub>2</sub>," *Opt. and Quantum Electron.* **32**, 43-48 (2000).
- 12 A. Major, I. Nikolakakos, J. S. Aitchison, A. I. Ferguson, N. Langford, and P. W. E. Smith, "Characterization of the nonlinear refractive index of the laser crystal Yb:KGd(WO<sub>4</sub>)<sub>2</sub>," *Appl. Phys. B* **77**, 433-436 (2003).

13. A. Major, J. S. Aitchison, P. W. E. Smith, F. Druon, P. Georges, B. Viana, and G. P. Aka, "Z-scan measurements of the nonlinear refractive indices of novel Yb-doped laser crystal hosts", *Appl. Phys. B* **80**, 199-201 (2005).
14. K. V. Yumashev, N. N. Posnov, P. V. Prokoshin, V. L. Kalashnikov, F. Mejid, I. G. Poloyko, V. P. Mikhailov, and V. P. Kozich, "Z-scan measurements of nonlinear refraction and Kerr-lens mode-locking with  $\text{Yb}^{3+}:\text{KY}(\text{WO}_4)_2$ ", *Opt. Quantum Electron.* **32**, 43-48 (2000).
15. R. Adair, L. L. Chase, and S. A. Payne, "Nonlinear refractive index of optical crystals", *Phys. Review B* **39**, 3337-3350 (1989).
16. N. Sarukura, Y. Ishida, H. Nakano, "Compression of intra-cavity chirped pulses from a cw passive mode-locked Ti:Sapphire laser," *Opt. Commun.* **77**, 49-52 (1990).
17. B. Chassagne, A. Ivanov, J. Oberlé, G. Jonusauskas, C. Rullière, "Experimental determination of the nonlinear refractive index in an operating Cr:forsterite femtosecond laser," *Opt. Commun.* **141**, 69-74 (1997).
18. V. Petrov, U. Griebner, D. Ehrt, and W. Seeber, "Femtosecond self mode locking of Yb:fluoride phosphate glass laser," *Opt. Lett.* **22**, 408-410 (1997).
19. H. Liu, J. Nees, and G. Mourou, "Diode-pumped Kerr-lens mode-locked YbKY(WO<sub>4</sub>)<sub>2</sub> laser," *Opt. Lett.* **26**, 1723-1725 (2001).
20. A. A. Lagatsky, C. T. A. Brown, and W. Sibbett, "Highly efficient and low threshold diode-pumped Kerr-lens mode-locked Yb:KYW laser," *Opt. Express* **12**, 3928-3933 (2004).
21. F. Brunner, G. J. Spuhler, J. Aus der Au, L. Krainer, F. Morier-Genoud, R. Paschotta, N. Lichtenstein, S. Weiss, C. Harder, A. A. Lagatsky, A. Abdolvand, N. V. Kuleshov, and U. Keller, "Diode-pumped femtosecond YbKGd(WO<sub>4</sub>)<sub>2</sub> laser with 1.1-W average power ," *Opt. Lett.* **25**, 1119-1121 (2000).
22. F. Brunner, T. Sudmeyer, E. Innerhofer, F. Morier-Genoud, R. Paschotta, V. E. Kisel, V. G. Shcherbitsky, N. V. Kuleshov, J. Gao, K. Contag, A. Giesen, and U. Keller, "240-fs pulses with 22-W average power from a mode-locked thin-disk YbKY(WO<sub>4</sub>)<sub>2</sub> laser," *Opt. Lett.* **27**, 1162-1164 (2002).
23. P. Klopp, V. Petrov, U. Griebner, and G. Erbert, "Passively mode-locked Yb:KYW laser pumped by a tapered diode laser," *Opt. Express* **10**, 108-113 (2002).
24. F. Druon, F. Balembos, P. Georges, A. Brun, A. Courjaud, C. Honninger, F. Salin, A. Aron, F. Mougel, G. Aka, and D. Vivien, "Generation of 90-fs pulses from a

- mode-locked diode-pumped  $\text{Yb}^{3+}:\text{Ca}_4\text{GdO}(\text{BO}_3)_3$  laser,” *Opt. Lett.* **25**, 423-425 (2000).
25. F. Druon, S. Chenais, P. Raybaut, F. Balembois, P. Georges, R. Gaum, G. Aka, B. Viana, S. Mohr, and D. Kopf, “Diode-pumped  $\text{Yb}:\text{Sr}_3\text{Y}(\text{BO}_3)_3$  femtosecond laser,” *Opt. Lett.* **27**, 197-199 (2002).
  26. G. Paunescu, J. Hein, and R. Sauerbrey, “100-fs diode-pumped  $\text{Yb}:\text{KGW}$  mode-locked laser,” *Appl. Phys. B* **79**, 555-558 (2004).
  27. F. Druon, F. Balembois, and P. Georges, “Ultra-short-pulsed and highly-efficient diode-pumped  $\text{Yb}:\text{SYS}$  mode-locked oscillators,” *Opt. Express* **12**, 5005-5012 (2004).
  28. E. Innerhofer, T. Sudmeyer, F. Brunner, R. Hring, A. Aschwanden, R. Paschotta, C. Honninger, M. Kumkar, and U. Keller, “60-W average power in 810-fs pulses from a thin-disk  $\text{YbYAG}$  laser,” *Opt. Lett.* **28**, 367-369 (2003).
  29. W. F. Krupke, “Ytterbium solid-state lasers –The first decade,” *IEEE J. Select. Topics Quantum Electron.* **6**, 1287-1296 (2000).
  30. C. Hönninger, R. Paschotta, M. Graf, F. Morier-Genoud, G. Zhang, M. Moser, S. Biswal, J. Nees, A. Braun, G. A. Mourou, I. Johannsen, A. Giesen, W. Seeber, and U. Keller, “Ultrafast ytterbium-doped bulk lasers and laser amplifiers,” *Appl. Phys. B* **69**, 3-17 (1999).
  31. A. Lucca, G. Debourg, M. Jacquemet, F. Druon, F. Balembois, P. Georges, P. Camy, J. L. Doualan, and R. Moncorgé, “High-power diode-pumped  $\text{Yb}^{3+}:\text{CaF}_2$  femtosecond laser,” *Opt. Lett.* **29**, 2767-2769 (2004).
  32. W. Ryba-Romanowski, “ $\text{YVO}_4$  crystals-puzzles and challenges,” *Cryst. Res. Technol.* **38**, 225-236 (2003).
  33. F. S. Ermeneux, C. Goutaudier, R. Moncorge, M. T. Cohen-Adad, M. Bettinelli, and E. Cavalli, “Comparative optical characterization of various  $\text{Nd}^{3+}:\text{YVO}_4$  single crystals,” *Opt. Mater.* **19**, 193-204 (1999).
  34. Y. F. Chen, “Design criteria for concentration optimization in scaling diode end-pumped lasers to high powers: influence of thermal fracture,” *IEEE J. Quantum Electron.* **35**, 234-239 (1999).
  35. J. Chen, F. Guo, N. Zhuang, J. Lan, X. Hu, and S. Gao, “A study on the growth of  $\text{Yb}:\text{YVO}_4$  single crystal,” *J. Cryst. Growth* **243**, 450-455 (2002).
  36. A. A. Lagatsky, A. R. Sarmani, C. T. A. Brown, W. Sibbett, V. E. Kisel, A. G. Selivanov, I. A. Denisov, A. E. Troshin, K. V. Yumashev, N. V. Kuleshov, V. N.

- Matrosov, T. A. Matrosova, and M. I. Kupchenko, “Yb<sup>3+</sup>-doped YVO<sub>4</sub> crystal for efficient Kerr-lens mode locking in solid-state lasers,” *Opt. Lett.* **30**, 3234-3236 (2005).
37. N. V. Kuleshov, A. A. Lagatsky, A. V. Podlipensky, V. P. Mikhailov, and G. Huber, “Pulsed laser operation of Yb-doped KY(WO<sub>4</sub>)<sub>2</sub> and KGd(WO<sub>4</sub>)<sub>2</sub>,” *Opt. Lett.* **22**, 1317-1319 (1997).
  38. V. E. Kisel, A. E. Troshin, N. A. Tolstik, V. G. Shcherbitsky, N. V. Kuleshov, V. N. Matrosov, T. A. Matrosova, and M. I. Kupchenko, “Spectroscopy and continuous-wave diode-pumped laser action of Yb<sup>3+</sup>:YVO<sub>4</sub>,” *Opt. Lett.* **29**, 2491-2493 (2004).
  39. J. Petit, B. Viana, P. Goldner, D. Vivien, P. Louiseau, and B. Ferrand, “Laser oscillation with low quantum defect in Yb:GdVO<sub>4</sub>, a crystal with high thermal conductivity,” *Opt. Lett.* **29**, 833-835 (2004).
  40. C. Kränkel, D. Fagundes-Peters, S. T. Fredrich, J. Johannsen, M. Mond, G. Huber, M. Bernhagen, and R. Uecker, “Continuous wave laser operation of Yb<sup>3+</sup>:YVO<sub>4</sub>,” *Appl. Phys. B* **79**, 543-546 (2004).
  41. V. E. Kisel, A. E. Troshin, V. G. Shcherbitsky, N. V. Kuleshov, V. N. Matrosov, T. A. Matrosova, M. I. Kupchenko, F. Brunner, R. Paschotta, F. Morier-Genoud, and U. Keller, “Femtosecond pulse generation with a diode-pumped Yb<sup>3+</sup>:YVO<sub>4</sub> laser,” *Opt. Lett.* **30**, 1150-1152 (2005).
  42. S. A Payne, L. L. Chase, H. W. Newkirk, L. K. Smith, and W. F. Krupke, “LiCaAlF<sub>6</sub>:Cr<sup>3+</sup>: a promising new solid-state laser material,” *IEEE J. Quantum Electron.* **24**, 2243-2252 (1999).
  43. C. Czeranowsky, “Resonatorinterne Frequenzverdopplung von diodengepumpten Neodym-Lasern mit hohen Ausgangsleistungen im blauen Spektralbereich,” PhD Dissertation, University of Hamburg (2002).

## **Chapter 7.**

### **Efficient Ultrashort-pulse Visible Sources.**

#### **7.1 Introduction.**

Explanations of nonlinear optical frequency up-conversion in near-infrared solid-state lasers are presented at the beginning of this chapter. This process can be deduced from the three-wave frequency interaction consisting in the sum frequency mixing (SFM). The objective of SHG is to produce femtosecond light pulses in the visible part of the spectrum that would be useful for applications such as photo-lithography, high density optical data storage, ranging, laser printing and display. The most important parameter required to achieve efficient up-conversion is phasematching and so a brief comparison is given between birefringent phasematching and quasi-phasematching. Indeed, the exploitation of the technique of periodic poling in quasi-phase matched crystals has greatly increased the utilisation of existing nonlinear crystals for optical frequency up-conversion. In the context of femtosecond lasers, some previous assessments were reported for frequency doubling in a beta-barium borate crystal (beta-BaB<sub>2</sub>O<sub>4</sub> or BBO) in an intracavity configuration [1]. However, this implementation involves a rather complicated alignment that limits the practicality of this approach. By contrast, the choice made in my research programme was to use a periodically-poled lithium tantalate (PPLT) crystal to produce femtosecond green pulses in an extracavity configuration. The pump source for this frequency doubling was the experimental diode-pumped, passively mode-locked Yb<sup>3+</sup>:KY(WO<sub>4</sub>)<sub>2</sub> (Yb:KYW) laser developed previously and described in Chapter 4 and 5. Evaluations to determine the second harmonic conversion efficiency, the temperature tuning characteristics, optimum grating period, and the dependence of the pulse durations on the focusing strength parameter were carried out.

#### **7.2 Nonlinear Wave Phenomena in a Dielectric Medium.**

Optical phenomena that induce intensity-dependent polarisation were discussed earlier in section 2.4. The susceptibility tensors  $\chi^{(1)}$  and  $\chi^{(2)}$  explain the ease of dipole polarisation

for the dielectric medium in linear and nonlinear response respectively. The roles of these coefficients can be explained by considering equation 2.4.1 in the form of  $P = \alpha E + \beta E^2$  where  $\alpha = \epsilon_0 \chi^{(1)}$  and  $\beta = \epsilon_0 \chi^{(2)}$ . In a three wave frequency mixing, the sum of the incoming electromagnetic waves is given as,  $E = E_1 \cos(\omega_1 t) + E_2 \cos(\omega_2 t)$ . Thus, the induced dipole polarisation can then be expressed as:-

$$P = \alpha(E_1 \cos \omega_1 t + E_2 \cos \omega_2 t) + \beta[2E_1 E_2 \cos(\omega_1 t) \cos(\omega_2 t) + E_1^2 \cos^2(\omega_1 t) + E_2^2 \cos^2 \omega_2 t] \quad (7.2.1)$$

By using the identity  $\cos 2\theta = 2\cos^2 \theta - 1$  and  $2\cos \theta_1 \cos \theta_2 = \cos(\theta_1 + \theta_2) + \cos(\theta_1 - \theta_2)$ , the equation above can be simplified to be:-

$$P = \alpha(E_1 \cos \omega_1 t + E_2 \cos \omega_2 t) + \beta E_1 E_2 (\cos(\omega_1 + \omega_2)t \cos(\omega_1 - \omega_2)t) + \frac{\beta}{2}(E_1^2 \cos(2\omega_1 t)) + \frac{\beta}{2}(E_2^2 \cos(2\omega_2 t)) + \frac{\beta}{2}(E_1^2 + E_2^2) \quad (7.2.2)$$

where  $\omega_1 < \omega_2 < \omega_3$  are angular frequencies with subscript “1” and “2” denote the incident waves while subscript “3” denotes the generated wave correspondingly. The first term in this equation that consists of  $\chi^{(1)}$  represents linear dielectric response and the remaining terms imply the roles of  $\chi^{(2)}$  in nonlinear response. This susceptibility is responsible for sum and difference frequency mixing (SFM, DFM) consisting in the second term and second harmonic generation of wave “1” and “2” in the third and fourth terms. The final term that consists of the sum of quadratical functions  $E_1^2$  and  $E_2^2$  explains the contribution of  $\chi^{(2)}$  for direct current electric field.

$\chi^{(2)}$  has finite values for crystals with non-centrosymmetric configurations and it is zero for centrosymmetric crystals. For the discussion in this part of my thesis, the roles of this second order nonlinearity are described for second harmonic generation (SHG) and sum frequency mixing (SFM). Both of these processes follow the conservation of energy that is given as:-

$$\omega_1 + \omega_2 = \omega_3 \quad (7.2.3)$$

Moreover, the intensity variation between the electric field of each interacting wave as a function of the propagation direction,  $z$  in a medium as deduced from [2,3] can be demonstrated in the coupled wave equations:-

$$\frac{dE_1}{dz} = -\frac{i\omega_1}{2n_1c} d_{eff} E_3 E_2^* e^{-i(\Delta k)z} \quad (7.2.4a)$$

$$\frac{dE_2}{dz} = -\frac{i\omega_2}{2n_2c} d_{eff} E_3 E_1^* e^{-i(\Delta k)z} \quad (7.2.4b)$$

$$\frac{dE_3}{dz} = -\frac{i\omega_3}{2n_3c} d_{eff} E_1 E_2 e^{+i(\Delta k)z} \quad (7.2.4c)$$

where  $n_1$ ,  $n_2$  are refractive indices of the incoming waves and  $n_3$  is the refractive index of the output wave respectively. The nonlinear tensor that maps the components of vector  $E$  to the components of vector  $P$  [see section 2.4] is represented by  $d_{eff}$ , where  $d_{eff} = \chi^{(2)}/2$  and it explains the strength of the nonlinear interaction. In addition,  $\Delta k$  in the exponential form of these equations is the resulting wavevector of  $k_1$ ,  $k_2$  and  $k_3$  and it is expressed as:-

$$\Delta k = k_3 - k_2 - k_1 \quad (7.2.5a)$$

$$= 2\pi \left( \frac{n_3}{\lambda_3} - \frac{n_2}{\lambda_2} - \frac{n_1}{\lambda_1} \right) \quad (7.2.5b)$$

where  $\lambda_1$ ,  $\lambda_2$  and  $\lambda_3$  are the corresponding wavelengths. In SHG, subscript “1” and “2” for the corresponding wavelengths, frequencies and electromagnetic fields of the incoming waves in the three wave frequency mixing are equal to each other and can be substituted by subscript “i1”. Meanwhile, subscript “i2” is used in this process instead of “3” for the generated values as will be discussed in the next section.

### 7.2.1 Phase-matched Second Harmonic Generation.

In this section, second harmonic generation (SHG) coupling by a  $\chi^{(2)}$  nonlinearity become the subject of particular interest. In this process, the angular frequency of the incident wave is represented by  $\omega_{i1}$  while the generated frequency is represented by  $\omega_{i2}$ . Before initiating any discussion about phase matching, the physical process of SHG is explained first. When an electromagnetic wave  $E(t)$  with an incident frequency  $\omega_{i1}$  interacts with a nonlinear transparent material, the atomic clouds in the material vibrate. In the linear case, the induced dipole polarisation can be described by:  $P = \epsilon_0 \chi^{(1)} E$  (equation 2.4.1) where the re-radiated wave has the same frequency as the input radiation.

However, at a sufficiently large effect of  $\epsilon_0 \chi^{(2)} E^2$  (see equation 2.4.1), this incident beam interacts through the second-order susceptibility,  $\chi^{(2)}$  of the material to produce a nonlinear polarisation that generates a second harmonic wave with the resulting frequency of  $\omega_{i2} = 2\omega_{i1}$ . By substituting the sum of electric field  $E = 2E_{i1} \cos(\omega_{i1}t)$  to equation 7.2.2, in the form of electric field this process can be described as:-

$$\begin{aligned}
 P &= \alpha E + \beta E^2 \\
 &= 2\alpha E_{i1} \cos(\omega_{i1}t) + 2E_{i1}^2 \beta [1 + \cos(2\omega_{i1}t)] \\
 &= 2E_{i1}^2 \beta + 2\alpha E_{i1} \cos(\omega_{i1}t) + 2E_{i1}^2 \beta \cos(2\omega_{i1}t) \quad (7.2.6)
 \end{aligned}$$

where  $E_{i1}$  is the electric field for the incoming beam. The first term in the equation above describes the direct current field in the crystal, the second term describes the fundamental frequency and the third term is the second harmonic frequency.

By considering the fundamental wavelength as  $\lambda_{i1}$  that travels at a velocity determined by  $n_\omega$ , the second harmonic wave acquires wavelength of  $\lambda_{i2}$  where  $\lambda_{i2} = \lambda_{i1}/2$  which travels at a velocity determined by  $n_{2\omega}$ .  $n_\omega$  is the refractive index of the fundamental frequency while  $n_{2\omega}$  is the refractive index of the second harmonic frequency. In general, due to material dispersion  $n_\omega$  is not equal to  $n_{2\omega}$  ( $n_{2\omega} > n_\omega$ ). This leads to alternating growth of the output harmonic waves as illustrated in figure 7.1(a). From this figure, maximum second harmonic wave power is observed for each odd number of the

coherence length due to constructive interference and minimum power is observed for each even number of the coherence length due to destructive interference.

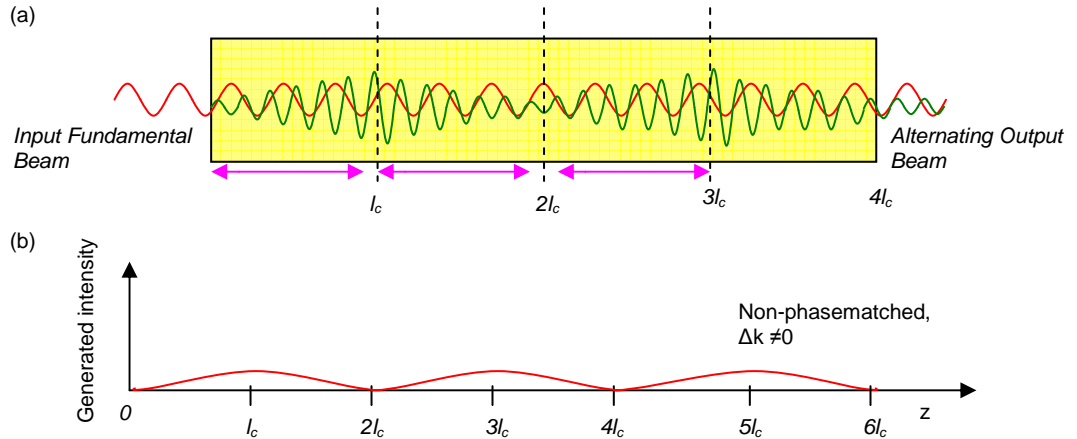


Figure 7.1. (a) Alternating growth of second harmonic waves (green colour) over the fundamental waves (red colour) in a non-phase matched crystal and (b) the corresponding generated intensity that implies an increase in the wavevector mismatch,  $\Delta k \neq 0$  [2].

This mechanism is explained with an increase in the second harmonic (SH) power from the fundamental to reach maximum at a distance  $z = l_c$  before reducing back to the fundamental when  $l_c \leq z \leq 2l_c$ . This produces a repetitive oscillation in the generated intensity of the second harmonic waves  $I_{2\omega}$ , for each even number of the coherence length ( $2l_c, 4l_c, 6l_c \dots$ ) that increases the wavevector mismatch  $\Delta k \neq 0$  as illustrated in figure 7.1(b). As a  $\pi$ -phase shift has been accommodated at  $z = l_c$ , a coherence length  $l_c$  is defined as the distance that implies a phase mismatch  $\Delta k \cdot l_c = \pi$  where:-

$$\Delta k = 2\pi \frac{2}{\lambda_{i1}} (n_{2\omega} - n_{\omega}) \quad (7.2.7)$$

and:-

$$l_c = \frac{\lambda_{i1}}{4(n_{2\omega} - n_{\omega})} \quad (7.2.8)$$

To address this mismatch mechanism, a technique that is known as phase matching [4] was introduced to achieve the best possible nonlinear conversion efficiency. Phase matching is required to enable several phase-sensitive nonlinear processes such as parametric amplification and oscillation, sum and difference frequency generation and in particular frequency doubling. This technique is implemented to maintain a proper phase

relationship between the interacting waves along the propagation direction of the beam. As the fundamental wave propagates through the crystal, the resulting wavevector is matched,  $\Delta k = 0$ , where the generated intensity grows exponentially due to continuous constructive interference between the relative phase of the interacting waves as illustrated in figure 7.2. This resulting wavevector  $\Delta k$ , consists of wavevectors for the fundamental  $k_{i1}$  and for the generated waves  $k_{i2}$  where  $\Delta k = k_{i2} - 2k_{i1}$ . This equation corresponds to the conservation of photon momentum that is given as:-

$$\frac{1}{c}(n_{2,\omega}\omega_{i2} - 2n_{\omega}\omega_{i1}) = 0 \quad (7.2.9)$$

The corresponding diagram for these processes is depicted in figure 7.3. The wavevector for phase matching scheme in a nonlinear medium can be achieved either collinearly or non-collinearly.

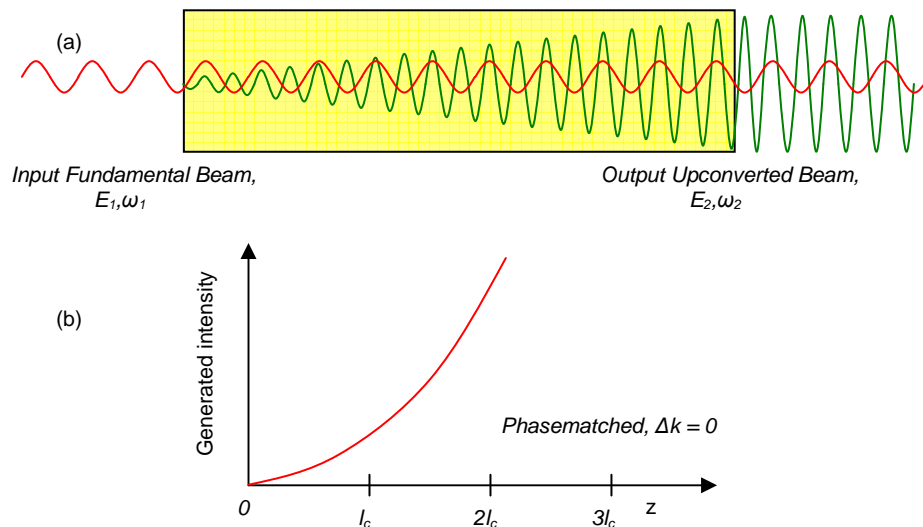


Figure 7.2. (a) Continuous growth of second harmonic waves (green colour) over the fundamental waves (red colour) and (b) the corresponding generated intensity in a phase-matched nonlinear crystal for the wavevector matching,  $\Delta k = 0$ .  $E_{i1}$  and  $E_{i2}$  are energies for the fundamental and generated waves that imply frequencies of  $\omega_{i1}$  and  $\omega_{i2}$  respectively [2].

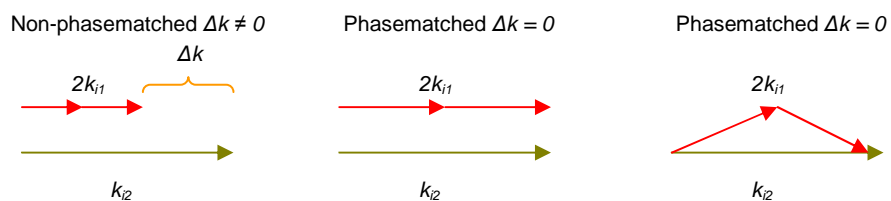


Figure 7.3. Wavevector diagram for non-phasematching condition over those of collinear and noncollinear phase matching condition for efficient second harmonic generation [2].

From equation 7.2.4, by expressing the electric field in the exponential form of  $E(z)e^{ikz}$ , the change in the strength for the corresponding fields in two wave interactions can be shown to be:-

$$\frac{dE}{dz} = \frac{-i\omega_{i1}}{n_{\omega}c} d_{eff} E_{i1}^* E_{i2} e^{-i\Delta kz} \quad (7.2.10a)$$

$$\frac{dE_{i2}}{dz} = \frac{-i\omega_{i2}}{2n_{2\omega}c} d_{eff} E_{i1}^2 e^{i\Delta kz} \quad (7.2.10b)$$

where  $E_{i1}$  and  $E_{i2}$  are the amplitudes of the fundamental and second harmonic fields,  $\frac{dE}{dz} = \frac{2dE_{i1}}{dz}$ , and  $z$  is the distance along the propagation direction of the beam,. With phase matching, the dispersion effects in the refractive index of the materials can be handled appropriately (especially by matching the refractive indices ( $n_{\omega}$  and  $n_{2\omega}$ ) in an anisotropic material).

## 7.2.2 Critical and Noncritical Phase Matching.

One of the widely used phase matching techniques involves the exploitation of birefringence in an anisotropic nonlinear crystal, so called birefringent phasematching (BPM) [5]. Birefringence refers to a material property where different refractive indices are obtained for distinct polarisations. These refractive indices depend on the direction of propagation, polarisation and frequency of the incident waves [see appendix D]. Two polarisation eigenstates occur in a birefringence material. The polarisation eigenstate that has a constant polarisation direction with angle is called as ordinary beam,  $o$  – beam while the remaining polarisation eigenstate that has angular dependence polarisation direction is called as extraordinary beam,  $e$  – beam. (More references about birefringence phase matching can be found in [3,6-8]). For the three-wave frequency mixing in an anisotropic crystal, two types of phase matching occur as indicated in table 7.1. In the type I phase matching, the fundamental beam consists of a single polarisation that is perpendicular to the second harmonic beam and the type II phase matching consists of a mixed polarisation of the fundamental beam with respect to the output beam.

Table 7.1. Two types of phase matching for the 3-wave frequency mixing where *o* stands for ordinary-beam and *e* stands for extraordinary beam.

	Type I ( $\omega_1 + \omega_2 \rightarrow \omega_3$ )	Type II ( $\omega_1 + \omega_2 \rightarrow \omega_3$ )
Positive	$e + e \rightarrow o$	$o + e \rightarrow o$ $e + o \rightarrow o$
Negative	$o + o \rightarrow e$	$o + e \rightarrow e$ $e + o \rightarrow e$

In birefringent phase matching critical angle, temperature, and compositional tuning [9] are required. Due to the angular sensitivity required, BPM is an example of *critical phase matching* (CPM). The term critical refers to the sensitivity of this process to the misalignment of the propagating beams, thus the proper adjustment of the crystal is required to ensure that the propagation direction of the pump wave is at the correct angle with respect to the optic axis. The limitations that exist in interaction length, spot size and acceptance angle are caused by the resulting Poynting vector walk-off [see appendix E] while tuning the angle. This leads to poor spatial overlap of the waves that suppresses the beam quality and decreases the nonlinear efficiency.

In contrast, non-critical phase matching (NCPM) can be initiated when the required propagation direction is aligned with one of the principal refractive index axes ( $x, y, z$ ). This process is also known as temperature phase matching as the tuning of the temperature dependent refractive index  $n(\lambda, T)$  is required to synchronise the relative phase velocities of the propagating beams. The advantages of NCPM are similar ray and wave directions that eliminate the existence of spatial walk-off. Therefore, higher efficiency in nonlinear frequency up-conversion  $\eta_{SHG}$  can be achieved. This physical effect was manifested in the assessment carried out for quasi-phase matched crystal [see figure 7.12].

Although temperature tuning is favourable for acquiring non-critical phase matching condition, the main drawback is due to the elevated temperature of the operating condition. On the other hand, the development of compositional tuning (tuning of birefringent material) is long and expensive even though non-critical phase matching is allowed at a more appropriate temperature. The requirement of birefringence in this tuning method reinforces continuing research to develop new nonlinear materials for optical

frequency up-conversion. However, this development process has proven to be difficult and expensive, thus alternative phase matching schemes have been developed for more practical solutions [see section 7.3].

### 7.2.3 Phase matching bandwidth.

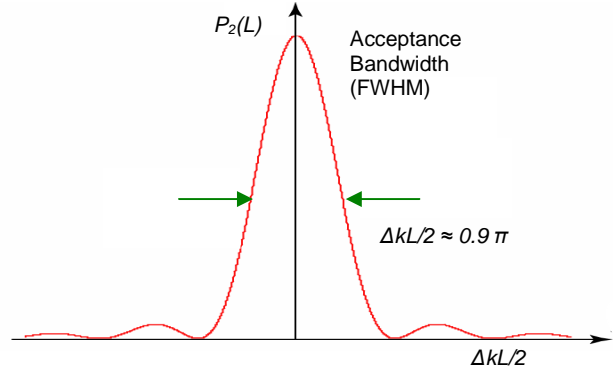


Figure 7.4. The ideal tuning curve for nonlinear frequency conversion [2].

In phase matching, the efficient nonlinear frequency conversion is limited in a finite frequency spectrum of the interacting waves. This is explained in an ideal tuning curve that has the form of  $\text{sinc}^2 \frac{\Delta k L}{2}$  as presented in figure 7.4 above. This tuning curve can be deduced from the nonlinear wave equation, where by inserting a nonlinear gain parameter,  $\Gamma$ , into equation (7.2.10b) the change in second harmonic amplitude field  $E_{i2}$  can then be expressed as:-

$$\frac{dE_{i2}}{dz} = \Gamma d_{\text{eff}} e^{i\Delta k z} \quad (7.2.11)$$

where  $\Gamma$  can be described as:-

$$\Gamma = -\frac{i\omega_{i2} E_{i1}^2}{2n_{2\omega} c} \quad (7.2.12)$$

where  $\omega_{i2} = 2\pi\nu_{i2}$ . The relation between  $\Gamma$  with the generated power over the crystal length  $L$  can be demonstrated to be:-

$$P_{2\omega}(L) = \Gamma^2 d_{eff}^2 L^2 \text{sinc}^2\left(\frac{\Delta k L}{2}\right) \quad (7.2.13a)$$

and:-

$$\text{sinc}^2\left[\frac{\Delta k L}{2}\right] = \left[\frac{\sin\left(\frac{\Delta k L}{2}\right)}{\frac{\Delta k L}{2}}\right]^2 \quad (7.2.13b)$$

These equations indicate the proportionality of the generated optical power with  $\text{sinc}^2 \frac{\Delta k L}{2}$ .

They also play important roles for an ideal tuning curve that describes the maximum second harmonic conversion efficiency ( $\eta_{SHG}$ ) in nonlinear interactions that affects the phasematching mechanism. This efficiency, which is influenced mainly by  $d_{eff}^2$  and  $L^2$ , is defined as the ratio between the generated power  $P_{2\omega}$  with respect to the fundamental power  $P_{\omega}$ ,  $\left(\eta_{SHG} = \frac{P_{2\omega}}{P_{\omega}}\right)$  and can be deduced from the height of central peak explicit in figure 7.4.

The full width at a half maximum (FWHM) that is measured from the central peak of this ideal tuning curve is known as acceptance bandwidth. It shows the frequency range over which an efficient phase matching process can operate. In the time domain this bandwidth limitation is explained by the group-velocity mismatch scheme that implies temporal walk-off and in the spatial domain it is explained in the angular dependence refractive index  $n_e(\theta)$ . Another important parameter that influences this acceptance bandwidth is the temperature dependence refractive index  $n(\lambda, T)$ . Both of these parameters  $[n_e(\theta), n(\lambda, T)]$  can be obtained from Sellmeir equation [10,11] where their appropriate tuning in a finite frequency range must be met for the optimisation of efficient nonlinear frequency up-conversion.

### 7.3 Quasi-Phase Matched Second Harmonic Generation.

Quasi-phasematching [4,7] is seen as a more viable technique because it offers some solutions to the drawbacks associated with birefringent phasematching. It increases the

practicality of existing materials and eliminates or reduces any critical requirements for angle or temperature tuning to obtain the phasematching condition of  $\Delta k = 0$ . In this technique, the oscillatory solution of  $\Delta k \neq 0$  is allowed by periodic reversal of the mismatch mechanism whenever the relative phase-mismatch of the interacting waves slips by  $\pi$ . This brings a continuing increase to the generated intensity of the second harmonic frequency  $I_{2\omega}$  for each coherence length in coincidence with the conventional phase matching scheme as demonstrated in figure 7.5.

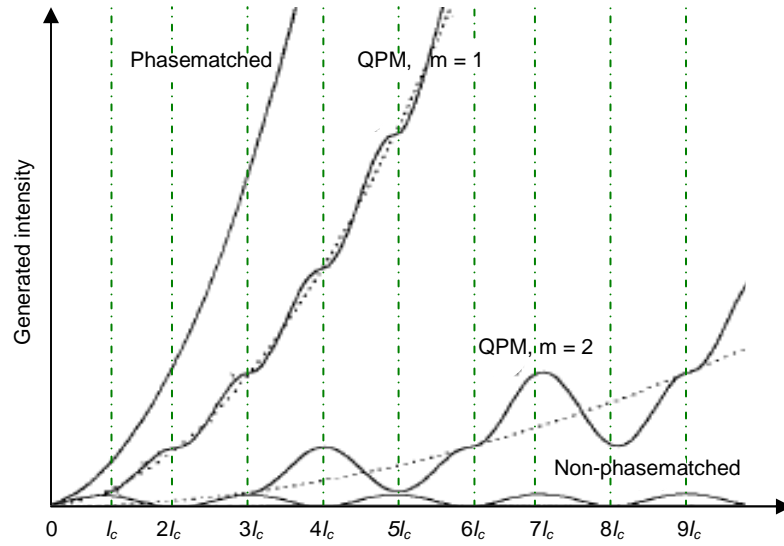


Figure 7.5. Efficient frequency conversion in the first-order ( $m=1$ ) and second-order ( $m=2$ ) quasi-phase matching (QPM) over the non phase-matched and phase-matched conditions. The dotted green lines show the optimised value of  $d_{eff}$  [2].

This technique is implemented by physically reversing the sign of the nonlinear coefficient  $d_{eff}$  which introduces an additional  $\pi$ -phase shift to the existing relative phase of the interacting waves to avoid destructive interference. The nonlinear wave equation of this process can be demonstrated as:-

$$\frac{dE_{i2}}{dz} \propto -d_{eff} E_{i1}^2 e^{i\Delta kz} = d_{eff} E_{i1}^2 e^{i(\Delta kz + \pi)} \quad (7.3.1)$$

Owing to the fact that  $\Delta k l_c = \pi$  whenever  $z = l_c$ , the resulting addition of the new  $\pi$ -phase shift is exactly cancelled by the reversal sign of  $d_{eff}$ . To allow the implementation of quasi-phasematching, a nonlinear coefficient with a grating period of

$\Lambda_g = 2l_c$  can be designed into the crystal.

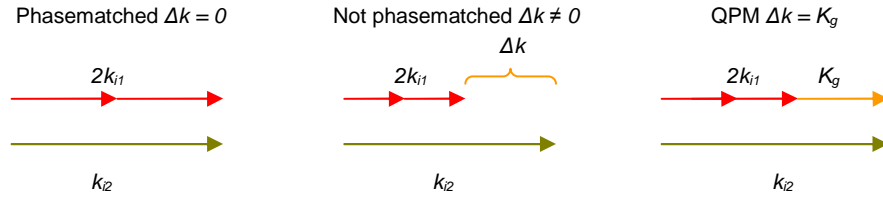


Figure 7.6. Wavevector diagram for efficient second harmonic generation.

Figure 7.6 above represents the mechanisms involved in phase matched/non-phase matched and quasi-phase matched conditions. The effect of adding the grating vector on quasi-phase matching is shown where the difference between the interacting wavevectors is equal to the generated one,  $\Delta k = K_g$ . With the introduction of this periodicity to the nonlinear coefficient, the equation for quasi-phases matching in (7.2.11) becomes:-

$$\frac{dE_{i2}}{dz} = \Gamma d_{eff} e^{i\Delta k z} = \Gamma |d_{eff}| e^{iK_g z} e^{i\Delta k z} = \Gamma |d_{eff}| e^{i\Delta k_Q z} \quad (7.3.2)$$

where the grating period wavevector  $K_g = \frac{2\pi}{\Lambda_g}$  and the resulting quasi-phase matching wavevector is described as:-

$$\Delta k_Q = \Delta k - K_g \quad (7.3.3)$$

Noncritical quasi-phase matching can be achieved by optimising the design of the grating period  $\Lambda_g$  on a nonlinear crystal to match the interacting wavevectors  $\lambda_{i1}$  and  $\lambda_{i2}$ . The tuning of  $K_g$  is preferable in most quasi-phase matching devices rather than that of angle-tuning. From equation (7.2.8) and (7.3.3) the period of grating wavelength  $\Lambda_g$  needed to be written on the bulk crystal is simplified as:-

$$2\pi \frac{2}{m\lambda_{i1}} (n_{2\omega} - n_\omega) - \frac{2\pi}{\Lambda_g} = 0 \quad (7.3.4a)$$

$$\Lambda_g = \frac{m\lambda_{i1}}{2(n_{2\omega} - n_\omega)} \quad (7.3.4b)$$

where  $m$  is the order of the quasi-phase matching. In most applications the typical period of  $\Lambda_g$  written on the bulk crystal is of the order of 5  $\mu\text{m}$  to 10  $\mu\text{m}$ .

From Fourier series analysis the periodic nonlinear coefficient  $d(z)$  for quasi-phases matching can be described as:-

$$d(z) = d_{\text{eff}} \sum_{m=-\infty}^{\infty} \left[ \left( \frac{2}{\pi \cdot m} \right) \sin \pi \cdot m \cdot D \right] e^{imK_g z} \quad (7.3.5)$$

where  $D = a/\Lambda_g$  is the duty cycle and  $a$  is the width of a domain section. From the equation above, it can be seen that for a given  $d_{\text{eff}}$ , the generated intensity  $I_{2\omega}$  for a higher-order quasi-phase matching is reduced by a factor of  $2/\pi \cdot m$  with respect to the conventional phase-matched interaction [figure 7.5]. The duty cycle for the optimisation of  $d_{\text{eff}} = 2/\pi m$  is  $D = 0.5$  for  $m = 1$  and  $D = 0.25$  for  $m = 2$ . To achieve first-order quasi-phase matching the sign of  $d_{\text{eff}}$  is reversed periodically for each coherence length  $l_c$  and for the achievement of second-order, the domain lengths of  $l_c$  and  $3l_c$  are alternated as illustrated in figure 7.5.

Quasi-phase matching (QPM) has several advantages when compared to birefringent phase matching. Instead of the homogenous crystal structure used in birefringent phase matching, QPM uses a crystal with spatially modulated nonlinear properties. It can be operated at convenient temperatures at any wavelength within the transparency region of the material. However, at shorter wavelengths, higher QPM orders must be selected for the grating period  $\Lambda_g$  due to the difficulty in obtaining grating features of  $<4 \mu\text{m}$  and this leads to some compromise in the maximum second harmonic conversion efficiency [figure 7.5]. The acceptance angle is large and spatial walk-off can be avoided due to the fact that the non-critical phase matching allows propagation of the interacting waves along the optical axis of the crystal. The interaction can exploit the highest component of the nonlinear susceptibility tensor of the material,  $\chi^{(2)}$ , without the requirements of direction imposed by BPM. For instance in lithium tantalate, a nonlinear tensor  $d_{31}$  that has a value up to 4  $\text{pmV}^{-1}$  is manipulated for BPM compared to the higher coefficient  $d_{33}$  of 26  $\text{pmV}^{-1}$  [6] for QPM. By accounting the reduction factor of  $2/\pi \cdot m$ , the

efficient coefficient  $d_{eff}$  of  $16.5 \text{ pmV}^{-1}$  can be accessed, thus allowing for higher up-converted efficiency over that of a conventional one. This technique can then increase the benefits of existing crystals, thus allowing the use of materials with no birefringence and even optically isotropic materials. In addition, tuning of quasi-phase matching is also possible with angle, temperature and grating period and this expands the range of selection for novel devices. Thus, the introduction of grating period as another adjustable phase matching parameter enhances flexibility for QPM devices. In contrast to conventional phase matching, quasi-phase matching can produce efficient frequency conversion even with crystals that are difficult to phase match using more established techniques. This gives a new dimension in the search for efficient nonlinear generation where the development of fabrication methods for already existing materials can be fully optimised, thus avoiding any unnecessary time and cost involved to search for completely novel materials having adequate birefringence properties.

#### **7.4 Periodically-poled Devices for Quasi-phase Matching.**

Initial quasi-phase matching attempts were performed as early as 1976 by stacking tens of micrometer thick crystal plates with alternating layers rotated ( $\pm d_{eff}$ ) [12]. However, this technique was not practical and this remained the case until the mid-1980s when a simpler method for phase matching known as periodic poling was introduced by reversing the ferroelectric domain polarity in a monolithic crystal [figure 7.7]. The ferroelectric materials favourable for quasi-phase matching techniques that have become the subject of current research interests include lithium niobate ( $\text{LiNbO}_3$ ) [13,14] with its isomorph lithium tantalate ( $\text{LiTaO}_3$ ) [15] and KTP ( $\text{KTiOPO}_4$ ) [16] with its isomorphs RTA ( $\text{RbTiOAsO}_4$ ) and KTA ( $\text{KTiOPO}_4$ ). Analytical approaches [7] to model effective nonlinear parameters that vary and involving tuning properties, periodic structures and generated intensity along the interaction length have been developed. The quasi-phase matched frequency conversion technique has now become well recognized following the implementation of electric field poling method based on direct e-beam and ion-beam writing [17,18] in  $\text{LiNbO}_3$  [19] and  $\text{LiTaO}_4$  crystal.

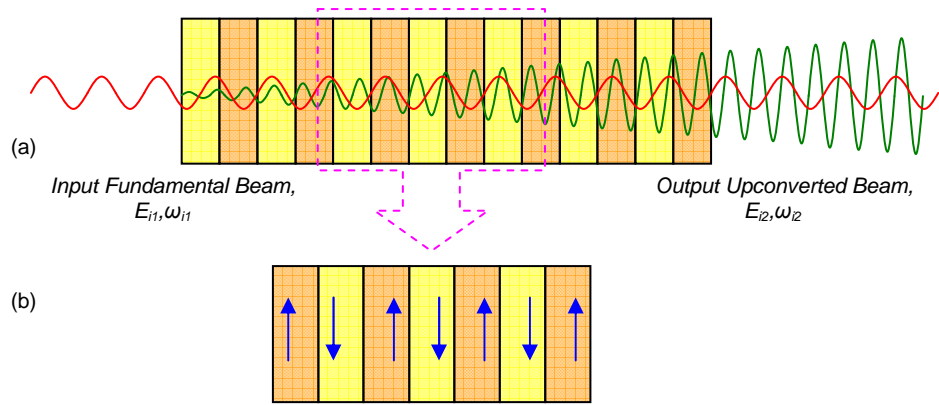


Figure 7.7. (a) Physical process in a quasi-phase matched crystal and (b) the corresponding periodic reversal in the sign of the nonlinear coefficient for each coherence length.

Current developments in periodically-poled devices have covered a wide transmission range from 0.35-5  $\mu\text{m}$  that is well-suited to nonlinear optics applications. The techniques used to fabricate periodically-poled ferroelectrics on mature substrate wafers such as lithography and planar processing have been very well developed for the microelectronics industry. These, for instance, allow the production of periodically-poled lithium niobate (PPLN) in large size and volume which to a large extent has been widely benefited from the use of LN for electronics [20] and integrated optics markets. Another beneficial property of LN is its straightforward fabrication using the Czochralski growth technique from a melt. A high quality optical grade boule with dimensions of 100 x 120 mm can be produced in one to two days. By contrast, although KTP has been widely used for nonlinear crystal in the laser industry, its production volume is far below that of LN. It is relatively difficult to grow from the solution growth and crystals of up to 20 mm length take typically 3-6 weeks to grow.

## 7.5 Frequency Doubling with a Thick Nonlinear Crystal in an Extracavity Configuration.

Second harmonic generation (SHG) of near-IR ultrafast lasers is an attractive technique to generate light in the visible range. The high peak intensities of the ultrafast pulses produce high nonlinearity while the short duration of the generated pulses are favourable for many applications such as time-resolved spectroscopy and studies in biology and photomedicine. In addition, their shorter wavelengths produce smaller spot sizes  $w(z)$  that exhibit higher

resolution performance, thus explaining the reason why compact coherent visible light pulses can be used for lithography, high density optical data storage, ranging, laser printing and display. A coherent green source can be obtained from the frequency doubling of passively mode-locked Nd-doped and Yb-doped lasers operating at wavelengths around 1  $\mu\text{m}$  [1,21]. In the femtosecond regime an upper limit for the nonlinear crystal length is set by the group-velocity mismatch (GVM). This mismatch is defined as the phenomenon when the pulses are separated in a medium due to the difference in the group velocities ( $v_g = \delta\omega/\delta k$ ) [section 2.4]. This leads to a temporal walk-off that broadens the output second harmonic pulses compared to the input pulses and restricts phase matching to a narrow second harmonic frequency range. When the delay between these two pulses becomes longer than the duration of the fundamental pulse, the beams have propagated along a GVM/non-stationary length,  $L_{nst}$ . This non-stationary length  $L_{nst}$  is defined as the distance at which two initially overlapped pulses at different wavelengths become separated by a time equal to the fundamental pulse duration  $\tau_{i1}$  that can be shown to be:-

$$L_{nst} = \tau_{i1} / \alpha \quad (7.5.1)$$

where the GVM parameter  $\alpha = 1/v_{i2} - 1/v_{i1}$  with  $v_{i2}$  and  $v_{i1}$  are the group velocities of the second harmonic and fundamental pulses respectively. This parameter ( $L_{nst}$ ) determines the choice of length  $L$  for the nonlinear media that are often in the order of hundreds of micrometers or less.  $L = L_{nst}$  ensures that the generated SH pulses have durations close to that of the fundamental pulses. However, a drawback arising from the reduction in the interaction length is a lower SHG efficiency.

To solve this limitation, thick nonlinear media are chosen in spite of the inevitable temporal broadening of the second harmonic pulses. It was demonstrated that highly efficient SHG is possible by single-pass frequency doubling of a focused femtosecond laser beam in a “thick” nonlinear crystal where the group-velocity mismatch (GVM) is significant [22,23]. For instance, 3 mm and 5 mm crystal lengths were used instead of the 100  $\mu\text{m}$  non-stationary length  $L_{nst}$  of  $\text{KNbO}_3$  when the fundamental pulses were 120 fs at an input wavelength of 858 nm [23]. For the unfocused fundamental beam under the conditions of a thick nonlinear crystal  $L_{nst} \ll L$ , the generated second harmonic pulses are

longer in time by a factor of  $L/L_{nst}$ . However, under conditions of tight focusing [24] the duration of the generated pulses can be close to that of the fundamental while the efficiency of the frequency conversion can also be increased. Despite the drawbacks associated with the length of the nonlinear media due to the effects of GVM, previous assessments on several crystals such as  $\text{KNbO}_3$  [22,23,25-27],  $\text{LiB}_3\text{O}_5$  and  $\beta$ -barium borate [28] have reported efficient frequency doubling of focused femtosecond pulses (120-200 fs) in a thick nonlinear media with a ratio of  $L/L_{nst} > 20$ . The conversion efficiency obtained in these experiments had exceeded 60 % while the duration of the generated near-transform limited SH pulses remained within the femtosecond regime with around 2-3 times temporal broadening with respect to the duration of the fundamental pulses [23]. Within this subject, the rapid development of Yb-doped femtosecond lasers as pump sources over the past few years thus represents a route towards the achievement of compact, highly efficient, and high peak power visible light sources.

## **7.6 Implementations.**

Two key components were used in this evaluation. The first was a SESAM-assisted Yb:KYW femtosecond laser as a fundamental beam source and the second was a thick nonlinear PPLT crystal in an extracavity configuration that became the subject of interest for efficient nonlinear second harmonic generation (SHG). The main reasons for placing this nonlinear crystal externally was because of the ease of alignment. Another reason was to avoid the increase of second harmonic power inside the laser cavity that reduces the fundamental power required for the initiation of stable mode locking scheme at SESAM.

### **7.6.1 Experimental Set-up.**

The femtosecond laser which was used as a pump source for SHG shown in figure 7.8 was designed to operate at a pulse repetition rate of 86 MHz. The gain material was a 1.2 mm long 10 at. %  $\text{Yb}^{3+}$  doped  $\text{KY}(\text{WO}_4)_2$  Brewster-angled crystal that was oriented in the cavity for propagation along the  $b(N_p)$  axis with its polarisation parallel to the crystalloptic  $N_m$ -axis. The two pump sources (LD1 and LD2) used to pump the gain material were single mode fibre-coupled polarisation-maintaining InGaAs diode lasers (JDS Uniphase)

emitting at 981 nm which produced a combined output power of 970 mW. Mirror 1 (M1) had a radius of curvature of 75 mm while mirror 2 (M2) had a radius of curvature of 100 mm. Both of these mirrors were designed for a high transmission up to  $\sim 98\%$  at a pump wavelength of 981 nm and a high reflectivity for the wavelength range between 1025 nm to 1100 nm. The SESAM with a modulation depth of 2% at 1045 nm was used for passive mode locking operation while a plane-wedged output coupler (OC) with 3% transmission was used at the laser wavelengths.

Aspherical lenses (AL) of 15 mm and spherical lenses of 63 mm were used in this assessment to collect and focus the pump beam into the gain medium, resulting in the pump beam waist,  $w_{p,0}$  of  $17\ \mu\text{m}$  ( $1/e^2$  intensity). From the ABCD matrix formalism, the laser beam waist,  $w_{l,o}$  focused on the crystal was  $18\ \mu\text{m}$  while the optimum laser beam waist  $w_{SESAM}$  focused on the SESAM was  $160\ \mu\text{m}$ .

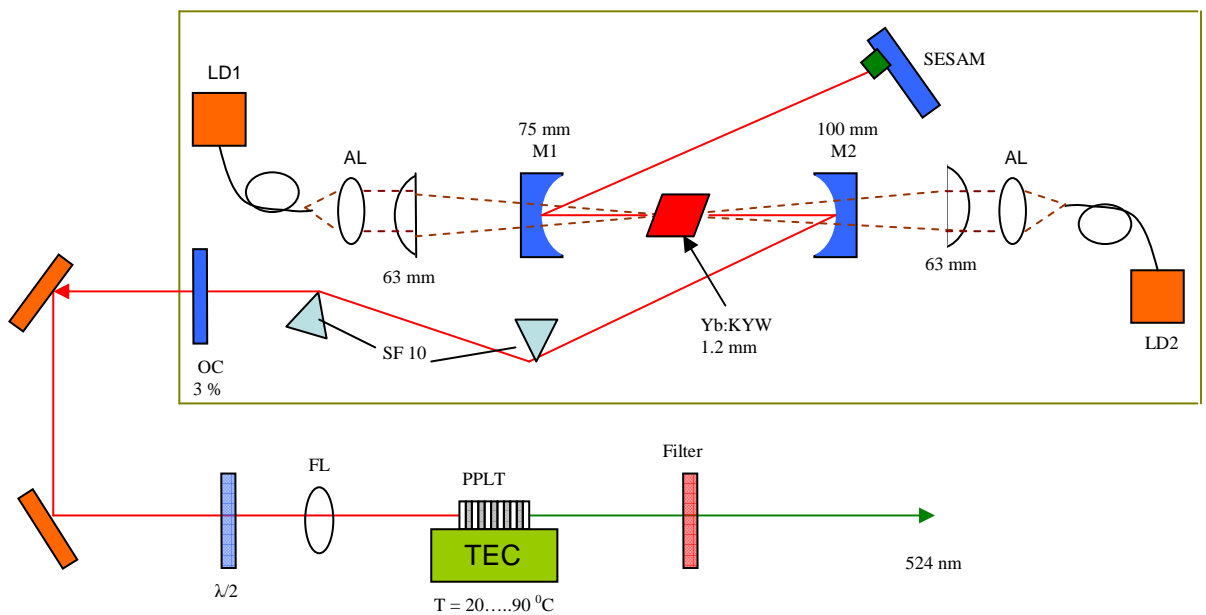


Figure 7.8. Schematic diagram of femtosecond green pulse generation in a PPLT crystal pumped by using a femtosecond Yb:KYW laser.

The output beam from the 3% output coupler was deviated by using two steering mirrors to pass through a half-wave plate, focusing lens (FL), quasi phase-matched crystal and a dichroic mirror (filter) before measurement of the resulting up-converted output beam was performed [figure 7.8]. The half-wave plate  $\lambda/2$  was used to control the input polarisation of the fundamental beam while a filter coated for a high reflectivity at 1050 nm and a high transmission at 524 nm was used to block the fundamental radiation. The

fundamental beam was collected and focused into the non-linear crystal by using focussing lenses  $f$  with focal lengths ranging from 4.5 mm to 40 mm as shown in table 7.2 This implies a series of fundamental beam waist radius  $w_{l,0}$  inside the nonlinear crystal from 2.1  $\mu\text{m}$  to 18.3  $\mu\text{m}$ . The confocal parameter,  $b$  which is the effective interaction length for nonlinear second harmonic generation is defined as twice the value of Rayleigh range  $z_R$  and can be shown to be:-

$$b = 2.z_R = \frac{2.\pi.n}{\lambda_{l1}} w_{l,0}^2 \quad (7.6.1)$$

where  $n = 2.14$  is the refractive index of the nonlinear crystal. The crystal length to confocal parameter ratios  $L/b$  that show the strength of focusing parameter inside the medium ranged from 62 to 0.8 and were determined to observe its correlation with the resulting second harmonic efficiency.

Table 7.2 Variable parameters used for efficient SH generation.

$f$ (mm)	$w_{l,0}$ ( $\mu\text{m}$ )	$b$ (mm)	$L/b$
40	18.3	4.3	0.8
25	11.9	1.82	1.9
15.4	7.0	0.62	5.6
8	3.7	0.176	20
4.5	2.1	0.056	62

### 7.6.2 Periodically-poled Lithium Tantalate.

Lithium tantalate (LT) that can be an appropriate crystal for nonlinear frequency up-conversion has previous restriction for this purpose due to its small birefringence properties. It is more difficult to grow and not commercially well developed due to its higher melting point up to 1530  $^{\circ}\text{C}$  compared to 1250  $^{\circ}\text{C}$  for LN. However, the introduction of the quasi-phase matched (QPM) frequency conversion technique has sped up the utilisation of periodically-poled lithium tantalate (PPLT) for the generation of visible light from near-infrared lasers. Lithium tantalate has similar poling parameters and coercive field as that of lithium niobate while its spontaneous polarisation  $P$  is slightly

lower [2]. It has several advantages over LN due to its wider transparency range in the UV/visible between 280 nm to 550 nm and nearly two times higher photorefractive damage threshold. It is operable at room temperature and can also be readily poled with a period as short as 1.75  $\mu\text{m}$  [29] in spite of its smaller nonlinear coefficient ( $d_{33} = 26 \text{ pmV}^{-1}$ ) than that of KTP or LN. All of these advantages have increased its potential utilisation for frequency up-conversion with high peak and average power sources for commercial applications. As a result, initial works have demonstrated the generation of UV and visible light by frequency doubling in a periodically poled LT [29-31].

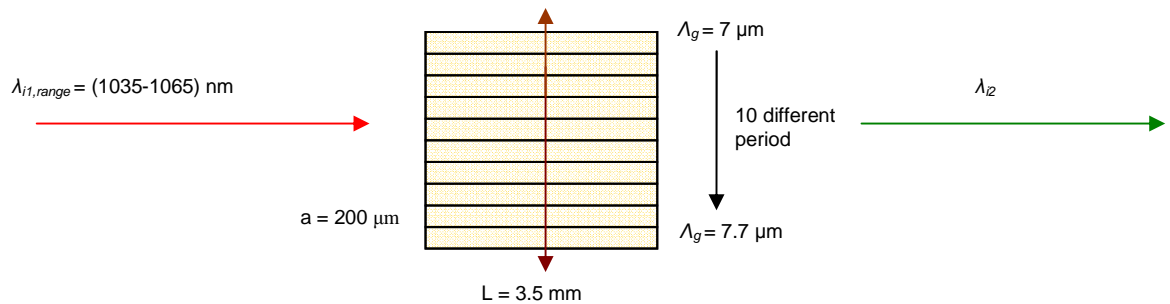


Figure 7.9. Schematic of the design of PPLT crystal where  $\lambda_{1,range}$  is the range of fundamental wavelength and  $\lambda_2$  is the second harmonic wavelength. The brown arrow show the direction for grating period tuning.

Based on the work done by previous investigators [22,23], the length of the PPLT crystal used in this assessment was chosen to be 3.5 mm. This choice was made to obtain efficient SHG in a thick nonlinear crystal with an approximate ratio of  $L/L_{nst} = 20$ . Although a shorter length of crystal could have been chosen a shorter interaction length  $b$  would have led to a lower conversion efficiency. Also, a longer crystal would have a wider spot size  $w(z)$  at the edge of the crystal and this would not be well matched to the grating domain width of 200  $\mu\text{m}$ . This crystal was placed on a copper plate and it was heated in the temperature range from 20  $^{\circ}\text{C}$  to 90  $^{\circ}\text{C}$  with an accuracy of 0.1  $^{\circ}\text{C}$ . The end faces of the PPLT crystal were optically polished and anti-reflection coated for both fundamental and second harmonic wavelength ranges.

The QPM order can be chosen from equation (7.3.4b), where the  $m$ -th order has to be selected first before writing the grating period on the crystal. For shorter wavelengths,  $\Lambda_g$  is short and a higher order of quasi phase matching ( $m \geq 2$ ) needs to be selected. However, in this assessment  $m = 1$  and the duty cycle  $D = 0.5$  were selected for the maximization of the nonlinear coefficient as shown in figure 7.5. Once the QPM order had been chosen, the QPM period of the different gratings was calculated in accordance with a temperature-

dependent Sellmeier equation for the congruent type of LT [32]. This  $\Lambda_g$  was designed to provide efficient frequency doubling of the fundamental beam in the range of 1035 nm to 1065 nm. Ten different gratings were written on the crystal with QPM domain periods ( $\Lambda_g$ ) varying in the range of 7.0 to 7.7  $\mu\text{m}$  and a width of 200  $\mu\text{m}$ . The conventional type-0 of nonlinear interaction ( $e + e \rightarrow e$  scheme) that exploits the  $d_{33}$  nonlinear coefficient of the crystal was used. During the experiment, we simply chose the most appropriate domain period that gave maximum output power for a given pump wavelength  $\lambda_{i1}$  at a given nonlinear crystal temperature. This was done by shifting the PPLT crystal vertically as shown in figure 7.9.

## 7.7 Experimental Results.

Before any SHG assessment was carried out in the extracavity configuration, the output pulses from the pumped source Yb:KYW femtosecond laser were fully characterised. The output beam had a slightly elliptical spatial mode with a 1.12:1 ratio of ellipticity and the beam quality  $M^2$  factor was measured to be 1.13 in the sagittal and 1.17 in the tangential directions respectively. Near transform-limited pulses were obtained over the output tuning range of 1037 nm to 1049 nm as shown in figure 7.10. Once the mode-locked pulses were initiated, subsequent adjustment of the optical elements in the laser cavity was performed to optimise the average output power. The shortest pulse duration obtained was 125 fs at a centre wavelength of 1045 nm. The spectral width was 10 nm and the average output power was 326 mW that corresponds to a peak power  $P_{pk}$  of 30 kW. However, for the most efficient second harmonic generation, this laser generated a maximum average output power of 394 mW and a peak power,  $P_{pk}$  as high as 32.7 kW. In this circumstance, the pulses were nearly transform-limited with durations of 140 fs and a corresponding spectral width of 8.7 nm at a centre wavelength of 1049 nm. As  $P_{pk}$  is inversely proportional to the pulse repetition rate  $\nu_{rep}$ , the longer cavity length for the pump laser in this assessment contributes to higher  $P_{pk}$  that is favourable for efficient nonlinear frequency up-conversion over that produced in a more compact configuration [see Chapter 4,5,6].

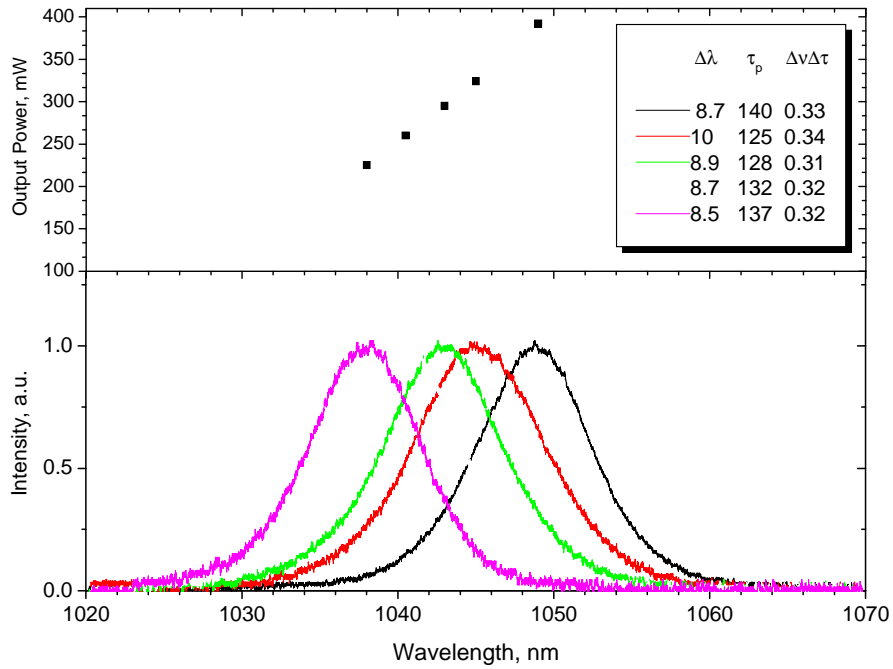


Figure 7.10. Optical spectra of the fundamental pulses (bottom) with the corresponding average output power (top).

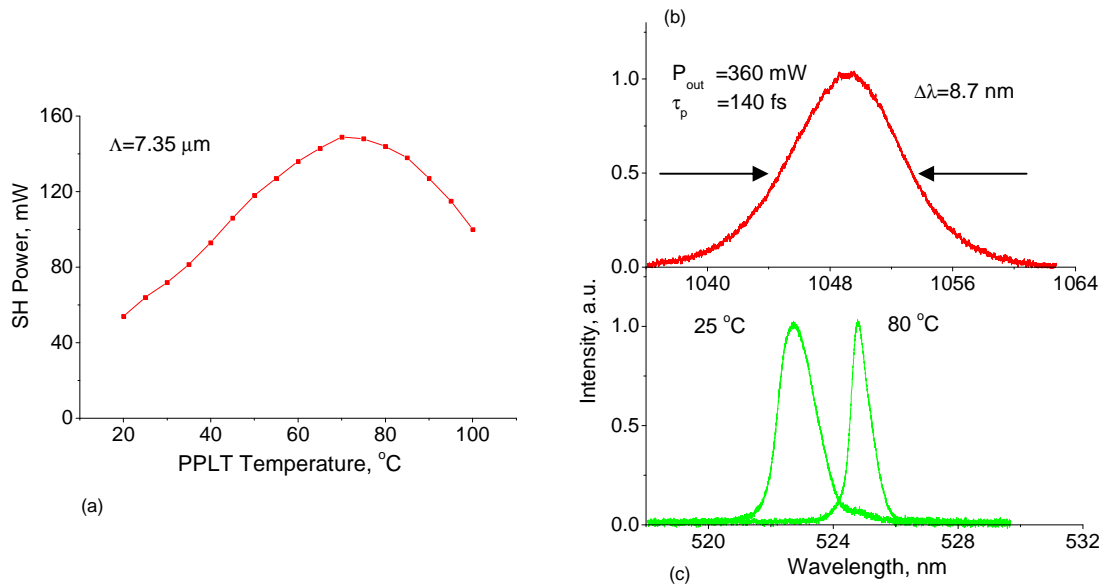


Figure 7.11. (a) Measured second harmonic power with the tuning of PPLT temperatures where (b) is the fundamental spectrum at 1049 nm and (c) is the corresponding SH green pulses at crystal temperatures of 25<sup>o</sup> C and 80<sup>o</sup> C respectively.

The PPLT temperatures were initially varied from 20<sup>o</sup> C to 100<sup>o</sup> C by using a temperature controller (TEC) to study the effect of temperature tuning for efficient frequency doubling in a quasi-phase matched crystal [figure 7.11(a)]. The optimum period grating ( $\Lambda_g$ ) during this operation was 7.35  $\mu\text{m}$  and the optical spectrum of the fundamental pulse with a duration of 140 fs at a centre wavelength of 1049 nm is shown in

figure 7.11(b). It can be seen from this figure that the second harmonic power increased with an increase in the PPLT temperature. At an optimum temperature of 70 °C a maximum second harmonic power of 150 mW was obtained with respect to the input beam power. Continued heating after this point led to a reduction in the output power.

By maintaining the same grating period of 7.35  $\mu\text{m}$ , the next evaluation was done to produce second harmonic generation from PPLT crystal at 25<sup>0</sup> C and 80<sup>0</sup> C. Figure 7.11(c) shows the optical spectra of the green pulses obtained. These evaluations were carried out for a focal length lens of 15.4 mm that implies a focusing strength parameter,  $L/b = 5.6$ . When tuned to a centre wavelength of 1045 nm, the fundamental pulse duration was measured to be 125 fs [figure 7.10]. This beam was passed through the PPLT crystal at room temperature with an incident pump power of 285 mW and a peak power of 26.5 kW. Green pulses with an average output power of 114 mW at a centre wavelength of 522.5 nm were thus produced. This corresponds to an optical-to-optical second harmonic conversion efficiency of 40 % with respect to the input pump power. However, at a wavelength tuning to 1049 nm an average output power of 360 mW was obtained. Owing to 3 % losses caused by the optical elements such as steering mirror, half-wave plate and focussing lens, the incident pump power on the PPLT crystal was measured to be 350 mW that gave a peak power up to 29 kW. The fundamental pulse duration was 140 fs and the spectral width was 8.7 nm [figure 7.11(b)]. The interaction of this wave with the crystal that was heated at 80<sup>0</sup> C produced an up-converted frequency signal at 525 nm with a maximum average output power of 150 mW. This corresponds to a second harmonic conversion efficiency of 43 % and a diode pump light-to-SH light conversion efficiency of 15 %. These excellent results can be attributed in large measure to the highly efficient performance of the diode-pumped Yb:KYW femtosecond laser achievable under a single-mode laser diode pumping [33,34]. These results also ascertain that the most important criterion for efficient harmonic generation was the peak power of the femtosecond pumped source. In addition, the importance of tuning the temperature dependence refractive index  $n(\lambda, T)$  for the optimisation of efficient nonlinear frequency up-conversion were also demonstrated.

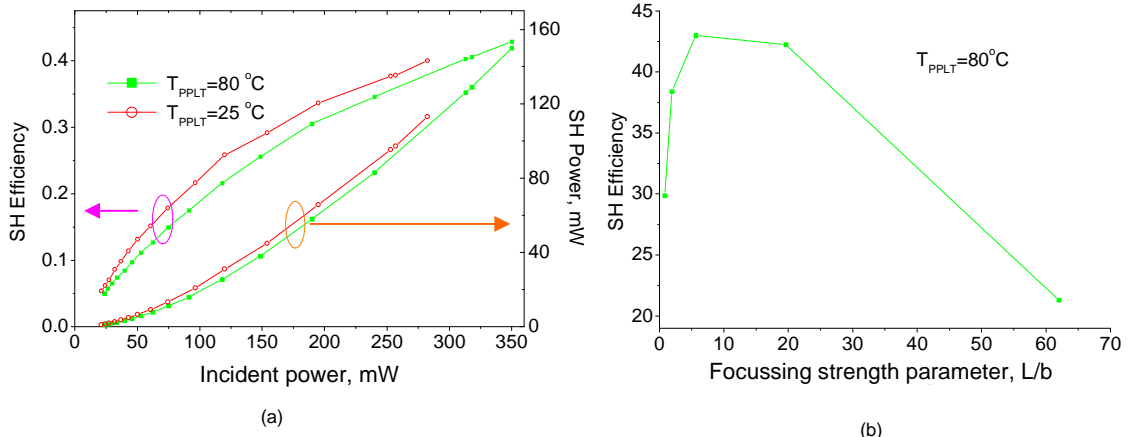


Figure 7.12. (a) Measured second harmonic efficiency (left-axis) and second harmonic power (right-axis) as a function of incident fundamental power, and (b) measured second harmonic conversion efficiency at  $80^{\circ}\text{C}$  with the variation of focussing strength parameter  $L/b$ .

Figure 7.12(a) shows the SH efficiency (left-axis) and the SH power (right-axis) as a function of fundamental power incident on the nonlinear PPLT crystal when heated to temperatures of  $25^{\circ}\text{C}$  and  $80^{\circ}\text{C}$ . The maximum power incident on the crystal at the room temperature (285 mW) was lower than that at  $80^{\circ}\text{C}$  (350 mW) due to its shorter fundamental pulse duration. These incident powers were not influenced by the crystal temperatures but they depend on the alignment of the output beam profiles from the laser set-up. However, at a given incident power, the shorter pulse duration at the room temperature operation produced a higher peak power than that of longer duration that gives an increase in SH power and the corresponding conversion efficiency. These results confirm that this highly efficient physical process is operable at a room temperature. This eliminates any cooling requirement and reduces heat dissipation from the crystal, thus increasing the overall cost-effectiveness of the device.

The next assessment was to observe the variation in SH conversion efficiency with changes in the focussing strength ratios inside the nonlinear PPLT at  $80^{\circ}\text{C}$ . Although the output beam from the pumped source can change over time, the laser was aligned to produce the same output pulses at the same centre wavelength with just a few nm differences as displayed in figure 7.10. It is shown in figure 7.12(b) that the maximum SH conversion efficiency can be obtained for  $L/b$  ratios between 10-15 that correspond with the use of 15.4 mm and 8 mm lenses. This is in agreement with the theoretical model description for the frequency doubling of focused femtosecond pulses in a “thick” nonlinear crystal [23]. In addition, the group velocity mismatch parameter,  $\alpha$ , between

two pulses was calculated to be 0.78 ps/mm in the LT crystal at a fundamental wavelength of 1048 nm. It was deduced that the nonstationary length  $L_{nst}$  was 184  $\mu\text{m}$  and the ratio  $L/L_{nst} = 19$  is compatible with the case of a “thick” nonlinear crystal [see section 7.5].

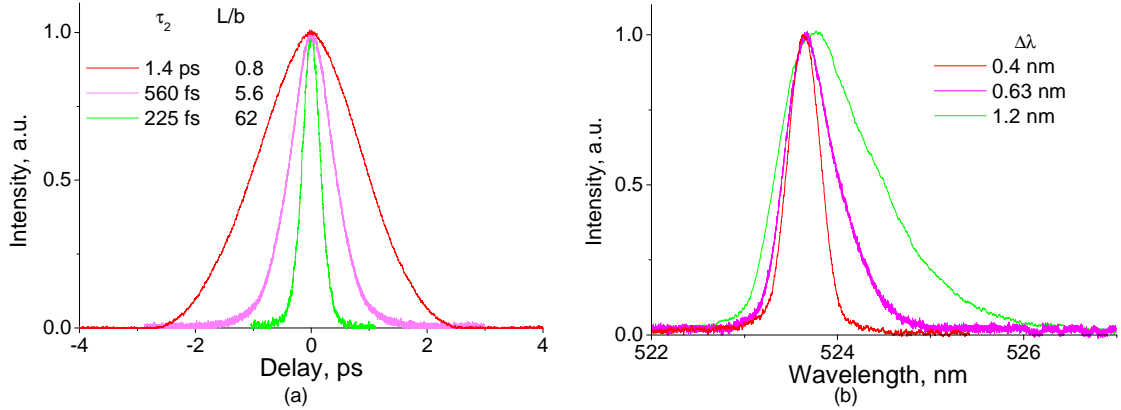


Figure 7.13. (a) Measured intensity autocorrelation and (b) the corresponding optical spectra of green pulses at a series of different focusing strength parameter  $L/b$ .

Temporal and spectral measurements of the generated SH pulses ( $\lambda_{i1} \approx 1049$  nm,  $\tau_{i1} \approx 140$  fs) were determined by plotting graphs of intensity autocorrelation as a function of delay (ps) and wavelength (nm) [figure 7.13]. The beam quality factor,  $M^2$  of the second harmonic output beam was determined to be 1.3 for weak focusing and 2.3 for strong focusing respectively. For weaker focusing, this  $k$  vector is more perpendicular to the crystal domain axis compared to that of a stronger one which explains the reason behind better  $M^2$  factor as depicted in figure 7.14. When  $L/b = 0.8$ , a pulse duration of 1.4 ps was obtained with a spectral width of 0.42 nm. However when  $L/b = 62$ , a shorter duration of 225 fs was obtained at a centre wavelength of 525 nm with a spectral width of 1.2 nm. Significantly, the duration bandwidth-product derived for the green pulses decreased from 0.6 under the weak focusing parameter to near the transform-limit of 0.3 under the conditions of stronger focusing. These results were the outcome of the difference in effective interaction length  $b$  of the interacting waves. For a given length of crystal as  $L \leq b$  under weak focusing condition, the separation between fundamental and second harmonic pulses were longer due to the longer interaction length. This increases group-velocity mismatch that is responsible for longer temporal walk-off in the nonlinear material. As the consequence, pulse broadening in the output up-converted beam occurs where its longer bandwidth product was due to an increase in the dispersion effect implicit in the material. This effect is illustrated in figure 7.14 below for two types of focusing

strength where under strong focusing the process is vice versa.. From the corresponding spectra of green pulses as shown in figure 7.13(b) it can be seen that a broader spectral width can be obtained with tighter focusing where the broadening arises mainly towards the longer wavelengths.

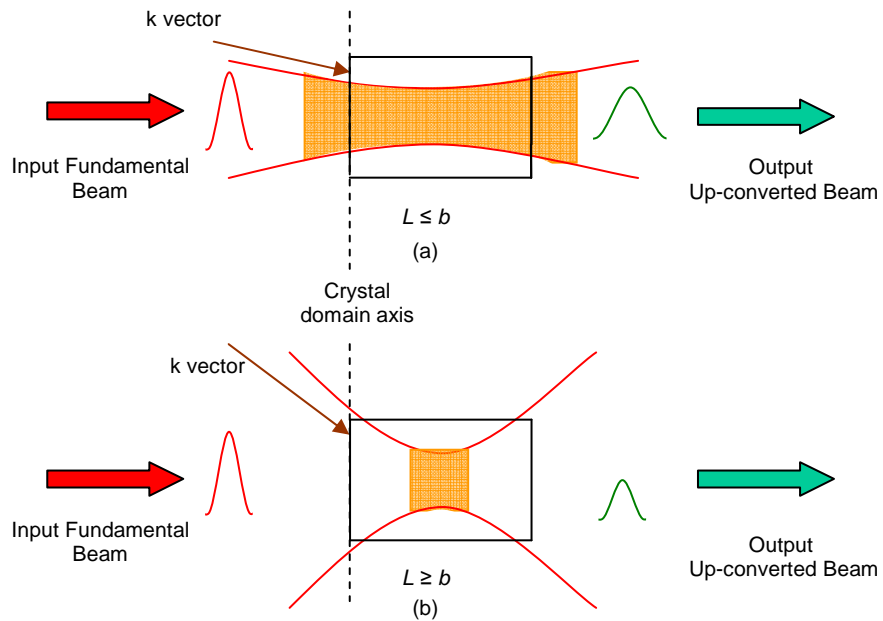


Figure 7.14. (a) Weak focusing condition that implies longer interaction length,  $b$  (orange region) and (b) strong focusing condition that implies shorter  $b$ . For longer  $b$ , the second harmonic pulses were broadened with wider duration bandwidth-product over that of shorter  $b$ .  $k$ -vector (brown arrow) explains better beam quality ( $M^2 = 1.3$ ) in (a) compared to poorer beam quality ( $M^2 = 2.3$ ) in (b).

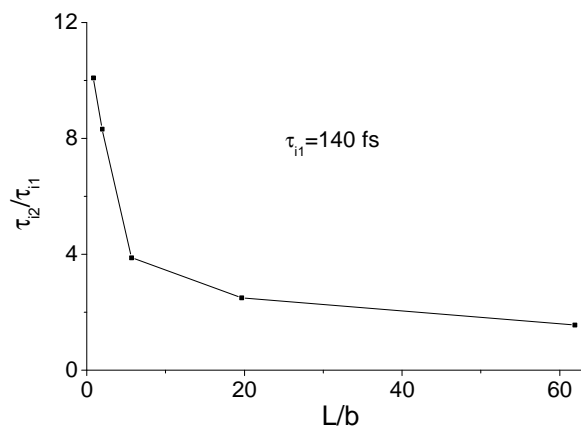


Figure 7.15. Ratio of green pulses to the infrared pulses as a function of focusing strength.

By comparing the ratio of the durations of the green pulses to those of the fundamental pulses as a function of the focusing strength parameter  $L/b$ , durations close to those of the fundamental pulses with a ratio of 1.6 were obtained under the conditions of strong focussing. This was some six times less than the ratio obtained in the weak

focusing conditions [figure 7.15]. In fact with tight focusing, the length of the nonlinear crystal can be substituted by the interaction length,  $b$ , where shorter  $b$  implies lower group velocity mismatch (GVM), thus results in a decrease in the green pulse durations.

## **7.8 Conclusion.**

A highly efficient frequency doubling of femtosecond pulses was successfully achieved in an extracavity configuration. The pump source was a Yb:KYW femtosecond laser where the single-pass doubling of this fundamental source in a PPLT nonlinear crystal generated visible light pulses in the green spectral region. Impressively, a maximum average output power of 150 mW was obtained that corresponded to the achievement of a second harmonic conversion efficiency of 43 % and a pump-diode light-to-harmonic light conversion efficiency of 15 %. The temporal characteristics of the frequency-doubled pulses as a function of focusing conditions in a thick nonlinear crystal regime have been investigated experimentally and pulses could be generated around 525 nm in the duration range of 1.4 ps to 225 fs. These results demonstrated that frequency doubling of the femtosecond Yb:KYW laser using thick nonlinear crystals in an extracavity configuration represented an excellent and practical source of ultrashort green pulses. Further up-conversion schemes such as sum-frequency generation involving the mixing of this green radiation with the fundamental will open up interesting possibilities for the production of ultrashort ultra-violet pulses.

## 7.9 References:-

1. B. Braun, C. Honninger, G. Zhang, U. Keller, F. Heine, T. Kellner, and G. Huber, "Efficient intracavity frequency doubling of a passively mode-locked diode-pumped neodymium lanthanum scandium borate laser," *Opt. Lett.* **21**, 1567-1569 (1996).
2. L. E. Myers, "Periodically-poled materials for nonlinear optics," *Advances in Lasers and Applications, Proceedings of the Fifty Second Scottish Universities Summer School in Physics, St. Andrews*, 141-180 (1998).
3. M. B. Agate, "Portable and efficient femtosecond Cr:LiSAF lasers," PhD. Thesis, School of Physics and Astronomy, U. of St. Andrews, 7:1-7:47 (2003).
4. J. A. Armstrong, N. Bloembergen, J. Ducuing, and P. S. Pershan, "Interactions between light waves in a nonlinear dielectric," *Phys. Rev.* **127**, 1918-1939 (1962).
5. F. Zernicke and J. E. Midwinter, "Applied nonlinear optics," John Wiley & Sons, New York, 153-176 (1973).
6. M. Houe and P. D. Townsend, "An introduction to methods of periodic poling for second harmonic generation," *J. Phys. D: Appl. Phys.* **28**, 1747-1763 (1995).
7. M. M. Fejer, G. A. Magel, D. H. Jundt, and R. L. Byer, "Quasi-phase-matched second harmonic generation: tuning and tolerances," *IEEE J. Quantum Electron.* **28**, 2631-2654 (1992).
8. K. Moutzouris, "Nonlinear frequency conversion in isotropic semiconductor waveguides," PhD. Thesis, School of Physics and Astronomy, U. of St. Andrews, 27-41 (2003).
9. N. P. Barnes, "Compositionally tuned lasers for remote sensing," *Opt. Mater.* **26**, 333-336 (2004).
10. D. N. Nikogosyan, "Properties of optical and laser-related materials," *A Handbook* Chichester (1998).
11. B. Zysset, I. Biaggio, and P. Gunter, "Refractive-indexes of orthorhombic KNBO<sub>3</sub> 1. dispersion and temperature dependence," *J. Opt. Soc. Am. B* **9**, 380-386 (1992).
12. D. E. Thompson, J. D. McMullen, and D. B. Anderson, "Second-harmonic generation in GaAs "stack of plates" using high power CO<sub>2</sub> laser radiation," *Appl. Phys. Lett.* **29**, 113-115 (1976).

13. E. J. Lim, M. M. Fejer, and R. L. Byer, "Second-harmonic generation of green light in periodically poled planar lithium niobate waveguide," *Electron. Lett.* **25**, 174-175 (1989).
14. J. Webjorn, F. Laurell, and G. Arvidsson, "Fabrication of periodically domain-inverted channel waveguides in lithium niobate for second harmonic generation," *J. Lightwave Technol.* **7**, 1597-1600 (1989).
15. K. Nakamura and H. Shimizu, "Poling of ferroelectric crystals by using interdigital electrodes and its application to bulk-wave transducers," *IEEE Ultrasonics Symp.*, 527-530 (1983).
16. C. J. Van der Poel, J. D. Bierlien, J. B. Brown, and S. Colak, "Efficient type-I blue second-harmonic generation in periodically segmented  $\text{KTiOPO}_4$  waveguides," *Appl. Phys. Lett.* **57**, 2074-2076, 1990.
17. S. Kurimura, I. Shimoya, and Y. Uesu, "Domain inversion by an electron-beam-induced electric field in  $\text{MgO}:\text{LiNbO}_3$ ,  $\text{LiNbO}_3$ , and  $\text{LiTaO}_3$ ," *Jpn. J. Appl. Phys.* **35**, L31-L33 (1996).
18. F. Mizuuchi and K. Yamamoto, "Domain inversion in  $\text{LiTaO}_3$  using an ion beam," *Electron. Lett.* **29**, 2064-2066 (1993).
19. I. A. Ghambaryan, R. Guo, R. K. Hovsepyan, A. R. Poghosyan, E. S. Vardanyan, and V. G. Lazaryan, "Periodically-poled structures in Lithium Niobate crystals: growth and photoelectric properties," *J. Optoelectron. Adv. Mater.* **5**, 61-68 (2003).
20. P. F. Bordui and M. M. Fejer, "Inorganic crystals for nonlinear optical frequency conversion," *Ann. Rev. Mater. Science* **23**, 321-379 (1993).
21. M. J. Lederer, M. Hildebrandt, V. Z. Kolev, B. Luther-Davies, B. Taylor, J. Dawes, P. Dekker, J. Piper, H. H. Tan, and C. Jagadish, "Passive mode locking of a self-frequency-doubling  $\text{Yb}:\text{YAl}_3(\text{BO}_3)_4$  laser," *Opt. Lett.* **27**, 436-438 (2002).
22. A. M. Weiner, A. M. Kan'an, and D. E. Leaird, "High-efficiency blue generation by frequency doubling of femtosecond pulses in a thick nonlinear crystal," *Opt. Lett.* **23**, 1441-1443 (1998).
23. B. Agate, A. Kemp, C. Brown, and W. Sibbett, "Efficient, high repetition-rate femtosecond blue source using a compact  $\text{Cr}:\text{LiSAF}$  laser," *Opt. Express* **10**, 824-831 (2002).
24. S. M. Saltiel, K. Koynov, B. Agate, and W. Sibbett, "Second-harmonic generation with focused beams under conditions of large group-velocity mismatch," *J. Opt. Soc. Am. B* **21**, 591-598 (2004).

25. S. Yu and A. M. Weiner, "Phase-matching temperature shifts in blue generation by frequency doubling of femtosecond pulses in  $\text{KNbO}_3$ ," *J. Opt. Soc. Am. B* **16**, 1300-1304 (1999).
26. D. Guzun, Y. Q. Li, and M. Xiao, "Blue light generation in single-pass frequency doubling of femtosecond pulses in  $\text{KNbO}_3$ ," *Opt. Commun.* **180**, 367-371 (2000).
27. Y. Q. Li, D. Guzun, G. Salamo, and M. Xiao, "High-efficiency blue-light generation by frequency doubling of picosecond pulses in a thick  $\text{KNbO}_3$  crystal," *J. Opt. Soc. Am. B* **20**, 1285-1289 (2003).
28. H. Wang and A. M. Weiner, "Second harmonic generation efficiency with simultaneous temporal walk-off, spatial walk-off, and depletion," Conference on Lasers and Electro-Optics, Trends in Optics and Photonics Series **89**, Opt. Soc. America, Washington DC, CThU1 (2003).
29. K. Mizuuchi, K. Yamamoto, and M. Kato, "Generation of ultraviolet light by frequency doubling of a red laser diode in a first-order periodically poled bulk  $\text{LiTaO}_3$ ," *Appl. Phys. Lett.* **70**, 1201-1203 (1997).
30. P. A. Champert, S. V. Popov, J. R. Taylor, and J. P. Meyn, "Efficient second-harmonic generation at 384 nm in periodically poled lithium tantalate by use of a visible Yb-Er-seeded fiber source," *Opt. Lett.* **25**, 1252-1254 (2000).
31. J. P. Meyn and M. M. Fejer, "Tunable ultraviolet radiation by second-harmonic generation in periodically poled lithium tantalate," *Opt. Lett.* **22**, 1214-1216 (1997).
32. A. Bruner, D. Eger, M. B. Oron, P. Blau, M. Katz, and S. Ruschin, "Temperature-dependent Sellmeier equation for the refractive index of stoichiometric lithium tantalate," *Opt. Lett.* **28**, 194-196 (2003).
33. A. A. Lagatsky, C. T. A. Brown, and W. Sibbett, "Highly efficient and low threshold diode-pumped Kerr-lens mode-locked Yb:KYW laser," *Opt. Express* **12**, 3928-3933 (2004).
34. A. A. Lagatsky, E. U. Rafailov, C. G. Leburn, C. T. A. Brown, N. Xiang, O. G. Okhotnikov, and W. Sibbett, "Highly efficient femtosecond Yb:KYW laser pumped by single narrow-stripe laser diode," *Electron. Lett.* **39**, 1108-1110 (2003).

## **Chapter 8**

### **Final Remarks.**

#### **8.1 Conclusion.**

The main objectives of this project related to the design, construction and characterisation of ultralow-threshold, compact and highly efficient solid-state femtosecond lasers. The gain media selected for lasing were based on Yb-doped crystals involving Yb<sup>3+</sup>-doped potassium yttrium tungstate [Yb<sup>3+</sup>:KY(WO<sub>4</sub>)<sub>2</sub>] or Yb:KYW and Yb<sup>3+</sup>-doped vanadium yttrium oxide [Yb<sup>3+</sup>:YVO<sub>4</sub>] or Yb:YVO<sub>4</sub> with emission around 1 μm. The main motivation within this PhD. project was to demonstrate femtosecond lasers that offered enhanced efficiency and robustness but with greater efficiency and lower cost to suit a wide range of applications including ultrafast spectroscopy, portable diagnostic measurements, terahertz generation, harmonic generation and optical parametric amplifiers and oscillators. This objective has been accomplished by reducing the number of optical elements required in the laser oscillators as described in Chapters 4 to 7.

In Chapter 4, a slope efficiency of 74 % was obtained with an optical-to-optical efficiency of 42 % in a 4-mirror resonator for continuous wave unmode-locked operation. The electrical-to-optical efficiency was ~ 12.6 % which was 2-3 times higher than that obtained in a previously reported Cr:LiSAF laser [1]. The laser was tunable from 1012 nm to 1069 nm in a simple and more compact configuration through the use of a single intracavity prism and these features are comparable to the assessment reported earlier by Lagatsky [2].

With the aim of further reducing the footprint of a Yb:KYW femtosecond laser, several combinations of chirped mirrors were used for dispersion control [see Chapter 5]. An important outcome of this work was the demonstration of the most efficient femtosecond laser yet reported where the optical-to-optical efficiency reached 37 %! The shortest pulse durations of 90 fs obtained are the shortest pulse durations measured to date for any SESAM-assisted mode-locked Yb-tungstate lasers [3]. These excellent performances were due to the exploitation of Kerr-lensing effects together with the low quantum defect of less than 0.14 in the gain materials [see table 2.2]. In this evaluation, it was found that a single chirped mirror with optimum negative dispersion between 800 fs<sup>2</sup> to 1000 fs<sup>2</sup> could be designed to produce output pulses within the sub-100 fs regime.

In a 3-mirror cavity Kerr-lens mode-locked Yb:YVO<sub>4</sub> laser [Chapter 6], transform-limited pulse durations as short as 61 fs were generated around 1050 nm. A related optical to-optical efficiency of 15 % was obtained and this shows the potential of this material for high peak power operation. The excellent thermal conductivity of 5.3 W/mK in this particular crystal enhanced its merit as an alternative choice of gain medium compared to that of Yb:YAG for an application of this type.

In the assessment of second harmonic generation in a PPLT crystal [Chapter 7], an efficiency of 40 % was achieved for the frequency-doubled output where 225 fs transform-limited pulses were produced at 525 nm. This laser system was operable at room temperature which avoided any unnecessary cooling requirement, thus adding to appeal of its overall operational efficiency. For any length of the nonlinear gain crystal between 3 mm and 5 mm selected for this process, the crystal length,  $L$  to beam confocal parameter,  $b$   $\left[ \frac{L}{b} \right]$  ratio to achieve maximum second harmonic efficiency was measured to be in the 10-15 range. This opens up the possibility of using a selection of crystal lengths within the ratio of  $\frac{L}{L_{nst}} \approx 20$  where  $L_{nst}$  is the nonstationary length [see subsection 7.5]. This increases the performance of visible femtosecond laser operation in terms of conversion efficiencies and pulse durations as will be discussed in the next section.

## 8.2 Future Work.

As a consequence of the excellent performances of Yb-doped femtosecond lasers designed and assessed within this project, further minimisation of the cavity length is suggested as shown in figure 8.1. This future work is a continuation of my current PhD. project [Chapter 4 and 5] which is aimed at improving optical-to-optical efficiency and reducing the pulse durations. The simplification of the laser oscillators can be done by employing a chirped output mirror with shorter radius of curvature/focal length of optical elements in the oscillators. The chirped output mirror chosen has double-chirped structure [figure 5.5] that can compensate for higher-order dispersion with negative dispersion between 700 fs<sup>2</sup> to 900 fs<sup>2</sup>. In quasi-three-level laser operation, by using high pump powers, it is also expected to improve the optical-to optical-efficiency of this system [figure 2.11]. The pump sources are two single-mode tapered InGaAs diode lasers where each pump source is

capable of producing a power of 3.5 W. By employing a Yb:KYW crystal as the gain medium, optical-to-optical efficiencies are expected to be more than 53 % [4] for Kerr-lens mode locking or more than 40 % for SESAM-assisted mode locking.

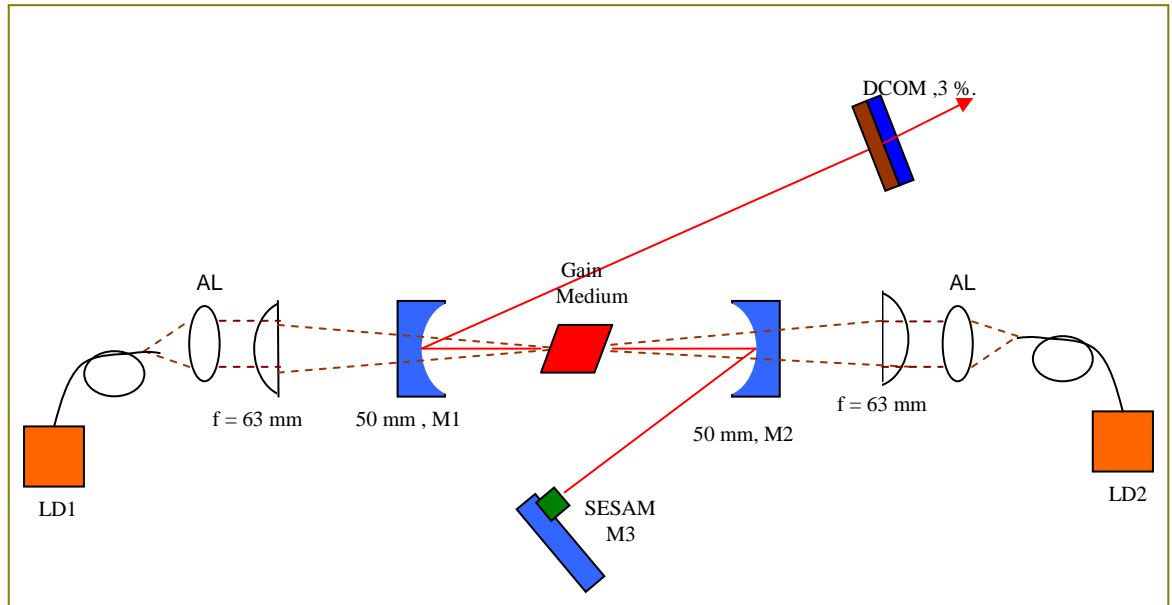


Figure 8.1 A schematic of a Yb-doped femtosecond laser for future implementation that incorporates shorter radii of curvature for mirrors 1 and 2 (M1, M2) and double-chirped-output mirror (DCOM).

For the initiation and stabilisation of the mode locking process, the SESAM used can be based on quantum well [figure 4.9] or quantum-dot structures [5,6]. If a quantum-well SESAM is chosen, it is expected that output pulse durations can be reduced towards 80 fs. This is made possible with the exploitation of stronger Kerr-lens effects with the higher pump power as well as the elimination of Fresnel reflection and impedance mismatch accomplished by the double-chirped output mirror structure. Improvement in this system can be achieved by the integration of double-chirped mirror structure into the semiconductor technology. Although this system is quite expensive and requires specialised fabrication, it would be justified on the basis of the shorter pulse durations to less than 80 fs as expected due to the large amount of negative dispersion in the mirror structure [section 5.3]. This device could also be integrated into a SESAM structure in a compact femtosecond-laser configuration.

A further idea would be to build a more compact, highly efficient, portable two-element or three-element cavity femtosecond laser based on this research work by the incorporation of a Brewster-cut crystal with mirror #1. In a three-element cavity, a double output chirped mirror with negative dispersion of approximately  $\leq 500 \text{ fs}^2$  would be

incorporated into mirror #2 and a SESAM employed as mirror #3. Results achieved from the characterisation of this system could be used to further build a two-cavity element laser. In this implementation, mirror #1 incorporated with a Brewster-cut crystal would have the required amount of negative double chirped dispersion. This mirror that would serve as an input mirror could also work as an output mirror while mirror #2 could be incorporated with a SESAM. The output beam emitting from mirror #1 would be diverted from the incident beam by using a 45° dichroic mirror. If this work produced a successful result, it would represent the first prototype hand-size femtosecond lasers in the world! This system would allow the production of higher repetition rates (> 1 GHz) for a range of applications such as high speed electro-optic sampling, microwave/millimetre-wave communications and photonics switching. Previous research done by Agate on a Cr:LiSAF laser had produced a compact shoebox-sized femtosecond lasers on a 22 x 28 cm<sup>2</sup> breadboard [7], so this would represent the next step in the miniaturisation process.

All the assessments mentioned above can be implemented by using a Yb:KYW or Yb:YVO<sub>4</sub> crystals as the gain media. Given the adequate thermal conductivity of the latter material (Yb:YVO<sub>4</sub>-up to 5.3 W/mK), this femtosecond laser offers particular promise for applications in high peak power laser operation, thin disc lasers, and as a pump source for harmonic generation, optical parametric oscillators and amplifiers (OPO/A). The main focus of high peak power operation would be for micromachining while OPO/OPAs are beneficial for nonlinear optics and other broadband tuning applications.

Continuing evaluations performed in Chapter 7 are recommended by using several lengths of nonlinear crystals from 3 mm, 3.5 mm and 4 mm to maximise the second harmonic conversion efficiencies. Owing to the fact that maximum second harmonic conversion efficiency were obtained within the ratio  $L/b$  of 10-15 [figure 7.12(b)], more assessments can be carried out within this range. Assessment at stronger  $L/b$  can also be done if possible to provide further insights into the optimisation of the nonlinear processes. The pump power used for second harmonic generation is built from the implementations suggested in paragraph 1 and 2 above. Once the optimum length of the crystal is determined, the study of the effects of different fundamental pulse durations  $\tau_{i1}$  on the second harmonic durations  $\tau_{i2}$  can be assessed on the optimum length of PPLT crystal at the room temperature or optimum temperature operating conditions.

The generation of ultrashort UV pulses by frequency mixing of fundamental pulses from Yb-doped femtosecond laser and green pulses from PPLT crystal can be used for third harmonic generation by using BBO ( $\beta\text{-BaB}_2\text{O}_4$ ) as the nonlinear crystal. The investigation of nonlinear waveguide materials such as PPLT and PPKTP can also be carried out for second and third harmonic generation. These ultrafast lasers having high peak intensity visible outputs have many applications in time-resolved spectroscopy and studies in photo-biology and photo-medicine. All the future work suggested here could also be expanded with the exploration of new Yb-doped materials such as Yb:CaLGO that is capable of generating sub-50 fs pulses and subsequent harmonic generation by using newly developed and periodically-poled nonlinear materials.

It should be evident from these concluding remarks that there remain a substantial number of research areas where further progress can be expected to be made in the design and development of “next generation” femtosecond lasers. The work to date, and in particular that described in this thesis, represents an interesting step in the evolution of increasingly efficient and practical tunable, femtosecond-pulse optical sources. In the author’s opinion the next generation of these lasers will find many new applications in the femto-science and femto-technology sectors that can be expected to expand or emerge in the future.

### 8.3 References.

1. B. Agate, B. Stormont, A. J. Kemp, C. T. A. Brown, U. Keller, and W. Sibbett, "Simplified cavity designs for efficient and compact femtosecond Cr:LiSAF lasers," *Opt. Commun.* **205**, 207-213 (2002).
2. A. A. Lagatsky, E. U. Rafailov, C. G. Leburn, C. T. A. Brown, N. Xiang, O.G. Okhotnikov, and W. Sibbett, "Highly efficient femtosecond Yb:KYW laser pumped by a single narrow stripe laser diode", *Electron. Lett.* **39**, 1108-1110 (2003).
3. P. Klopp, V. Petrov, U. Griebner, G. Erbert, "Passively mode-locked Yb:KYW laser pumped by a tapered diode laser," *Opt. Express* **10**, 108-113(2002).
4. A. A. Lagatsky, C. T. A. Brown, and W. Sibbett, "Highly efficient and low threshold diode-pumped Kerr-lens mode-locked Yb:KYW laser," *Opt. Express* **12**, 3928-3933 (2004).
5. A. McWilliam, A. A. Lagatsky, C. T. A. Brown, W. Sibbett, A. E. Zhukov, V. M. Ustinov, A. P. Vasil'ev, and E. U. Rafailov, "Quantum-dot-based saturable absorber for femtosecond mode-locked operation of a solid-state laser," *Opt. Lett.* **31**, 1444-1446 (2006).
6. A. A. Lagatsky, E. U. Rafailov, W. Sibbett, D. A. Livshits, A. E. Zhukov, and V. M. Ustinov, "Quantum-dot based saturable absorber with p-n junction for mode locking of solid-state lasers," in *Conference on Lasers and Electro-Optics/International Quantum Electronics Conference and Photonic Applications Systems Technologies, Technical Digest (CD)* (Optical Society of America, 2004), paper CThV6.
7. B. Agate, B. Stormont, A. J. Kemp, C. T. A. Brown, U. Keller, and W. Sibbett, "Simplified Cavity Designs for Efficient and Compact Femtosecond Cr:LiSAF Lasers," *Opt. Commun.* **205**, 207-213 (2002).

## Publications.

### **Journal Papers.**

1. A. A. Lagatsky, E. U. Rafailov, A. R. Sarmani, C. T. A. Brown, W. Sibbett, L. Ming, and P. G. R. Smith, "Efficient femtosecond green-light source with a diode-pumped mode-locked  $\text{Yb}^{3+}:\text{KY}(\text{WO}_4)_2$  laser," *Opt. Lett.* **30**, 1144-1146 (2005).
2. A. A. Lagatsky, A. R. Sarmani, C. T. A. Brown, W. Sibbett, V. E. Kisel, A. G. Selivanov, I. A. Denisov, A. E. Troshin, K. V. Yumashev, N. V. Kuleshov, V. N. Matrosov, T. A. Matrosova, and M. I. Kupchenko, " $\text{Yb}^{3+}$ -doped  $\text{YVO}_4$  crystal for efficient Kerr-lens mode locking in solid-state lasers," *Opt. Lett.* **30**, 3234-3236 (2005).
3. A. A. Lagatsky, A. R. Sarmani, C. G. Leburn, E. U. Rafailov, M. A. Cataluna, B. Agate, C. T. A. Brown, and W. Sibbett, "Diode-based ultrafast lasers," *OSA Trends in Optics and Photonics (TOPS), Advanced Solid-State Photonics (Optical Society of America, Washington) Proceedings* **98**, 640-645 (2005).
4. A. A. Lagatsky, E. U. Rafailov, A. R. Sarmani, C. T. A. Brown, W. Sibbett, L. Ming, and P. G. R. Smith, "Efficient femtosecond green generation in a periodically-poled  $\text{LiTaO}_3$  crystal using a diode-pumped  $\text{Yb}:\text{KYW}$  laser," *OSA Trends in Optics and Photonics (TOPS), Advanced Solid-State Photonics (Optical Society of America, Washington) Proceedings* **98**, 483-488 (2005).

### **Conference Presentations.**

1. A. A. Lagatsky, A. R. Sarmani, C. T. A. Brown, W. Sibbett, V. E. Kisel, A. G. Selivanov, I. A. Denisov, A. E. Troshin, K. V. Yumashev, N. V. Kuleshov, V. N. Matrosov, T. A. Matrosova, and M. I. Kupchenko, "Low threshold and efficient Kerr-lens mode-locking on a diode-pumped femtosecond  $\text{Yb}:\text{YVO}_4$  laser," paper WC3, *Advanced Solid-state Photonics 2006*, Nevada, USA.
2. A. A. Lagatsky, E. U. Rafailov, A. R. Sarmani, C. T. A. Brown, W. Sibbett, L. Ming, and P. G. R. Smith, "Efficient femtosecond green generation in a periodically poled  $\text{LiTaO}_3$  crystal using a diode-pumped  $\text{Yb}:\text{KYW}$  laser," *Advanced Solid-State Photonics 2005 (ASSP)*, Vienna, Austria.

3. A. A. Lagatsky, E. U. Rafailov, A. R. Sarmani, C. T. A. Brown, W. Sibbett, L. Ming, and P. G. R. Smith, "Efficient frequency doubling of femtosecond pulses in a periodically-poled LiTaO<sub>3</sub> crystal at room temperature," paper CA8-3-Tue, European Conference on Lasers and Electro-optics 2005 (E-CLEO), Munich.
4. A. R. Sarmani, A. A. Lagatsky, C. T. A. Brown, and W. Sibbett, "Low threshold and highly efficient prismless diode-pumped femtosecond Yb:KYW laser," paper CA4-2-Thu, European Conference on Lasers and Electro-optics 2005 (E-CLEO), Munich.
5. A. A. Lagatsky, A. R. Sarmani, C. T. A. Brown, W. Sibbett, V. E. Kisel, A. E. Troshin, N. V. Kuleshov, V. N. Matrosov, T. A. Matrosova, M. I. Kupchenko, A. G. Selivanov, I. A. Denisov, and K. V. Yumashev, "Low threshold diode-pumped Kerr-lens mode-locked Yb:YVO<sub>4</sub> laser," paper CP1-1-Thu, European Conference on Lasers and Electro-optics 2005 (E-CLEO), Munich.

## Appendices

### **Appendix A: A simple dielectric chirped mirror, $-455 \pm 200 \text{ fs}^2$ (Layertec, GmbH).**

To compensate for positive dispersion scheme implicit in the laser cavity, LAYERTEC offers dispersive femtosecond laser optics with the required bandwidth needed for this assesment (Figures 1-9 demonstrates the optical properties of negative dispersive mirrors for the wavelength range around  $1 \mu\text{m}$  that are feasible for Yb-doped femtosecond lasers). The three important properties that need to be considered while designing a chirped mirror are such as transmission, reflection and group delay dispersion spectra. For the first chirped mirror incorporated in this assessment, the transmission property is “zero’ within the wavelength range of 880 nm to 1240 nm as depicted in figure 1. The transmission spectrum of this chirped mirror exhibits large oscillations outside the wavelength range of operation. For the wavelength range between 960 nm to 1200 nm, the reflection property is maximum that favours the optimisation of laser operation within this spectral region [figure 2]. In addition, a smooth group delay dispersion spectrum with small oscillations that range from  $-100 \text{ fs}^2$  at 1000 nm to  $-600 \text{ fs}^2$  at 1055 and 1085 nm was designed in this chirped mirror as shown in figure 3. At maximum designed wavelength of 1100 nm, this mirror was dispersionless.

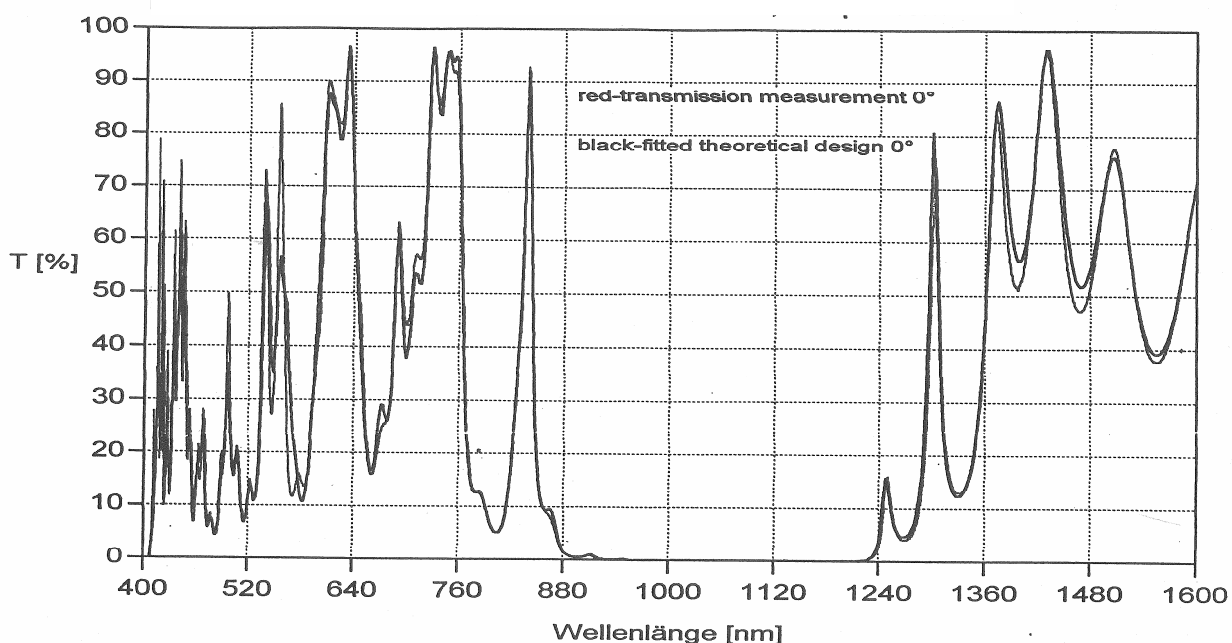


Figure 1. Transmission property in the first chirped mirror.

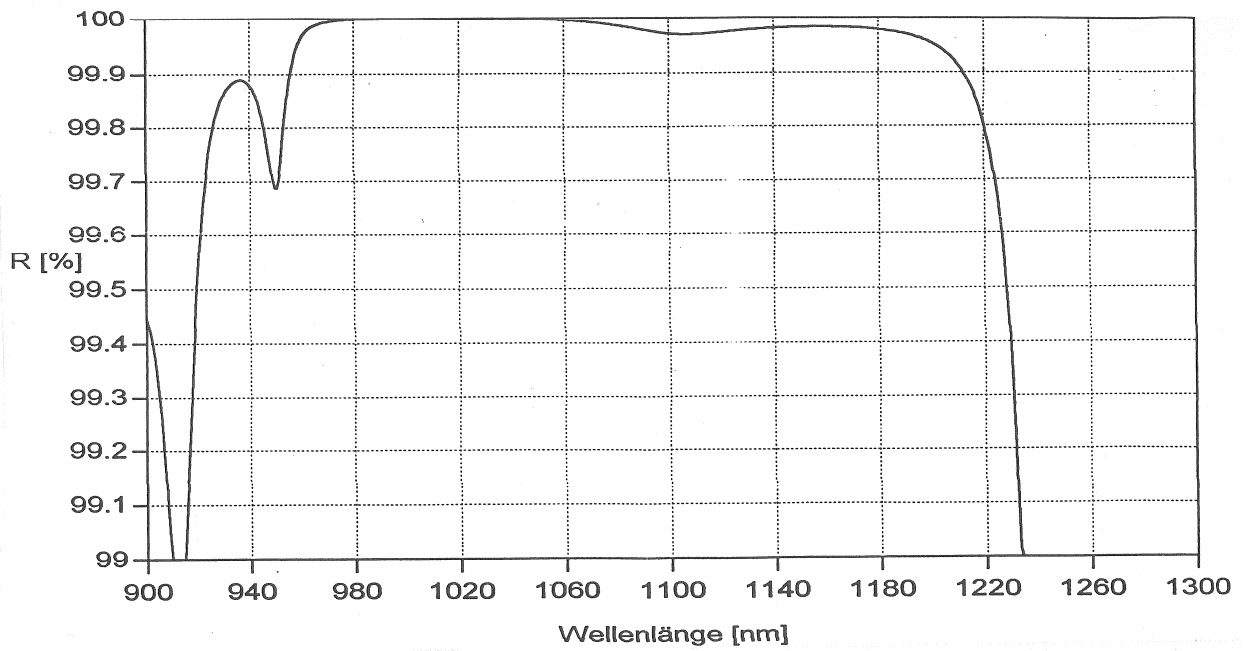


Figure 2. Reflection property in the first chirped mirror.

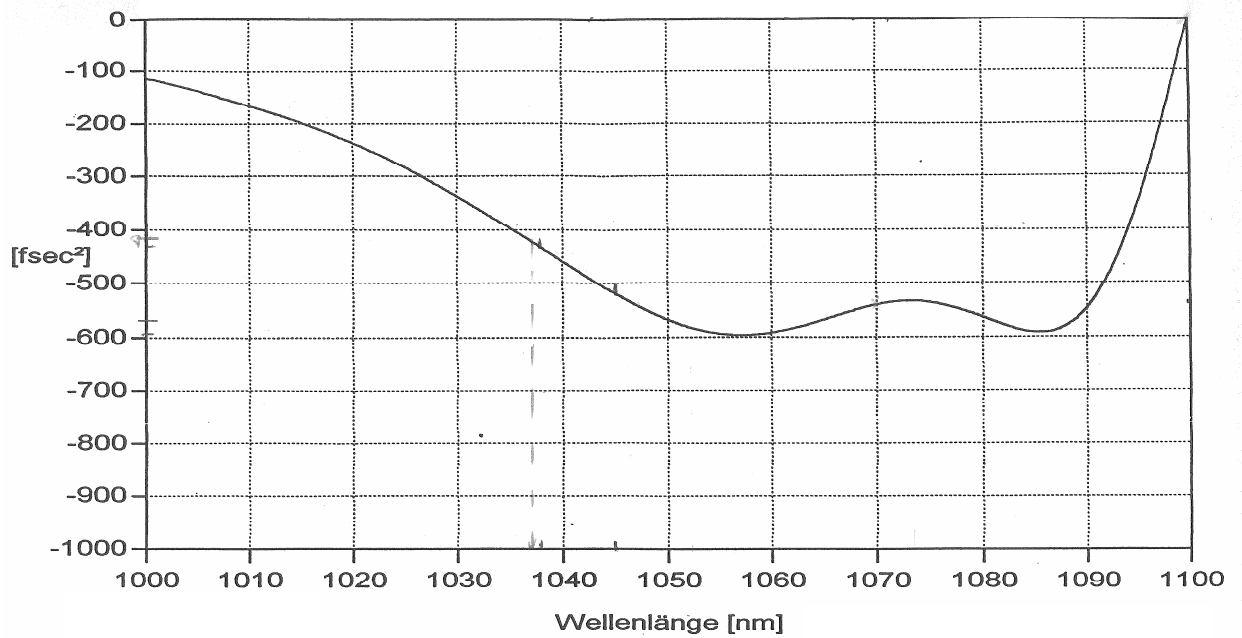


Figure 3. Group delay dispersion spectrum between  $-455 \pm 200 \text{ fs}^2$  in the first chirped mirror for the laser wavelength range between 1012 to 1069 nm.

## Appendix B: A simple dielectric chirped mirror, $-370 \pm 50 \text{ fs}^2$ (Layertec, GmbH).

In this second chirped mirror, the transmission and reflection properties are similar to the first chirped mirror as presented in figure 4 and 5. However, the value of group delay dispersion is lower for the designed wavelengths between 950 nm to 1100 nm as shown in figure 6. Minimum oscillation for the group delay dispersion spectrum can also be seen which favour the optimisation of femtosecond operation. At 950 nm, the value of group delay dispersion designed on this mirror was  $-15 \text{ fs}^2$  before increasing to  $-425 \text{ fs}^2$  at 1025 nm. At around 1080 nm, this mirror was dispersionless before implying positive dispersion effect up to 1100 nm.

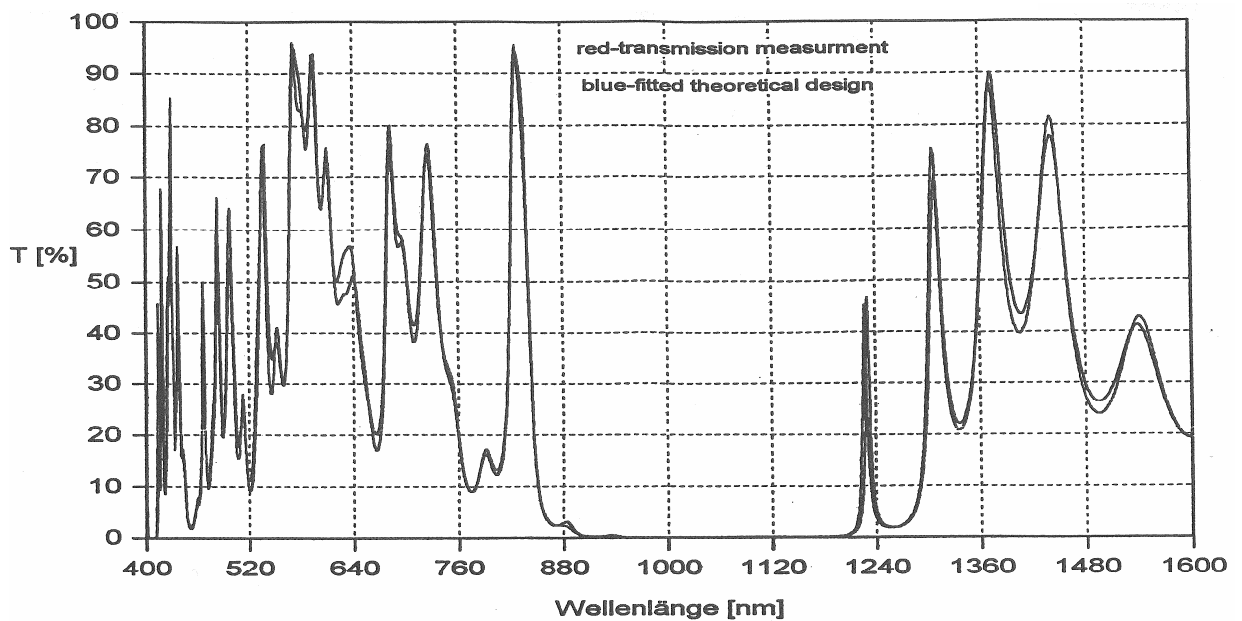


Figure 4. Transmission property in the second chirped mirror.

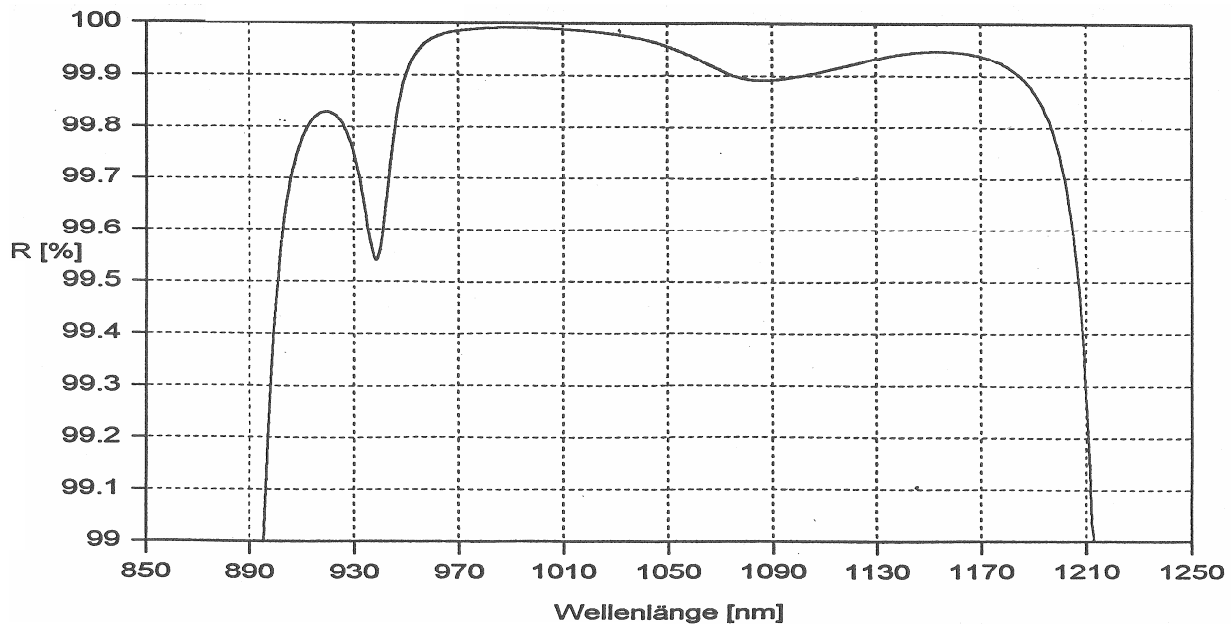


Figure 5. Reflection property in the second chirped mirror.

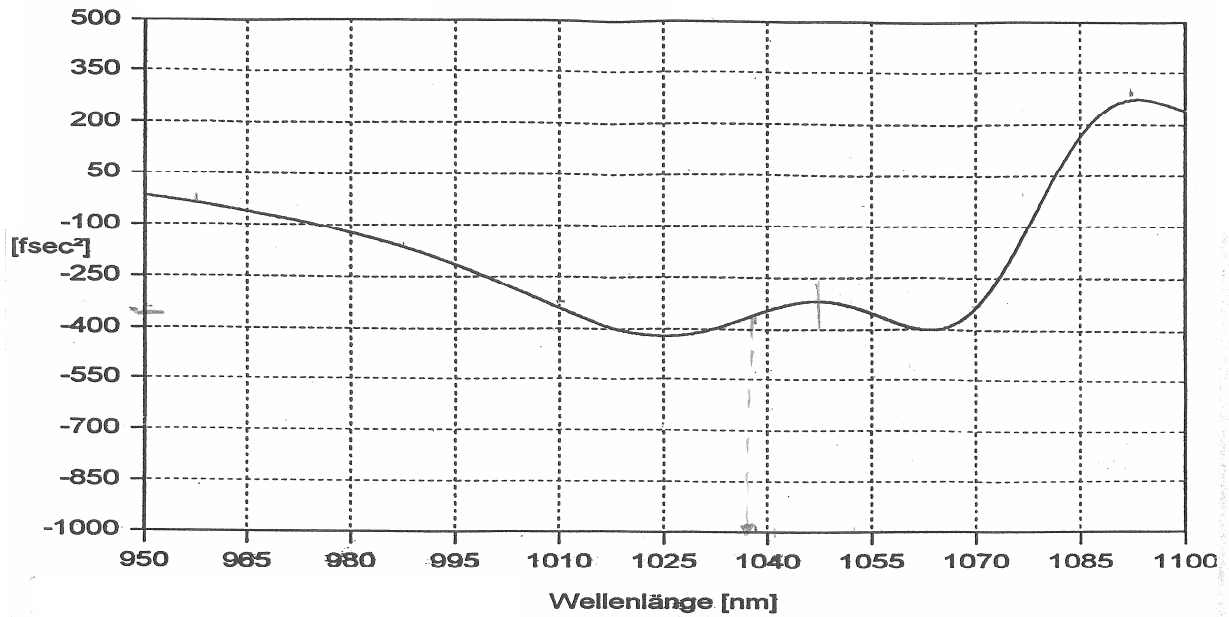


Figure 6. Group delay dispersion spectrum of  $-375 \pm 50 \text{ fs}^2$  in the second chirped mirror for the laser wavelength range between 1012 to 1069 nm.

### Appendix C: A simple dielectric chirped mirror, $-110 \pm 20 \text{ fs}^2$ (Layertec, GmbH).

In the third chirped mirror implemented in this assessment, the minimum transmission property within the wavelength range of 940 nm to 1180 nm [figure 7] was narrower compared to the two chirped mirrors discussed before. The range of maximum reflectivity of this mirror was also narrower between 960 nm to 1140 nm [figure 8]. However, these properties were sufficient for the laser wavelength of operation between 1012 to 1069 nm carried out in this PhD-research project. For the designed wavelengths between 930 nm to 1155 nm, the oscillation of group delay dispersion spectrum varies from  $0 \text{ fs}^2$  to  $-110 \text{ fs}^2$  before increasing back to  $-200 \text{ fs}^2$  [figure 9].

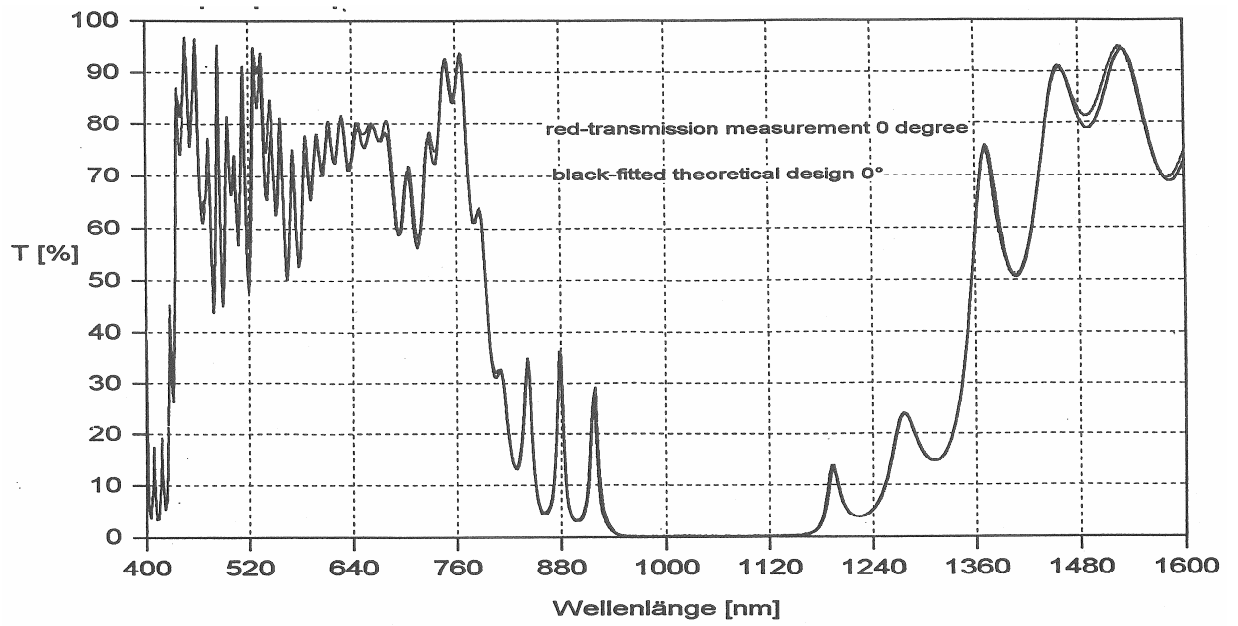


Figure 7. Transmission property in the third chirped mirror.

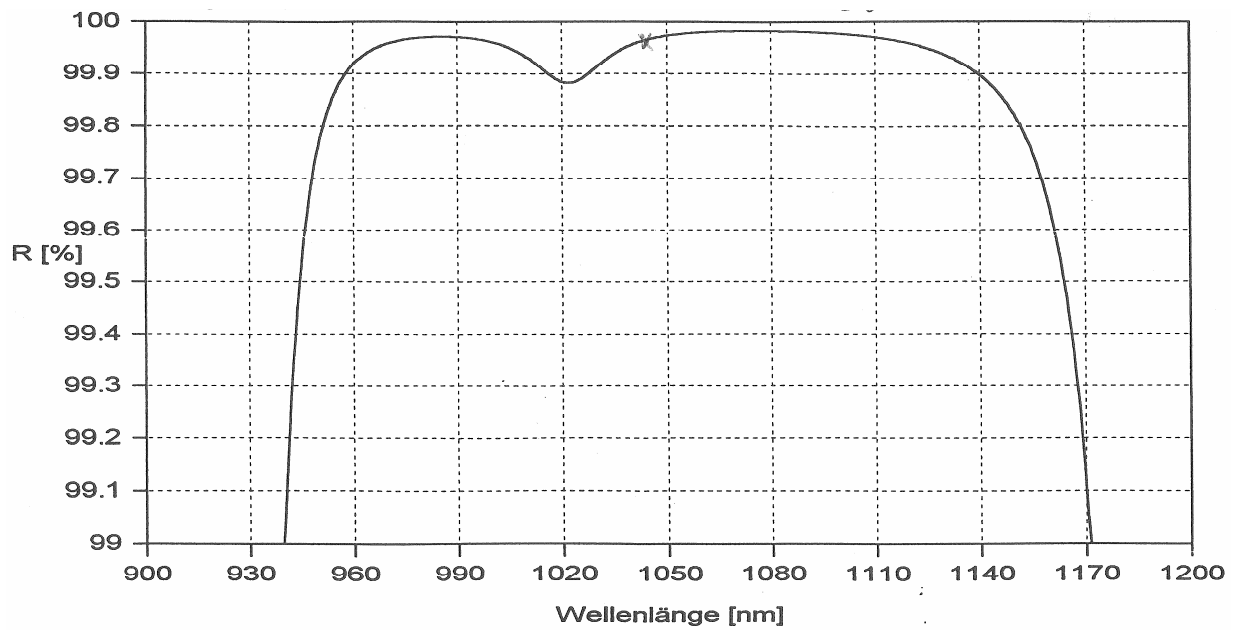


Figure 8. Reflection property in the third chirped mirror.

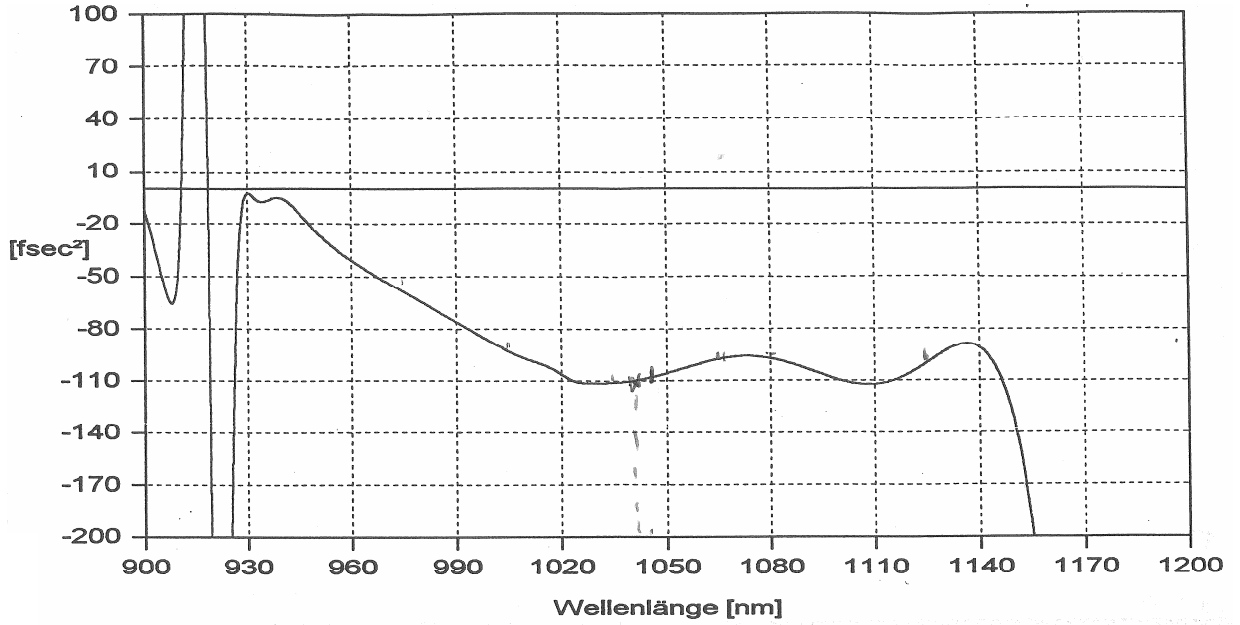


Figure 9. Group delay dispersion spectrum of  $-110 \pm 20 \text{ fs}^2$  in the third chirped mirror for the laser wavelength range between 1012 to 1069 nm.

#### Appendix D: Birefringent Phase Matching.

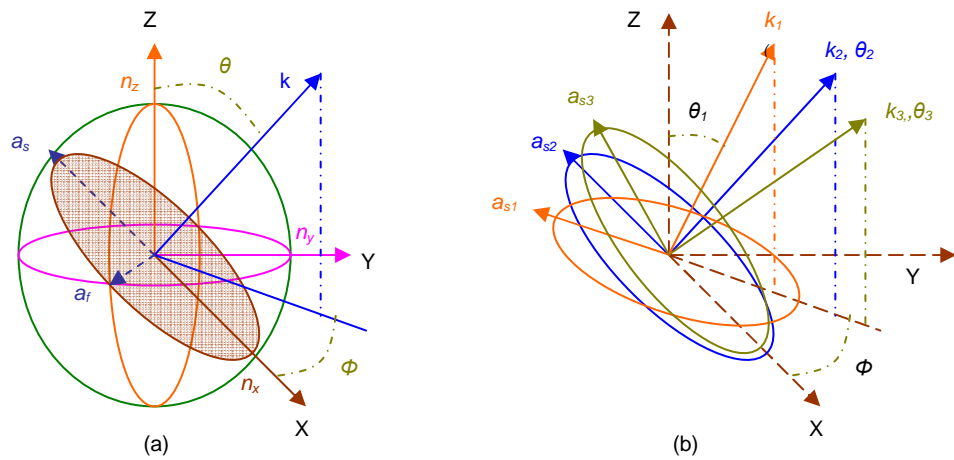


Figure 10. Three-dimensional index ellipsoid for a biaxial crystal where (a) consists of two polarisation eigenstates  $a_s$  and  $a_f$  and (b) shows angular dependence polarisation direction for  $a_s$  at three different angles  $\theta_1, \theta_2$  and  $\theta_3$ . Subscript “s” represents slow-ray and subscript “f” represents fast-ray [1].

One of the widely used phase matching techniques involves the exploitation of birefringence in an anisotropic nonlinear crystal, so called birefringent phasematching (BPM) [2]. Birefringence refers to a material property where different refractive indices are obtained for distinct polarisations. These refractive indices depend on the direction of propagation, polarisation and frequency of the incident waves. In a three dimensional index ellipsoid, the principal refractive indices of the crystal  $n_x, n_y$  and  $n_z$  along the axes

$x$ ,  $y$  and  $z$  can be depicted in figure 10. This crystal is said to be biaxial because it consists of two optic axes as  $n_x \neq n_y \neq n_z$  where  $n_x < n_y < n_z$ . The optical axis is defined as the propagation direction in a crystal where the refractive indices for both ordinary ( $o$ ) and extraordinary ( $e$ ) polarisation indices are equal. The wavevector direction  $k$  has an angle  $\theta$  and  $\phi$  from the  $z$ -axis and  $x$ -axis respectively [figure 10(a)]. By considering " $x-y$ " axis in the horizontal plane and " $z$ " axis in the vertical plane, two polarisation eigenstates  $a_s$  and  $a_f$  lie perpendicular to the wavevector  $k$  as shown in the shaded region. Subscript " $s$ " with a larger value of light velocity signifies the slow-ray along the vertical plane while subscript " $f$ " that has a smaller value of light velocity signifies the fast-ray along the horizontal plane. The refractive indices for these two polarisation eigenstates,  $n_f$  and  $n_s$  are given as:-

$$\frac{1}{n_f} = \frac{\sin^2 \phi}{n_x^2} + \frac{\cos^2 \phi}{n_y^2} \quad (1)$$

and:-

$$\frac{1}{n_s} = \frac{\cos^2 \theta \cos^2 \phi}{n_x^2} + \frac{\cos^2 \theta \sin^2 \phi}{n_y^2} + \frac{\sin^2 \theta}{n_z^2} \quad (2)$$

The polarisation eigenstate  $a_f$  that has a constant polarisation direction with angle is called as ordinary beam,  $o$ -beam while the remaining polarisation eigenstate  $a_s$  that has angular dependence polarisation direction is called as extraordinary beam,  $e$ -beam. The latter physical scheme is depicted in figure 10(b) where the direction of  $a_s$  varies at three different positions as the wavevectors  $k_1$ ,  $k_2$  and  $k_3$  propagate at the corresponding angles of  $\theta_1$ ,  $\theta_2$  and  $\theta_3$  from the  $z$ -axis vertically. For simplification, another polarisation eigenstate  $a_f$  is not shown because it doesn't change with the polarisation angle  $\theta$ . However, this angular constant polarisation state is always perpendicular to either  $a_{s1}$ ,  $a_{s2}$  or  $a_{s3}$  at these three different positions.

For a uniaxial crystal that consists of an optic axis, two of the indices for principal axes  $x$ ,  $y$  and  $z$  are equivalent to each other where either  $n_x = n_y < n_z$  or  $n_x < n_y = n_z$ . The two of the indices that have similar values are named as ordinary beam and another

remaining index is named as extraordinary beam  $n_e$ . For  $n_e > n_0$  the crystal is said to be positive and for  $n_e < n_0$  the crystal is said to be negative. Figure 11 below demonstrates a three-dimensional index ellipsoid for a positive uniaxial crystal where  $z$  is taken as the optic axis. The shaded region in (a) depicts two polarisation eigenstates in a full analogy with those in figure 10(a) where  $a_o$  that indicates the ordinary beam is used instead of  $a_f$  in the horizontal plane to and  $a_e$  that indicates the extraordinary beam is used instead of  $a_s$  in the vertical plane.

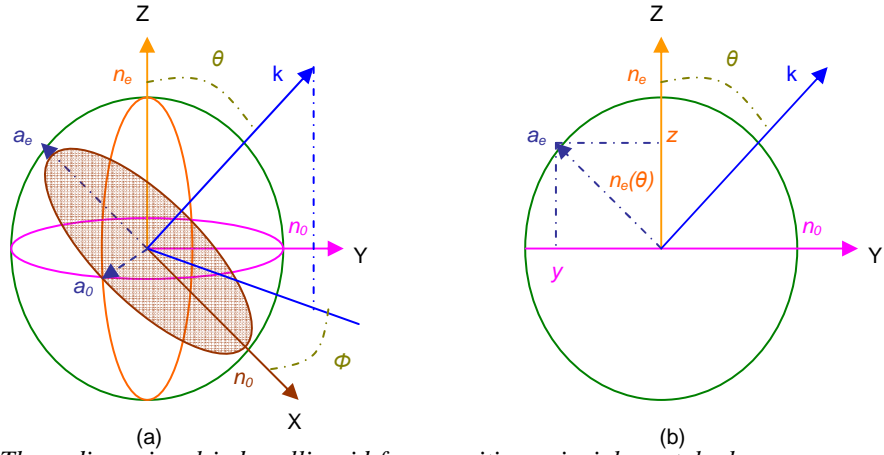


Figure 11. (a) Three-dimensional index ellipsoid for a positive uniaxial crystal where  $n_e > n_0$  and (b) the corresponding two-dimensional index ellipsoid in the  $z - y$  plane [1].

From figure 11(b), the simplification to the two-dimensional index ellipsoid in the  $z - y$  plane is presented to demonstrate the origins of the refractive indices equation for both polarisation eigenstates  $a_o$  and  $a_e$ . Based on the ellipsoidal formula of  $\frac{y^2}{n_o^2} + \frac{z^2}{n_e^2} = 1$ , these indices are deduced to be:-

$$\frac{1}{n_e^2(\theta)} = \frac{\sin^2 \theta}{n_e^2} + \frac{\cos^2 \theta}{n_o^2} \quad (3)$$

where  $y = n_e(\theta) \cos \theta$  is the length of the radius at  $y -$  axis and  $z = n_e(\theta) \sin \theta$  is the length of the radius at  $z -$  axis. However, the diagram at  $x - y$  plane for the wavevector propagation angle of  $\phi$  is not shown. This is because at similar refractive indices  $n_o$ , we obtain  $\sin^2 \phi + \cos^2 \phi = 1$ . The refractive index of this extraordinary beam  $n_e(\theta)$  depends on the propagation angle  $\theta$  as manifested by its property variation from  $n_e$  to  $n_o$  [figure

11(b)]. The medium doesn't imply any birefringence property when the wavevector propagates along the optic axis ( $\theta = 0$ ). This is because both polarisation eigenstates undergo the same refractive indices  $n_o$ . However, with the increase of the propagation angle  $\theta$  with respect to the optic-axis, both polarisation eigenstates exhibit two refractive indices  $n_o$  and  $n_e$  through the medium. Maximum value of  $n_e$  is obtained for positive ( $n_e > n_o$ ) and minimum value of  $n_e$  for negative ( $n_e < n_o$ ) uniaxial crystal as the wavevector propagates perpendicular to the optic-axis.

### References:-

1. K. Moutzouris, "Nonlinear frequency conversion in isotropic semiconductor waveguides," PhD. Thesis, School of Physics and Astronomy, U. of St. Andrews, 27-41 (2003).
2. F. Zernicke and J. E. Midwinter, "Applied nonlinear optics," John Wiley & Sons, New York, 153-176 (1973).

### Appendix E: Poynting Vector Walk-off.

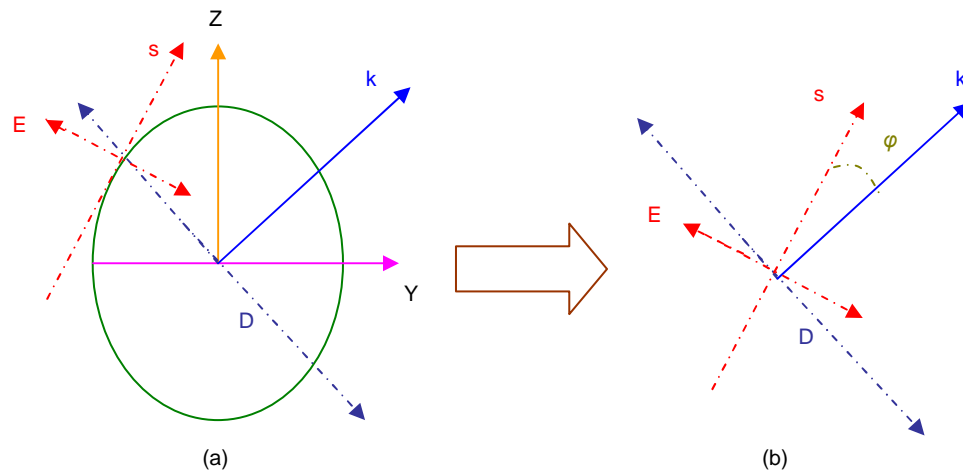


Figure 12. (a) Geometrical position of Poynting vector direction in a birefringent medium and (b) the corresponding walk-off angle  $\varphi$  between the wavevector  $k$  and ray direction  $s$ .

In Poynting Vector walk-off the electric field  $E$  is not parallel to the displacement field  $D$ . This is as the consequence of the deviation of the ray direction  $s$  (direction of flow energy) from the wavevector  $k$  with the angle of  $\varphi$  [figure 12(b)]. This leads to poor spatial overlap of the involving waves that suppresses the beam quality of the spot size. Another contribution of this poor spatial overlap is the decrease in the nonlinear efficiency.

**Appendix F: Basic Parameters that influence CW lasing performance in Yb:YVO<sub>4</sub> laser.**

In the geometrical design of Yb:YVO<sub>4</sub> laser that consists of especially three-mirror cavity, two types of assessments were carried out as mentioned in Chapter 6. The first was CW evaluation that employs 3 % and 1 % output couplers and the second was Kerr-lens mode locking evaluation that employs a 1 % output coupler at the end mirror. For the first assessment in CW configuration all the results obtained were simplified in table 1 to facilitate comparisons done between theoretical and experimental results.

*Table 1. A list of material and laser parameters for Yb:YVO<sub>4</sub> laser implementing 3 % and 1 % output coupler [Chapter 6].*

Three-mirror cavity Yb:YVO <sub>4</sub> femtosecond laser.		
Output Coupler, $T_{oc}$ (%)	3	1
Repetition rate, $f_{rep}$ (MHz.)	104.5	104.5
Pump source (nm)	981	981
Abs. coefficient, $\alpha$ (cm <sup>-1</sup> )	8	8
Crystal length, $l$ (mm)	2	2
Abs. Power, $P_{abs}$ (mW)	380	401
Pump Abs. Efficiency, $\eta_{abs}$ .	0.77	0.81
Pump beam waist, $w_{p,o}$ ( $\mu$ m)	17	17
Laser beam waist, $w_{l,o}$ ( $\mu$ m).	18 x 36	18 x 36
Pump spot size average, $w_p$ ( $\mu$ m)	17.8	17.8
Laser spot size average, $w_l$ ( $\mu$ m)	18.7 x 37.4	18.8 x 36.6
Yb-ions concentration, $N_{yb}$ (cm <sup>-3</sup> ).	$3.8 \times 10^{20}$	$3.8 \times 10^{20}$
Emission wavelength, $\lambda_{se}$ (nm).	1033	1047
Yb-absorption loss, $L_{yb}$ .	0.021	0.006
Absorption cross-section at emission wavelength, $\sigma_{abs}^{\lambda_{se}}$ (cm <sup>2</sup> ).	$2.76 \times 10^{-22}$	$7.47 \times 10^{-23}$

Output Coupler, $T_{oc}$ (%)	3	1
Experimental Threshold Power, $P_{th}$ (mW).	129	82
Max. Output Power, $P_{out}$ (mW)	164	146
Optical-to-optical efficiency (%).	43	36
Slope-efficiency (%).	69	47
Double-pass losses, $L_d$ .	0.009	0.009
Emission cross-section at emission wavelength, $\sigma_{se}^{\lambda_{se}}$ (cm <sup>2</sup> ).	$3.57 \times 10^{-21}$	$1.79 \times 10^{-21}$
Theoretical Threshold Power, $P_{th}$ (mW) (these values were calculated based on the spot sizes average over the length of the crystal)	148	113

## Acknowledgements

First of all, I would like to thank Prof. Wilson Sibbett, my current supervisor who allow me to undertake PhD. degree in his group and keep me on the right track towards my overall PhD. project. All your support, trust and kind words over the last few years have been the source of inspirations to continue my PhD. project until the final stages. The opportunity given to learn and obtain valuable knowledge from this group is greatly appreciated. I will take this golden opportunity to continue my research in solid-state femtosecond lasers.

To Alexander Lagatsky, thanks a lot for your effort and patience in giving me the guidance to finish both the experimental work and the thesis writing. Your help by far, has not only speeded up the accomplishment of this PhD project but has also given me the confidence and strength to continue my research work in South Africa.

(Kepada Alexander Lagatsky, terima kasih banyak-banyak terhadap segala usaha dan kesabaran dalam memberi tunjuk-ajar untuk menyiapkan eksperimen dan laporan tesis. Bantuanmu sehingga kini, bukan sahaja mempercepatkan penyiapan projek PhD ini tetapi telah memberikan saya keyakinan dan kekuatan untuk meneruskan penyelidikan di South Africa. Pengalaman manis yang dikongsi bersama ketika di makmal dan Munich akan diingati selalu selama-lamanya.)

Special thanks also must be given to my superfriends Tom Brown and Christopher Leburn who proof read some of my thesis and gave ideas/suggestions. To the special members of W-squad including Ben Agate, Pascal Fischer and Alan McWilliam thanks a lot for your support and answering some of my questions relating to my work. Your willingness to let me borrow various bit of equipment through the duration of my PhD project and for providing the happiest working environment in the world of femtosecond lasers. The wonderful experience that we have together during Munich conference can't be forgotten especially your effort to try to answer my question about the mystery of  $1+1=?$  at the time when we have had meals together. I would also like to give a mention to other members of W-squad including Edik Rafailov, Helen Little (previous member), Maria Ana Cataluna, Douglas McRobbie, Fiona Bain and Craig McDougall. For Edik, don't forget our password and Russian greetings. For those people who I forget to put their name here, I wish your success and *May God bless you* ! For Antonia Carruthers, thanks a lot to teach me MatchCad model at the last stage of my thesis writing.